

**Univerzita Karlova / Charles University**

**Lékařská fakulta v Plzni / Faculty of Medicine in Pilsen**

Studijní program: Anatomie histologie a embryologie

Ph.D. study program: Anatomy, histology and embryology

Studijní obor / Branch of study: D4AH5112



**Mgr. Lucie Vrabcová**

**INTERAKCE BUNĚK S NANOMATERIÁLY A JEJICH VYUŽITÍ  
V BIOMEDICÍNĚ**

**THE CELL-NANOMATERIAL INTERACTIONS AND THEIR  
APPLICATION IN BIOMEDICINE**

Dizertační práce / Ph.D. Thesis

Školitel / Supervisor: Doc. RNDr. Marie Hubálek Kalbáčová, Ph.D.

Plzeň / Pilsen 2019

**Prohlášení:**

Prohlašuji, že jsem závěrečnou práci zpracovala samostatně a že jsem uvedla všechny použité informační zdroje a literaturu. Tato práce ani její podstatná část nebyla předložena k získání jiného nebo stejného akademického titulu.

**Statement of authorship:**

I declare that I prepared the Ph.D. thesis independently and that I stated all the information sources and literature. This work or a substantial portion thereof has not been submitted to obtain another academic degree or equivalent.

V Plzni / In Pilsen

Podpis / Signature

Firstly, I would like to express my sincere gratitude to my supervisor Doc. Marie Hubálek Kalbáčová, Ph.D. for the support of my Ph.D. study and related research, for her patience, motivation and immense knowledge. Her guidance helped me in research and writing of this thesis. My sincere thanks also goes to Ing. Lucie Vištejnová, Ph.D. who helped me with practical and theoretical basics of my early work in the lab. I am also grateful to Ing. Jan Džugan, Ph.D.; Prof. Minoru Fujii, Ph.D.; Assoc. Prof. Ádám Gali, Ph.D., DSc and Prof. Ing. Václav Švorčík, DrSc. and their teams for preparation of such unique nanomaterials and for their cooperation and effort in comprehension despite our different scientific orientation. Special thanks belong to my amazing colleagues and friends from Prague and Pilsen - Pavla, Martina, Blanka, Tonda, Tereza and Iveta. I thank them for their help, support and friendly atmosphere in both laboratories.

Finally, I would like to thank my beloved parents, husband and son for their care, love, support and patience.

## **Abstract**

Nanomaterials entered the biomedicine already at the beginning of the millennium and they still bring new and unique advances and possibilities for treatment, diagnosis and regeneration, thus they continue to facilitate the development of personalized medicine. Interactions at nanoscale allow until then unconceivable opportunities to influence processes on molecular level. The completely new perspectives of nanomaterial applications jointly raise attention concerning health and environmental safety issues. Although a lot of novel biomedical applications of nanomaterials have emerged, the vast majority is still found to be at the stage of a concept. The consistent basic *in vitro* research of elemental interactions of nanomaterial with biological environment should represent an essential part of its development.

The concern of this thesis was to describe the cytocompatibility and interactions of two types of nanomaterials with different human cells. First, ultra-fine grain titanium was tested for prospective use in implant development. We confirmed its positive effect mainly on the growth of osteoblasts and recommended the further pre-clinical trials of this material in a form of a bone or dental implant. Second, several types of ultra-small (< 5 nm) nanoparticles of different origin (silicon, gold and platinum) were described in various conditions to obtain information about their time- and concentration-dependent cytotoxic potential and behavior in cell culture. The formation of protein layer on nanoparticle surface, which naturally occurs in biological fluids, proved to be a crucial parameter for interactions with various cell types. For subsequent research, a series of modifications of mentioned nanoparticles were proposed in order to improve their performance in living organism.

This thesis elucidates the importance of basic *in vitro* evaluation of nanomaterials and emphasizes the need of interdisciplinary cooperation in this complex topic of integration nanotechnology into biomedicine.



## Table of Contents

1 Novel Approaches in Regenerative Medicine.....	8
2 Biomaterials .....	9
2.1 Definition and Types.....	9
2.2 Biomaterials in Regenerative Medicine .....	10
2.3 Biocompatibility and <i>In Vitro</i> Evaluation .....	11
3 Nanomaterials .....	14
3.1 Definition and History of Nanomaterials.....	14
3.2 Pros and Cons of Nanomaterials in Biomedicine .....	16
3.3 Nanosurfaces .....	18
3.3.1 Important Aspects for Application in Biomedicine .....	18
3.3.2 Bio-implants with Nanosurface.....	20
3.3.3 Cells Interactions with Nanosurfaces.....	22
3.3.4 Nanostructured Titanium .....	25
3.4 Nanoparticles.....	26
3.4.1 Applications of Nanoparticles in Biomedicine .....	26
3.4.2 Interactions of Nanoparticles <i>In Vitro</i> and <i>In Vivo</i> .....	28
3.4.3 Cellular Uptake and Trafficking of Nanoparticles.....	31
3.4.4 Quantum Dots and Silicon Based Nanoparticles .....	34
3.4.5 Gold and Platinum Nanoparticles .....	35
4 Aims of the Thesis .....	37
5 Materials and Methods.....	38
5.1 Methods of PART I. - Unpublished Data (B) .....	40
5.1.1 Evaluation of Biological Responses of Human Dermal Fibroblasts and Human Keratinocyte Cell Line to Ultra-Fine Grain Titanium.....	40

5.1.2	Detection of Inflammatory Cytokines IL-8 and TNF- $\alpha$ after Exposure of Human Blood Samples to Ultra-Fine Grain Titanium .....	40
5.1.3	Detection of Collagen Type I in Collected Cultivation Media after Cultivation with Ultra-Fine Grain Titanium .....	41
5.2	Methods of PART II. – Unpublished Data (E) .....	42
5.2.1	Evaluation of Cytotoxicity of Silicon-Carbide Nanoparticles .....	42
5.3	Methods of PART III. - Unpublished Data (F).....	43
5.3.1	Colocalization of Selected Endocytic Cell Structures with Silicon Quantum Dots .....	43
5.3.2	Live Imaging of Cells Interacting with Silicon Quantum Dots .....	45
6	Results.....	46
6.1	PART I: Ultra-Fine Grain Titanium (A, B) .....	48
6.1.1	Publication A: Biological evaluation of ultra-fine titanium with improved mechanical strength for dental implant engineering .....	49
6.1.2	Unpublished data (B): Evaluation of Biological Responses of Human Dermal Fibroblasts and Human Keratinocyte Cell Line to Ultra-Fine Grain Titanium.....	51
6.1.3	Unpublished data (B): Detection of Inflammatory Cytokines IL-8 and TNF- $\alpha$ after Exposure of Human Blood Samples to Ultra-Fine Grain Titanium .....	59
6.1.4	Unpublished data (B): Detection of Collagen Type I in Collected Cultivation Media after Cultivation with Ultra-Fine Grain Titanium.....	63
6.2	PART II: Silicon-based Nanoparticles – Cytotoxicity and Basic Imaging (C-E) .....	65
6.2.1	Publication C: The impact of doped silicon quantum dots on human osteoblasts .....	66
6.2.2	Publication D: Silicon Quantum Dots and Their Impact on Different Human Cells.....	68

6.2.3 Unpublished data (E): Evaluation of Cytotoxicity of Silicon-Carbide Nanoparticles.....	70
6.3 PART III: Silicon Quantum Dots – Advanced Visualization (F) .....	72
6.3.1 Unpublished data (F): Colocalization of Selected Endocytic Cell Structures with Silicon Quantum Dots.....	73
6.3.2 Unpublished data (F): Live Imaging of Cells Interacting with Silicon Quantum Dots .....	79
6.4 PART IV: Gold and Platinum Nanoparticles (G) .....	81
6.4.1 Publication G: Preparation of Noble Nanoparticles by Sputtering – Their Characterization .....	81
7 Discussion .....	83
8 Conclusions .....	93
9 Complete List of Authors’ Publications.....	96
10 List of Abbreviations.....	97
11 References .....	99
12 Original Publications Used for Ph.D. Thesis in Full.....	116

# 1 Novel Approaches in Regenerative Medicine

Increasing average age of the population places demands on a longtime maintaining of the quality of life. Tissues of a human body are no longer capable of sustaining of their proper functions due to age, chronic disease, damage or simply limited regenerative capacity of certain organs (Baddour et al., 2012). Regenerating the damaged tissues, which have not the possibility to recover by themselves, is the main concern of regenerative medicine. This biomedical approach promotes the rapid development of the novel therapies, which offers a complex recovery without undesired side-effects while avoiding the exacting organ transplantation or a lifelong treatment by medications. General restoration of a structure and function of the damaged tissues and organs is the crucial description differing regeneration from reparation where the restitution is based on epithelial proliferation and fibrosis which mostly cause the unpleasant scarring (Mason and Dunnill, 2007). Original concept of regenerative medicine still changes through the time as it accommodates to the interdisciplinary linkage and to the novel discoveries in the field of therapeutic techniques.

Nowadays, due to the fast progress in medical technologies regenerative medicine also encompass tissue engineering, early recognition of the development of the disease by the wide range of diagnostic systems, targeted drug delivery systems and microelectronic devices (Eberli, 2014; Williams, 2009). Treating complex diseases by promoting the self-healing processes in organism cannot be considered as a straightforward therapy but it calls for the interplay of synthetic materials, cells and a cascade of factors affecting their mutual interactions (Qi et al., 2015). The same criteria must be met also for diagnostic or targeted delivery techniques where the outcomes of therapy are highly dependent on the reactions of the inner environment of the body and the material used.

Employing the aspects of cell biology, material science and biomedical engineering into one therapeutic discipline enables a whole new look into the treatment of former end-stage diseases (Atala, 2012).

## **2 Biomaterials**

### **2.1 Definition and Types**

Biomaterials are one of the essential cornerstones of human tissue resurgence as they can replace or repair damaged tissue structures. First attempts of definition of the term „biomaterial“ were completed on Consensus Conference on Definitions in Biomaterials Science by the European Society for Biomaterials in 1987 (Williams, 1987) and later were modified to its preferred definition in 1999 as „a material intended to interface with biological systems to evaluate, treat, augment or replace any tissue, organ or function of the body“ (Williams, 1999). According to IUPAC definition from 2012 biomaterial is described as “a material exploited in contact with living tissues, organisms, or microorganisms” (Vert et al., 2012) but here we must point out that the main scope of biomaterials is focused on health care (Williams, 2009).

Technological advancements still change the original definitions and expectations determined for biomaterials more than 50 years ago. The former idea of inert substance with mostly passive functions has been replaced by the design of materials with bio-inductive properties (Keane and Badylak, 2014). Recent approach tries to involve biomaterials in active regeneration to help the renewal of the nonfunctional tissue by supporting the healing process of the organism.

According to the material science, biomaterials encompass substances based on metal, ceramics and polymer or they form a composite of different materials (synthetic or nature-derived). Moreover, some of the materials listed under the groups mentioned above can be categorized as biodegradable in the classification (Ferraro, 2016). The strict sorting concept according to the type of material has become very confusing as the techniques of nanotechnology and self-assembly enabled fabrication of the brand new complex structures purposefully developed for utilization in health care (Williams, 2009).

Evolution of biomaterials started with substances whose mechanical properties matched to the structure of the damaged tissue without invoking undesirable reactions of the body. Such conditions were met by the first pure metals or alloys e.g. 18-8 stainless steel in 1920 (Fazel, 2011) or by polyester fiber Dacron® in 1953

(Batty et al., 2015; Keane and Badylak, 2014). Further research led to the development of improved materials with value added for superior tissue integration (hydroxyapatite coating), degradability (collagen) or anti-inflammatory activity (antiseptic or antibiotic coating). Currently, only materials with the enhanced bioactivity find their way to the clinical use and can be either artificially synthesized or based on natural materials. Improving the bioactive properties of synthetic materials can be achieved by a) coupling with the proteins naturally occurring in extracellular matrix (ECM), e.g. growth factors or adhesive proteins (He et al., 2008; Zhu et al., 2009) or b) changing physical and mechanical properties of the material by surface treatment (micro- and nanofabrication) or c) by size and shape adjustment of particles (Broz et al., 2009; Chen et al., 2014; Toy et al., 2014). Natural materials mostly focus on the most authentic imitation of the ECM by forming so called ECM scaffolds based predominantly on nature-derived polymers (Badylak et al., 2011; Valentin et al., 2010).

## **2.2 Biomaterials in Regenerative Medicine**

Broad spectrum of biomaterials serves as universal tool in many applications in human medicine. Indeed it should be mentioned that for certain biomaterial there is an application specificity therefore the success in some type of application cannot be automatically expected in different one (Keane and Badylak, 2014).

History of biomaterials in regenerative medicine is dated back to the first aseptic surgery techniques which facilitated the fixation of long bone fractures by the use of metallic screws and implants. First joint replacements by metal alloys followed in rapid succession (Parida et al., 2012). Implantable bone plates, joints and dental devices still make up the majority of biomaterials used in tissue replacement. Another extension of application potential is recorded with the synthetic polymers and their utilization as corneal, blood vessel and heart valve replacements. In general, implantable devices represent the highly diverse group of material types of different origin (artificial, nature-derived), structure (composites of more materials), shapes (fibers, sheets, films, etc.) and forms (solid, foam, soft fillings, etc.).

A completely new direction in regenerative medicine has been created due to the connection to recent findings in the field of physics and chemistry. From this

point on, optical (Parak et al., 2003) or magnetic (Pankhurst et al., 2009) properties of the new materials have led the way to the novel imaging and real-time sensing techniques (Liu et al., 2015; Mattoussi et al., 2012; Nichols et al., 2013). Knowledge of the physicochemical properties of certain materials also enabled introduction of the incoming therapeutic methods based on cell-specific targeting e.g. cancer-cytotoxic probes (Kotler et al., 2013; Lin et al., 2015), drug delivery systems (Wang et al., 2015, 2014) or gene therapy (Kim et al., 2015).

Nowadays, biomaterials in regenerative medicine can be sorted either by the way of their use or by their site-specificity (organ, body system) (Parida et al., 2012). Systemic summary of various biomedical applications of biomaterials is listed in Table 1. The most important aspects common for all biomaterials with the intention of clinical use include biocompatibility, systematical inert properties (non-inflammatory, non-allergic, non-carcinogenic) and possible manufacturability and reasonable financial demands.

<b>Biomedical utilization</b>	<b>Example</b>
tissue replacement	joint prostheses, vascular grafts, artificial heart valve
defect correction	bone plates and screws, contact lens, mammoplasty
drug delivery	targeted drug release, gene therapy
diagnosis	imaging techniques, biosensors
ex vivo research	gene transfer via non-viral vectors

**Table 1** – Different approaches of biomaterial utilization in biomedicine

### **2.3 Biocompatibility and *In Vitro* Evaluation**

The essential principle of biomaterials to distinguish them from any other material is the fact that they can co-exist with the human body tissues while keeping their inert properties assuring harmless effect towards the recipient. This statement gave the foundation to the subject of biocompatibility. Biological and chemical inactivity has always been of capital importance since the introduction of the first generation of the long-term implantable medical devices more than 60 years ago. Biocompatibility in this early biomaterial research was defined as a summary of situations, which must not occur after the contact of the biomaterial with the human tissue. The primary parameters for selection of the materials were based on the local

or systemic non-toxicity, non-immunogenicity, non-thrombogenicity, non-carcinogenicity and many other harmless principles (Williams, 2008).

In general, biocompatibility should not be considered as a simple attribute of certain material but more likely as the whole concept of abilities to perform its desired functions. Therefore we have to keep in mind that biocompatibility should not be solely reliant on the intrinsic characteristics of the material but depends on the site and situation of intended use (Naahidi et al., 2013). Anatomical location is of a crucial importance when evaluating biocompatibility as the reactions to the presence of biomaterial can significantly vary in dependence to the certain tissue. Therefore we cannot predict if the required or undesired adverse effect will occur when the site-specificity of the biomaterial is not respected (Nicolette et al. 2011; Anderson et al. 2008). Moreover, as it was mentioned before, biomaterials are used in still more complex situation including drug delivery, osteoinduction of implantable devices or real-time biosensing, where the inactivity of the material is definitely out of their intention. Hence, the redefined paradigm of biocompatibility as a beneficial ability for medical therapy was proposed by D. F. Williams in 2008 (Williams, 2008).

Immense variability of tissue responses to the different biomaterials creates very challenging field for the standardization of the processes for testing of biocompatibility. Development of such standards must be dynamic and continuous because of the rapid progress in technologies (Hanks et al., 1996). Many challenges emerge when we become conscious of the fact, that biocompatibility influence a variety of external issues e.g. the final design of the device (Pizzoferrato et al., 1994; Polikov et al., 2005) and the patient-to-patient variability. Risk assessment therefore requires performing the biocompatibility studies on each new material in the most detailed way. In addition, since the amount of new materials increases quickly every year there is a need of a simple, fast and consistent initial *in vitro* screening to evaluate whether the material is suitable for more complex testing. Above that, outputs of such *in vitro* models should be in good correlation to the very comprehensive *in vivo* situation.

Significant efforts have been focused on this difficult task and so many guidelines have been produced until the standard guideline document ISO 10933-1 was first issued (International Organization for Standardization, 2009). Initial stage of biocompatibility evaluation *in vitro* is called cytotoxicity tests and they consist



merely from morphological observations, viability test, or adhesion assessment. Second stage focuses on the functional evaluation such as inhibition of the proliferation, inhibition of metabolic activity or phagocytosis index. In this phase mostly continuous cells lines are chosen because of their uniform characteristics and fast growth which allow to perform large number of tests in a short period of time. Further evaluations include immunomodulation activity, bone-forming activity or modulation of coagulation for which the primary cells such as macrophages or osteoblasts are a more suitable choice (Pizzoferrato et al., 1994).

Extreme sensitivity of *in vitro* testing assures the recognition of even very low toxicity potential of the material as this conditions lack the possibility of elimination of the waste products. The overestimation of the cytotoxicity together with the limited time for estimations are the major drawbacks of the *in vitro* biocompatibility evaluation. On the other hand, *in vitro* tests are a valuable tool for investigation of specific interactions even at the molecular level and clarification of the changes in cell functions. Accompanied with the results from histological or blood analysis, cell culture *in vitro* evaluations open up the way for the biomaterial to advanced pre-clinical tests *in vivo*.

## 3 Nanomaterials

### 3.1 Definition and History of Nanomaterials

The prefix “nano-” itself labels and refers to very small-sized object as it originates from the Greek word meaning “dwarf”. In the modern era, signifying certain subject, activity or industry with the “nano” label becomes increasingly popular within the scientific world although many of these designations are not even precisely defined (Buzea et al., 2007). In metric system, nanometer represents the  $10^{-9}$  m and the dimensions of the objects in this range of length are termed as nanoscaled. The size reliance is fundamental for all the definitions of nanomaterial created so far though the exact size range is inconsistent among them.

International and many national regulatory organs have proposed numerous nanomaterial definitions and terminologies with the core aspects concerning external dimensions, solubility, new properties, aggregation or distributional thresholds (Boverhof et al., 2015). Nowadays, only definitions of the normative character on European or global level should be accepted to avoid conflicted descriptions. In 2011 European Commission published Recommendations on the definition of nanomaterial as follows: *“Nanomaterial is natural, incidental or manufactured material containing particles, in an unbound state or as an aggregate or as an agglomerate and where, for 50 % or more of the particles in the number size distribution, one or more external dimensions is in the size range 1 nm - 100 nm. In specific cases and where warranted by concerns for the environment, health, safety or competitiveness the number size distribution threshold of 50 % may be replaced by a threshold between 1 and 50 %.”* (EU Commission, 2011). Alongside, the Recommendations advert to the ISO document of terminology and definitions of nano-objects which was revised in 2015 as ISO TS 80004-2 (International Organization for Standardization, 2015). According to ISO definitions, nanomaterial is described as a material with at least one external nanoscaled dimension or exhibiting internal structure in the nanoscale. The term “nanoscale” in here denotes the length interval approximately from 1 nm to 100 nm. In accordance with the number of nanoscaled external dimensions ISO characterizes the different shapes forming nano-objects, which is schematically illustrated in Fig. 1.

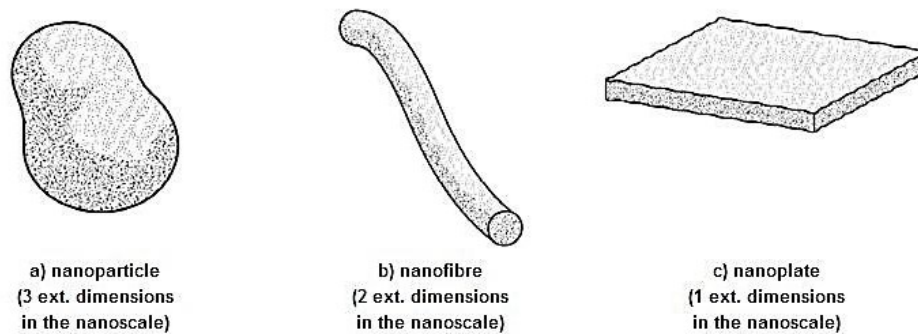


**Figure 1** – Illustrational scheme of various shapes of nano-objects. Adopted from ISO TS 80004-2 (International Organization for Standardization, 2015).

Naturally occurring nanomaterials have always been an integral part of our environment both in the inorganic and organic systems. Hence, many of them could only be discovered thanks to recent advances in technology, which help us to localize, isolate and describe the vast range of their structural and chemical varieties. As a common natural substance, nanomaterials can be found in volcanic ash, sand, dust or in biological matter (Lohse, 2013). Some prominent representatives have already been used for research purposes and their structure have been studied and emulated in order to create a template for synthetic nanomaterials with desired properties for diverse functions, e.g. lotus leave inspired the development of hydrophobic fabrics and coatings (Feng et al., 2002). As well as the natural ones, also so called incidental synthetic nanomaterials are present in our environment in a large extent as they are the secondary product of human activity (combustion engines, mining).

Numerous man-crafted nanomaterials can be traced back to the ancient times with the first understanding and manipulation of the material (colloidal gold and silver in glass). With the sophisticated instrumentation of the modern era starts the actual development of nanotechnology. Although the ideas of nanoscale manipulations were proposed before, the inception of the concept of the engineering on the atomic scale is linked to Richard P. Feynman and his ground-breaking speech on the meeting of the American Physical Society in 1959 called “There’s Plenty of Room at the Bottom” (Feynman, 1960). In 1974, the term nanotechnology was coined for the first time by Norio Tamiguchi and this field of intentionally machined

nanomaterials started to develop extremely fast. Following decades have brought a number of significant discoveries - Buckminsterfullerene “buckyball” (C<sub>60</sub>) in 1985 awarded by Nobel Prize in Chemistry, semiconductor quantum dots in 1985, carbon nanotubes in 1991 and scanning force microscope as a unique tool for quantitative and qualitative description of nanomaterials. In the early 2000's the rapid increase in nanomaterial engagement in consumer products fabrication was recorded (sun-screens, batteries, digital cameras).

Nanomaterials owe their unique properties to two factors which radically change their behavior in contrast to the original chemically identical bulk material: a) quantum confinement – phenomena of delocalized electron states causing discontinuous quantum effects and b) surface effects – smoothly scalable effects related to the fraction of atoms at the surface (Roduner, 2006). Both of these aspects influence the nanomaterial final mechanical, optical, electrical, and magnetic properties as well as chemical reactivity (Buzea et al., 2007). Nowadays, two main strategies are used for fabrication of almost every nanomaterial. First called bottom-up technique provides *de novo* synthesis of products as the nanoscale versions of the bulk material. Typical outcome structures of this approach are quantum dots or carbon nanotubes. The other technique works the other way around, thus it makes use of already existing materials and modifies them to reach the nanostructure. This strategy is called by the term of top-down technique and enables the fabrication of various nanopatterned substrates (Verma et al., 2011). It could be stated, that all current microelectronics is fabricated using this approach.

### **3.2 Pros and Cons of Nanomaterials in Biomedicine**

Biological systems and their building materials very often feature hierarchical structure and thereby form natural functional nanomaterials as it was mentioned in chapter 3.1. Hierarchical structures of many biological materials have been studied from the smallest nanoscale to the macroscale, moreover, the arrangement of the particular features in building blocks of organisms has been submitted to the detailed examination to connect structure to its mechanical, biological and chemical properties (Bechtle et al., 2010). The longest investigations have been performed on the structure of a bone (Reznikov et al., 2014; Rho et al., 1998). Bone is a part of the

family of mineralized connective tissue which is distinguished by a complex seven-level hierarchical structure of different organic and inorganic components (Fig. 2) working in a concert to provide its unique supportive, protective and storage functions.

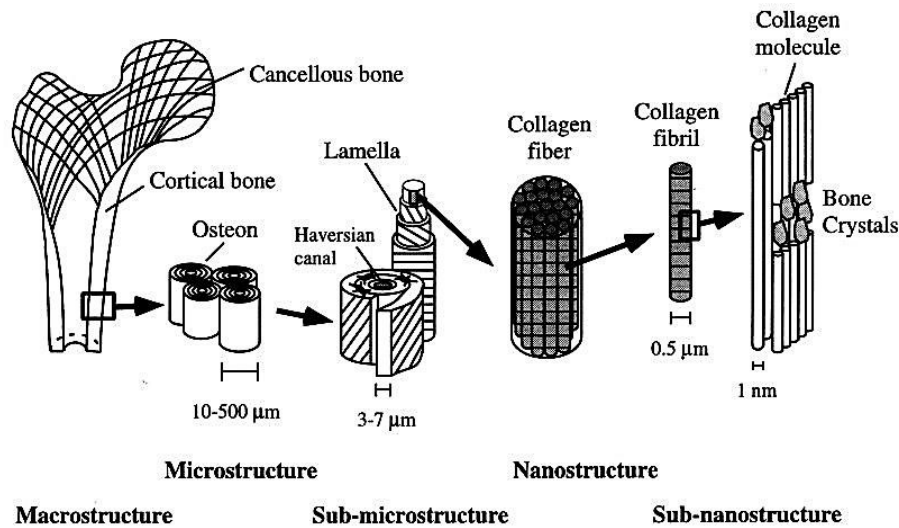


**Figure 2** – Hierarchical organization of the bone structure. Adopted from (Rho et al., 1998).

Nanomaterials can mimic surface as well as inner properties of such natural tissues. Many bottom-up and top-down fabrication techniques are currently available to produce “smart” complex nanomaterials which can not only imitate the natural tissue environment but also influence the cellular responses at the molecular level (Engel et al., 2008). Nanometer dimensions enable the direct interaction of cells and their surroundings so the tunable physicochemical and biomimetic properties of nanomaterials help to overcome the limitations associated with the actual regeneration strategies (Zhang and Webster, 2009). Integration of nanotechnology and medicine (sometimes inaccurately denoted as nanomedicine) opens up new possibilities for controlling the biochemical and mechanical microenvironment of the human body tissues. The appropriate design of selected nanomaterial can further facilitate the cell growth and modification and also deliver agents and track specific regions or cells within the body (Verma et al., 2011).

The unusual properties of nanomaterials indeed raise awareness about their possible unrecognized negative or even toxic effect for the biological systems and the environment. Incidental and many commercial nanomaterials (cosmetics,

sporting goods, waterproof clothing) surround us in everyday life for many decades and their global expansion caused the birth of a new type of toxicology discipline – nanotoxicology. Involvement of nanomaterials in biomedicine raises concerns especially because of their affection of cellular and subcellular processes, uncontrolled deposition in the body or undesired penetration through the biological membranes due to the formation of complexes with proteins (Nel et al., 2006). The unexpected effects can be avoided by a proper compliance of series of the nanotoxicology requirements: a) sufficient characterization of nanomaterial, b) respecting of the good scientific practice and standard operation protocols, c) use of appropriate controls and reference materials (Krug, 2014). Still, of course, it cannot be guaranteed whether any adverse effect occurs from a long-term point of view, thus, researchers must be motivated to first of all pursue and publish also the negative studies equally as the “positive” ones.

### **3.3 Nanosurfaces**

#### **3.3.1 Important Aspects for Application in Biomedicine**

From the perspective of nanomaterial classification, nanosurfaces (NS) can be described either as one-dimensional since they exhibit nanoscale structure only in one dimension or as two-dimensional (2D) when considering their plate-like shape. The term of NS can be further specified or subdivided to nanolayers, nanofilms or nanocoatings. The confinement to the nanoscale may be produced by artificial or self-assembly deposition on a substrate (bottom-up) or the surface of the original sample may be mechanically or chemically degraded (top-down). It follows that the actual nanostructure may be of a different origin than the base substrate therefore it serves as a coating to provide the unique nano-related properties to the selected bulk material. The latter approach keeps the characteristics of the bulk material (stiffness, chemical composition) while amending only the surface topography.

Nanomaterials in the form of a sheet, a film or a coating have an unambiguous purpose in biomedicine and that is the nano-assisted *in-situ* tissue regeneration (e.g. chronic wound healing). The influence of devices with nanostructured surface is immense as they enhance a vast array of processes necessary for a proper healing in a

cell-material contact site, moreover, they can attract endogenous stem cells to the affected area (Qi et al., 2015). Directing cellular processes like extracellular matrix deposition, attachment/adhesion of required cell type with subsequent fast proliferation and differentiation into designated lineage is enabled by creation of the convenient nano/microenvironment (Lutolf et al., 2009). The resulting biological performance of the surface is dependent on several properties – roughness/porosity, chemistry, wettability, stiffness, charge and surface energy and usually affecting one variable causes alteration of the others (Gittens et al., 2011; Kalbacova et al., 2009). In general, surface roughness and chemistry are considered as independent parameters, though in practice it is complicated to prove it. Cell responses to the biocompatible nanomaterials of different combination of surface characteristics maintain the logical sequence of the contact-adhesion-spreading-proliferation events however unfavorable substrates exhibit low efficiency and prolonged periods of induction of subsequent processes (Liu et al., 2007). General rule for designing NS is to keep the high degree of hydrophilicity and surface energy and to adjust the stiffness of the material to the requirements of the type of adherent cells (Rehfeldt et al., 2007; Rupp et al., 2006).

Above all, roughness of the surface and specifically the nano- and microscale topography represent the crucial feature for interaction of cell cytoskeleton with material, thus profoundly influence the cell and tissue behavior through mimicking the extra-cellular matrices. The unique architecture of topography increases protein adsorption and bioactivity prior to the actual cell adhesion. Promotion of protein (fibronectin, vitronectin, laminin) attachment occurs due to significantly increased surface area of nano-topography and such thoroughly assembled protein basis stimulate cell adhesion and induces proliferation as illustrated in Fig. 3 (Zhang and Webster, 2009).

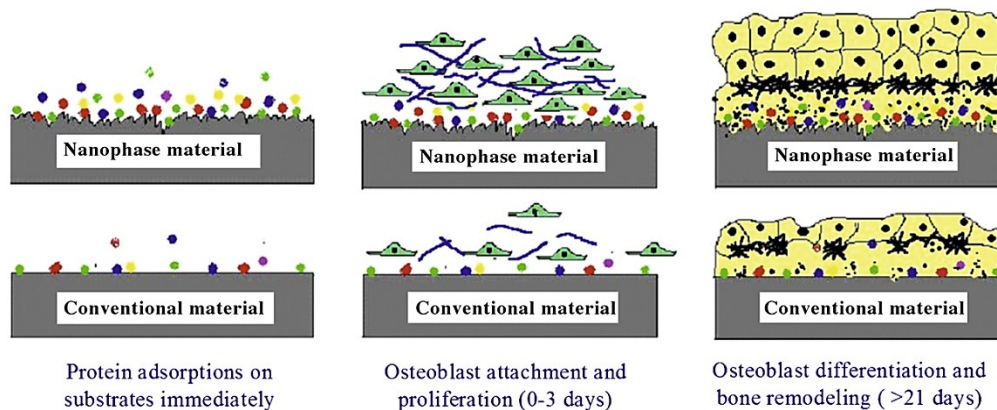


**Figure 3** – Comparison of nanosurface to conventional materials in the promotion of cell responses. Adapted from (Zhang and Webster, 2009).

The impact of topography is more pronounced when certain strategies of patterning are employed. Cells detect and respond to the topographical features based on their size and organization on the surface. Micro-sized dimensions correspond to the size of the whole cell thus the recognition is driven by the whole-cell guidance (Dalby et al., 2014). Such phenomena rather suppress cell proliferation though it is effective in promoting the differentiation of cells (Saito et al., 2010; Schwartz et al., 2009). On the other hand nano-sized dimensions may have a major impact on cellular responses as their dimensions correlate to the cell-surface receptors (Dalby et al., 2014). Moreover, disordered arrangement of the features of the same size has positive influence on cell differentiation compared to the ordered patterns (Dalby et al., 2007).

### 3.3.2 Bio-implants with Nanosurface

The surface treatment to nanoscale provides additional functionality to biomaterials and enables their tailoring to the needs of implantable devices. Nanostructured implants make use on the places of contact with the damaged tissue where they can play a key role in stimulating regeneration. Conventional implants, anyhow made from cytocompatible materials, still lack the long-lasting lifespan inside the tissues and gradual rejection occurs eventually in majority of the cases in the range of 10 – 15 years (Zhang and Webster, 2009).

Utilization of nanostructured implants takes place both in hard and soft tissue regeneration accordingly to the mechanical characteristics of the material. Synthetic and natural biodegradable polymers or carbon nanotubes prevail in the implantology



of soft tissues. Nowadays, the greatest emphasis in soft tissue engineering besides biocompatibility is placed on the right timing of biodegradation to guarantee enough time for sufficient attachment, spreading (eventually orientation) and growth of the right cell type on the affected area and to start degradation at the very end of the new tissue formation. The significant achievements are made mainly in vascular and skin regeneration where especially biodegradable polymers (e.g. PLGA, PLLA, PCL) are used in a form of composite nanofibers (Hasirci et al., 2006). Promises are also made for neural and lately for bladder tissue regeneration. In these cases, we talk about the implants as scaffolds since most of them act as the whole 3D frame nanostructure to let the tissue grow throughout the whole implant and their surface characteristics are not emphasized.

On the other hand, the hard tissue (bone, teeth, cartilage) regeneration often requires not only promotion of the healing processes but also sufficient mechanical resistance to keep the supportive competence of the tissue. In bone tissue regeneration the three ways of implant integration are described: osteoconductivity (mechanical support), osteogenicity (cell attraction) and osteoinductivity (cell differentiation) (Hasirci et al., 2006). Crucial for bone remodeling is the cooperation of bone-forming (osteoblasts) and bone resorbing (osteoclasts) cells. Osteoclasts prepare the surface of the previously-formed bone by the resorption of small cracks leaving the upper structure formed into numerous micro- and nanofeatures which are subsequently recognized by osteoblasts (Mulari et al., 2004). Many studies confirmed that the micro-scale pits and irregular nano-scale roughness on the surface of the implant represent the most suitable osteogenic and osteoinductive material (Chen et al., 2012; Gittens et al., 2011; Ostrovska et al., 2015). Integration of the implant to the bone tissue is a fundamental prerequisite to prevent loosening in load-bearing conditions. Various nanophase metals and ceramics have been designed up to date as bone implants, often with the use of hydroxyapatite as a coating because of its high similarity to the mineral component of the bone (Kokubo et al., 2003). Polymer and composite scaffolds as alternatives to metals are also on the rise in hard tissue regeneration; however, their use is limited to the non-load-bearing applications now. For now, the same situation is with cartilage and dental implant, where the nanostructured mechanically resistant implants are still more preferred (Burns et al., 2009; Guida et al., 2013).

### 3.3.3 Cells Interactions with Nanosurfaces

In standard situations, cells are not in direct contact with the artificial substrate. Contact is mediated by their interaction with protein layer which adheres to the surface of the material in the first place. Origin of this protein layer is in the standard supplemented cultivation media or in the body fluid for *in vitro* and *in vivo* conditions, respectively (Dhowre et al., 2015; Mager et al., 2011). The dynamics and highly complex structure of natural cellular environment still represents considerable challenge for translation into biomaterial and healthcare research.

In order to make up the highly organized tissue, adhesion-dependent (adherent) cells need to be anchored to their environment and they need to communicate and cooperate with each other. All the mentioned processes are possible thanks to the matter in the inter-cellular space which is denoted as extracellular matrix (ECM). Formation of ECM was crucial for the evolution of multicellular organisms and in most of the tissues ECM represents the vast majority of their total volume. ECM can be described as heterogeneous protein-based matrix which involves supportive, binding and freely mobile structures. Cells manage to form ECM via secretion of molecules of different abilities - structural support, elasticity, cell behavior regulation, tensile forces resistance etc. Furthermore, cells actively remodel ECM by the secretion of proteolytic enzymes (e.g. cathepsins, metalloproteinases) and they also release soluble factors controlling local and distant environment (Dhowre et al., 2015).

The main constituents of ECM are fiber proteins collagens which work as a skeleton for structural support of the matrix and enable binding of other proteins (Kim et al., 2011). In a bone tissue, collagens (type I and type V) make up 90% of the whole ECM. Next, elasticity of ECM is provided by protein elastin and the actual contact with cell membrane proteins is mediated by proteins like fibronectin, vitronectin and laminin, which present various peptidic motifs serving as ligands for binding of cell membrane receptors called integrins.

As it was mentioned at the beginning of this chapter 3.3.3, the very first contact of artificial substrate with biological environment initiates coating of the surface with proteins. Qualitative and quantitative assembly of this layer is determined by the composition of the biological fluid, protein concentration, size and mainly by specific surface-protein interactions mediated by surface properties (Rabe et al.,

2011). Many studies were conducted to improve cell-material interactions via preliminary adsorption or directed coating the material by specific peptides to mimic ECM. The most well-known example in general use is the peptidic sequence of ECM ligands – RGD (Arg-Gly-Asp) which was first discovered in fibronectin (Verrier et al., 2002; Zhu et al., 2009).

Synchronization of cells and their close surrounding on the interface is essential for cohesion of the whole tissue as it influences adhesion, spreading, proliferation, migration and differentiation of cells (Cai and Heilshorn, 2014). Anchoring to the surface by adhesion is crucial for survival and proper function of adherent cells. Adhesion of cells to ECM represents a few-phase event. At first, weak physicochemical forces (ionic, van der Waalls bonds) get involved and the early cell attachment is mediated by electrostatic interactions. Following biological adhesion starts with the transmembrane proteins integrins recognizing ECM ligands and formation of the first receptor-ligand pair. This specific integrin binding provides mechanical connection of inner cytoskeleton to ECM and enables the transmembrane signalization and gene expression regulation (Anselme, 2000). In latter phase the total adhesion strength is increased by the formation of numerous receptor-ligand bonds and the cytoskeleton undergo the active reorganization. Cell body flattens and spreads along the surface which causes the enlargement of the contact area. Adhesion strength amplifies as reorganization of cytoskeleton continues and more adhesion sites establish. Morphologic changes in cell shape and size (flattening, spreading) may be one of the indicators of the cell-ECM attachment (Ahmad Khalili and Ahmad, 2015). Simplified scheme of cell-material contact is illustrated in Fig. 4.

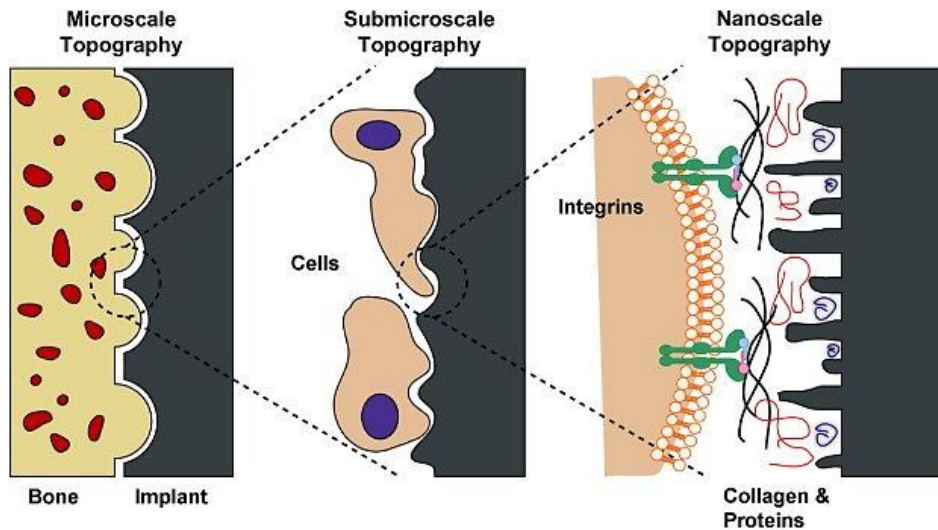


**Figure 4** – Schematic model of cell-nanosurface interactions on different scales. Adopted from (Gittens et al., 2011).

Sites of mature adhesions between cells and ECM substrate are molecular complexes referred to as focal adhesions (FA) or adhesion plaques and are typical for *in vitro* cell culture environment as this tight junctions (10 – 15 nm) occurs only rarely *in vivo* (endothelial cell resisting high hydrodynamic stress) (Anselme, 2000). The formation of FA occurs in cells with low motility and is promoted by the connection of ECM proteins with external part of cell membrane receptors (integrins) which further mediate interaction to the cytoskeleton proteins (actin) via intermediate proteins (talin) and more transduction proteins (vinculin, paxillin, tensin). FA thus translate the external mechanical and topographical information about the substrate to the intracellular environment and contribute to the maintenance of cell shape by influencing the actin cytoskeleton architecture.

The significant influence of proteins adsorbed on nanosurface on cellular behavior was confirmed by many *in vitro* studies which evaluated cell characteristics in presence or absence of serum proteins in culture media (Audiffred et al., 2010; Kalbacova et al., 2012; Verdanova et al., 2012). The important outcome of these works suggests that in initial serum-free conditions cell adhesion, proliferation and size are affected mainly due to different attachment mechanisms including hydrogen or van der Waalls bonds between the bare substrate and non-integrin receptors (glycoproteins). In following phase, cells start to produce ECM proteins and thus the non-specific sites of attachment are replaced by FA and proliferation or

differentiation of cells may continue in the same manner as in serum-enriched conditions. Although it is important to emphasize that the initial phase is crucial and further cell-material interactions could be negatively influenced.

Topographical features of nanosurface are of a special importance in formation of FA, especially in their localization, size and shape. FA formed on smooth surfaces are usually smaller with uniform distribution along the cell membrane whereas in the case of rough surface FA are preferentially localized in cell extensions (Anselme et al., 2000; Ostrovska et al., 2015). FA translated information of the state of external environment influence the cellular size and shape variability among different substrate topography as it was confirmed for various cell types (Chen et al., 2012; Teng et al., 2012), moreover, such information could lead to differences in ECM protein (mainly collagen) production (Kubo et al., 2009; Zhao et al., 2010).

### **3.3.4 Nanostructured Titanium**

Titanium (Ti) still represents one of the most widely used metallic material for implants in trauma surgery and in oral and orthopedic medicine (Mishnaevsky Jr. et al., 2014). The mentioned medical disciplines deal with ensuring the best possible performance of implanted devices to lower the recurrence of operational interventions to the body. In this field, one significant challenge still resists and that is the creation of an artificial implant which would exhibit high fracture toughness while meet the mechanical elastic properties of the hard connective tissue. Ti exceeds other materials in several mechanical and biomedical characteristics. Corrosion resistance is provided by the passive layer of  $\text{TiO}_2$  which spontaneously creates an inert barrier on the surface preventing any ion release thus ensuring Ti the status of highly biocompatible material (Browne and Gregson, 2000). Light weight, high formability and low elastic modulus enable easy fabrication of low-weight implants durable in the bending stress conditions (Greger et al., 2009). However, the mechanical strength under the long-term cyclic loading conditions has always been a major drawback of commercially pure Ti (cp Ti).

Addition of alloying elements allowed the significant improvement of fatigue strength yet even the most widely used alloy Ti-6Al-4V deals with the problem of slow leach-out of metal ions and their gradual accumulation in organism (Browne and Gregson, 2000). The brand new approach in manufacturing of cp Ti

encompasses the nanostructuring concept of grain refinement (Polyakov et al., 2014; Valiev et al., 2006). Inner nanostructure bestow cp Ti the desirable mechanical strengthening qualities, while it enables further surface treatment by nanostructuring of a different type (mechanical grinding, sand blasting, acid etching) for facilitated cell attachment (Estrin et al., 2011; Ostrovska et al., 2015). The correct tissue ingrowth is the best possible fixation mechanism of the implant, so only proper incorporation can assure the full use of all mechanical properties of nanostructured cp Ti to endure the shear forces nearby the implant either in bone or dental regeneration.

### **3.4 Nanoparticles**

#### **3.4.1 Applications of Nanoparticles in Biomedicine**

According to dimensionality, nanoparticles (NPs) are described as 3D nanomaterials since they exhibit nanoscale size in all 3 dimensions. From the morphological point of view, we distinguish various shapes (spherical, cylindrical, oval or cubic) which may be uniform in the whole sample in the case of engineered NPs or they could represent a collection of different shapes which occurs mainly in natural or incidental NPs (dust, emission vapors). Dispersions of one type of synthesized NPs are usually bound to carrier phase which in the vast majority is liquid (colloid, suspension). Though NPs dispersions also exist as aerosols or they could be freely assembled in a powder formulation (Buzea et al., 2007). The importance must be attached to the agglomeration tendencies, whereas some kind of NPs in defined conditions can only exist in an agglomerate state, thus their behavior corresponds to much larger particles (Bruinink et al., 2015). When considering the final effect of synthesized NPs, the mostly discussed issues involve composition, charge, size distribution or solubility. And even more variables join, when biomedical application is under consideration (biodegradability, clearance, interactions with proteins etc.).

A wide range of tunable NPs properties projects into numerous applications across biomedicine and generally can be divided into 3 categories: therapeutics, diagnostics and imaging (Parveen et al., 2012). All categories preferably use NPs as

nanoscale probes with the size similar to the proteins which allow us to target or even influence various processes on sub-cellular level. Specific targeting and consequently effective delivery of therapeutic agents have the potential to replace traditional medicines because of avoiding the undesirable side effects especially with anti-cancer chemotherapeutics. Loading chemotherapeutics onto NPs and their potency against various cancers have been successfully demonstrated with doxorubicin, paclitaxel or carboplatin (Elbially et al., 2019; Ma et al., 2019; Zhu et al., 2017). Some types of NPs display anti-tumour activity by themselves through radiosensitization, photothermal therapy or magnetic hyperthermia (Zarschler et al., 2016). Targeting is achieved by passive or active principles using enhanced permeability of affected tissue or conjugation of specific ligands, respectively (Lin et al., 2015; Polo et al., 2017). Besides drugs, other cargos for promising future delivery via NPs are vaccines, antimicrobial agents or genes.

Molecular diagnostics represents sensitive alternative to the present-day clinical laboratory techniques. Detection of different proteins, pathogens, cancer cells or low-expressed biomarkers of a disease in blood assays or tissue biopsies is usually based on spectroscopic evaluation of optical or magnetic quantities of used NPs (Cho and Irudayaraj, 2013; Medley et al., 2008; Shin et al., 2014). Multiplex detection combined with modern instrumentation enables multimodal analysis of several different analytes at once. The incoming approach represents the *in vivo* biosensors which connect non-invasive quantification with immediate real-time monitoring (Rong et al., 2017).

Optical imaging may highly improve disease diagnosis and treatment as it determines the spread and localization of disease for guided intervention as well as positively confirms the site-specific drug delivery. Optical methods for NPs detection include fluorescence, bioluminescence, Raman spectroscopy and optical coherence tomography and can be successfully exploited both for *in vitro* and *in vivo* conditions (Biffi et al., 2015). Imaging of structural and functional information on molecular level makes NPs a valuable tool in biomedical research and the development of optically stable, bright, biocompatible and targeted nanoscale systems drives one of the fastest growing fields of nanotechnology (Parveen et al., 2012). The inner body environment constitutes a highly demanding area with various limitations for appropriate imaging and subsequent analysis. Thus, efforts are addressed to improve

tissue penetration with the use of near-infrared fluorescence which also ensures the correct interpretation of image analysis, while it overcomes the undesirable excitation of tissue autofluorescence (Hilderbrand and Weissleder, 2010). The novel platform represents the multimodal optical imaging which utilizes multifunctional NPs to combine optical imaging with the detection on different physical basis, such as magnetic resonance imaging, positron emission tomography or computed tomography (Biffi et al., 2015; Bradbury et al., 2012).

All mentioned biomedical applications of NPs relate to both inorganic (metallic, silicon, semiconductor) and organic (polymers, liposomes) materials, however, inorganic NPs predominantly work as imaging and diagnostic agents while organic NPs are mostly employed in targeted delivery. Generally, NPs move medicine towards the personalized single system tailored to the individual needs with the combination of therapy and diagnostic imaging – so called theranostics (Ryu et al., 2014).

### **3.4.2 Interactions of Nanoparticles *In Vitro* and *In Vivo***

Reduction of all of the material spatial dimensions to nanoscale grants unique physicochemical properties to the resulting NPs. The source of their exceptional behavior is based on the dramatically increased surface area and therefore the raise of number of atoms located on the surface. This high surface to volume ratio evokes increased reactivity of NPs towards their environment which could be both favorable and undesirable. In any case, the immense need of determination of such interactions intensively grows when considering the application of NPs in highly-reactive biological environment.

*In vitro* biocompatibility assessment of NPs must take into account a series of pitfalls which emerge from the high reactivity. The colloidal stability cannot be evaluated in the original carrier fluid (water, ethanol) but it must be related to the biological media containing mixture of proteins, nutrients, antibiotics, salts or buffers. Agglomeration tendencies may be significantly increased under these conditions (Bruinink et al., 2015; Catalano et al., 2015). Great influence also lies in the correct dosing of NPs as the unsuitable overdose may cause immense agglomeration which makes evaluation of NPs cytotoxicity and uptake by the cells difficult (Wittmaack, 2011a). Moreover, based on this knowledge it needs to be



emphasized that the right dose quantification should be performed in terms of reactive surface area rather than in volume concentration or total number of NPs (Rivera-Gil et al., 2013; Wittmaack, 2011b). The possible cross-reaction with analytes and dyes in biochemical viability assays and also interference with optical measurements can lead to misinterpretation of NPs cytotoxicity. The issue is summarized in excellent guidance publication for nanotoxicity testing by Ong et al. which also provides solutions for certain conflicts in measurements (Ong et al., 2014). Optical properties such as photoluminescence are fundamental to serve the purpose of detection of specific NPs. Nevertheless, the interference with constituents of biological fluids in extra- and intracellular space may lead to significant photoluminescence decay or complete quenching (Khani et al., 2011; Zhang et al., 2008).

For *in vivo* applications, additional NPs interaction-based challenges emerge. Primarily, this includes unfavorable pharmacokinetics and biodistribution. Here comes into play the uptake by phagocytic mononuclear cells which removes NPs from the circulation and consequently causes their accumulation in spleen or liver. This effect can be minimized by decoration of the surface by polyethylene glycol chains (PEGylation) as a charge neutral and hydrophilic polymer (Hamidi et al., 2006). There are two routes of clearance of non-biodegradable NPs from the body - renal and hepatic pathway. The ultrafiltration in kidneys is dependent on the size, charge and shape and, in a simplified way, only very small NPs of size  $\leq 6$  nm are able to pass through the pores in glomerulus (Zarschler et al., 2016). Any bigger NPs are eliminated through the liver where the degradation of NPs in the lysosomes of hepatocytes takes place (Briley-Saebo et al., 2004). Potential risk arises when the degradation is not possible or is significantly decreased which leads to the accumulation effect and activation of the cell death (Lovrić et al., 2005). When mentioning the size, it must be highlighted that the diameter of NPs in biological fluid significantly differs from the diameter of bare NPs. Resulting hydrodynamic diameter may be even several times bigger and is generated by the adsorption of biological components and formation of surface corona.

Bio-corona or protein corona (PC) is established at the interface of the artificial material and biological environment. PC endows NPs with new biological identities which are substantially different from the original synthetic ones which only refer to

size, shape and chemistry (Monopoli et al., 2012). The formation of PC starts right after the exposure of NPs to the biological fluid with the adsorption of high-abundant proteins and then successively ensues the replacement by the proteins with higher affinities – so-called Vroman effect (Hirsh et al., 2013). Adsorption of proteins is a dynamic process and we distinguish two PC layers according to the dynamical and affinity aspects. Hard corona tightly bounds to the bare surface of NPs and its composition changes slowly in the range of several hours. Fast exchanging outer layer called soft corona consists mainly from components of a lower affinity (Casals et al., 2010) (Fig. 5).

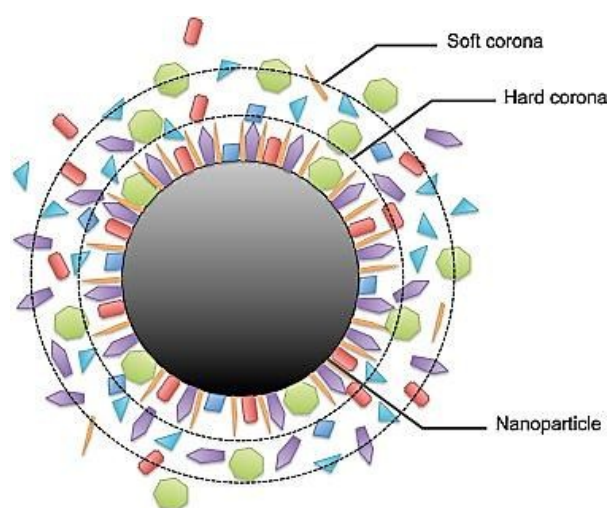


**Figure 5** – Schematic representation of nanoparticle protein corona composition. Adopted from (Wolfram et al., 2014).

The structure of PC highly affects the cellular uptake and intracellular trafficking of NPs (Guarnieri et al., 2011; Monteiro-Riviere et al., 2013) and may also hinder the targeting ligand (Albanese et al., 2014; Salvati et al., 2013). Furthermore the conformational changes in adsorbed proteins can cause activation of unintentional signaling pathways (Deng et al., 2011). Moreover, comparative *in vitro* and *in vivo* experiments can be conflicted due to even subtle differences in composition of PC (Hadjidemetriou et al., 2015). On the other hand, the understanding of the processes on the interface can help to overcome limitations which are consequent upon the PC formation. Modification of the NPs surface by selected biomolecules can therefore induce the binding of the specific proteins of PC and enhance the desired properties of NPs (Prapainop et al., 2012).

### 3.4.3 Cellular Uptake and Trafficking of Nanoparticles

PC-influenced change of NPs properties (size, charge, aggregation) express a direct linkage to alteration of the internalization of NPs into the cells. The amount of internalized NPs and the way of entry into the cells is highly specific and the experimental set-up requires very detailed procedure compliance to obtain consistent results. Presence or absence of PC strongly affects the uptake mechanism and consequently the rate of accumulation and intracellular fate of NPs (Catalano et al., 2015; Guarnieri et al., 2011; Monteiro-Riviere et al., 2013). Additionally, PC is not the only decisive factor as internalization processes turn out to be dependent on cell type, charge, concentration and diameter of the NPs whether with or without PC (Calatayud et al., 2014; Perevedentseva et al., 2013; Yu et al., 2012). Considerable number of studies has been focused on understanding of the route of the NPs uptake and the correlation of such phenomena to their physicochemical properties. However, to define universal denominator which would predict the cellular behavior in relation to NPs characteristics is still far from being resolved since there is an immense amount of diverse studies those results simply cannot be jointly evaluated due to differences in experimental design.

Recently, three main strategies are used for NPs intracellular delivery: passive, facilitated or direct (Damalakiene et al., 2013). The latter one involves specific physical or mechanical techniques which lead to direct transport of NPs into the intracellular space (microinjection, electroporation). Facilitated delivery is another designation for targeted delivery via marking the NPs surface by specific functional molecule and together with passive delivery represents a major challenge for nanotechnology to design tailored NPs with desired amount of internalization to the aimed cells. Up to date, the vast majority of studies incline to the theory that the active process of endocytosis is the main way of entry of NPs into the cells. Passive penetration through plasma membrane is still suggested for very small NPs which entry may be further facilitated by their positively charged surface that enables better adherence to the negatively charged cell membrane (Rothen-Rutishauser et al., 2006; Wang et al., 2012). However, such non-regulated pass through plasma membrane poses a risk of uncontrolled accumulation of NPs inside the cells or even membrane rupture leading to higher cytotoxicity (Treuel et al., 2013). Fortunately, the harmful passive penetration is negligible from the perspective of the overall cellular uptake,

equally as the innocuous passive diffusion through the pore defect in intact plasma membrane (Damalakiene et al., 2013). It is suggested that these passive uptake mechanisms may play important role during long-term exposure to low NPs concentrations (Treuel et al., 2013).

Endocytosis thus represents the dominant pathway of NPs uptake and further trafficking through intracellular space. General term of endocytosis encompass processes based on invagination of plasma membrane followed by forming of intracellular vesicles for final sorting (early endosomes), distribution (late endosomes) and degradation (lysosomes) of the exogenous material. Typically, endocytosis falls into two broad categories based on their specificity to the accepted material: selective and non-selective mechanisms (Fig. 6). Selective processes involves receptor-mediated uptake called clathrin- and caveolin-dependent or independent endocytosis. Macropinocytosis (= phagocytosis in phagocytic cells) and micropinocytosis make up the group of non-selective mechanisms which are designated to ingestion of large-sized or dissolved small molecules, respectively. For the uptake of given type of NPs by the cells several distinct types of endocytosis may be used at the same time (Firdessa et al., 2014). Many efforts were put into correlation of the size of NPs to the type of endocytic pathway yet the outcomes are rarely uniform and often conflicting (Rejman et al., 2004; Yan et al., 2012). However, it was confirmed that small NPs (approx. 10 nm) need to accumulate on the plasma membrane in sufficient amount to be able to trigger the pit formation and therefore the endocytosis while large NPs (approx. 100 nm) do not need the previous accumulation to reach the same effect (Jiang et al., 2011, 2010). Based on this knowledge, all internalization studies must involve appropriate techniques for precise distinctions of incorporated NPs from membrane-attached NPs whereas neglecting this fact leads to misleading results (Feliu et al., 2016).

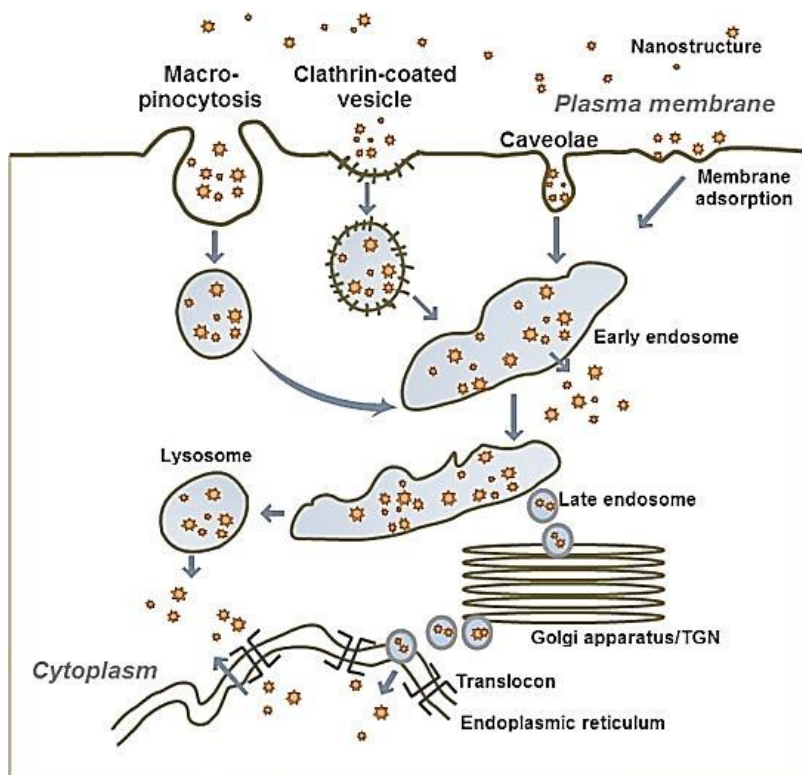


**Figure 6** – Illustrative scheme of possible nanoparticle uptake by different pathways of endocytosis. Adopted from (Papasani et al., 2012).

Only very few studies were conducted to describe the process of metabolism or excretion of NPs from the cells. Biodegradable NPs are expected to be degraded in endosome-lysosomal vesicular complex (Barthel et al., 2014) and the metabolism is very often evaluated on the basis of decreased optical characteristics, primarily fluorescence. Nevertheless, for example very stable fluorescence quantum dots may exhibit only blue shift of their emission and do not give information about the extent of their degradation as they can be detected *in vivo* even after many months (Fitzpatrick et al., 2009). On the other hand, certain NPs do not undergo any type of degradation and the insufficient excretion cannot compensate the fast accumulation in cells which leads to higher cytotoxicity (Fucikova et al., 2014). Exocytosis of NPs is prevalently considered as a much slower process than endocytosis and the rate is dependent on the size of NPs – the larger size of incorporated NPs the longer it takes to remove them to the cell exterior (Iversen et al., 2011).

### 3.4.4 Quantum Dots and Silicon Based Nanoparticles

Cellular imaging by fluorescence markers has been a challenge for nanotechnology at the end of the last century. Until that time, many dyes and contrast agents were unstable and unreliable in the terms of long-time detection. Considerable advancement was achieved when the focus aimed at the so-called quantum dots (QDs) which were firstly synthesized in early 1980's (Ekimov et al., 1985). QDs are heterogeneous semiconductor nanocrystals characterized by natural bright and long-lasting fluorescence (photoluminescence). Other physicochemical parameters which predicted their biological fate include water solubility, small size and possible surface modification or coating. QDs usually consist of a colloidal core surrounded by one or more layers of coatings forming a QD shell. This shell prevents the core from leaching out the elements from the core, increases solubility and enables additional surface treatment by conjugation with various ligands (Derfus et al., 2004; Michalet et al., 2005; Zhang and Monteiro-Riviere, 2009).

First and still successful QDs are constituted on the basis of cadmium (CdSe, CdTe, CdS) and their first biological study was carried out in 2004 with the high expectations of nontoxicity (Chen and Gerion, 2004). Unfortunately, a few years later considerable cytotoxicity was revealed and potential use of QDs based on cadmium for *in vivo* or long-term *in vitro* imaging was not recommended (Schwerdtle et al., 2010). However, QDs as imaging probes are still of special interest in biomedical research, especially in immunohistochemistry and *ex vivo* imaging (Tang et al., 2017), and their development aims at the utilization of non-toxic elements for synthesis.

Attractive chemical alternative for biomedical purposes represents the use of silicon (Si) which is a common trace element in a human body. Si-based NPs (SiNPs) may be in porous or crystalline form of pure or SiO<sub>2</sub> (silica) material. All mentioned formulations are distinguished by the exceptional biocompatibility which is based on their natural slow degradation of Si into orthosilicic acid which is effectively excreted from the body through urine system when accumulated (Boguszewska-Czubara and Pasternak, 2011). The efficient intrinsic photoluminescence of SiNPs facilitates their detection without any necessary intervention into their structure or tagging the surface with a dye. Moreover, there are reports that SiNPs possess higher photostability than organic dyes usually used in

bioimaging (Shen et al., 2011). The origin of photoluminescence properties of SiNPs is probably dependent on quantum confinement and surface state effects and the emission is exhibited in the yellow-red part of the visible spectra based on their chemical purity (Fucikova et al., 2011). With the quantum yield around 10%, there is a sufficient chance of their detection by the means of conventional fluorescence microscopy. Moreover, the lifetime of excited state reaches to 100  $\mu$ s and thus makes it possible to better resolve the signal from the surrounding noise with the autofluorescence lifetime of ca 5 ns (Fucikova et al., 2011; Ostrovska et al., 2016). Many studies have already proposed different forms of SiNPs for in vitro and vivo applications, mainly in the field of bioimaging (Korhonen et al., 2016; Zhong et al., 2015).

#### **3.4.5 Gold and Platinum Nanoparticles**

As it is generally known, metallic materials have accompanied the mankind since ancient time (preparation of tools, decorative use). Unlike base metals, noble metals exhibit very important characteristics for them to be utilized in medicine. First, there is the unique resistance to corrosion in liquid or gaseous environment even in high temperatures and second, it is their non-reactivity with other substances. Besides that, the most well-known noble metals – gold (Au), silver (Ag) and platinum (Pt) demonstrate antimicrobial activities which altogether with their physical attributes made them suitable for treatment of infections already in ancient era (Pal et al., 2014).

Scaling the size of noble metals to nano level gives rise to the new properties such as unique optical feature – localized surface plasmon resonance which enables their easy optical detection based on emission of light of specific wavelength after excitation. This size- and shape-dependent property causes different coloring of noble metal colloids (Eustis and El-Sayed, 2006). Nano-scaling also allows extensive decoration of the surface of noble metal nanoparticles with peptides, antibodies or tumor markers which finds use especially in cancer diagnosis and treatment (Conde et al., 2012). Other than medical applications of noble metal NP include catalysis, photography, non-linear optics and photonics (Rai et al., 2016).

Gold is undoubtedly the most important noble metal from historical and medicinal point of view. As a bulk material, gold exhibits series of antimicrobial and

antitumor activities and is often present in different kinds of medical devices and implants (Kim et al., 2017; Svedman et al., 2006). Owing to this favorable activities, gold in a form of NP (AuNP) can often act in multimodal way when used in biomedicine. Simultaneously, AuNP can work as therapeutics, diagnostic tools and drug carriers mainly in cancer treatment. When used for imaging purposes, AuNP profit from their capability of prolongation of the retention time in the body while enhancing contrast for more precise visualization of the tumor (Hainfeld et al., 2006). Conjugates of AuNP with anticancerous drug increase efficacy of the treatment in comparison to the drug itself which was reported in the work of Madhusudhan et al. (2014) for the conjugates of doxorubicin in cervical carcinoma. Similarly AuNP act as vehicle for drug delivery in anti-HIV treatment and also HIV-1 antigen detection (He et al., 2014). Different application of AuNP represents the analysis of cell adhesion in tissue engineering e.g. by the means of surface-enhanced Raman spectroscopy (Coluccio et al., 2016) or improvement of cell adhesion to the material by coating of its surface (Slepička et al., 2013).

Platinum NP (PtNP) have received a great deal of attention for their antioxidant activity. Such ability can be used in reducing of cellular oxidative stress which stands behind many inflammatory-induced diseases (neurodegenerative diseases, asthma, diabetes etc.) or in reducing of bone loss (Rai et al., 2016). Peroxidase-like activity of some PtNP nanohybrids (e.g. with graphen oxide) are promising systems which could replace existing colorimetric immunoassays due to possible direct detection or higher specificity to cancer cells (Kim et al., 2014; Zhang et al., 2014). Moreover, Manikandan et al. (2013) reported successful photothermal treatment by different sizes of PtNP of Neuro 2A cell lines.

Noble metals thus can find their application potential in different biomedical disciplines.



## **4 Aims of the Thesis**

- I. To evaluate biological responses of different cell types to the ultra-fine grain titanium with different surface treatment and to provide overall insight into the cell adhesion and proliferation for subsequent pre-clinical trials.
- II. To describe elemental reactions of human cells to fluorescence silicon-based nanoparticles of different types with regard to their cytotoxicity and internalization into cells in presence or absence of proteins in cultivation medium.
- III. To optimize and standardize protocols for advanced microscopic imaging of fluorescence silicon nanoparticles in cell cultures.
- IV. To determine the viability of human osteoblasts in the presence of gold and platinum nanoparticles of different concentrations.

## **5 Materials and Methods**

Materials and methods are described in detail in publications A, C, D, G. The enclosed list contains methods that were performed by author of this thesis. Materials and methods of all unpublished data (B, E, F) are described below in detail (see in 5.1, 5.2, 5.3).

### **Tested materials:**

- Ultra-fine grain titanium (**A, B**)
- Silicon quantum dots – T1100 (**C, D, F**)
- Silicon quantum dots – T1050 (**C**)
- Silicon-carbide nanoparticles (**E**)
- Golden and platinum nanoparticles (**G**)

### **Culture of cells:**

- Human osteoblast-like cell line SAOS-2 (**A-G**)
- Human mesenchymal stem cells (**A**)
- Human dermal fibroblasts (**B**)
- Spontaneously immortalized human keratinocyte cell line HaCaT (**B**)

### **(Immuno)fluorescently stained structures:**

- nuclei (DAPI staining) (**A-C**)
- actin stress fibers (phalloidin Alexa488) (**A, B**)
- focal adhesions (vinculin) (**A, B**)
- late endosomes (M6PR) (**F**)
- lysosomes (LAMP2) (**F**)

### **Cell Imaging by Light Microscopy (A-G)**

### **Cell Imaging by Fluorescence Wide-field Microscopy (A-C, E, F)**

### **Cell Imaging by Fluorescence Confocal Microscopy (C, F)**

## **Live-cell Imaging (F)**

### **Advanced Image Analyses:**

- Cell number determination (**A, B**)
- Cell area determination (**A, B**)
- 3D reconstruction of confocal microscope images (**C, F**)

*ImageJ (Rasband, W.S., ImageJ, U.S. National Institutes of Health, Bethesda, Maryland, USA, <http://imagej.nih.gov/ij/>, 1997-2016) and Cell Profiler (Broad Institute, USA) softwares were used.*

### **Other Analyses:**

- Metabolic activity assessment (MTS assay) (**A-E, G**)
- Enzyme-linked immunosorbent assay (ELISA) - determination of the amount of inflammatory cytokines (IL-8 a TNF- $\alpha$ ) and collagen type I (**B**)

### **Statistical Analyses:**

- Shapiro–Wilk test (**A-D, G**)
- Nonparametric Wilcoxon matched pairs test (**A-D, G**)
- ANOVA with a subsequent post-hoc Fischer LSD test (**A-D, G**)
- Pearson's correlation coefficient (**F**)
- Manders split coefficients (**F**)

*STATISTICA Software (StatSoft, Czech Republic) and ImageJ (Rasband, W.S., ImageJ, U.S. National Institutes of Health, Bethesda, Maryland, USA, <http://imagej.nih.gov/ij/>, 1997-2016) were used.*

## **5.1 Methods of PART I. - Unpublished Data (B)**

### **5.1.1 Evaluation of Biological Responses of Human Dermal Fibroblasts and Human Keratinocyte Cell Line to Ultra-Fine Grain Titanium**

#### **Cell Cultivation**

Normal human dermal fibroblasts (NHDF) were obtained from the skin of donors undergoing cosmetic plastic after giving the written consent. After isolation from the dermis, NHDF were cultured in Dulbecco's modified Eagle's medium (DMEM) (Biochrom, UK) supplemented with 10% heat-inactivated fetal bovine serum (FBS) (HyClone, USA), 0.3 mg ml<sup>-1</sup> glutamine (Biochrom, UK), 100 U ml<sup>-1</sup> penicillin (HyClone, USA), 0.1 mg ml<sup>-1</sup> streptomycin (HyClone, USA), 10 mg ml<sup>-1</sup> gentamicin (Biowest, France) and 1% non-essential amino acids (GE Healthcare, UK). NHDF were seeded at a density of 10 000 cells per cm<sup>2</sup> and cultured up to the 5th passage for experimental purposes.

Immortalized human keratinocyte cell line HaCaT (Contipro, Czech Republic) was cultured in DMEM (Sigma-Aldrich, USA) supplemented with heat-inactivated 10 % FBS (PAA, Canada), 10 mg ml<sup>-1</sup> gentamicin (Biowest, France) and 0.3 mg ml<sup>-1</sup> glutamine (Biochrom, UK). The cells were seeded at a density of 12 000 cells per cm<sup>2</sup>.

All following procedures are identical to those described in detail in Publication A.

### **5.1.2 Detection of Inflammatory Cytokines IL-8 and TNF- $\alpha$ after Exposure of Human Blood Samples to Ultra-Fine Grain Titanium**

#### **Sample Preparation**

Heparinized freshly collected blood samples of 6 ml volume were obtained from four healthy donors after giving written consent. Every blood sample was diluted with 6 ml Roswell Park Memorial Institute media (RPMI). 1 ml of the diluted blood was added to ultra-fine grain titanium (UFG-Ti) samples after their proper sterilization (Publication A). The same amount of diluted blood

was placed on polystyrene (PS) control and to lipopolysaccharide (1 and 10  $\mu\text{g ml}^{-1}$ ) representing positive control. Diluted blood was incubated with UFG-Ti samples for 6 hours at 37°C. After 6 hours incubation, diluted blood was centrifuged at 300xg for 6 minutes and supernatants were collected on ice and frozen at -80°C.

#### **Cytokine Assessment**

On the day of the assessment, supernatants were let to thaw at the room temperature and further used in enzyme-linked immunosorbent assay (ELISA) for IL-8 and TNF- $\alpha$  detection (ELISA To Go, eBioscience, USA). Procedure was realized according to manufacture protocol. Optical density was measured using a microplate reader (Synergy H1, BioTek) at 450 nm subtracting the background at 540 nm.

### **5.1.3 Detection of Collagen Type I in Collected Cultivation Media after Cultivation with Ultra-Fine Grain Titanium**

#### **Sample Preparation**

The SAOS-2 cells (DSMZ, Germany) were seeded onto UFG-Ti samples and PS control in the same way as it is described in Publication A. Cells were incubated at 37°C in humidified 5% CO<sub>2</sub> atmosphere for the time lapse of 14 days. On 5th, 8th, 12th and 14th day of incubation, previous cultivation media was collected and frozen at -80°C. Fresh new cultivation media was added to the cells until the time point of next collection.

#### **Collagen Type I Assessment**

On the day of the assessment, frozen samples of cultivation media were let to thaw at the room temperature. Before the procedure all samples were diluted 1:100 with reagent diluent belonging to the used kit and then processed in enzyme-linked immunosorbent assay (ELISA) for Human Pro-Collagen I  $\alpha$ 1/COLIA1 detection (DuoSet ELISA, R&D Systems, USA). Procedure was realized according to manufacture protocol. Optical density was measured using a microplate reader (Synergy H1, BioTek) at 450 nm subtracting the background at 540 nm.

## **5.2 Methods of PART II. – Unpublished Data (E)**

### **5.2.1 Evaluation of Cytotoxicity of Silicon-Carbide Nanoparticles**

#### **Cell Cultivation**

The SAOS-2 cells (DSMZ, Germany) were cultured in DMEM (Gibco, USA) and supplemented with 10 000 U ml<sup>-1</sup> penicillin (Biosera, France), 10 mg ml<sup>-1</sup> streptomycin (Biosera, France), 0.3 mg ml<sup>-1</sup> glutamine (Biosera, France) and for purposes of initial seeding of the cells also with 15% heat-inactivated FBS (Gibco, USA). For experimental purposes, cells were seeded at a density of 10 000 cells per cm<sup>2</sup> onto a 96-well plate in triplets (100 µl) and further cultured for 24 hours in a humidified 5% CO<sub>2</sub> atmosphere at 37°C.

Two types of cultivation media were used further in the experiments – DMEM with 10 000 U ml<sup>-1</sup> penicillin, 10 mg ml<sup>-1</sup> streptomycin and 0.3 mg ml<sup>-1</sup> glutamine with no serum proteins (serum-free) or supplemented with 5% FBS (serum-supplemented). The final concentrations of silicon-carbide nanoparticles (SiCs) in the media used for cell treatment consisted of 250 µg ml<sup>-1</sup>, 100 µg ml<sup>-1</sup> and 50 µg ml<sup>-1</sup>. The cells were gently rinsed with phosphate buffered saline (PBS) prior to the addition of the cultivation media containing SiCs. Subsequently, the cells were cultivated to different time points depending on the time of assessment (24 hour or 48 hours). In the case of the serum-free media, an additional volume of 50 µl of the medium with 5% FBS was added after 6 hours of cultivation and cultivated for an additional 18 hours or 42 hours (for total cultivation time 24 hours or 48 hours respectively).

#### **Cytotoxicity Assessment**

The cytotoxicity of various concentrations of SiCs in different media was assessed by means of the measurement of the metabolic activity of the cells at 24 and 48 hours following the addition of SiCs to the cells. Assessment was performed by means of MTS assay (Cell Titer96® AqueousOne, Promega, USA). The principle of this colorimetric assay is described in detail in Publications A, C and D. The assay was performed according to the manufacture protocol. The cells were rinsed three times with PBS and then incubated for 2 hours with an MTS reagent diluted DMEM with 5% of FBS. Optical density was measured using a microplate reader (Synergy H1, BioTek)

at 490 nm subtracting the background at 655 nm. The subtraction of blank values was conducted for each type of medium separately. All the results obtained were compared to the results of the control cells cultivated in a medium supplemented with 5% FBS; the results were expressed as percentages.

### **5.3 Methods of PART III. - Unpublished Data (F)**

#### **5.3.1 Colocalization of Selected Endocytic Cell Structures with Silicon Quantum Dots**

##### **Cell Cultivation**

The SAOS-2 cells (DSMZ, Germany) were cultured in DMEM (Gibco, USA) and supplemented with 10 000 U ml<sup>-1</sup> penicillin (Biosera, France), 10 mg ml<sup>-1</sup> streptomycin (Biosera, France), 0.3 mg ml<sup>-1</sup> glutamine (Biosera, France) and for purposes of initial seeding of the cells also with 15% heat-inactivated FBS (Gibco, USA). For experiments, the cells were seeded at a density of 10 000 cells per cm<sup>2</sup> onto cell imaging cover glass with 8 chambers in doublets (400 µl) and further cultured for 24 hours in a humidified 5% CO<sub>2</sub> atmosphere at 37°C.

Silicon quantum dots (SiQDs) went through the evaporation process prior to the final dilution in appropriate cultivation media. Procedure is described in detail in Publication C. Two types of cultivation media were used – serum-free and serum-supplemented with 5% of FBS (see 5.2.1. Cell Cultivation). Final concentration of SiQDs in both media was 200 µg ml<sup>-1</sup>. The cells were gently rinsed with PBS prior to the addition of the cultivation media containing SiQDs (300 µl). Subsequently, the cells were cultivated to different time points (1 hour, 4 hours or 24 hours). In the case of 24 hours experiment, an additional volume of 150 µl of media with 15% FBS was added to the serum-free media and the equal volume of 5% FBS media was added to the serum-supplemented media after 6 hours of cultivation.

### **Fluorescent Staining of Cells**

After 1, 4 and 24 hours, the cells were gently washed 3 times with PBS and immediately fixed in 4 % paraformaldehyde. Then, selected endocytic structures were marked by following primary antibodies - mouse monoclonal anti-M6PR (2G11) (1:200, Abcam, UK) for late endosomes and mouse monoclonal anti-LAMP 2 (1:50, Abcam, UK) for lysosomes. Secondary antibody Alexa Fluor 568-conjugated goat anti-mouse (1:1000, Thermo Fisher, USA) was used for visualization of all mentioned endocytic structures.

### **Imaging of Fluorescently Stained Cells**

2D and 3D images of the stained cells with SiQDs were acquired using Olympus IX83 microscope (Olympus, Japan) equipped with confocal scanning unit CSU-W1 (Yokogawa, Japan) with dual monochrome digital sCMOS camera for multi-channel imaging (Olympus, Japan). The SiQDs were excited using 405 nm diode laser with the exposition time of 2000 ms and the emission was detected using Cy5 700-775 nm filter. For the detection of stained organelles, the excitation 561 nm of diode laser was used. Emission was detected by TRITC 609-654 nm filter. More 2D images were acquired with respect solely to the 24 hour experiments by means of a Leica TCS SP8X confocal laser scanning microscope (Leica Microsystems). The SiQDs were excited using a pulse continuum white light laser (475–499 nm) and emissions were collected via a hybrid detector at 700–795 nm. The elimination of cell autofluorescence from SiQDs signals was achieved by the gating of signal detection with a 5 ns delay from the excitation pulse. Multiple line accumulation scanning and prolonged pixel dwell were set so as to allow for the more intense and precise imaging of the SiQDs. All the confocal 3D images were acquired by means of a Leica DFC365 FX monochrome digital CCD camera.

All 2D and 3D images were further analyzed by means of Fiji software (Schindelin et al., 2012). The same software with JaCoP plugin was also used for numerical interpretation of colocalization (signal overlap). Specifically, Pearson's correlation coefficient and Manders split coefficient.



### 5.3.2 Live Imaging of Cells Interacting with Silicon Quantum Dots

#### Cell Cultivation

The SAOS-2 cells (DSMZ, Germany) were cultured in McCoy's 5A medium without phenol red (HyClone, USA) supplemented with heat-inactivated 15 % FBS (GE Healthcare, UK), 10 000 U ml<sup>-1</sup> penicillin (Sigma-Aldrich, USA) and 10 µg ml<sup>-1</sup> streptomycin (Sigma-Aldrich, USA). For the experimental purposes, the cells were seeded at a density of 15 000 cells per cm<sup>2</sup> onto cell imaging dish with 145 µm glass bottom (500 µl) and further cultured for 24 hours in a humidified 5% CO<sub>2</sub> atmosphere at 37°C.

SiQDs went through the evaporation process prior to the final dilution in appropriate cultivation media. Procedure is described in detail in Publication C. Final concentration of SiQDs in cultivation media was 100 µg ml<sup>-1</sup>. The cells were gently rinsed with PBS prior to the addition of the cultivation media containing SiQDs.

#### Live Imaging

Right after the addition of SiQDs, the cells were transferred into pre-heated stage top chamber, which maintain stable temperature (37°C), humidity and 5% CO<sub>2</sub> level for incubation stability during the imaging (OKOlabs, Italy). Chamber was placed onto the stage of Nikon TE 2000E-C1si microscope (Nikon, Japan). SiQDs were excited with fluorescence wide-field 120W Mercury Vapor Short Arc LAMP through 330 – 380 nm UV2A filter cube with G2A emission filter (590 nm). Exposition time was set to 10 seconds and for more intense signal, also gain was 4 times increased. Images were acquired with Nikon DS-Qi1Mc digital CCD camera (Nikon, Japan). First image was taken after 30 minutes from SiQDs addition and then after every 30 minutes until cell were still alive. Simultaneously, DIC (Nomarski) phase contrast images were acquired. Further image analysis was realized in NIS-Elements software (Nikon, Japan).

## 6 Results

In order to retain the consistency of the topics, the thesis is divided into four parts. Each of them summarizes publications and other unpublished results related to their common topic. All parts correspond to the aims of the thesis.

Part I is focused on different types of biological testing of ultra-fine grain titanium.

Part II focuses on biological evaluation of silicon nanoparticles of different origin.

Part III sums up the work on advanced visualization of silicon nanoparticles inside the cells.

Part IV focuses on the influence of gold and platinum nanoparticles on human osteoblasts.

### PART I

A) **Lucie Ostrovská**, Lucie Vištejnová, Jan Džugan, Peter Sláma, Tomáš Kubina, Egor Ukraintsev, Dana Kubies, Milena Králíčková, Marie Hubálek Kalbáčová (2016): **Biological evaluation of ultra-fine titanium with improved mechanical strength for dental implant engineering**. Journal of Materials Science 51, 3097-3110. IF = 2.993

#### B) Unpublished Data:

- Evaluation of Biological Responses of Human Dermal Fibroblasts and Human Keratinocyte Cell Line to Ultra-Fine Grain Titanium
- Detection of Inflammatory Cytokines IL-8 and TNF- $\alpha$  after Exposure of Human Blood Samples to Ultra-Fine Grain Titanium
- Detection of Collagen Type I in Collected Cultivation Media after Cultivation with Ultra-Fine Grain Titanium

## PART II

- C) **Lucie Ostrovská**, Antonín Brož, Anna Fučíková, Tereza Bělinová, Hiroshi Sugimoto, Takashi Kanno, Minoru Fujii, Jan Valenta, Marie Hubálek Kalbáčová (2016): **The impact of doped silicon quantum dots on human osteoblasts**. RSC ADVANCES 6, 63403-63413. IF = 2.936
- D) Tereza Bělinová, **Lucie Vrabcová**, Iva Machová, Anna Fučíková, Jan Valenta, Hiroshi Sugimoto, Minoru Fujii, Marie Hubálek Kalbáčová (2018): **Silicon Quantum Dots and Their Impact on Different Human Cells**. Phys. Status Solidi B, 255, 1700597. IF = 1.729
- E) **Unpublished Data:**
- Evaluation of Cytotoxicity of Silicon-Carbide Nanoparticles

## PART III

- F) **Unpublished Data:**
- Colocalization of Selected Endocytic Cell Structures with Silicon Quantum Dots
  - Live Imaging of Cells Interacting with Silicon Quantum Dots

## PART IV

- G) Markéta Pišlová, Marie Hubálek Kalbáčová, **Lucie Vrabcová**, P. Slepíčka, Zdeňka Kolská, V. Švorčík (2018): **Preparation of Noble Nanoparticles by Sputtering – Their Characterization**. Digest Journal of Nanomaterials And Biostructures 13, 1035-1044. IF = 0.673

All publications mentioned above are included in full at the end of the thesis.

## 6.1 PART I: Ultra-Fine Grain Titanium (A, B)

Part I of the thesis describes fundamental interactions of cells in direct contact with **ultra-fine grain titanium (UFG-Ti)** with different surface treatment. This novel form of titanium with superior mechanical properties belongs to a new generation of traditionally used titanium dental implants. Such material has a potential in fabrication of long-term dental implants which can ensure stable performance in load-bearing conditions. Although pure titanium excels with its unique biocompatibility, new process of manufacture may cause unexpected change in cell responses. Verification of cytocompatibility, proper cell adhesion and non-inflammatory behavior is therefore crucial for any following pre-clinical trials. Moreover, surface topography is of capital importance in initial cell adhesion and further proliferation and differentiation. Hence, experiments in PART I also focus on feedback evaluation of different surface treatment and subsequent suggestions on modifications for practical application.

Publication A depicts biological responses of two types of human cells cultivated on six types of UFG-Ti – osteoblasts SAOS-2 (osteosarcoma-derived cell line) and mesenchymal stem cells. Monitored parameters include cell proliferation, cell area, metabolic activity, cell morphology and adhesion at two different time points (2 hours and 48 hours). Additionally, further unpublished work (B) follows up the same experimental set-up with another two types of human cells – primary dermal fibroblasts and keratinocytes HaCaT (skin-derived aneuploid transformed cell line). Later on, determination of production of two inflammatory cytokines (IL-8 and TNF- $\alpha$ ) provided elemental insight into immunogenicity of UFG-Ti. Influence of surface topography of UFG-Ti on cell ECM production was also marginally detected by measuring the amount of collagen type I in cultivation media during long time cultivation of SAOS-2 cells.

This research is based on cooperation of biological, mechanical and chemical sectors. In publication A, biological part was performed by the author of the thesis while other work was done by colleagues from COMTES FHT a.s., Dobřany (fabrication of UFG-Ti samples, mechanical characterization), Institute of Physics, Academy of Sciences of the Czech Republic, Prague (topography characterization) and Institute of Macromolecular Chemistry, Academy of Sciences of the Czech

Republic, Prague (wettability measurement). Unpublished work (B) was performed by the author of this thesis.

### **6.1.1 Publication A: Biological evaluation of ultra-fine titanium with improved mechanical strength for dental implant engineering**

**Lucie Ostrovská**, Lucie Vištejnová, Jan Džugan, Peter Sláma, Tomáš Kubina, Egor Ukraintsev, Dana Kubies, Milena Králíčková, Marie Hubálek Kalbáčová (2016): Biological evaluation of ultra-fine titanium with improved mechanical strength for dental implant engineering. *Journal of Materials Science* 51, 3097-3110. IF = 2.993

Grain refinement belongs to the new approaches in improvement of mechanical characteristics of commercially pure titanium, which is used for dental and orthopedic implants for decades. Refining the basal grain size of titanium to nanoscale can extend the longevity and enhance resistance to the long-term loading stress of the final product. Additionally, when developing new functional implant, surface characteristics must be taken into account. For better acceptance of the implant by the organism it is crucial to stimulate cell attachment and further cell proliferation on the surface which also help to prevent bacterial infection in the interface. Remodelation of the implant surface to mimic extracellular environment of the bone tissue can be achieved by mechanical or chemical techniques.

The aim of this publication was to evaluate the cytocompatibility of UFG-Ti samples fabricated by the ECAP-Conform process, which is one of the most developed techniques for metal nanostructuring. Three different grain sizes Z ( $\leq 1 \mu\text{m}$ ), M ( $4.61 \mu\text{m}$ ) and S ( $30 \mu\text{m}$ ) a two types of mechanical surface treatment - polishing (p) and grinding (g) were the variables of the manufacturing. Thus, six types of UFG-Ti samples were evaluated, i.e., Zp, Zg, Mp, and Mg, representing the new titanium materials with improved mechanical properties, and Sp and Sg, representing the original Ti material. Topographical and mechanical characterization of individual UFG-Ti samples is illustrated in Fig. 3 in publication A. Polystyrene for cell cultivation was used as a control material (PS control). Experiments were performed with the human osteoblast-like cell line SAOS-2 and human mesenchymal stem cells (hMSCs). Cells were seeded on sterilized UFG-Ti samples and after 2 and

48 hours the cell number and cell area were evaluated. At 48 hours only, morphology and focal adhesions (SAOS-2 cells only) of the cells were examined together with metabolic activity measurement by MTS assay.

During the first 2 hours, number of SAOS-2 cells adhered to the surface of all UFG-Ti samples was significantly higher compared to the number of cells on PS control (Fig. 5a in publication A). Significant difference remained even after 48 hours although the rate of cell number increase was not so pronounced suggesting successive slower growth of SAOS-2 cells on UFG-Ti samples (Fig. 5c in publication A). From the initial adhesion, reported area of SAOS-2 cells cultivated on UFG-Ti samples was smaller compared to the cells on PS control, yet the differences were mostly not significant. However, differences accentuated with the time and after 48 hours, SAOS-2 cells grown on UFG-Ti samples evinced approximately 20% cell area reduction in comparison to the control cells (Fig. 6b in publication A). Despite the smaller size, morphology of SAOS-2 cells after 48 hours cultivation on UFG-Ti samples displayed the same cuboidal-like shape like the cells on PS control. (Fig. 7b,c in publication A). Interestingly, the cells cultured on ground samples displayed noticeable focal adhesion plaques (Fig. 8e–g in publication A) on the extensions of the cells while on polished samples focal adhesions were localized on the basal pole of the cells. Thus, cells grown on polished samples displayed strong similarity with the cells cultured on the PS control (Fig. 8b–d in publication A). No significant difference in metabolic activity was observed between the UFG-Ti samples and the PS control and among UFG-Ti samples (Fig. 4a in publication A).

hMSCs showed some differences in their interactions with UFG-Ti. The slower increase in cell number on UFG-Ti samples than on the PS control was even more pronounced (Fig. 5d in publication A), which led to the lowered cell number on the UFG-Ti samples after 48 h in comparison to the PS control. The same trend was observed in cell area evaluation where the cell size differences on UFG-Ti samples versus PS control enlarge with the time. The cell areas of hMSCs cultivated on UFG-Ti after 48 hours were almost 50% smaller in comparison to PS control (Fig. 6c in publication A). Unlike SAOS-2 cells, hMSCs cultured on ground samples displayed noticeable elongation and filopodia extensions. Polished samples enabled the growth and spreading of hMSCs in all directions; thus, their morphology varied (Fig. 7e,f in publication A). Visualization of focal adhesion was not realized with hMSCs. Slight

decrease in metabolic activity was observed for ground M and S samples, otherwise no differences compared to PS control and among samples were observed (Fig. 4b in publication A).

This publication evaluated short-time biological responses of SAOS-2 cells and hMSCs to newly developed UFG-Ti. We demonstrated that this material is suitable for the growth of both cell types, yet osteoblasts prosper on it even more; thus, UFG-Ti demonstrated its potential for future bone implant development.

### **6.1.2 Unpublished data (B): Evaluation of Biological Responses of Human Dermal Fibroblasts and Human Keratinocyte Cell Line to Ultra-Fine Grain Titanium**

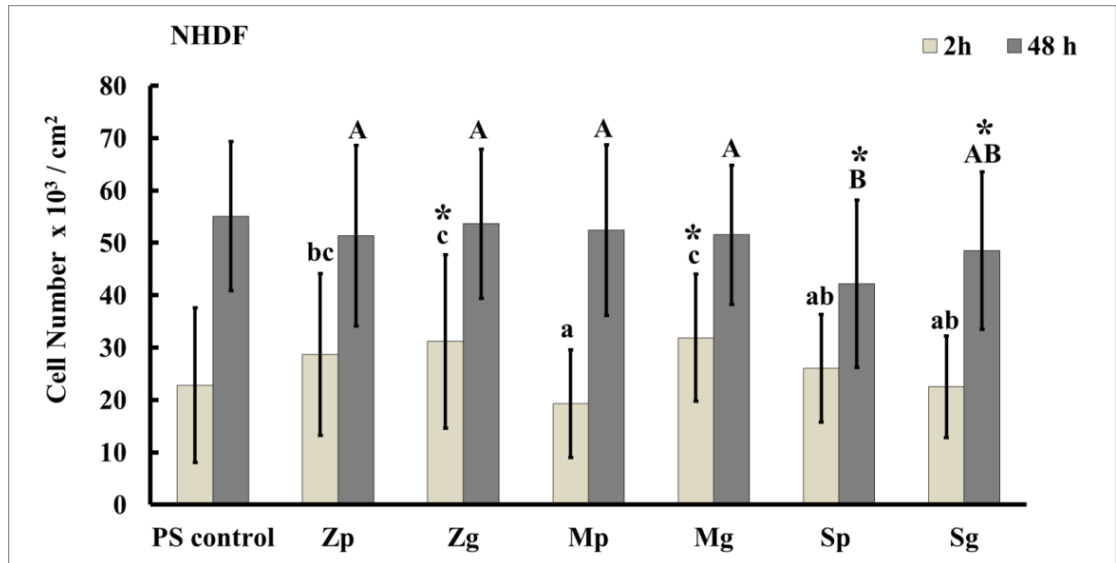
Previous findings from the publication A confirmed the suitability of newly developed UFG-Ti for the growth and proliferation of human osteoblasts SAOS-2 and hMSCs. In the following work, we verified whether such material can be also used as a substrate for the growth of human dermal fibroblasts (NHDF) and human keratinocytes cell line (HaCaT). The results of publication A revealed considerable influence of surface topography on different cell types attachment, morphology and rate of proliferation. Dermal fibroblasts and especially keratinocytes differ from previously used cell types by their preference in the substrate quality, as they grow on much softer surfaces in their natural environment. As it was mentioned, UFG-Ti has a potential mainly in future bone or dental implant development. However, skin-penetrating devices (e.g. intraosseous transcutaneous amputation prostheses) are generally fabricated from titanium and its alloys and they struggle with the proper attachment of the cells on the interface. Confirmation of the cytocompatibility of UFG-Ti to dermal fibroblasts and keratinocytes may expand its scope of activity in the field of implantology.

All experiments were performed with the same UFG-Ti samples under the same conditions and experimental set-up as it is described in Publication A. Visualization of focal adhesion was not evaluated.

From the beginning, the number of NHDF cells adhered to the surface of UFG-Ti samples was very similar to PS control (Fig. B1). Yet after 48 hours the number of cells on some samples (especially on both S samples) was lower compared to PS control suggesting the significantly slower growth of NHDF. The same trend as in publication A was observed with cell area evaluation. After 2 hours, there were no differences in NHDF size between UFG-Ti samples and PS control, not even among the samples, except for Sp sample. But with the time, cells on UFG-Ti samples showed significant cell area reduction when compared to the cells on PS control (Fig. B2). Similarly to hMSCs, NHDF expressed the dependence of cell morphology on surface topography. NHDF seeded onto polished samples displayed variable shapes and grew mostly in multi-layers, while the cells on ground samples grew uniformly in one layer elongated in one direction (Fig. B4b,c). Metabolic activity of cells on all UFG-Ti samples showed only small differences from the cells cultivated on PS control (Fig. B3), however, no cytotoxic effect (reduction under 75% control) (Flahaut et al., 2006) was detected.



(a)



(b)

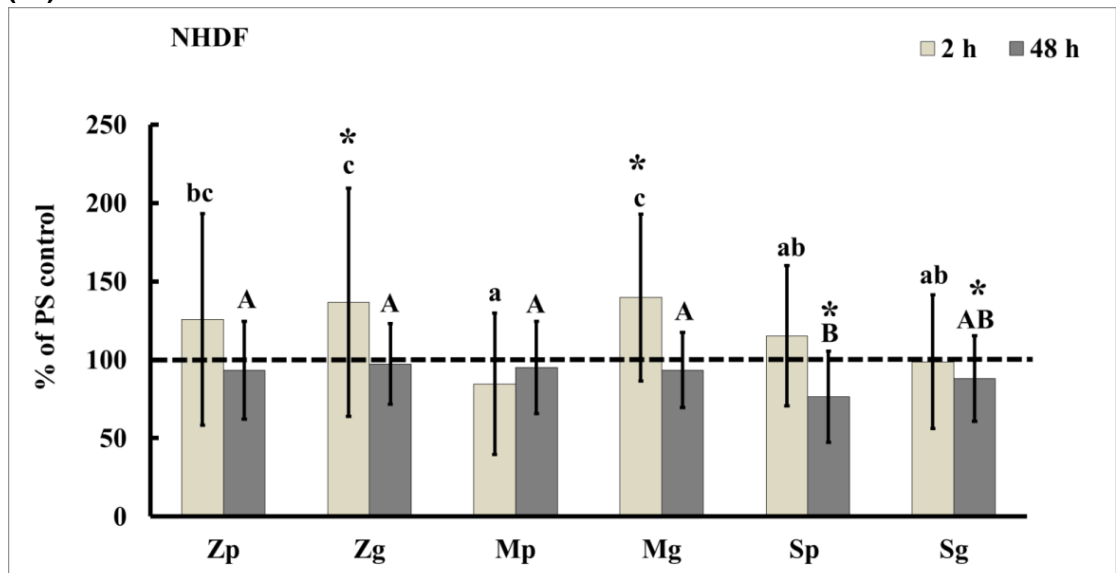


**Figure B1: Cell number of dermal fibroblasts (NHDF) after 2 and 48 h of cultivation on UFG-Ti samples. a) values of cell number/cm<sup>2</sup>, b) relative values expressed as a percentage of PS control (dashed line). Asterisk (\*) means a significant difference from PS control (Wilcoxon matched-pairs test,  $p < 0.05$ ). Groups marked with different lower-case letters (2 h) or with different upper-case letters (48 h) express significant inter-group difference within samples (ANOVA, LSD post hoc test,  $p < 0.05$ ).**

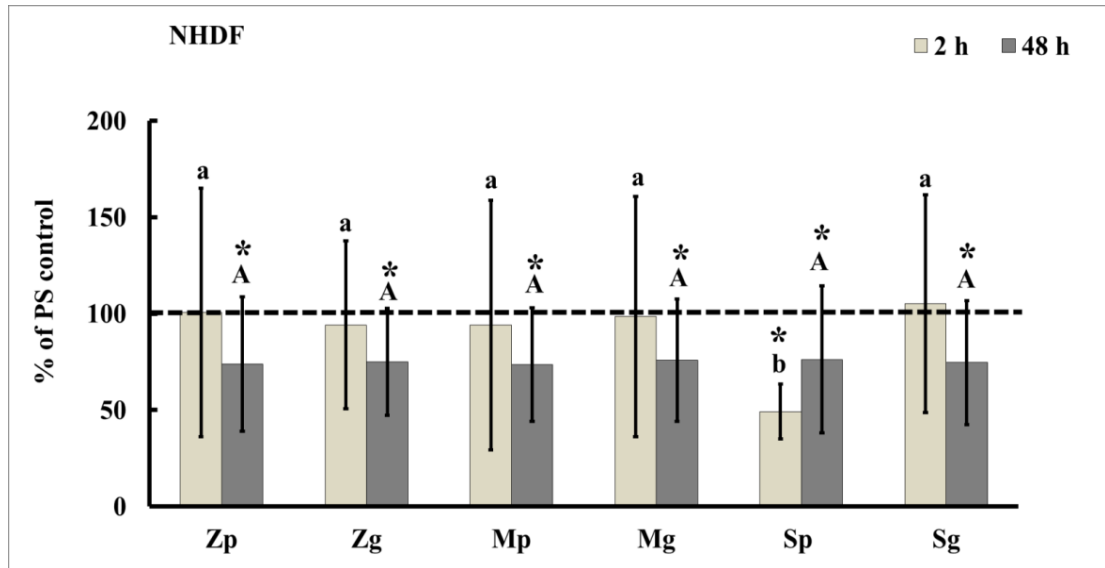


**Figure B2: Cell area of dermal fibroblasts (NHDF) after 2 and 48 h of cultivation on UFG-Ti samples.** Relative values expressed as a percentage of PS control (dashed line). Asterisk (\*) means a significant difference from PS control (Wilcoxon matched-pairs test,  $p < 0.05$ ). Groups marked with different lower-case letters (2 h) or with different upper-case letters (48 h) express significant inter-group difference within samples (ANOVA, LSD post hoc test,  $p < 0.05$ ).

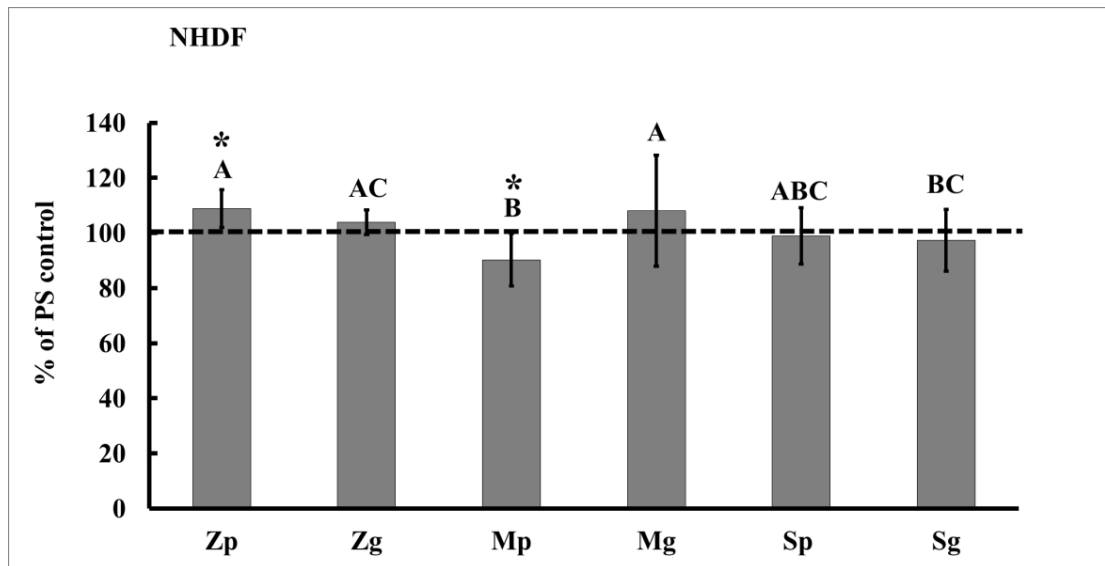


**Figure B3: Metabolic activity of dermal fibroblasts (NHDF) after 48 h of cultivation on UFG-Ti samples.** Relative values expressed as a percentage of PS control (dashed line). Asterisk (\*) means a significant difference from PS control (Wilcoxon matched-pairs test,  $p < 0.05$ ). Groups marked with different letters express significant inter-group difference within samples (ANOVA, LSD post hoc test,  $p < 0.05$ ).

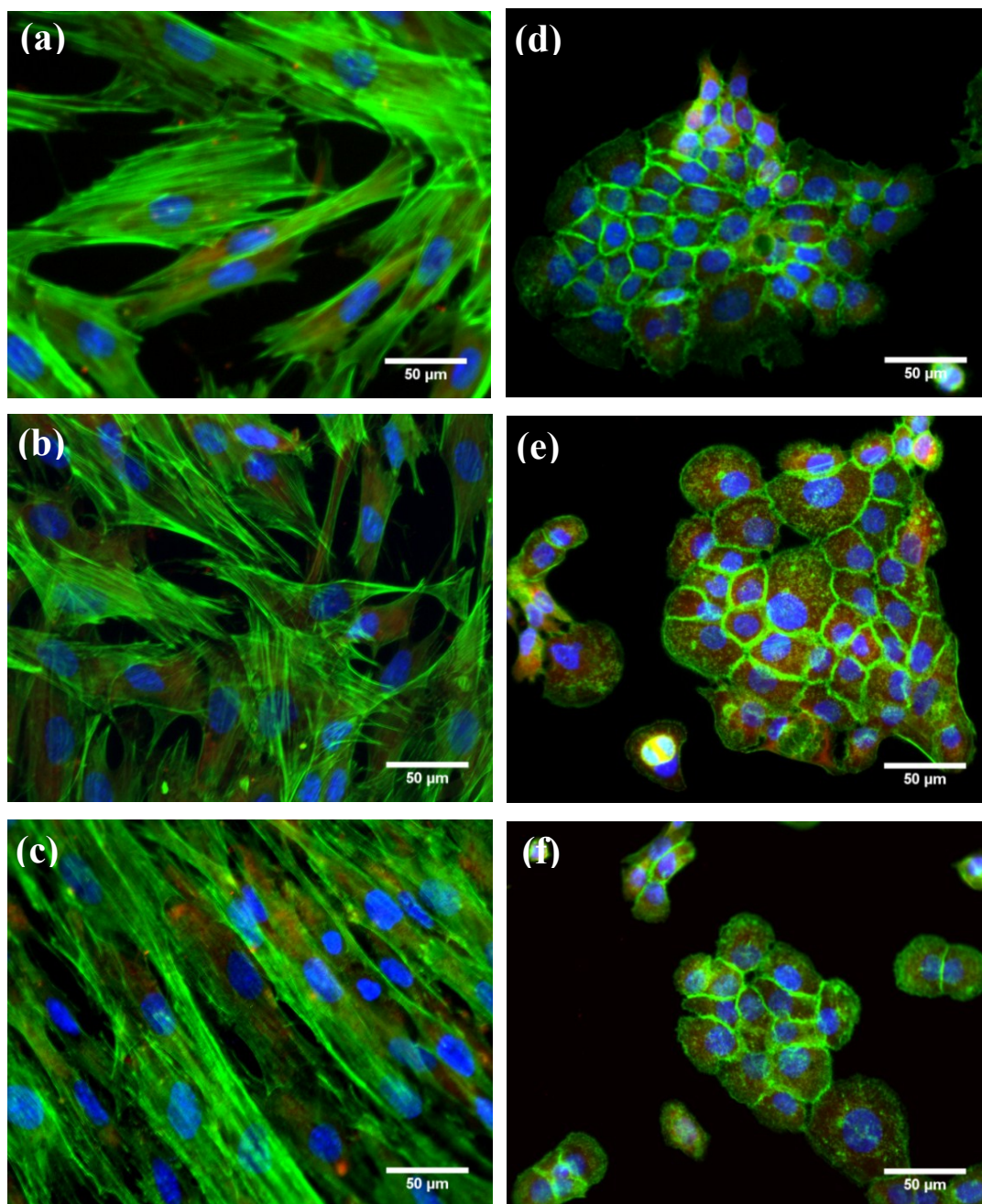
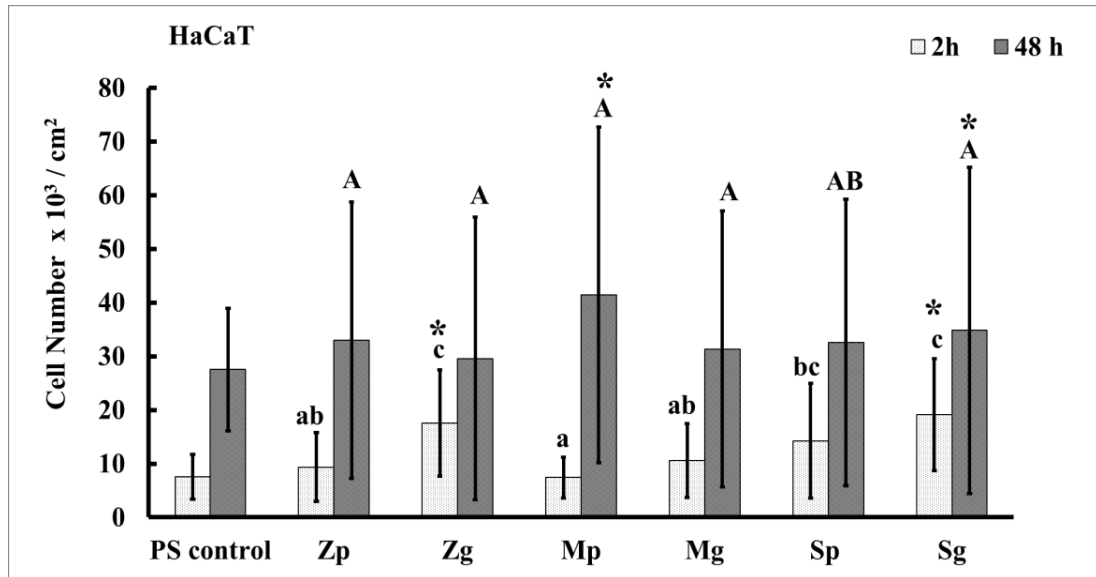


**Figure B4: Representative images of cells on different substrates after 48 h of cultivation.** Dermal fibroblasts (NHDF) (a–c) and keratinocytes HaCaT (d–f) on PS control (a, d), polished sample (b, e), ground sample (c, f). Actin cytoskeleton stained by phalloidin-AF488 (green), nucleus stained by DAPI (blue), vinculin as a protein of focal adhesions stained by indirect immunofluorescent staining (secondary antibody conjugated with AF568 - red).

Specific growth of HaCaT cells made the cell number and cell area very difficult to assess. Keratinocytes form tight multi-layer clusters; thus, the single cell recognition is greatly intricate. After 2 hours, the number of HaCaT cells on polished UFG-Ti samples was similar to the number of cells on PS control while slightly more cells were found on ground samples (Zg and Sg significantly). Accuracy of the following cell number measurement at 48 hours was negatively influenced by the increase of the amount of the cells in clusters which is expressed by quite large deviations (Fig. B5a). Growth of the cells was also probably slowed down as it is illustrated in Fig. B5b. Cell area after 2 hours was not assessed due to insufficient size of the HaCaT cells for measurement. After 48 hours though, the size of the cells on UFG-Ti samples showed no difference to the cells on PS control (Fig. B6). No specific morphology alterations were observed on UFG-Ti samples. However, the way of growth was dependent on the surface – on polished samples HaCaT cells formed large high-dense layers similar to PS control and minimum cells was found around in isolated clusters (Fig. B4e). On contrary, HaCaT cells cultivated on ground samples formed many smaller clusters not binding to each other (Fig. B4f). Values of metabolic activity of HaCaT cells on all UFG-Ti samples were lower than on PS control, yet the decrease was not statistically significant (Fig. B7).

This work extended our knowledge about short-time cell biological responses to UFG-Ti. Characteristics of dermal fibroblasts on UFG-Ti samples resemble the results we obtain previously from mesenchymal stem cells. Keratinocytes did not show evident results about the suitability of UFG-Ti for their prosper growth.

(a)



(b)

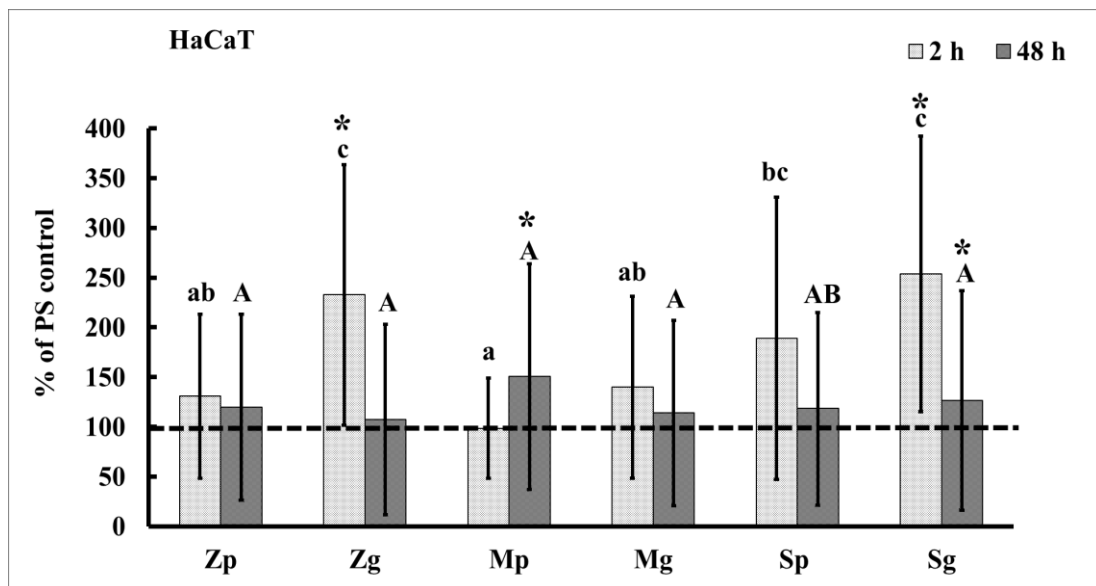


**Figure B5: Cell number of keratinocytes (HaCaT) after 2 and 48 h of cultivation on UFG-Ti samples. a) values of cell number/cm<sup>2</sup>, b) relative values expressed as a percentage of PS control (dashed line). Asterisk (\*) means a significant difference from PS control (Wilcoxon matched-pairs test,  $p < 0.05$ ). Groups marked with different lower-case letters (2 h) or with different upper-case letters (48 h) express significant inter-group difference within samples (ANOVA, LSD post hoc test,  $p < 0.05$ ).**

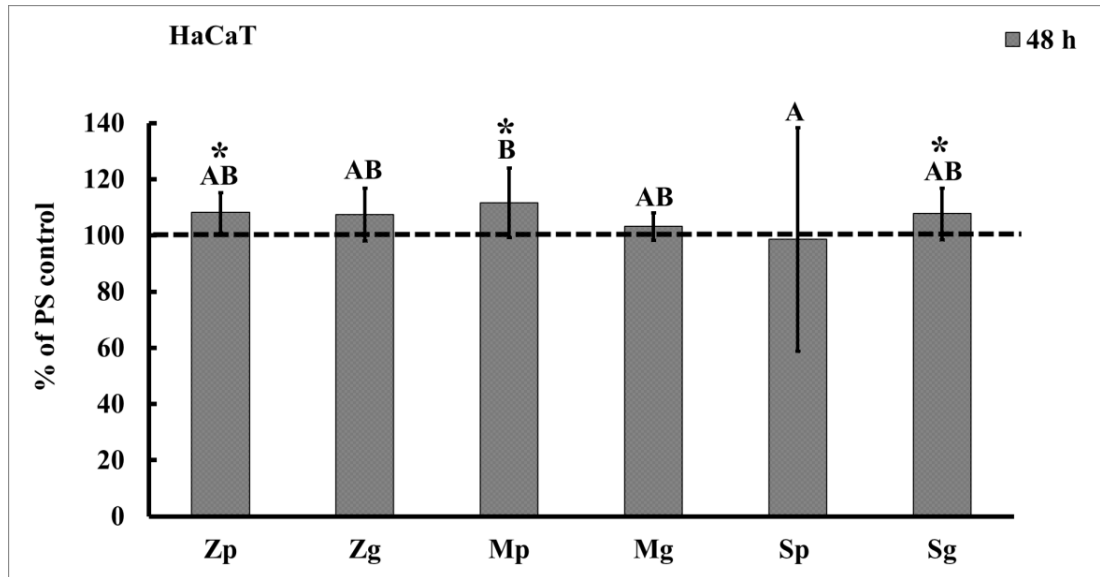


**Figure B6: Cell area of keratinocytes (HaCaT) after 48 h of cultivation on UFG-Ti samples.** Relative values expressed as a percentage of PS control (dashed line). Asterisk (\*) means a significant difference from PS control (Wilcoxon matched-pairs test,  $p < 0.05$ ). Groups marked with different letters express significant inter-group difference within samples (ANOVA, LSD post hoc test,  $p < 0.05$ ).

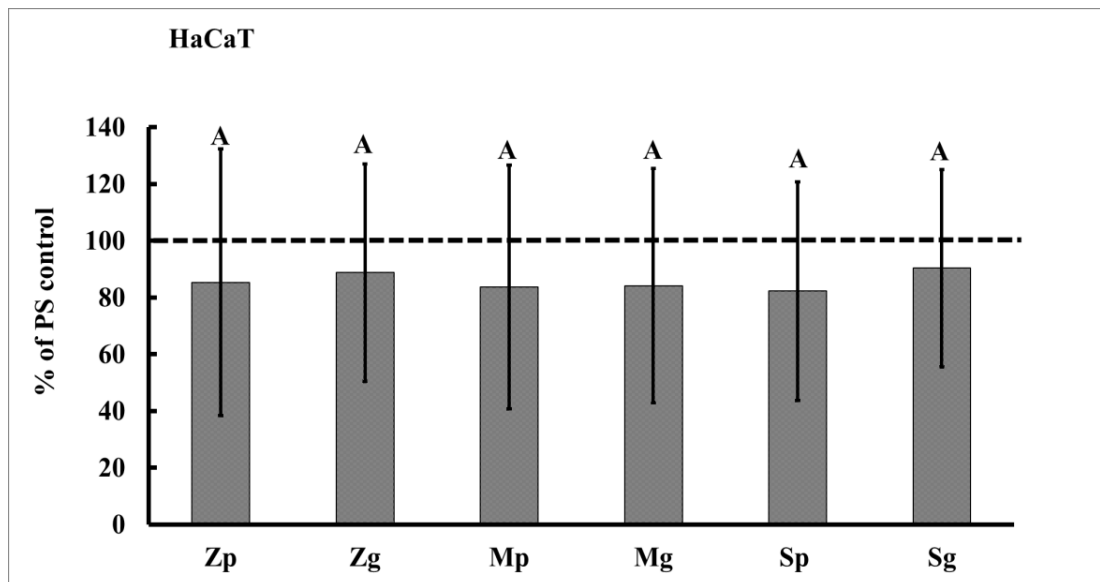


**Figure B7: Metabolic activity of keratinocytes (HaCaT) after 48 h of cultivation on UFG-Ti samples.** Relative values expressed as a percentage of PS control (dashed line). Asterisk (\*) means a significant difference from PS control (Wilcoxon matched-pairs test,  $p < 0.05$ ). Groups marked with different letters express significant inter-group difference within samples (ANOVA, LSD post hoc test,  $p < 0.05$ ).

### **6.1.3 Unpublished data (B): Detection of Inflammatory Cytokines IL-8 and TNF- $\alpha$ after Exposure of Human Blood Samples to Ultra-Fine Grain Titanium**

Assessment of cytocompatibility of UFG-Ti with four different cell types concluded the first cell part of UFG-Ti biological evaluation. Subsequent experiments aimed to the determination of the UFG-Ti tendency to the induction of inflammation. To mimic the inner body environment, freshly collected blood samples were used for the assessment. Production of two representative inflammatory cytokines in blood plasma – interleukin 8 (IL-8) and tumor necrosis factor  $\alpha$  (TNF- $\alpha$ ) was measured after short-time incubation with UFG-Ti samples.

Blood samples were taken from four healthy donors and then each one of them was cultivated with all six UFG-Ti samples for 6 hours. Polystyrene for cell cultivation was used again as a control material (PS control). Lipopolysaccharide (LPS) was used as a positive control of inflammation process. Afterwards, supernatants from centrifuged blood samples were collected and frozen until the day of the measurement. The evaluation of the amount of produced cytokines was performed for every donor separately and then average values from all donors were used for the final determination.

The results for IL-8 from all the donors were considerably similar (Fig. B8a). Summary evaluation revealed significant increase in the production of IL-8 on all UFG-Ti samples than on PS control. Moreover, the surface topography of UFG-Ti showed a very strong influence on the IL-8 production. Significantly higher amount of IL-8 was detected on ground samples compared to polished samples. While all the polished samples exhibited very similar values of IL-8 amount, the Zg sample significantly exceeded the other two ground samples in the produced amount of IL-8 (Fig. B8b). It should be noted that none of the UFG-Ti samples increased the IL-8 production to the level of inflammatory values (LPS).

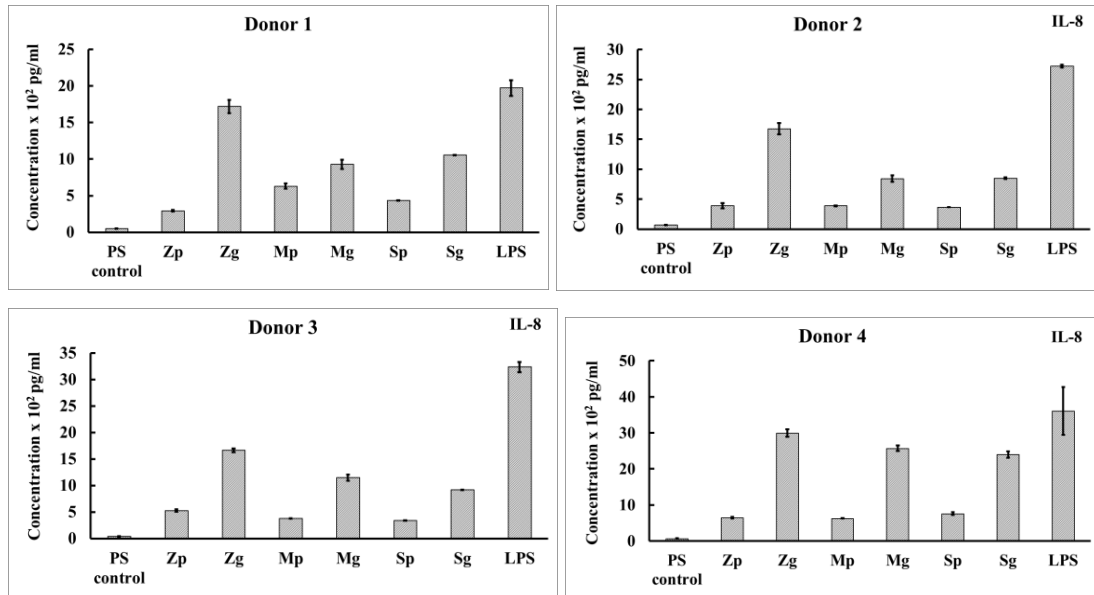
Similar trend was observed also in TNF- $\alpha$  measurement. All UFG-Ti samples induced the TNF- $\alpha$  production significantly more than PS control. Noticeable difference was also found between the amount of TNF- $\alpha$  on polished and ground samples. Ground samples increased the TNF- $\alpha$  production more than polished samples, yet the difference was not statistically significant (Fig. B9b). In this case,

large standard deviations were caused by the extensively different reactions of the donors (Fig. B9a). Eventually, none of the UFG-Ti samples increased the TNF- $\alpha$  production to the level of inflammatory values (LPS).

In this work, we acquired brand new information about the immunogenicity of UFG-Ti. Based on the results, inflammatory reaction to the substrate was detected, yet most of the samples were far from reaching the health hazard level.



**(a)**



**(b)**

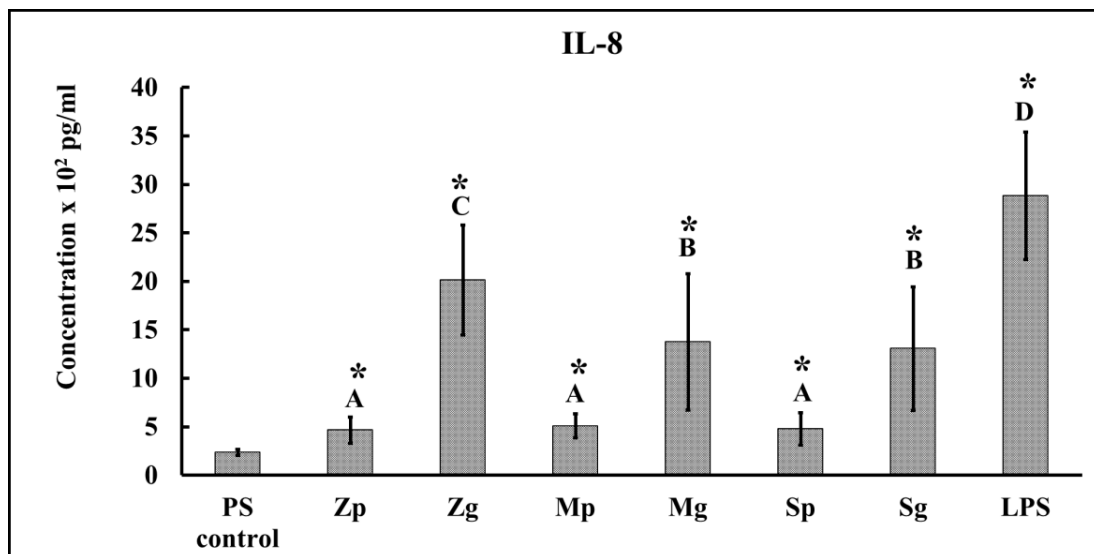
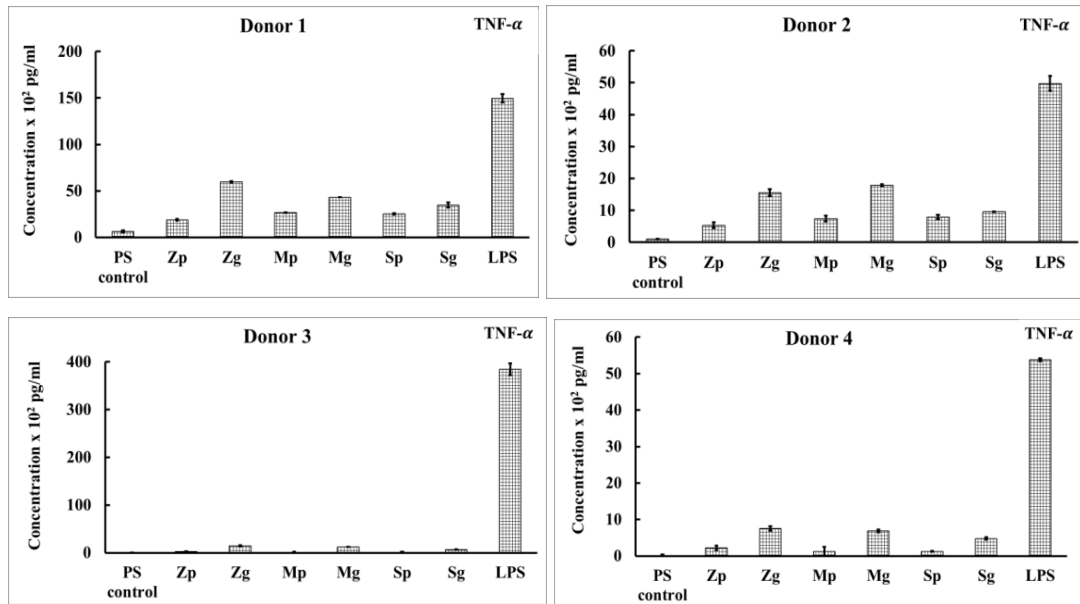


**Figure B8: Production of inflammatory cytokine IL-8 after 6 h incubation with UFG-Ti samples. a)** Results obtained from every donor separately, **b)** final average values from all donors. Asterisk (\*) means a significant difference from PS control (Wilcoxon matched-pairs test,  $p < 0.05$ ). Groups marked with different letters express significant inter-group difference within samples (ANOVA, LSD post hoc test,  $p < 0.05$ ).

(a)



(b)

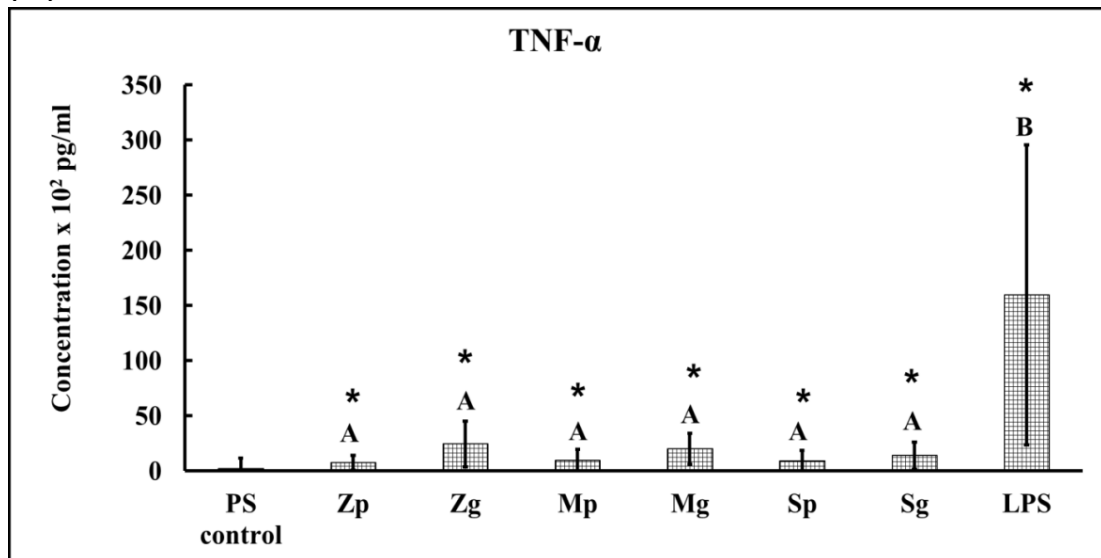


**Figure B8: Production of inflammatory cytokine TNF- $\alpha$  after 6 h incubation with UFG-Ti samples. a)** Results obtained from every donor separately, **b)** final average values from all donors. Asterisk (\*) means a significant difference from PS control (Wilcoxon matched-pairs test,  $p < 0.05$ ). Groups marked with different letters express significant inter-group difference within samples (ANOVA, LSD post hoc test,  $p < 0.05$ ).

#### **6.1.4 Unpublished data (B): Detection of Collagen Type I in Collected Cultivation Media after Cultivation with Ultra-Fine Grain Titanium**

In the final assessment of the biological responses to UFG-Ti we returned to the cultivation of cells. We obtained the fundamental knowledge about the initial phase of interactions of UFG-Ti in the biological environment. The aim of this work was to determinate the fate of cells adhered to the UFG-Ti in a longer time period. As osteoblasts showed the best results from all tested cell types on the material, the SAOS-2 cell line was used for the experimental purposes again. The sign of osteoblasts good prosperity and terminal osteocyte differentiation is the production of collagen type I. Quantification of the produced amount of collagen type I by SAOS-2 cells was performed at four selected time points during 14 days of cultivation.

SAOS-2 cells were seeded and cultivated the same way and under the same condition as it is described in Publication A. Nevertheless, this time, every 5th, 8th, 12th and last 14th day of cultivation the medium from each UFG-Ti sample was collected and frozen until the day of assessment.

The results showed that at every time point the production of collagen type I was higher on UFG-Ti samples than on PS control (Fig. B9). Production of collagen type I increased with the time for 12 days. After this time point, the production starts to decrease, yet the same trend was observed also on PS control. Sum amount of collagen type I produced during the 14 days of cultivation suggests no relevant differences among UFG-Ti samples, though statistical analysis was not performed due to the lack of data (Fig. B10).

Described work was devoted to the evaluation of long-time condition of osteoblasts on UFG-Ti. From the obtained data it could be deduced that UFG-Ti samples stimulate osteoblasts to produce high quantity of collagen type I; thus UFG-Ti samples still prove their application potential for bone or dental implant development. It should be mentioned, that this work touches the topic only marginally and the results should not be considered as a final conclusion.

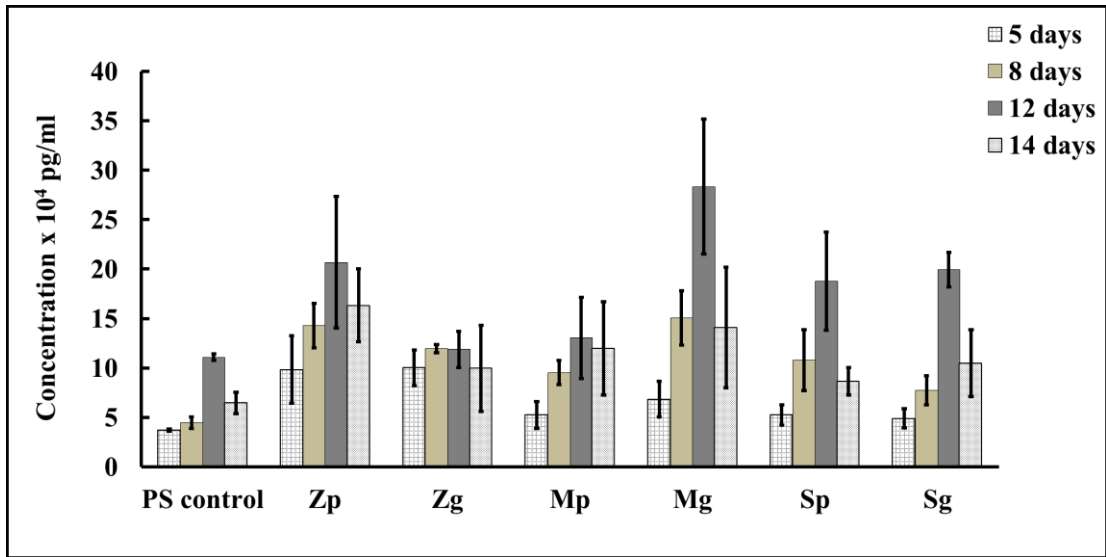


**Figure B9: Measured production of collagen type I by osteoblasts (SAOS-2) cultivated on UFG-Ti samples at different time points of incubation.**

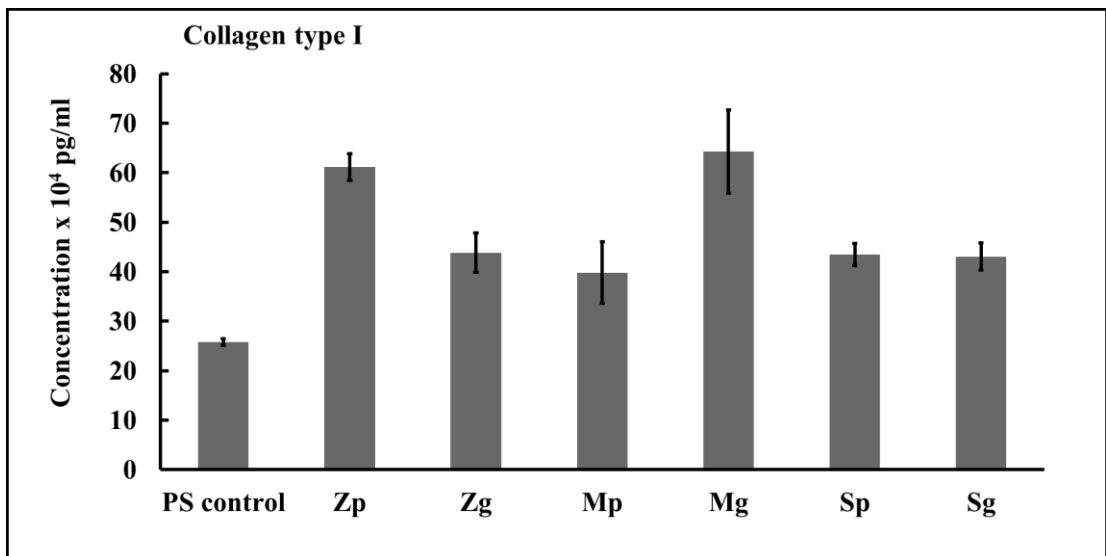


**Figure B10: Sum collagen type I production by osteoblasts (SAOS-2) cultivated on UFG-Ti during 14 days.**

## 6.2 PART II: Silicon-based Nanoparticles – Cytotoxicity and Basic Imaging (C-E)

Part II of the thesis describes elemental reactions of different human cell types to fluorescence **silicon-based nanoparticles**. Silicon nanoparticles emerge the immense interest in nanomedicine based on their unique chemical-physical properties and entail the rapid progress of this field. Silicon biodegradability predicted the possible use of silicon-based nanoparticles in biomedicine especially for development of the brand-new therapeutic and imaging techniques. Currently, the ultra-small nanoparticles which were used in this study (diameter  $\leq 4$  nm) still lack sufficient biological scientific background since there are only several conflicting publications. Cytotoxicity assessment is of the greatest concern as this makes up the most important initial step for any further biological application. Moreover, for better understanding of the causes of the cytotoxicity there is a need of description of specific cell–nanoparticle interactions on the elemental level.

Publication C aims to the determination of the appropriate concentration of two types of silicon-boron quantum dots (SiQDs) based on the influence on metabolic activity of human osteoblasts cell line (SAOS-2). Obtained results were put into correlation with the cellular uptake of both SiQDs evaluated by means of fluorescence wide-field and confocal microscopy. Above that, presence or absence of fetal bovine serum (FBS) in the cultivation media was selected as the main variable in all experiments and its influence on basal cell-SiQDs interactions was discussed. Publication D enlarges the findings of cytotoxicity of one of the SiQDs from publication C. Human monocytic cell line (THP-1), primary hMSCs and SAOS-2 cells were employed to the similar cytotoxicity experiments based on the knowledge from publication C. Moreover, determination of necrosis was added to the evaluation. Different types of silicon nanoparticles – silicon-carbide (SiCs) were tested in unpublished data (E) with the same experimental set-up as used in the previous work with SiQDs.

The extensive cooperation of different scientific fields was employed in this research. The author of the thesis performed the biological part of the work (publication C and unpublished data E) and in publication D figured as a mental

assistance for the experiments. Further work was done by colleagues from Department of Electrical and Electronic Engineering, Graduate School of Engineering, Kobe, Japan and Wigner Research Centre for Physics, Budapest, Hungary (fabrication and optical characterization of SiQDs and SiCs, respectively) and from Faculty of Mathematics and Physics, Prague, Czech Republic (advanced optical characterization and zeta potential measurement).

### **6.2.1 Publication C: The impact of doped silicon quantum dots on human osteoblasts**

**Lucie Ostrovská**, Antonín Brož, Anna Fučíková, Tereza Bělinová, Hiroshi Sugimoto, Takashi Kanno, Minoru Fujii, Jan Valenta, Marie Hubálek Kalbáčová (2016): The impact of doped silicon quantum dots on human osteoblasts. RSC ADVANCES 6, 63403-63413. IF = 2.936

Up to the present, the main application spectrum of SiQDs was found in the field of optics and electronics, yet their unique properties revealed its significant potential for the use in biology and medicine. Biocompatibility and natural biodegradability of SiQDs inspired the idea of the expansion into the field of biology. In addition, natural photoluminescence with high quantum yields and low photobleaching coefficients present rare prerequisites for imaging, bio-sensing or drug delivery without any further redundant intervention into their structure. Nevertheless, biocompatibility of any newly synthesized silicon-based nanoparticles must be confirmed together with the determination of the highest possible non-toxic concentration. For future bio-medical application, it is also inevitable to understand the interactions of SiQDs in biological environment.

In this first paper, two chemically identical SiQDs with different size and peak emission were tested for cytotoxicity at various concentrations (25, 50 and 125  $\mu\text{g ml}^{-1}$ ) at different time points (6, 24 and 48 hours) on SAOS-2 cells in the presence or absence of FBS in the cultivation medium (+/- FBS). Mentioned types of SiQDs were synthesized using different annealing temperatures which implies its designation - 1100 (4 nm size, 850 nm peak emission) and 1050 (3 nm size, 750 nm

peak emission). Detailed characterization of SiQDs is described in publication C (Fig. 1, 2, 3, 4). At 2, 6 and 24 hours cellular uptake of both SiQDs ( $50 \mu\text{g ml}^{-1}$ ) in +/- FBS cultivation media was evaluated using fluorescence wide-field and confocal microscopy.

At the 6 hour time-point, SiQD 1100 in the + FBS medium did not significantly influenced metabolic activity of SAOS-2 cells irrespective of concentration (Fig. 5a in publication C). On the other hand, SiQD 1050 (the lowest and middle concentration) increased cell metabolic activity and the same trend was observed even after 24 hours of incubation, yet the increase was not significant. SiQD 1100 decreased the metabolic activity after 24 hours at the highest concentration and after 48 hours the decrease was measured also for the middle concentration. Also SiQD 1050 decreased metabolic activity after 48 hours but only at the highest concentration (Fig. 5b in publication C). In the – FBS medium, SiQD 1100 affected metabolic activity only at highest concentration after 6 hours while SiQD 1050 did not affected cell behavior at any concentration. After 24 hours also middle concentration of SiQD 1100 strongly decreased cell metabolic activity while more dramatic situation appeared with SiQD 1050 where all tested concentration decreased metabolic activity to cytotoxic level. Eventually, both SiQDs exhibited cytotoxic effect at all concentration after 48 hours in – FBS medium (Fig. 5c,d in publication C).

Visual inspection of SiQD 1100 in + FBS medium showed that the first signal could not be detected until 24 hours inside the cells. Until that time, all detected signal originated from the clusters formed outside the cell (Fig. 6a,c in publication C). Importantly, no morphological alterations were observed after the incorporation of SiQDs 1100 after 24 hours. In the case of SiQDs 1050, very strong fluorescence signal was detected from the very start of microscopy observation, yet it was apparent that the signal originated from huge foggy aggregates covering the cells from the outside. This finding was confirmed by confocal imaging after 24 hours where only a very weak signal was detected inside the cells while most of the SiQDs 1050 were found in culture medium (Fig. 6b,d in publication C). SiQD 1100 in – FBS medium were detected inside the cells from the beginning (2 hours) and their concentration increased over time causing the changes in morphology after 24 hours

(Fig. 7a,c in publication C). Moreover, form of the signal inside the cells was diffused while in + FBS medium, the signal was detected in vesicular structures. SiQD 1050 in – FBS media was not possible to detect at any time point inside the cells but significant structural changes in cell morphology were observed after 24 hours (Fig. 7b,d in publication C).

This publication tested two types of SiQDs in biological environment for the very first time. Cytotoxicity assessment provided information about the toxic concentrations and microscopy imaging revealed the processes standing behind the measured cytotoxicity. All further work with silicon-based nanoparticles followed the experimental set-up from this publication.

### **6.2.2 Publication D: Silicon Quantum Dots and Their Impact on Different Human Cells**

Tereza Bělinová, Lucie Vrabcová, Iva Machová, Anna Fučíková, Jan Valenta, Hiroshi Sugimoto, Minoru Fujii, Marie Hubálek Kalbáčová (2018): Silicon Quantum Dots and Their Impact on Different Human Cells. *Phys. Status Solidi B*, 255, 1700597. IF = 1.729

Based on the results from publication C, following study aimed to the testing of SiQDs on different cell types. From the two tested SiQDs, only one (SiQD 1100) was selected for further detailed research as it demonstrated better results for possible bio-applications. Prospective utilization of SiQDs in human medicine influenced the selection of tested cell types. Immune cells will be the first cells to encounter SiQDs after their application into organism; thus, monocytic cell line (THP-1) was chosen in a first place. hMSCs were chosen as the representative primary cells to compare their results with the results obtained from the cell lines. Finally, SAOS-2 cells were used again as already well-established cell line in interactions with SiQDs. Evaluation of metabolic activity was this time accompanied with the cell death (necrosis) detection. Presence of FBS stayed as an important variable in all experiments.



All three cell types were employed in evaluation of cytotoxicity with SiQDs concentrations of 25, 50 and 100  $\mu\text{g ml}^{-1}$ . Time-points of 6, 24 and 48 hours were used for SAOS-2 cells and 6 and 24 hours for the rest of the cell types. THP-1 cells were used in two stages – suspension monocytes and adherent macrophages. Determination of necrosis (lactate dehydrogenase LDH) was carried out with SAOS-2 cells and hMSCs after 6, 24, 48 hours and 6, 24 hours, respectively. The same concentrations of SiQDs as in cytotoxicity experiments were employed.

Metabolic activity of SAOS-2 cells in +FBS medium decreased with the time only at the highest concentration of SiQDs where the cytotoxic level was attained already after 6 hours. In –FBS medium, the level of cytotoxicity was reached after 48 hours also in the middle concentration of SiQDs (Fig. 2a,b in publication D). hMSCs decreased significantly their metabolic activity after 24 hours in almost all concentrations of SiQD both in + and – FBS medium. None of the values decreased to the cytotoxic level though (Fig. 2c,d in publication D). Monocytes THP-1 in + FBS medium showed increase of the metabolic activity in the first 6 hours in all concentrations of SiQDs and at 24 hours no differences with the control were detected. In – FBS medium the initial increase was not observed and at 24 hours the level of cytotoxicity was attained in the middle and the highest concentration of SiQDs (Fig. 2e,f in publication D). Macrophages THP-1 in + FBS medium showed the 6 hours increase of metabolic activity only in the highest concentration of SiQDs, while after 24 hours the highest concentration evinced the lowest values. In – FBS medium the situation was comparable to monocytes, yet the decrease was more dramatic in all concentrations of SiQDs (Fig. 2g,h in publication D).

Significantly higher LDH concentrations compared to negative control were detected from SAOS-2 cells in + FBS medium in the highest concentration of SiQDs after 48 hours. In – FBS medium this situation occurred already after 24 hours (Fig. 3a,b in publication D). hMSCs on the other hand exhibited only negligible amount of LDH, irrespective to concentration of SiQDs or presence of FBS (Fig. 3c,d in publication D).

This publication extended our knowledge about the cytotoxicity of SiQDs to primary hMSCs and immune cell line THP-1. Additionally, the possible way of

death in the presence of SiQDs was assessed for SAOS-2 cell line and for primary hMSCs.

### **6.2.3 Unpublished data (E): Evaluation of Cytotoxicity of Silicon-Carbide Nanoparticles**

Previous studies in publications C and D performed with SiQDs motivated the need of the comparison with some other type of silicon-based nanoparticles. Well-established methodology of nanoparticle cytotoxicity evaluation on SAOS-2 cells enabled the employment of different silicon nanoparticles doped with carbide atoms (SiCs) without protracted initial verification of the experimental set-up. Tested SiCs exhibited even smaller average diameter than previously used SiQDs – only 2nm. Among their properties similar to SiQDs, the long-time stability in water was their main benefit. Unfortunately, their peak emission was determined in 450 nm, which ruled out the possibility of correct visualization as this value totally overlaps with the cell autofluorescence.

Cytotoxic evaluation was carried out in very similar manner as it was described in both publications C and D. Time-points of the assessment were set at 24 and 48 hours with the concentrations 50, 100 and 250  $\mu\text{g ml}^{-1}$  of SiCs. Experiments were performed with SAOS-2 cells in presence or absence of FBS.

Cell metabolic activity in + FBS media at 24 hours was significantly decreased in middle and the highest concentration of SiCs, the highest concentration even reached the cytotoxicity level - 25% reduction of metabolic activity (Fig. E1). Surprisingly, after 48 hours metabolic activity increased in all concentrations of SiCs, yet the highest concentration was still considered cytotoxic. The similar situation after 24 hours was observed also in –FBS medium. Furthermore, although after 48 hours metabolic activity also increased, all SiCs concentrations reached the level of cytotoxicity. Surprisingly, the negative influence of FBS absence was not apparent until 48 hour time-point.

This research was inspired by previous publications with SiQDs. Acquired results showed that even though all silicon-based nanoparticles are considered

biocompatible and non-cytotoxic, there is always a need of detailed study of cytotoxicity to set conditions in which this type of nanomaterial really fulfill its desired characteristics of biocompatibility (concentration, environment).

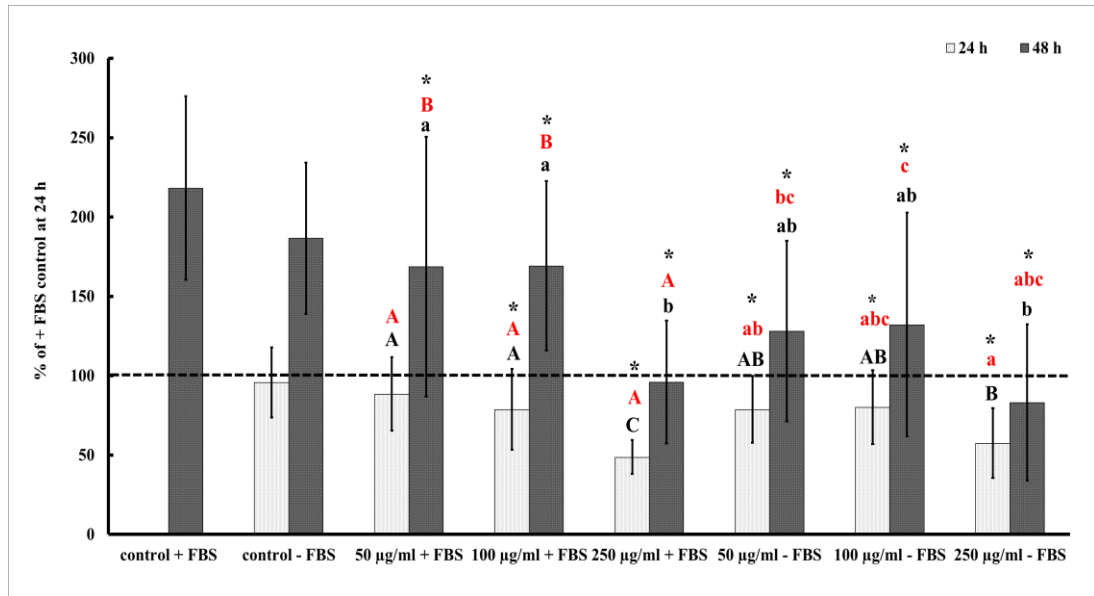


**Figure E1: Metabolic activity of osteoblasts (SAOS-2) cultivated with different concentrations of SiCs in presence or absence of FBS after 24 and 48 hours.** Relative values are expressed as a percentage of + FBS control at 24 hours (dashed line). Asterisk (\*) means a significant difference from appropriate time and +/- FBS control (Wilcoxon matched-pairs test,  $p < 0.05$ ). Groups marked with different black upper-case letters (24 h), black lower-case letters (48 h), red upper-case letters (+ FBS) or red lower-case letters (- FBS) express significant inter-group difference within variables (ANOVA, LSD post hoc test,  $p < 0.05$ ).

### **6.3 PART III: Silicon Quantum Dots – Advanced Visualization (F)**

Part III of the thesis is devoted to the work made on advanced microscopic imaging of SiQDs in cell culture. In publication C we described the way of SiQDs visualization by the means of fluorescence wide-field and confocal microscopy. Final results of imaging were preceded by the long and challenging process to set up the correct technical adjustment. The most demanding tasks were to acquire sufficient strong signal from SiQDs as the emission peak lies in near-infra red part of the light spectrum and to distinguish the SiQDs signal from inner cell autofluorescence. Final setting enabled further detailed imaging of the SiQDs entry and movement inside the cells. The way of entry and subsequent movement of such small nanoparticles is not easy to detect. Tracking SiQDs in time inside the cells is a very extensive subject of research and this study strived to optimize the visualization techniques to obtain reliable and replicable results.

The first section of Part III relates to the detection of SiQDs signal inside the SAOS-2 cells at different time-points and its spatial correlation with the fluorescently stained endocytic structures, specifically, late endosomes and lysosomes. Colocalization analysis of these two fluorescent signals was carried out on 2D and 3D projections. Experiments were performed in the presence or absence of FBS. The second section summarizes the work on live imaging of SAOS-2 cells in time after the addition of SiQDs. Fluorescent signal of SiQDs together with bright-field imaging of cell morphology was tracked until the cell death.

The first section was entirely performed by the author of this thesis while the second section was performed under supervision of colleague from the Institute of Physiology, Academy of Sciences of the Czech Republic, Prague.

### **6.3.1 Unpublished data (F): Colocalization of Selected Endocytic Cell Structures with Silicon Quantum Dots**

First image analysis in publication C indicated that specific conditions must be met for SiQDs to enter the cell in detectable amount. Based on visualization conclusions from publication C, only SiQD 1100 were selected for following detailed study of their internalization in SAOS-2 cells. Furthermore, the presence or absence of FBS in cultivation media after the addition of SiQDs to the cells seemed to have a deep impact on the final amount of SiQDs inside the cell and the type of the detected signal herein (vesicle-like or diffuse form). In this study we aimed to prove whether cells use endocytosis in order to internalize and further process SiQDs. Signal from two endocytic structures (late endosomes and lysosomes) was colocalized in time with the signal from SiQDs by software analysis and their final interrelation was expressed by Pearson's correlation coefficient and Manders split coefficient. Pearson's correlation coefficient expresses the result as +1 for perfect correlation, 0 for no correlation, and -1 for perfect anti-correlation. Manders split coefficient is proportional to the amount of fluorescence of the colocalizing pixels or voxels in each color channel. An image with an overlap coefficient equal to 0.5 implies that 50% of both components of the image overlap with the other part of the image. If the number of objects is not equal or similar then determination of two colocalization coefficients M1 and M2 is the proper method.

Statistical expression of colocalization by mentioned coefficients was also compared with each other and their suitability for our estimations was discussed. Moreover, fluorescent images were acquired in 2D and 3D projections and their mutual correspondence of colocalization results was compared.

SAOS-2 cells were cultivated with the concentration of  $200 \mu\text{g ml}^{-1}$  of SiQDs in the presence of FBS in cultivation media. Endocytic structures – late endosomes and lysosomes were immunofluorescently stained with appropriate antibodies (M6PR and LAMP2, respectively) at 1, 4 and 24 hours. 2D and 3D images of two-channel acquisition (SiQDs + endocytic structures) were obtained and then further analyzed.

The signal of SiQDs was mostly detected on the outside of the cell membrane. Nevertheless, in the case of FBS presence, the signal was more intense suggesting the clustering of SiQDs (Fig. F1). The 3D spatial placement of SiQDs inside the cells also confirmed localized vesicle-like signal (Fig. F2). The SiQDs signal in FBS absence was hard to detect inside the cells and was usually diffuse (Fig. F3). This finding led to elimination of FBS-free cultivation conditions from the overall colocalization analysis due to irrelevant results. Both findings about the influence of FBS presence or absence on SiQDs' signal type and placement correspond to the results of publication C.

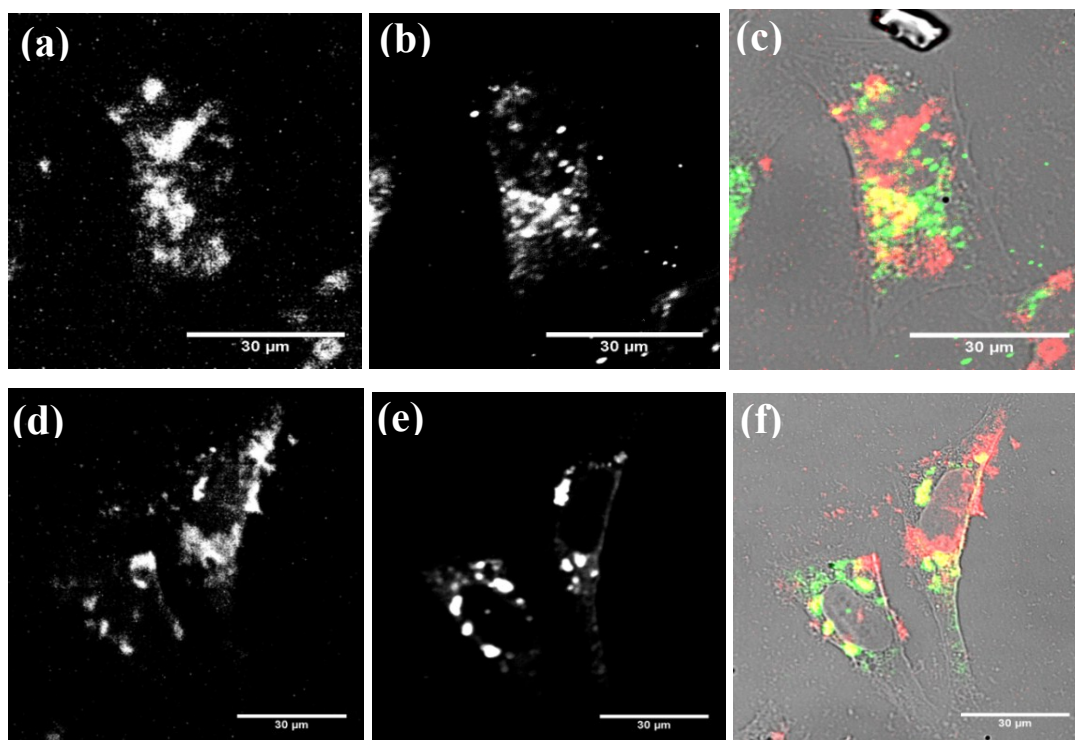


**Figure F1: Representative images of osteoblasts (SAOS-2) cultivated with SiQDs in the presence of FBS after 24 hours.** After cultivation, SAOS-2 cells were stained for visualization of late endosomes (a-c) and lysosomes (d-f). (a,d) acquired SiQDs signal (700-775 nm), (b) late endosomes stained by indirect immunofluorescent staining - M6PR + secondary antibody conjugated with AF568 (609-654 nm), (e) lysosomes stained by indirect immunofluorescent staining – LAMP2 + secondary antibody conjugated with AF568 (609-654 nm), (c,f) merge of the two fluorescent channels with bright-field Nomarski contrast (artificial colorization: red – SiQDs, green – endocytic structures, yellow – overlap indicating colocalization).

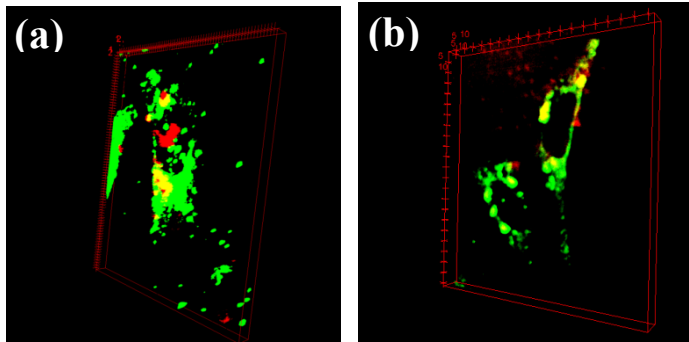


**Figure F2: Representative 3D images of osteoblasts (SAOS-2) cultivated with SiQDs in the presence of FBS after 24 hours.** Merge images of two fluorescent channels with artificial colors - late endosomes (green) and SiQDs signal (red) **(a)** or lysosomes (green) and SiQDs signal (red) **(b)**. Yellow color indicates colocalization of both channels.

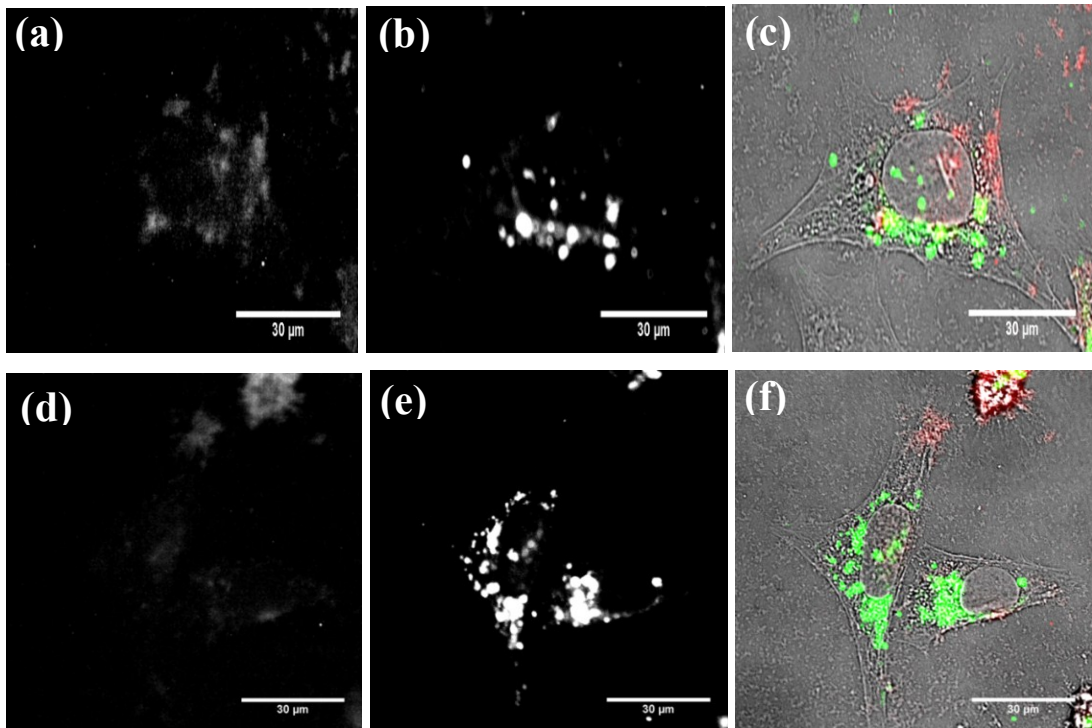


**Figure F3: Representative images of osteoblasts (SAOS-2) cultivated with SiQDs in the absence of FBS after 24 hours.** After cultivation, SAOS-2 cells were stained for visualization of late endosomes **(a-c)** and lysosomes **(d-f)**. **(a,d)** acquired SiQDs signal (700-775 nm), **(b)** late endosomes stained by indirect immunofluorescent staining - M6PR + secondary antibody conjugated with AF568 (609-654 nm), **(e)** lysosomes stained by indirect immunofluorescent staining – LAMP2 + secondary antibody conjugated with AF568 (609-654 nm), **(c,f)** merge of the two fluorescent channels with bright-field Nomarski contrast (artificial colorization: red – SiQDs, green – endocytic structures, yellow – overlap indicating colocalization).



Unsuitability of Pearson's correlation coefficient for our estimations was evident already during image analysis. As it turned out, this coefficient is very sensitive to irregular noise in images. Moreover, no colocalization (value lower than 0.5) of endocytic structures and SiQDs signal was not detected at any time point (Fig. F4). However, comparison of 2D and 3D projection for colocalization analysis showed very similar results. On the other hand, interpretation of two-channel overlap by Manders split coefficients was much easier. It consists of two coefficients - M1 and M2 to show how much certain channel overlaps the other (%). M1 coefficients are shown in graphs and indicate the portion of overlapping SiQDs signal with endocytic structures. M2 coefficients indicate the portion of overlapping endocytic structures with SiQDs signal which did not interpret principally the colocalization of SiQDs, thus they are not presented in graphs. The highest portion of colocalization (over 70%) of SiQDs was detected at 1 hour with M6PR (Fig. F5). More differences were observed between 2D and 3D projection analysis. Colocalization of SiQDs with M6PR implies that the amount of SiQDs in M6PR decreases in time. In the case of LAMP2, the situation with colocalization with SiQDs is not so unambiguous.

This research provided rough information about the way of SiQDs entry into the cells, yet endocytosis was not certainly confirmed. Manders split coefficient was approved as more suitable for interpretation of colocalization than Pearson's coefficient. However, in this case, only more detailed 3D images should be used for evaluations, as with Manders split coefficient there were detected differences between 2D and 3D analysis.

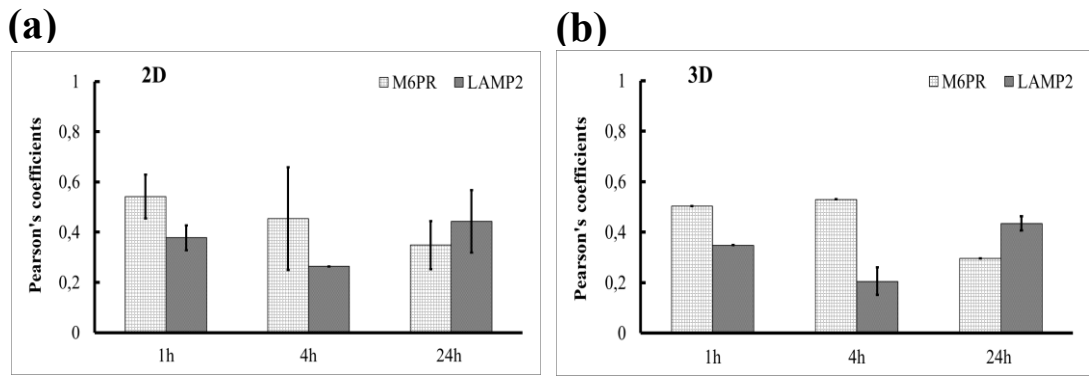


**Figure F4: Pearson's correlation coefficient values showing colocalization of SiQDs with late endosomes and lysosomes in the presence of FBS after 1, 4 and 24 hours. Analysis based on images from 2D (a) and 3D (b) projection.**

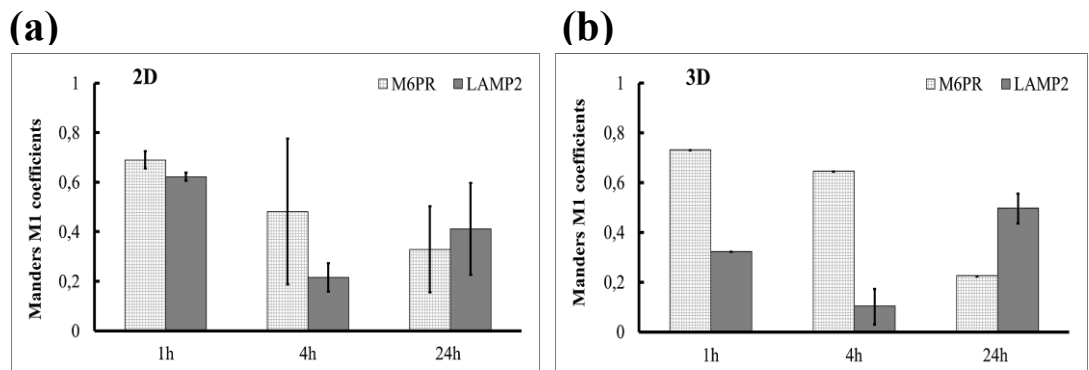


**Figure F5: Manders M1 split coefficient values showing proportional overlap of SiQDs with late endosomes and lysosomes in presence of FBS after 1, 4 and 24 hours. Analysis based on images from 2D (a) and 3D (b) projection.**

### 6.3.2 Unpublished data (F): Live Imaging of Cells Interacting with Silicon Quantum Dots

Visualization of SiQDs in cell cultures in time was actually the first imaging experiment of SiQDs; thus, this study preceded all previous experiments. The principal task of these experiments was to estimate the time-points of first SiQDs entry into the cells, the loss of SiQDs signal due the processing in cell or the cell death. This information would therefore lead the experimental set-up of following visualization studies. Live tracking of SiQDs on their way from the cultivation medium through the cell membrane and their subsequent accumulation inside the cell would give us important connection with the measured time-dependent SiQDs cytotoxicity. In order to ensure stable and convenient environment for cells during imaging, only standard cultivation method (15% FBS supplemented medium) was employed.

After the addition of  $100 \mu\text{g ml}^{-1}$  SiQDs to SAOS-2, cells were transferred into the preheated chamber on the table top of Nikon microscope. Images were acquired approximately every 30 minutes until the cell death. Maximum overall time-lapse of the experiment was 24 hours, however, only first 180 min are presented in this thesis (Fig. F6)

All experiments showed large similarity in time-lapse cell viability. The first images were taken after 30 minutes from the SiQDs addition to the SAOS-2 cells (Fig. F6). Inside the selected cells, there were already plenty of small vesicles emitting SiQDs signal. Amount of the SiQDs signal increased in time, but after 90 minutes from the addition, cells started to shrink and the SiQDs signal faded away. After 150 minutes, observed selected cells detached from the surface and in next 30 minutes were dead. SiQDs signal vanished together with the cells. However, even cells with less or no SiQDs signal died in the same manner. Moreover, the cells tracked after the 180 min time-point died even faster which suggested that the main reason for cell death was the long-time exposure to the extensive UV irradiation. In all experiments cells started to die quickly after the acquisition of the first image.

This study quit the live imaging experiments due to excessive cell death after immense UV irradiation needed for SiQDs excitation. Thus, all further experiments were performed on fixed cells.

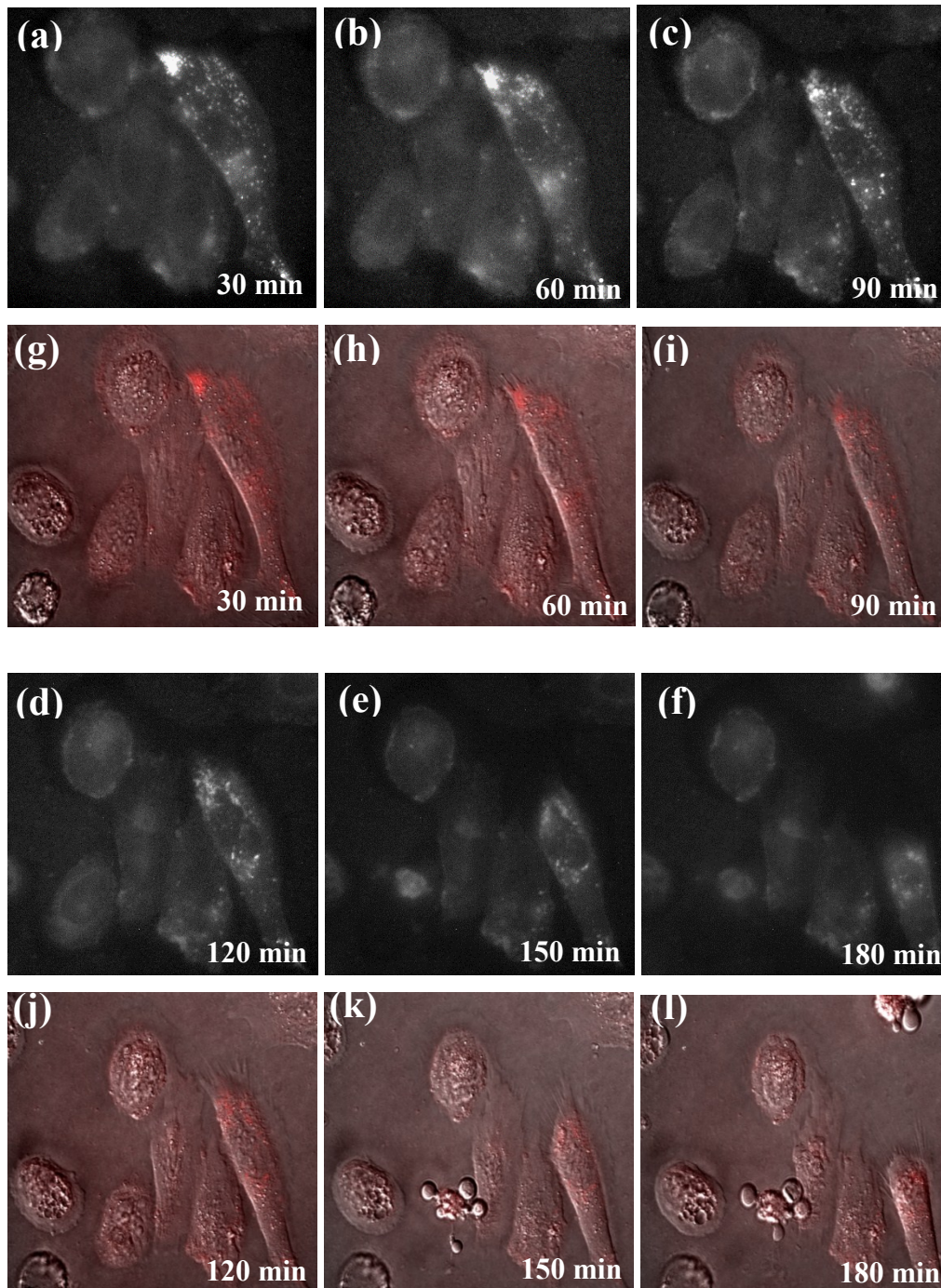


**Figure F6: Time-lapse images of osteoblasts (SAOS-2) from 30 to 180 minutes after SiQDs addition to cultivation medium. (a-f) fluorescent images of SiQDs signal, (g-l) merged images of fluorescent SiQDs channel and bright-field Nomarski contrast (SiQDs in red).**

## 6.4 PART IV: Gold and Platinum Nanoparticles (G)

### 6.4.1 Publication G: Preparation of Noble Nanoparticles by Sputtering – Their Characterization

Markéta Pišlová, Marie Hubálek Kalbáčová, **Lucie Vrabcová**, P. Slepíčka, Zdeňka Kolská, V. Švorčík (2018): Preparation of Noble Nanoparticles by Sputtering – Their Characterization. Digest Journal of Nanomaterials And Biostructures 13, 1035-1044. IF = 0.673

Besides silicon-based nanoparticles, also metal nanoparticles were tested for their cytotoxicity in accordance with the established protocols from PART II. Unlike silicon-based nanoparticles, gold (AuNPs) and platinum (PtNPs) nanoparticles are not biodegradable and they do not emit the natural photoluminescence. However, the main potential of these nanoparticles in human medicine lies in the antitumor and antibacterial activity (AuNPs) or antioxidant activity and photothermal treatment (PtNPs). Several approaches are used to prepare metal-based nanoparticles, yet only the physical methods do not pose a risk for utilization in biomedicine. AuNPs and PtNPs tested in this publication were prepared by direct sputtering into liquid medium of polyethylene glycol (PEG). By this method, stable nanoparticles of unified shape and size were fabricated.

This research is based on the cooperation of biological and chemical sectors. The biological part was performed by the author of the thesis while preparation and characterization of the nanoparticles was done by colleagues from Department of Solid State Engineering, University of Chemistry and Technology, Prague and from Faculty of Science, J. E. Purkyně University, Ústí nad Labem.

Cytotoxicity of spherical AuNPs (diameter of 6.3 nm) and rod PtNPs (1.5 x 4.2 and 1.5x7.9 nm) (Fig. 4 in publication G) was evaluated on cell culture of SAOS-2 cells in standard cultivation medium after 24 hours. Gradually increasing concentrations of both nanoparticles were used for testing of their influence on cell metabolic activity – 0.56, 2.8, 5.6, 8.4, 11.2 and 14 mg L<sup>-1</sup> of AuNPs and 0.6, 3, 6, 9, 12 and 15 mg L<sup>-1</sup> of PtNPs.

Despite the similar concentrations of AuNPs and PtNPs, more cytotoxic effect was observed in case of SAOS-2 cells treated with AuNPs (Fig. 6 in publication G). No significant decrease in metabolic activity in comparison to untreated cells was detected for the two lowest concentrations of AuNPs while in the case of PtNPs no significant decrease was observed for the three lowest concentrations. Cytotoxic effect was observed in cells treated with AuNPs of  $11.2 \text{ mg L}^{-1}$ , whereas the same effect was observed with PtNPs only after using  $15 \text{ mg L}^{-1}$  (Fig. 6 in publication G). Representative images of the influence of the lowest and highest concentrations of both nanoparticles on SAOS-2 cells viability are illustrated in Fig. 7 in publication G.

In this publication we estimated the cytotoxic concentrations of AuNPs and PtNPs under the standard cell cultivation conditions. This fundamental study was extended by additional experiments with AuNPs with different PEG termination and the results were published in the paper of my follower (Reznickova et al., 2019)

## 7 Discussion

This thesis is based on the study of two types of nanomaterials with the intended use in biomedicine. First part is dedicated to ultra-fine grain titanium as a surface nanomaterial and other three parts focus on nanoparticles of different origin.

Standard (S) and two novel **UFG-Ti materials** (Z and M) with improved mechanical properties for prospective development of various medical implants are described in **Part I of the thesis** (publication A, unpublished data B). Commercially pure titanium is long-time distinguished for its exceptional biocompatibility, yet the new manufacturing technique must prove its suitability for fabrication of the titanium material with the same or even improved characteristics for utilization in biomedicine. Moreover, from the perspective of cell biology, the surface treatment is of capital importance due to the significant influence on the adhesion, growth, and morphology of cultivated cells (Naddeo et al., 2015; Ren et al., 2018). Evaluation of these initial short-term interactions of cells with UFG-Ti samples was performed in a first place to determine whether this material initiates proper cell adhesion in sufficient amount of cells which would be followed by adequate proliferation and possibly differentiation to form final tissue.

First, bone-related cells – human osteoblasts and mesenchymal stem cells were selected for the testing of cytocompatibility as they will prospectively commonly interact with UFG-Ti in a form of dental or orthopedic implant. Osteoblasts, represented by cell line SAOS-2, showed comparable or better results on all UFG-Ti samples than PS control. The initial attachment (2 hours) of SAOS-2 cells on UFG-Ti was increased, yet the further growth (48 hours) was slightly slowed down compared to PS control, which indicates that the cells tried to adapt to the uneven surface. This statement corresponds to the results of metabolic activity after 48 hours, where higher cell number on UFG-Ti samples did not cause increase in metabolic activity possibly because of the adaptation process. The same situation was observed also with primary hMSCs, yet the increase of initial adhesion was not as much dramatic as with SAOS-2 cells. Consequently, the slower growth led to lower cell number on all UFG-Ti samples than on PS control which together with metabolic activity results suggest noticeable demands of UFG-Ti surface on hMSCs

adaptation. This finding is consistent with several cytocompatibility studies of different titanium materials (Kubo et al., 2009; Medvedev et al., 2017; Richert et al., 2008). Unfortunately, despite very similar experimental set-up, most of the current studies focus mainly on the comparison of influence of different surface topographies among the titanium samples without correlation to standard cultivation material (polystyrene) (Gui et al., 2018; Kang et al., 2018; Ren et al., 2018). Lack of this information, though, cannot reliably report, whether such material induces sufficient proliferation as standard cultivation material is specially designed to promote cell adhesion and growth. Furthermore, both cell types displayed significantly smaller size on all UFG-Ti samples than on PS control after 48 hours. Zinger et al. hypothesized, that this phenomena is caused by integrating the cell mass deep into the surface structures resulting in smaller yet thicker cells, however, cell thickness was not estimated in our study (Zinger et al., 2004).

Later assessment with SAOS-2 cells only, was focused on production of collagen type I during long-time cultivation (14 days) on UFG-Ti samples. In the course of cultivation, higher production of collagen type I was detected on all UFG-Ti samples than on PS control. This may be caused either by higher number of SAOS-2 cells on UFG-Ti samples, which was determined at 48 hours, or by stimulation to differentiation by rugged surface. Influence of surface topography of titanium on osteoblasts collagen type I production was studied with inconsistent results from no effect to significant increase of production by several research groups (Iwaya et al., 2008; Mariscal-Muñoz et al., 2016; Zhao et al., 2010).

Until this point, no significant influence of the type of surface treatment (polishing vs. grinding) on cells was detected. Finally, differences were revealed in morphology and focal adhesions observations after 48 hours of cultivation. Although, SAOS-2 cells cultured on both UFG-Ti samples displayed the same shape as on PS control, their focal adhesions on ground samples were usually placed on the cells extensions while on polished samples most of the focal adhesions were found in the basal pole of the cells. The surface of polished samples comprised of predominantly continuous nanotopography, thus the cell anchoring to the surface took place on the whole bottom pole of the cell. In contrary, ground samples as a combination of micro/nano topography with numerous peaks and valleys force the cells to adhere onto the elevated structures and form “bridges” among these



structures in order to anchor the whole cell (Lagonegro et al., 2018). hMSCs cultivated on polished surfaces displayed variable shapes and diverse orientation of growth as they were not limited by fluctuating topography features. Moreover, more solitary cells were found on this type of surface. Ground samples more or less directed the cells growth along the valleys and around higher peaks which resulted in formation of cells elongated in variable directions and connected tightly one to another. This finding is consistent with many other studies (Babuska et al., 2018; Chen et al., 2012; Teng et al., 2012), where mostly micro/nano topography is confirmed as a suitable surface for future hard tissue implants as it resembles natural bone structure (Mulari et al., 2004).

Although both mentioned cell types resemble with their interactions to UFG-Ti samples, the apparent difference in cell morphology and spreading led to the employment of another primary cell type and immortalized cell line for evaluation of cell responses to UFG-Ti. Therefore, further assessment was performed on primary human dermal fibroblasts and keratinocyte cell line HaCaT, which both represent the soft tissue as a contrast to osteoblasts representing hard tissue. Integrity of soft-tissue-implant interface is crucial for the proper function of special types of titanium implants. Such bone-anchored transcutaneous implants overcome problems of conventional amputation prostheses (pain, necrosis) by direct contact to the skeleton through the support of soft tissue (Chen et al., 2009).

As it was expected, NHDF exhibited very similar results to hMSCs in all observed characteristics (cell proliferation, cell area, cell morphology and metabolic activity), confirming the statement, that primary cells interactions with an artificial material are specific and more sensitive (Markhoff et al., 2017). Yet it should be noted, that principally the cell area assessments were highly influenced by the state of the donor at the time of the cells isolation. On the other hand, HaCaT displayed ambiguous results. Their initial attachment was higher on UFG-Ti samples than on PS control yet their further proliferation rate was not assessed. Metabolic activity was decreased insignificantly and cell area was comparable to the cells on PS control. However, the way of growth was affected by surface treatment resulting in forming incoherent layers of a small number of cells on ground samples which assume further problems with integrity of the whole tissue. The same findings were described by several studies where cells derived from soft-tissue preferred simple

nanostructured topography to the more roughed surface (Pendegrass et al., 2008; Tan et al., 2017).

Besides the biocompatibility, the biological lifespan of an implant is defined also by its low immunogenicity. Detection of inflammatory cytokines IL-8 and TNF- $\alpha$  in blood samples during 6 hours cultivation revealed increased values of both cytokines compared to PS control. Moreover, significantly higher amount was detected on ground samples, which in case of TNF- $\alpha$  is apparent only in the comparison of individual donors. Increased levels of cytokines caused by the presence of titanium material with micro/nano topography was observed in many studies (Markhoff et al., 2017; Östberg et al., 2015). Importantly, the profound inflammatory response (comparison with LPS control) was not attained by any of the UFG-Ti sample. The research of Lamers et al. rationalized the increased values of inflammatory cytokines on textured surface by macrophage activation to induce a wound healing rather than inflammatory response (Lamers et al., 2012).

In summary, all tested UGF-Ti samples with both surface modifications were stated as biocompatible with all tested cell types. Yet the best results were obtained for osteoblasts-like cells, which is a favorable outcome in the perspective of orthopedic or dental implant development.

**Part II of the thesis** (publications C and D, unpublished data E) focuses on the assessment of cytotoxicity of **silicon-based nanoparticles** to various cell types under different cultivation conditions accompanied with microscopic visualization of their presence inside the cells. Last decade, the main challenge in development of silicon nanoparticles for bioimaging was their stability in polar solvents (aqueous biological fluids) while maintaining the unique photoluminescence. Several approaches were proposed to prevent undesired agglomeration and alteration of optical characteristics e.g. micelle encapsulation (Erogbogbo et al., 2008) or stabilization by organic ligands (Hessel et al., 2012), but other difficulties (impossible functionalization, high sensitivity of luminescence to organic ligand) emerged. Preserving the inorganic nature of silicon nanoparticles to retain high photoluminescence quantum yield became an important task for their potential utilization in biology and biomedicine.

Initially, all-inorganic silicon quantum dots co-doped with boron and phosphorus were studied with respect to their impact on different human cells. The

unique technique of preparation is based on formation of the core which is protected by heavily doped shell; thus photoluminescence of the core is less sensitive to the environment. Moreover, negative surface of the shell ensures the long-time SiQDs stability in water (Fujii et al., 2016). Due to their high stability, emission peak in near-infra red ranges and environment-friendly character, the possible use in bio-imaging was proposed. Since the evaluation of cytotoxicity was the very first time, when this type of SiQDs was introduced to the biological environment, this study practically represents a basic research. At first, SiQD 1100 (size of 4 nm) and 1050 (size of 3 nm) were selected for the testing and despite their identical chemical nature, significant differences arose in biological environment of the SAOS-2 cell culture. Particularly, the presence of FBS proteins, which causes the protein corona formation, radically affected behavior of both SiQDs types. The formation and structure of the protein corona (PC) is crucial for the fate of nanoparticles in biological fluids since PC influences nanoparticle uptake and the way of entry into the cells (Catalano et al., 2015; Ho et al., 2018; Long et al., 2018). The presence of FBS caused cytotoxicity effect of SiQD 1100 only at the highest ( $125 \mu\text{g ml}^{-1}$ ) concentration after 24 hours while for SiQD 1050 such effect was detected only after 48 hours. However, possible positive conclusion for SiQD 1050 was denied by subsequent microscopic inspection, where extensive amount of protein/SiQD 1050 agglomerates covering the cells from the outside was detected. Only negligible amount of SiQD 1050 was observed in 3D inside the cells, thus we hypothesized that most of SiQD 1050 were attached in agglomerates and were not available for cellular uptake. Aggregation of some types of nanoparticles in biological fluids remains unexplained, yet this effect was reported in many studies (Calatayud et al., 2014; Hemelaar et al., 2017). On the other hand, SiQD 1100 were detected inside the cells in the presence of FBS after 24 hours in a form of vesicles which suggested their potential uptake by endocytosis. Furthermore, both SiQDs harmed the SAOS-2 cells earlier and at a lower concentration in the absence of FBS. In the case of SiQD 1050 the cytotoxic effect was determined already after 24 hours at all concentrations. Fluorescence microscopy partly clarified this finding when different signal distribution inside the cells was detected for SiQD 1100. Observed diffuse signal in the cytoplasm indicated that SiQD 1100 enter the cells by different routes in dependence on the presence or absence of FBS. In contrary, despite their cytotoxic

effect, SiQD 1050 were not detected in the cells. These contradictory results may be explained by substantially lower quantum efficacy of SiQD 1050 which renders them more difficult for observation by means of fluorescence microscopy or by so called “blue-shift” of emission spectra due to degradation of SiQD 1050 inside the cells which was also described in the work of Jin et al. (Jin et al., 2018).

Additionally, SiQD 1100 were employed for detailed study of their uptake and trafficking inside the SAOS-2 cells due to their more stable behavior in cell culture. This research is summarized in **PART III of the thesis** (unpublished data E and F). Real-time tracking of nanoparticles in cell culture is not usually performed in the studies, since most of the experiments are conducted on cells fixed at selected time points. Anyway, imaging of live cells in time enables visualization of nanoparticle trajectories inside the cells (Ferrati et al., 2010) or accompanied with vital staining enables observation of nanoparticle internalization through the membrane into inner cell compartments (Pang et al., 2016). In our case, we were interested in fundamental information about the approximate time-point of SiQD 1100 uptake by SAOS-2 cells and the subsequent fate of their signal inside the cells as these experiments preceded all following visualization studies with SiQD 1100. In order to obtain the correct sufficient signal of SiQD 1100, the high mercury lamp intensity of 330 – 380 nm (UV) was used for excitation for prolonged (10 seconds) exposition time. In most of the cells, SiQD 1100 signal was detected already after 30 minutes upon addition which is in agreement with the research of Ohta et al. where the same concentration of different type of SiQDs was observed inside the endothelial cells (Ohta et al., 2012). The mentioned publication further describes the gradual accumulation of SiQDs inside the cells until reaching the plateau value around 200 minutes. Unfortunately, this result of our real-time live imaging could not be estimated due to mentioned immense UV irradiation which led to cell death over first 180 minutes. Consequently, we stated that SiQD 1100 are not suitable for live-imaging as long as mentioned short wavelengths are necessary for their excitation. Moreover, for biological applications not only harmful effect but also the limited tissue penetration of UV light should be taken into account (Shi et al., 2018).

Next time-lapse imaging followed on the results of publication C. This time, the aim was to assess whether SiQD 1100 are internalized into the SAOS-2 cell by endocytosis and if so, then at which time-point they are present in late endosomes or

lysosomes. Since the formation of PC apparently influenced the accumulation of SiQD 1100 in vesicular structures inside the cells, this study was performed only in the presence of FBS in cultivation medium. Interpretation of colocalization by Manders split coefficient in our case was more clear and relevant than traditionally used Pearson's correlation coefficient (Ji et al., 2018; Pang et al., 2016). The outcome of colocalization assessment revealed the initial (1 hour) high spatial correlation of SiQD 1100 with late endosomes which further decreased in time. This trend was estimated both for Manders and Pearson's coefficient as well as for 2D and 3D projections. The colocalization of SiQD 1100 with lysosomes showed in all cases the lowest values at 4 hour time-points while the highest portion of colocalization was mostly estimated at 24 hours. The indistinct time-lapse influence cannot imply whether SiQD 1100 are finally trafficked and accumulated in lysosomes as this finding was approved by lot of researchers (Damalakiene et al., 2013; Ji et al., 2018; Wang et al., 2018; Zhang and Monteiro-Riviere, 2009). On the other hand, Pang et al. similarly observed significant colocalization of silicon nanoparticles with late endosomes at 4 hours with further decreasing trend until 8 hours. Since no colocalization was determined for lysosomes, authors suggest that nanoparticles escaped from late endosome into cell cytoplasm (Pang et al., 2016).

Subsequently in the study of **PART II of the thesis**, we estimated the influence of PC formation on cytotoxic potential of SiQD 1100 in hMSCs, macrophages and monocytes THP-1. As SAOS-2 cells represent osteosarcoma cell line, certain differences in nanoparticle uptake were expected as it was reported in literature (Lunov et al., 2011; Osaka et al., 2009). And indeed, primary hMSCs exhibited noticeable resistance to SiQD 1100 impact both in the presence and absence of FBS. Also LDH detection showed higher incidence of necrosis in SAOS-2 than in hMSCs. This statement is consistent with the research of Faedmaleki et al. with silver nanoparticles which revealed their anticancer potential due to significant higher inhibitory effect on malignant HepG2 cell line than on primary hepatocytes (Faedmaleki et al., 2014). Both forms of THP-1 cell line showed initial stimulation of metabolic activity in the presence of FBS which may be connected with the early inflammatory response facilitated by protein corona. Actually, the lack of FBS during cultivation with SiQD 1100 significantly harmed both monocytes and macrophages.

Next in **PART II of the thesis**, silicon-carbide nanoparticles were employed to the same test of cytotoxicity in the perspective of protein corona formation. This type of nanoparticle resembles the SiQD with long-time stability in aqueous solutions and high photoluminescence (Botsoa et al., 2008). The anticipated biocompatibility of SiCs arose from the research of chemically inert bulk SiC material (Yakimova et al., 2007), yet as we know, the nanostructuring may reveal unforeseen characteristics. Previously, SiCs were already tested by other colleagues by AlamarBlue Cell Viability Assay Kit on human cervical adenocarcinoma cells (HeLa) to determine half maximal inhibitory concentration ( $IC_{50} = 227,5 \mu\text{g ml}^{-1}$ ) (Beke et al., 2013). We observed negative effect of SiCs on SAOS-2 cells in the presence of FBS only at the highest concentration ( $250 \mu\text{g ml}^{-1}$ ), but unlike SiQDs, the metabolic activity still increased in time. The time-dependent increase of metabolic activity was also observed in the absence of FBS, yet all the tested concentration were stated as cytotoxic after 48h. These results indicate that SiCs rather inhibit the SAOS-2 cells, yet in the absence of proteins from FBS the inhibition causes more significant damage. Thus for standard conditions we came to similar conclusion as Beke et al. but it should be emphasized that both tests were performed with carcinoma cell lines (Beke et al., 2013). Moreover to the comparison of both studies, in the case of Beke et al. the direct injection of SiCs into hippocampal CA1 pyramidal cells was employed in order to visualize them by two-photon excitation which showed a significant response. In our case, though, only cell-mediated uptake was visualized, yet no specific SiCs signal was observed even after two-photon excitation. We attribute this distinction to the disproportionate amount of SiCs inside the cells after direct injection and after passive cell uptake. Accordingly, insufficient amount of SiCs in cells could not be detected due to immense autofluorescence of the cells in the emission range of SiCs.

Nanoparticles of metal origin were used for cytotoxicity evaluation in **PART IV of the thesis** (publication G). Platinum and especially gold nanoparticles have been tested for various biomedical applications for decades (antibacterial, antiviral, anticancer treatment, nano-enzyme activity), yet still new difficulties in their preparation emerge as the new findings in the field of cytotoxicity are continuously discovered (Soenen et al., 2015). Specific harmful effect of both AuNPs and PtNPs is still not fully understood, but currently, significant influence on metal nanoparticles

cytotoxicity is attributed to the contaminants from synthesis processes (endotoxins, organic solvents, toxic reagents) (Pedone et al., 2017). Due to this knowledge, mainly the physical or so called “green” synthesis (Siegel et al., 2013) of metal nanoparticles is nowadays preferred for prospective applications in biology and biomedicine. AuNPs and PtNPs in our study were prepared by physical method of direct sputtering into liquid polyethylene glycol which represents simple and environmentally friendly synthesis with reproducible results. Since the cytotoxicity tests were performed for the first time with these types of Au and PtNPs, study of their behavior in cultivation media was employed prior to the actual evaluation with SAOS-2 cells. The initial divergent characteristics of size, shape and zeta potential between AuNPs and PtNPs dramatically changed after their addition into cell cultivation medium resulting in equalization of the mentioned parameters. Similar situation was described by Tlotleng et al. in their study of gold nanoparticles with different surface functionalization which original different characteristics equalized in the contact with proteins and salts from cultivation medium (Tlotleng et al., 2016). Surprisingly, despite their final comparable characteristics and concentrations used, more cytotoxic effect was evaluated for AuNPs after 24 hours cultivation. It is apparent, that the origin of the cytotoxicity still lies in the fundamental differences of these two metals which may cause variable reactivity or catalytic activity in biological environment. The importance of the thorough cytotoxicity assessment of specific nanoparticles should be highlighted as it is demonstrated by comparison of our results with the work of Hashimoto et al., where oppositely platinum nanoparticles demonstrated more cytotoxic effect than golden nanoparticles (Hashimoto et al., 2016).

In conclusion to this nanoparticle section, our studies provided important information about the crucial influence of even slight differences in nanoparticle characteristics which can lead to extensively dissimilar behavior in the cell culture environment. We tested three different types of fluorescent silicon-based nanoparticles (SiQD 1100, SiQD 1050 and SiCs) and two types of metal nanoparticles (AuNPs and PtNPs) and despite their resembling structure (silicon-based nanoparticles) and size, significantly different interactions were observed with standard SAOS-2 cell line. Principally, the influence of proteins from FBS forming PC caused immense differences between the behavior of even chemically identical

SiQD 1100 and SiQD 1050. We addressed this discrepancy to the possibly different structure of PC caused by differing surface chemistry (zeta potential). Taken together, generalization of nanoparticle cytotoxicity based simply on the material characteristics should always be avoided. Moreover, it is emphatically advised to perform initial *in vitro* experiments from the perspective of future biomedical utilization to mimic the prospective environment of the organism.



## 8 Conclusions

- I. The evaluation of biological responses of four different cell types to six samples of **ultra-fine grain titanium** (three types of grain sizes with two types of surface treatment) consisted of proliferation, metabolic activity and cell area assessment accompanied with cell morphology description. Osteoblasts (SAOS-2 cell line) demonstrated positive feedback on all UFG-Ti samples in mentioned criteria for cytocompatibility. Different distribution of focal adhesion plaques of SAOS-2 cells on samples with diverse surface treatment correlated with their topography features. Collagen type I production by SAOS-2 cells showed increase on all UFG-Ti samples compared to polystyrene (PS) control. Primary cells represented by hMSCs and NHDF evinced distinct sensitivity to the UFG-Ti samples which was manifested by successive adaptation to the surface. For keratinocytes (HaCaT cell line), UFG-Ti was not considered as a suitable material for their prosper growth. Low immunogenicity of UFG-Ti was approved by inflammatory cytokines detection in blood samples. All UFG-Ti samples were confirmed as stimulating surfaces for the growth of osteoblasts and thus this material was recommended for future bone or dental implant development.
  
- II. Description of elemental reactions of cells to fluorescent **silicon co-doped quantum dots** SiQD 1100 (4 nm), SiQD 1050 (3 nm) and fluorescent **silicon carbide nanoparticles** SiCs (2 nm) elucidated crucial role of protein corona on nanoparticle final cytotoxicity. Although SiQD 1050 exhibited low cytotoxic effect towards SAOS-2 cells, visual inspection revealed their huge aggregation with proteins in cultivation medium which hindered their uptake by cells. Nevertheless, such effect would have fatal consequences upon application into living organism. Significant cytotoxic effect of SiQD 1050 was observed in

protein corona absence, yet it was not possible to detect them inside the cells due to possible photoluminescence shift.

Cytotoxic concentrations of SiQD 1100 were estimated for SAOS-2 cells, hMSCs and monocytic cell line THP-1 (monocytes, macrophages) in the presence and absence of protein corona. Primary hMSCs demonstrated higher resistance to SiQD 1100 than the cell lines. Both forms of THP-1 cells were stimulated by SiQD 1100 with protein corona during first six hours.

Microscopic visualization of SiQD 1100 in SAOS-2 cells confirmed their presence inside the cells both with and without protein corona although the pathways of uptake probably differ.

Cytotoxic concentrations were also estimated for SiCs in culture of SAOS-2 cells in the presence and absence of protein corona. Following detailed studies were further performed by my colleagues.

The results provided information about the in vitro cytotoxicity of silicon-based nanoparticles and clarified the relation of cytotoxic effect with the complex interactions of nanoparticles and biological environment.

- III. Optimization of protocols for **microscopic imaging of fluorescent silicon nanoparticles** were performed with SiQD 1100 as they place high demands on visualization in biological environment. Specific characteristics of silicon photoluminescence were implemented into technical adjustment of wide-field and confocal microscopes. Resulting protocols enabled visualization of silicon nanoparticles with low quantum efficiencies even in near-infra red ranges of visible spectra. Additionally, proposed standardized experimental set-up facilitated separation of the positive silicon nanoparticle signal from the cell autofluorescence, yet further optimizations have to be employed as this protocol did not fit to silicon carbide nanoparticles with emission peak (450 nm) in biological autofluorescence highest emission range.

**Advanced imaging** techniques enabled 3D spatial visualization of SiQD 1100 inside the SAOS-2 cells and colocalization of their signal with late

endosomes and lysosomes which suggested possible time-dependent internalization of SiQD 1100 with protein corona inside late endosomes. Another technique of real-time live imaging was not recommended for visualization of SiQD 1100 due to excessive cell death after UV irradiation.

Established protocols for different microscopes will continue to facilitate the imaging of any new type of silicon-based nanoparticles in cell cultures.

- IV. Determination of SAOS-2 cells viability in the presence of the **gold and platinum nanoparticles** was performed according to the well-established protocols for cytotoxicity testing of silicon-based nanoparticles. Despite similar characteristics of both nanoparticles in cell cultivation medium, AuNPs were confirmed as more cytotoxic than PtNPs. Evaluation were conducted only under standard cultivation conditions at single time-point (24 hours). Further detailed evaluations were already performed by my colleagues based on this research.

## 9 Complete List of Authors' Publications

**Lucie Ostrovská**, Lucie Vištejnová, Jan Džugan, Peter Sláma, Tomáš Kubina, Egor Ukraintsev, Dana Kubies, Milena Králíčková, Marie Hubálek Kalbáčová (2016): **Biological evaluation of ultra-fine titanium with improved mechanical strength for dental implant engineering.** Journal of Materials Science 51, 3097-3110. IF = 2.993

**Lucie Ostrovská**, Antonín Brož, Anna Fučíková, Tereza Bělinová, Hiroshi Sugimoto, Takashi Kanno, Minoru Fujii, Jan Valenta, Marie Hubálek Kalbáčová (2016): **The impact of doped silicon quantum dots on human osteoblasts.** RSC ADVANCES 6, 63403-63413. IF = 2.936

Tereza Bělinová, **Lucie Vrabcová**, Iva Machová, Anna Fučíková, Jan Valenta, Hiroshi Sugimoto, Minoru Fujii, Marie Hubálek Kalbáčová (2018): **Silicon Quantum Dots and Their Impact on Different Human Cells.** Phys. Status Solidi B, 255, 1700597. IF = 1.729

Markéta Pišlová, Marie Hubálek Kalbáčová, **Lucie Vrabcová**, P. Slepíčka, Zdeňka Kolská, V. Švorčík (2018): **Preparation of Noble Nanoparticles by Sputtering – Their Characterization.** Digest Journal of Nanomaterials And Biostructures 13, 1035-1044. IF = 0.673

## 10 List of Abbreviations

2D	two-dimensional
3D	three-dimensional
ANOVA	analysis of variance
AuNPs	gold nanoparticles
cpTi	commercially pure titanium
DAPI	4',6-diamidino-2-phenylindole
DMEM	Dulbecco's modified eagle medium
ECAP	equal-channel angular pressing
ECM	extracellular matrix
ELISA	enzyme-linked immunosorbent assay
FA	focal adhesions
FBS	fetal bovine serum
HaCaT	spontaneously transformed aneuploid immortal keratinocyte cell line from adult human skin
hMSCs	human mesenchymal stem cells
IL-8	interleukin 8
LAMP2	lysosome-associated membrane protein 2
LDH	lactate dehydrogenase
LPS	lipopolysaccharide
M1, M2	Manders split coefficients
M6PR	mannose-6-phosphate receptor
MTS	(3-(4,5-dimethylthiazol-2-yl)-5-(3-carboxymethoxyphenyl)-2-(4-sulfophenyl)-2H-tetrazolium)
NHDF	normal human dermal fibroblasts
NPs	nanoparticles
NS	nanosurface
PBS	phosphate buffered saline
PC	protein corona
PS	polystyrene surface control
PtNPs	platinum nanoparticles
QDs	quantum dots

RGD	arginine-glycine-aspartate peptidic sequence
RPMI	Roswell Park Memorial Institute medium
SAOS-2	sarcoma osteogenic cell line
SiCs	silicon carbide nanoparticles
SiNPs	silicon nanoparticles
SiQDs	silicon quantum dots
THP-1	spontaneously immortalized monocyte-like cell line
TNF- $\alpha$	tumour necrosis factor $\alpha$
UFG-Ti	ultra-fine grain titanium

## 11 References

- Ahmad Khalili, A., Ahmad, M.R., 2015. A Review of Cell Adhesion Studies for Biomedical and Biological Applications. *Int. J. Mol. Sci.* 16, 18149–18184. <https://doi.org/10.3390/ijms160818149>
- Albanese, A., Walkey, C.D., Olsen, J.B., Guo, H., Emili, A., Chan, W.C.W., 2014. Secreted Biomolecules Alter the Biological Identity and Cellular Interactions of Nanoparticles. *ACS Nano* 8, 5515–5526. <https://doi.org/10.1021/nn4061012>
- Anselme, K., 2000. Osteoblast adhesion on biomaterials. *Biomaterials* 21, 667–681. [https://doi.org/10.1016/S0142-9612\(99\)00242-2](https://doi.org/10.1016/S0142-9612(99)00242-2)
- Anselme, K., Bigerelle, M., Noel, B., Dufresne, E., Judas, D., Iost, A., Hardouin, P., 2000. Qualitative and quantitative study of human osteoblast adhesion on materials with various surface roughnesses. *J. Biomed. Mater. Res.* 49, 155–166. [https://doi.org/10.1002/\(SICI\)1097-4636\(200002\)49:2<155::AID-JBM2>3.0.CO;2-J](https://doi.org/10.1002/(SICI)1097-4636(200002)49:2<155::AID-JBM2>3.0.CO;2-J)
- Atala, A., 2012. Regenerative medicine strategies. *J. Pediatr. Surg.* 47, 17–28. <https://doi.org/10.1016/j.jpedsurg.2011.10.013>
- Audiffred, J.F., De Leo, S.E., Brown, P.K., Hale-Donze, H., Monroe, W.T., 2010. Characterization and applications of serum-free induced adhesion in jurkat suspension cells. *Biotechnol. Bioeng.* 106, 784–793. <https://doi.org/10.1002/bit.22728>
- Babuska, V., Palan, J., Kolaja Dobra, J., Kulda, V., Duchek, M., Cerny, J., Hrusak, D., 2018. Proliferation of Osteoblasts on Laser-Modified Nanostructured Titanium Surfaces. *Mater.* 1996-1944 11, 1827. <https://doi.org/10.3390/ma11101827>
- Baddour, J.A., Sousounis, K., Tsonis, P.A., 2012. Organ repair and regeneration: An overview. *Birth Defects Res. Part C Embryo Today Rev.* 96, 1–29. <https://doi.org/10.1002/bdrc.21006>
- Badylak, S.F., Hoppo, T., Nieponice, A., Gilbert, T.W., Davison, J.M., Jobe, B.A., 2011. Esophageal Preservation in Five Male Patients After Endoscopic Inner-Layer Circumferential Resection in the Setting of Superficial Cancer: A Regenerative Medicine Approach with a Biologic Scaffold. *Tissue Eng. Part A* 17, 1643–1650. <https://doi.org/10.1089/ten.tea.2010.0739>
- Barthel, A.-K., Dass, M., Dröge, M., Cramer, J.-M., Baumann, D., Urban, M., Landfester, K., Mailänder, V., Lieberwirth, I., 2014. Imaging the intracellular degradation of biodegradable polymer nanoparticles. *Beilstein J. Nanotechnol.* 5, 1905–1917. <https://doi.org/10.3762/bjnano.5.201>
- Batty, L.M., Norsworthy, C.J., Lash, N.J., Wasiak, J., Richmond, A.K., Feller, J.A., 2015. Synthetic Devices for Reconstructive Surgery of the Cruciate Ligaments: A Systematic Review. *Arthrosc. J. Arthrosc. Relat. Surg.* 31, 957–968. <https://doi.org/10.1016/j.arthro.2014.11.032>
- Bechtle, S., Ang, S.F., Schneider, G.A., 2010. On the mechanical properties of hierarchically structured biological materials. *Biomaterials* 31, 6378–6385. <https://doi.org/10.1016/j.biomaterials.2010.05.044>
- Beke, D., Szekrényes, Z., Pálfi, D., Róna, G., Balogh, I., Maák, P.A., Katona, G., Czirány, Z., Kamarás, K., Rózsa, B., Buday, L., Vértessy, B., Gali, A., 2013.

- Silicon carbide quantum dots for bioimaging. *J. Mater. Res.* 28, 205–209. <https://doi.org/10.1557/jmr.2012.296>
- Biffi, S., Voltan, R., Rampazzo, E., Prodi, L., Zauli, G., Secchiero, P., 2015. Applications of nanoparticles in cancer medicine and beyond: optical and multimodal in vivo imaging, tissue targeting and drug delivery. *Expert Opin. Drug Deliv.* 12, 1837–1849. <https://doi.org/10.1517/17425247.2015.1071791>
- Boguszewska-Czubara, A., Pasternak, K., 2011. Silicon in medicine and therapy. *J. Elemntology.* <https://doi.org/10.5601/jelem.2011.16.3.13>
- Botsoa, J., Lysenko, V., Géloën, A., Marty, O., Bluet, J.M., Guillot, G., 2008. Application of 3C-SiC quantum dots for living cell imaging. *Appl. Phys. Lett.* 92, 173902. <https://doi.org/10.1063/1.2919731>
- Boverhof, D.R., Bramante, C.M., Butala, J.H., Clancy, S.F., Lafranconi, M., West, J., Gordon, S.C., 2015. Comparative assessment of nanomaterial definitions and safety evaluation considerations. *Regul. Toxicol. Pharmacol.* 73, 137–150. <https://doi.org/10.1016/j.yrtph.2015.06.001>
- Bradbury, M.S., Phillips, E., Montero, P.H., Cheal, S.M., Stambuk, H., Durack, J.C., Sofocleous, C.T., Meester, R.J.C., Wiesner, U., Patel, S., 2012. Clinically-translated silica nanoparticles as dual-modality cancer-targeted probes for image-guided surgery and interventions. *Integr. Biol.* 5, 74–86. <https://doi.org/10.1039/C2IB20174G>
- Briley-Saebo, K., Bjørnerud, A., Grant, D., Ahlstrom, H., Berg, T., Kindberg, G.M., 2004. Hepatic cellular distribution and degradation of iron oxide nanoparticles following single intravenous injection in rats: implications for magnetic resonance imaging. *Cell Tissue Res.* 316, 315–323. <https://doi.org/10.1007/s00441-004-0884-8>
- Browne, M., Gregson, P.J., 2000. Effect of mechanical surface pretreatment on metal ion release. *Biomaterials* 21, 385–392. [https://doi.org/10.1016/S0142-9612\(99\)00200-8](https://doi.org/10.1016/S0142-9612(99)00200-8)
- Broz, A., Baresova, V., Kromka, A., Rezek, B., Kalbacova, M., 2009. Strong influence of hierarchically structured diamond nanotopography on adhesion of human osteoblasts and mesenchymal cells. *Phys. Status Solidi A* 206, 2038–2041. <https://doi.org/10.1002/pssa.200982203>
- Bruinink, A., Wang, J., Wick, P., 2015. Effect of particle agglomeration in nanotoxicology. *Arch. Toxicol.* 89, 659–675. <https://doi.org/10.1007/s00204-015-1460-6>
- Burns, K., Yao, C., Webster, T.J., 2009. Increased chondrocyte adhesion on nanotubular anodized titanium. *J. Biomed. Mater. Res. A* 88A, 561–568. <https://doi.org/10.1002/jbm.a.31899>
- Buzea, C., Pacheco, I.I., Robbie, K., 2007. Nanomaterials and nanoparticles: Sources and toxicity. *Biointerphases* 2, MR17–MR71. <https://doi.org/10.1116/1.2815690>
- Cai, L., Heilshorn, S.C., 2014. Designing ECM-mimetic materials using protein engineering. *Acta Biomater., Biological Materials* 10, 1751–1760. <https://doi.org/10.1016/j.actbio.2013.12.028>
- Calatayud, M.P., Sanz, B., Raffa, V., Riggio, C., Ibarra, M.R., Goya, G.F., 2014. The effect of surface charge of functionalized Fe<sub>3</sub>O<sub>4</sub> nanoparticles on protein adsorption and cell uptake. *Biomaterials* 35, 6389–6399. <https://doi.org/10.1016/j.biomaterials.2014.04.009>



- Casals, E., Pfaller, T., Duschl, A., Oostingh, G.J., Puentes, V., 2010. Time Evolution of the Nanoparticle Protein Corona. *ACS Nano* 4, 3623–3632. <https://doi.org/10.1021/nn901372t>
- Catalano, F., Accomasso, L., Alberto, G., Gallina, C., Raimondo, S., Geuna, S., Giachino, C., Martra, G., 2015. Factors Ruling the Uptake of Silica Nanoparticles by Mesenchymal Stem Cells: Agglomeration Versus Dispersions, Absence Versus Presence of Serum Proteins. *Small* 11, 2919–2928. <https://doi.org/10.1002/sml.201400698>
- Chen, F., Gerion, D., 2004. Fluorescent CdSe/ZnS Nanocrystal–Peptide Conjugates for Long-term, Nontoxic Imaging and Nuclear Targeting in Living Cells. *Nano Lett.* 4, 1827–1832. <https://doi.org/10.1021/nl049170q>
- Chen, G.J., Wang, Z., Bai, H., Li, J.M., Cai, H., 2009. A preliminary study on investigating the attachment of soft tissue onto micro-arc oxidized titanium alloy implants. *Biomed. Mater.* 4, 015017. <https://doi.org/10.1088/1748-6041/4/1/015017>
- Chen, S., Zhang, C., Jia, G., Duan, J., Wang, S., Zhang, J., 2014. Size-dependent cytotoxicity of europium doped NaYF<sub>4</sub> nanoparticles in endothelial cells. *Mater. Sci. Eng. C* 43, 330–342. <https://doi.org/10.1016/j.msec.2014.07.029>
- Chen, X., Cai, K., Lai, M., Zhao, L., Tang, L., 2012. Mesenchymal Stem Cells Differentiation on Hierarchically Micro/Nano-Structured Titanium Substrates. *Adv. Eng. Mater.* 14, B216–B223. <https://doi.org/10.1002/adem.201180073>
- Cho, I.-H., Irudayaraj, J., 2013. In-situ immuno-gold nanoparticle network ELISA biosensors for pathogen detection. *Int. J. Food Microbiol.* 164, 70–75. <https://doi.org/10.1016/j.ijfoodmicro.2013.02.025>
- Coluccio, M.L., De Vitis, S., Strumbo, G., Candeloro, P., Perozziello, G., Di Fabrizio, E., Gentile, F., 2016. Inclusion of gold nanoparticles in mesoporous silicon for the SERS analysis of cell adhesion on nano-structured surfaces. *Microelectron. Eng., Micro and Nano Technologies for Biology and Life Sciences* 158, 102–106. <https://doi.org/10.1016/j.mee.2016.03.045>
- Conde, J., Doria, G., Baptista, P., 2012. Noble metal nanoparticles applications in cancer. *J. Drug Deliv.* 2012, 751075. <https://doi.org/10.1155/2012/751075>
- Dalby, M.J., Gadegaard, N., Oreffo, R.O.C., 2014. Harnessing nanotopography and integrin-matrix interactions to influence stem cell fate. *Nat. Mater.* 13, 558–569. <https://doi.org/10.1038/nmat3980>
- Dalby, M.J., Gadegaard, N., Tare, R., Andar, A., Riehle, M.O., Herzyk, P., Wilkinson, C.D.W., Oreffo, R.O.C., 2007. The control of human mesenchymal cell differentiation using nanoscale symmetry and disorder. *Nat. Mater.* 6, 997–1003.
- Damalakiene, L., Karabanovas, V., Bagdonas, S., Valius, M., Rotomskis, R., 2013. Intracellular distribution of nontargeted quantum dots after natural uptake and microinjection. *Int. J. Nanomedicine* 8, 555–568. <https://doi.org/10.2147/IJN.S39658>
- Deng, Z.J., Liang, M., Monteiro, M., Toth, I., Minchin, R.F., 2011. Nanoparticle-induced unfolding of fibrinogen promotes Mac-1 receptor activation and inflammation. *Nat. Nanotechnol.* 6, 39–44. <https://doi.org/10.1038/nnano.2010.250>

- Derfus, A.M., Chan, W.C.W., Bhatia, S.N., 2004. Probing the Cytotoxicity of Semiconductor Quantum Dots. *Nano Lett.* 4, 11–18. <https://doi.org/10.1021/nl0347334>
- Dhowre, H.S., Rajput, S., Russell, N.A., Zelzer, M., 2015. Responsive cell–material interfaces. *Nanomed.* 10, 849–871. <https://doi.org/10.2217/nnm.14.222>
- Eberli, D. (Ed.), 2014. *Cells and Biomaterials in Regenerative Medicine*. InTech. <https://doi.org/10.5772/58497>
- Ekimov, A.I., Efros, A.L., Onushchenko, A.A., 1985. Quantum size effect in semiconductor microcrystals. *Solid State Commun.* 56, 921–924. [https://doi.org/10.1016/S0038-1098\(85\)80025-9](https://doi.org/10.1016/S0038-1098(85)80025-9)
- Elbially, N.S., Fathy, M.M., AL-Wafi, R., Darwesh, R., Abdel-dayem, U.A., Aldahri, M., Noorwali, A., AL-ghamdi, A.A., 2019. Multifunctional magnetic-gold nanoparticles for efficient combined targeted drug delivery and interstitial photothermal therapy. *Int. J. Pharm.* 554, 256–263. <https://doi.org/10.1016/j.ijpharm.2018.11.021>
- Engel, E., Michiardi, A., Navarro, M., Lacroix, D., Planell, J.A., 2008. Nanotechnology in regenerative medicine: the materials side. *Trends Biotechnol.* 26, 39–47. <https://doi.org/10.1016/j.tibtech.2007.10.005>
- Erogbogbo, F., Yong, K.-T., Roy, I., Xu, G., Prasad, P.N., Swihart, M.T., 2008. Biocompatible Luminescent Silicon Quantum Dots for Imaging of Cancer Cells. *ACS Nano* 2, 873–878. <https://doi.org/10.1021/nn700319z>
- Estrin, Y., Ivanova, E.P., Michalska, A., Truong, V.K., Lapovok, R., Boyd, R., 2011. Accelerated stem cell attachment to ultrafine grained titanium. *Acta Biomater.* 7, 900–906. <https://doi.org/10.1016/j.actbio.2010.09.033>
- EU Commission, 2011. Recommendations on the definition of nanomaterial. Off. J. Eur. Union 2011.
- Eustis, S., El-Sayed, M.A., 2006. Why gold nanoparticles are more precious than pretty gold: Noble metal surface plasmon resonance and its enhancement of the radiative and nonradiative properties of nanocrystals of different shapes. *Chem. Soc. Rev.* 35, 209–217. <https://doi.org/10.1039/B514191E>
- Faedmaleki, F., Shirazi, F.H., Salarian, A.-A., Ashtiani, H.A., Rastegar, H., 2014. Toxicity Effect of Silver Nanoparticles on Mice Liver Primary Cell Culture and HepG2Cell Line. *Iran. J. Pharm. Res.* 13, 235–242.
- Fazel, R. (Ed.), 2011. *Biomedical Engineering - From Theory to Applications*. InTech. <https://doi.org/10.5772/2629>
- Feliu, N., Hühn, J., Zyuzin, M.V., Ashraf, S., Valdeperez, D., Masood, A., Said, A.H., Escudero, A., Pelaz, B., Gonzalez, E., Duarte, M.A.C., Roy, S., Chakraborty, I., Lim, M.L., Sjöqvist, S., Jungebluth, P., Parak, W.J., 2016. Quantitative uptake of colloidal particles by cell cultures. *Sci. Total Environ.* 568, 819–828. <https://doi.org/10.1016/j.scitotenv.2016.05.213>
- Feng, L., Li, S., Li, Y., Li, H., Zhang, L., Zhai, J., Song, Y., Liu, B., Jiang, L., Zhu, D., 2002. Super-Hydrophobic Surfaces: From Natural to Artificial. *Adv. Mater.* 14, 1857–1860. <https://doi.org/10.1002/adma.200290020>
- Ferraro, A., 2016. Biomaterials and therapeutic applications. *IOP Conf. Ser. Mater. Sci. Eng.* 108, 012021. <https://doi.org/10.1088/1757-899X/108/1/012021>
- Ferrati, S., Mack, A., Chiappini, C., Liu, X., Bean, A.J., Ferrari, M., Serda, R.E., 2010. Intracellular trafficking of silicon particles and logic-embedded vectors. *Nanoscale* 2, 1512–1520. <https://doi.org/10.1039/C0NR00227E>

- Feynman, R.P., 1960. There's Plenty of Room at the Bottom. *Caltech Eng. Sci.* 23, 22–36.
- Firdessa, R., Oelschlaeger, T.A., Moll, H., 2014. Identification of multiple cellular uptake pathways of polystyrene nanoparticles and factors affecting the uptake: Relevance for drug delivery systems. *Eur. J. Cell Biol.* 93, 323–337. <https://doi.org/10.1016/j.ejcb.2014.08.001>
- Fitzpatrick, J.A.J., Andreko, S.K., Ernst, L.A., Waggoner, A.S., Ballou, B., Bruchez, M.P., 2009. Long Term Persistence and Spectral Blue Shifting of Quantum Dots in vivo. *Nano Lett.* 9, 2736–2741. <https://doi.org/10.1021/nl901534q>
- Flahaut, E., Durrieu, M.C., Remy-Zolghadri, M., Bareille, R., Baquey, Ch., 2006. Investigation of the cytotoxicity of CCVD carbon nanotubes towards human umbilical vein endothelial cells. *Carbon, Toxicology of Carbon Nanomaterials* 44, 1093–1099. <https://doi.org/10.1016/j.carbon.2005.11.007>
- Fucikova, A., Valenta, J., Pelant, I., Kalbacova, M.H., Broz, A., Rezek, B., Kromka, A., Bakaeva, Z., 2014. Silicon nanocrystals and nanodiamonds in live cells: photoluminescence characteristics, cytotoxicity and interaction with cell cytoskeleton. *RSC Adv.* 4, 10334–10342. <https://doi.org/10.1039/C3RA47574C>
- Fucikova, A., Valenta, J., Pelant, I., Kusova, K., Brezina, V., 2011. Nanocrystalline silicon in biological studies. *Phys. Status Solidi C* 8, 1093–1096. <https://doi.org/10.1002/pssc.201000547>
- Fujii, M., Sugimoto, H., Imakita, K., 2016. All-inorganic colloidal silicon nanocrystals—surface modification by boron and phosphorus co-doping. *Nanotechnology* 27, 262001. <https://doi.org/10.1088/0957-4484/27/26/262001>
- Gittens, R.A., McLachlan, T., Olivares-Navarrete, R., Cai, Y., Berner, S., Tannenbaum, R., Schwartz, Z., Sandhage, K.H., Boyan, B.D., 2011. The effects of combined micron-/submicron-scale surface roughness and nanoscale features on cell proliferation and differentiation. *Biomaterials* 32, 3395–3403. <https://doi.org/10.1016/j.biomaterials.2011.01.029>
- Greger, M., Černý, M., Kander, L., Kliber, J., 2009. Structure and Properties of Titanium for Dental Implants. *Metalurgija* 48, 249–252.
- Guarnieri, D., Guaccio, A., Fusco, S., Netti, P.A., 2011. Effect of serum proteins on polystyrene nanoparticle uptake and intracellular trafficking in endothelial cells. *J. Nanoparticle Res.* 13, 4295–4309. <https://doi.org/10.1007/s11051-011-0375-2>
- Gui, N., Xu, W., Abraham, A.N., Myers, D.E., Mayes, E.L.H., Xia, K., Shukla, R., Qian, M., 2018. A comparative study of the effect of submicron porous and smooth ultrafine-grained Ti-20Mo surfaces on osteoblast responses. *J. Biomed. Mater. Res. A* 106, 2020–2033. <https://doi.org/10.1002/jbm.a.36402>
- Guida, L., Oliva, A., Basile, M.A., Giordano, M., Natri, L., Annunziata, M., 2013. Human gingival fibroblast functions are stimulated by oxidized nanostructured titanium surfaces. *J. Dent.* 41, 900–907. <https://doi.org/10.1016/j.jdent.2013.07.009>
- Hadjidemetriou, M., Al-Ahmady, Z., Mazza, M., Collins, R.F., Dawson, K., Kostarelos, K., 2015. In Vivo Biomolecule Corona around Blood-Circulating, Clinically Used and Antibody-Targeted Lipid Bilayer Nanoscale Vesicles. *Acs Nano* 9, 8142–8156. <https://doi.org/10.1021/acsnano.5b03300>

- Hainfeld, J.F., Slatkin, D.N., Focella, T.M., Smilowitz, H.M., 2006. Gold nanoparticles: a new X-ray contrast agent. *Br. J. Radiol.* 79, 248–253. <https://doi.org/10.1259/bjr/13169882>
- Hamidi, M., Azadi, A., Rafiei, P., 2006. Pharmacokinetic consequences of pegylation. *Drug Deliv.* 13, 399–409.
- Hanks, C.T., Wataha, J.C., Sun, Z., 1996. In vitro models of biocompatibility: A review. *Dent. Mater.* 12, 186–193. [https://doi.org/10.1016/S0109-5641\(96\)80020-0](https://doi.org/10.1016/S0109-5641(96)80020-0)
- Hashimoto, M., Yamaguchi, S., Sasaki, J.-I., Kawai, K., Kawakami, H., Iwasaki, Y., Imazato, S., 2016. Inhibition of matrix metalloproteinases and toxicity of gold and platinum nanoparticles in L929 fibroblast cells. *Eur. J. Oral Sci.* 124, 68–74. <https://doi.org/10.1111/eos.12235>
- Hasirci, V., Vrana, E., Zorlutuna, P., Ndreu, A., Yilgor, P., Basmanav, F.B., Aydin, E., 2006. Nanobiomaterials: a review of the existing science and technology, and new approaches. *J. Biomater. Sci. Polym. Ed.* 17, 1241–1268.
- He, Q., Zhu, Z., Jin, L., Peng, L., Guo, W., Hu, S., 2014. Detection of HIV-1 p24 antigen using streptavidin–biotin and gold nanoparticles based immunoassay by inductively coupled plasma mass spectrometry. *J. Anal. At. Spectrom.* 29, 1477–1482. <https://doi.org/10.1039/C4JA00026A>
- He, X., Ma, J., Jabbari, E., 2008. Effect of Grafting RGD and BMP-2 Protein-Derived Peptides to a Hydrogel Substrate on Osteogenic Differentiation of Marrow Stromal Cells. *Langmuir* 24, 12508–12516. <https://doi.org/10.1021/la802447v>
- Hemelaar, S., Nagl, A., Bigot, F., Rodríguez-García, M., Vries, M., Chipaux, M., Schirhagl, R., 2017. The interaction of fluorescent nanodiamond probes with cellular media. *Microchim. Acta* 184, 1001–1009. <https://doi.org/10.1007/s00604-017-2086-6>
- Hessel, C.M., Reid, D., Panthani, M.G., Rasch, M.R., Goodfellow, B.W., Wei, J., Fujii, H., Akhavan, V., Korgel, B.A., 2012. Synthesis of Ligand-Stabilized Silicon Nanocrystals with Size-Dependent Photoluminescence Spanning Visible to Near-Infrared Wavelengths. *Chem. Mater.* 24, 393–401. <https://doi.org/10.1021/cm2032866>
- Hilderbrand, S.A., Weissleder, R., 2010. Near-infrared fluorescence: application to in vivo molecular imaging. *Curr. Opin. Chem. Biol., Molecular Imaging* 14, 71–79. <https://doi.org/10.1016/j.cbpa.2009.09.029>
- Hirsh, S.L., McKenzie, D.R., Nosworthy, N.J., Denman, J.A., Sezerman, O.U., Bilek, M.M.M., 2013. The Vroman effect: Competitive protein exchange with dynamic multilayer protein aggregates. *Colloids Surf. B Biointerfaces* 103, 395–404. <https://doi.org/10.1016/j.colsurfb.2012.10.039>
- Ho, Y.T., Kamm, R.D., Kah, J.C.Y., 2018. Influence of protein corona and caveolae-mediated endocytosis on nanoparticle uptake and transcytosis. *Nanoscale* 10, 12386–12397. <https://doi.org/10.1039/C8NR02393J>
- International Organization for Standardization, 2015. ISO/TS 80004-2:2015 Nanotechnologies - Vocabulary -Part 2: Nano-objects.
- International Organization for Standardization, 2009. ISO 10993-1:2009. Biological evaluation of medical devices — Part 1: Evaluation and testing within a risk management process.

- Iversen, T.-G., Skotland, T., Sandvig, K., 2011. Endocytosis and intracellular transport of nanoparticles: Present knowledge and need for future studies. *Nano Today* 6, 176–185. <https://doi.org/10.1016/j.nantod.2011.02.003>
- Iwaya, Y., Machigashira, M., Kanbara, K., Miyamoto, M., Noguchi, K., Izumi, Y., Ban, S., 2008. Surface Properties and Biocompatibility of Acid-etched Titanium. *Dent. Mater. J.* 27, 415–421. <https://doi.org/10.4012/dmj.27.415>
- Ji, X., Wang, C., Tang, M., Guo, D., Peng, F., Zhong, Y., Song, B., Su, Y., He, Y., 2018. Biocompatible protamine sulfate@silicon nanoparticle-based gene nanocarriers featuring strong and stable fluorescence. *Nanoscale* 10, 14455–14463. <https://doi.org/10.1039/C8NR03107J>
- Jiang, X., Musyanovych, A., Röcker, C., Landfester, K., Mailänder, V., Nienhaus, G.U., 2011. Specific effects of surface carboxyl groups on anionic polystyrene particles in their interactions with mesenchymal stem cells. *Nanoscale* 3, 2028–2035. <https://doi.org/10.1039/C0NR00944J>
- Jiang, X., Weise, S., Hafner, M., Röcker, C., Zhang, F., Parak, W.J., Nienhaus, G.U., 2010. Quantitative analysis of the protein corona on FePt nanoparticles formed by transferrin binding. *J. R. Soc. Interface* 7, S5–S13. <https://doi.org/10.1098/rsif.2009.0272.focus>
- Jin, Y., Kim, D., Roh, H., Kim, S., Hussain, S., Kang, J., Pack, C.-G., Kim, J.K., Myung, S.-J., Ruoslahti, E., Sailor, M.J., Kim, S.C., Joo, J., 2018. Tracking the Fate of Porous Silicon Nanoparticles Delivering a Peptide Payload by Intrinsic Photoluminescence Lifetime. *Adv. Mater.* 30, 1802878. <https://doi.org/10.1002/adma.201802878>
- Kalbacova, M., Broz, A., Kalbac, M., 2012. Influence of the fetal bovine serum proteins on the growth of human osteoblast cells on graphene. *J. Biomed. Mater. Res. A* 100A, 3001–3007. <https://doi.org/10.1002/jbm.a.34231>
- Kalbacova, M., Rezek, B., Baresova, V., Wolf-Brandstetter, C., Kromka, A., 2009. Nanoscale topography of nanocrystalline diamonds promotes differentiation of osteoblasts. *Acta Biomater.* 5, 3076–3085. <https://doi.org/10.1016/j.actbio.2009.04.020>
- Kang, Y., Ren, X., Yuan, X., Ma, L., Xie, Y., Bian, Z., Zuo, J., Wang, X., Yu, Z., Zhou, K., Wei, Q., 2018. The Effects of Combined Micron-Scale Surface and Different Nanoscale Features on Cell Response [WWW Document]. *Adv. Mater. Sci. Eng.* <https://doi.org/10.1155/2018/6526913>
- Keane, T.J., Badylak, S.F., 2014. Biomaterials for tissue engineering applications. *Semin. Pediatr. Surg., Regenerative Medicine in Pediatric Surgery* 23, 112–118. <https://doi.org/10.1053/j.sempedsurg.2014.06.010>
- Khani, O., Rajabi, H.R., Yousefi, M.H., Khosravi, A.A., Jannesari, M., Shamsipur, M., 2011. Synthesis and characterizations of ultra-small ZnS and Zn(1-x)FexS quantum dots in aqueous media and spectroscopic study of their interactions with bovine serum albumin. *Spectrochim. Acta. A. Mol. Biomol. Spectrosc.* 79, 361–369. <https://doi.org/10.1016/j.saa.2011.03.025>
- Kim, D.-Y., Kim, M., Shinde, S., Sung, J.-S., Ghodake, G., 2017. Cytotoxicity and antibacterial assessment of gallic acid capped gold nanoparticles. *Colloids Surf. B Biointerfaces* 149, 162–167. <https://doi.org/10.1016/j.colsurfb.2016.10.017>
- Kim, J., Wilson, D.R., Zamboni, C.G., Green, J.J., 2015. Targeted polymeric nanoparticles for cancer gene therapy. *J. Drug Target.* 23, 627–641. <https://doi.org/10.3109/1061186X.2015.1048519>

- Kim, M.I., Kim, M.S., Woo, M.-A., Ye, Y., Kang, K.S., Lee, J., Park, H.G., 2014. Highly efficient colorimetric detection of target cancer cells utilizing superior catalytic activity of graphene oxide–magnetic-platinum nanohybrids. *Nanoscale* 6, 1529–1536. <https://doi.org/10.1039/C3NR05539F>
- Kim, S.-H., Turnbull, J., Guimond, S., 2011. Extracellular matrix and cell signalling: the dynamic cooperation of integrin, proteoglycan and growth factor receptor. *J. Endocrinol.* 209, 139–151. <https://doi.org/10.1530/JOE-10-0377>
- Kokubo, T., Kim, H.-M., Kawashita, M., 2003. Novel bioactive materials with different mechanical properties. *Biomaterials, Focus on Biomaterials Science in Asia* 24, 2161–2175. [https://doi.org/10.1016/S0142-9612\(03\)00044-9](https://doi.org/10.1016/S0142-9612(03)00044-9)
- Korhonen, E., Rönkkö, S., Hillebrand, S., Riikonen, J., Xu, W., Järvinen, K., Lehto, V.-P., Kauppinen, A., 2016. Cytotoxicity assessment of porous silicon microparticles for ocular drug delivery. *Eur. J. Pharm. Biopharm.* 100, 1–8. <https://doi.org/10.1016/j.ejpb.2015.11.020>
- Kotler, M.L., Garabano, N.I., David Gara, P., Casas, O.R., Dodat, D., Finkelstein, S.E., Mantz, C., Fernandez, E., Gonzalez, M.C., 2013. Application of Silicon Nanoparticles (SI-NPs) for Radiation-Induced Cytotoxicity via Generation of Reactive Oxygen Species (ROS). *Int. J. Radiat. Oncol., Proceedings of the American Society for Radiation Oncology 55th Annual Meeting ASTRO's 55th Annual Meeting* 87, S652–S653. <https://doi.org/10.1016/j.ijrobp.2013.06.1728>
- Krug, H.F., 2014. Nanosafety Research—Are We on the Right Track? *Angew. Chem. Int. Ed.* 53, 12304–12319. <https://doi.org/10.1002/anie.201403367>
- Kubo, K., Tsukimura, N., Iwasa, F., Ueno, T., Saruwatari, L., Aita, H., Chiou, W.-A., Ogawa, T., 2009. Cellular behavior on TiO<sub>2</sub> nanonodular structures in a micro-to-nanoscale hierarchy model. *Biomaterials* 30, 5319–5329. <https://doi.org/10.1016/j.biomaterials.2009.06.021>
- Lagonegro, P., Trevisi, G., Nasi, L., Parisi, L., Manfredi, E., Lumetti, S., Rossi, F., Macaluso, G.M., Salviati, G., Galli, C., 2018. Osteoblasts preferentially adhere to peaks on micro-structured titanium. *Dent. Mater. J.* 37, 278–285. <https://doi.org/10.4012/dmj.2017-008>
- Lamers, E., Walboomers, X.F., Domanski, M., Prodanov, L., Melis, J., Luttge, R., Winnubst, L., Anderson, J.M., Gardeniers, H.J.G.E., Jansen, J.A., 2012. In vitro and in vivo evaluation of the inflammatory response to nanoscale grooved substrates. *Nanomedicine Nanotechnol. Biol. Med.* 8, 308–317. <https://doi.org/10.1016/j.nano.2011.06.013>
- Lin, G., Wang, X., Yin, F., Yong, K.-T., 2015. Passive tumor targeting and imaging by using mercaptosuccinic acid-coated near-infrared quantum dots. *Int. J. Nanomedicine* 10, 335–345. <https://doi.org/10.2147/IJN.S74805>
- Liu, F., He, X., Zhang, J., Zhang, H., Wang, Z., 2015. Employing Tryptone as a General Phase Transfer Agent to Produce Renal Clearable Nanodots for Bioimaging. *Small* 11, 3676–3685. <https://doi.org/10.1002/smll.201500287>
- Liu, X., Lim, J.Y., Donahue, H.J., Dhurjati, R., Mastro, A.M., Vogler, E.A., 2007. Influence of substratum surface chemistry/energy and topography on the human fetal osteoblastic cell line hFOB 1.19: Phenotypic and genotypic responses observed in vitro. *Biomaterials* 28, 4535–4550. <https://doi.org/10.1016/j.biomaterials.2007.06.016>

- Lohse, S., 2013. Nanoparticles Are All Around Us. *Sustain. Nano*. URL <http://sustainable-nano.com/2013/03/25/nanoparticles-are-all-around-us/> (accessed 5.9.17).
- Long, J., Li, X., Kang, Y., Ding, Y., Gu, Z., Cao, Y., 2018. Internalization, cytotoxicity, oxidative stress and inflammation of multi-walled carbon nanotubes in human endothelial cells: influence of pre-incubation with bovine serum albumin. *RSC Adv.* 8, 9253–9260. <https://doi.org/10.1039/C8RA00445E>
- Lovrić, J., Cho, S.J., Winnik, F.M., Maysinger, D., 2005. Unmodified Cadmium Telluride Quantum Dots Induce Reactive Oxygen Species Formation Leading to Multiple Organelle Damage and Cell Death. *Chem. Biol.* 12, 1227–1234. <https://doi.org/10.1016/j.chembiol.2005.09.008>
- Lunov, O., Syrovets, T., Loos, C., Beil, J., Delacher, M., Tron, K., Nienhaus, G.U., Musyanovych, A., Mailänder, V., Landfester, K., Simmet, T., 2011. Differential Uptake of Functionalized Polystyrene Nanoparticles by Human Macrophages and a Monocytic Cell Line. *ACS Nano* 5, 1657–1669. <https://doi.org/10.1021/nn2000756>
- Lutolf, M.P., Gilbert, P.M., Blau, H.M., 2009. Designing materials to direct stem-cell fate. *Nature* 462, 433–441. <https://doi.org/10.1038/nature08602>
- Ma, Z., Wan, H., Wang, W., Zhang, X., Uno, T., Yang, Q., Yue, J., Gao, H., Zhong, Y., Tian, Y., Sun, Q., Liang, Y., Dai, H., 2019. A theranostic agent for cancer therapy and imaging in the second near-infrared window. *Nano Res.* 12, 273–279. <https://doi.org/10.1007/s12274-018-2210-x>
- Madhusudhan, A., Reddy, G.B., Venkatesham, M., Veerabhadram, G., Kumar, D.A., Natarajan, S., Ming-Yeh Yang, Anren Hu, Singh, S.S., 2014. Efficient pH Dependent Drug Delivery to Target Cancer Cells by Gold Nanoparticles Capped with Carboxymethyl Chitosan. *Int. J. Mol. Sci.* 15, 8216–8234. <https://doi.org/10.3390/ijms15058216>
- Mager, M.D., LaPointe, V., Stevens, M.M., 2011. Exploring and exploiting chemistry at the cell surface. *Nat. Chem.* 3, 582–589. <https://doi.org/10.1038/nchem.1090>
- Manikandan, M., Hasan, N., Wu, H.-F., 2013. Platinum nanoparticles for the photothermal treatment of Neuro 2A cancer cells. *Biomaterials* 34, 5833–5842. <https://doi.org/10.1016/j.biomaterials.2013.03.077>
- Mariscal-Muñoz, E., Costa, C.A.S., Tavares, H.S., Bianchi, J., Hebling, J., Machado, J.P.B., Lerner, U.H., Souza, P.P.C., 2016. Osteoblast differentiation is enhanced by a nano-to-micro hybrid titanium surface created by Yb:YAG laser irradiation. *Clin. Oral Investig.* 20, 503–511. <https://doi.org/10.1007/s00784-015-1533-1>
- Markhoff, J., Krogull, M., Schulze, C., Rotsch, C., Hunger, S., Bader, R., 2017. Biocompatibility and Inflammatory Potential of Titanium Alloys Cultivated with Human Osteoblasts, Fibroblasts and Macrophages. *Mater.* 10, 52. <https://doi.org/10.3390/ma10010052>
- Mason, C., Dunnill, P., 2007. A brief definition of regenerative medicine. *Regen. Med.* 3, 1–5. <https://doi.org/10.2217/17460751.3.1.1>
- Mattoussi, H., Palui, G., Na, H.B., 2012. Luminescent quantum dots as platforms for probing in vitro and in vivo biological processes. *Adv. Drug Deliv. Rev., Biological Interactions of Nanoparticles* 64, 138–166. <https://doi.org/10.1016/j.addr.2011.09.011>

- Medley, C.D., Smith, J.E., Tang, Z., Wu, Y., Bamrungsap, S., Tan, W., 2008. Gold Nanoparticle-Based Colorimetric Assay for the Direct Detection of Cancerous Cells. *Anal. Chem.* 80, 1067–1072. <https://doi.org/10.1021/ac702037y>
- Medvedev, A.E., Neumann, A., Ng, H.P., Lapovok, R., Kasper, C., Lowe, T.C., Anumalasetty, V.N., Estrin, Y., 2017. Combined effect of grain refinement and surface modification of pure titanium on the attachment of mesenchymal stem cells and osteoblast-like SaOS-2 cells. *Mater. Sci. Eng. C* 71, 483–497. <https://doi.org/10.1016/j.msec.2016.10.035>
- Michalet, X., Pinaud, F.F., Bentolila, L.A., Tsay, J.M., et al, 2005. Quantum Dots for Live Cells, in Vivo Imaging, and Diagnostics. *Science* 307, 538–44.
- Mishnaevsky Jr., L., Levashov, E., Valiev, R.Z., Segurado, J., Sabirov, I., Enikeev, N., Prokoshkin, S., Solov'yov, A.V., Korotitskiy, A., Gutmanas, E., Gotman, I., Rabkin, E., Psakh'e, S., Dluhoš, L., Seefeldt, M., Smolin, A., 2014. Nanostructured titanium-based materials for medical implants: Modeling and development. *Mater. Sci. Eng. R Rep.* 81, 1–19. <https://doi.org/10.1016/j.mser.2014.04.002>
- Monopoli, M.P., Åberg, C., Salvati, A., Dawson, K.A., 2012. Biomolecular coronas provide the biological identity of nanosized materials. *Nat. Nanotechnol.* 7, 779–786. <https://doi.org/10.1038/nnano.2012.207>
- Monteiro-Riviere, N.A., Samberg, M.E., Oldenburg, S.J., Riviere, J.E., 2013. Protein binding modulates the cellular uptake of silver nanoparticles into human cells: Implications for in vitro to in vivo extrapolations? *Toxicol. Lett.* 220, 286–293. <https://doi.org/10.1016/j.toxlet.2013.04.022>
- Mulari, M.T.K., Qu, Q., Härkönen, P.L., Väänänen, H.K., 2004. Osteoblast-like Cells Complete Osteoclastic Bone Resorption and Form New Mineralized Bone Matrix In Vitro. *Calcif. Tissue Int. N. Y.* 75, 253–61. <http://dx.doi.org.ezproxy.is.cuni.cz/10.1007/s00223-004-0172-3>
- Naahidi, S., Jafari, M., Edalat, F., Raymond, K., Khademhosseini, A., Chen, P., 2013. Biocompatibility of engineered nanoparticles for drug delivery. *J. Controlled Release* 166, 182–194. <https://doi.org/10.1016/j.jconrel.2012.12.013>
- Naddeo, P., Laino, L., La Noce, M., Piattelli, A., De Rosa, A., Iezzi, G., Laino, G., Paino, F., Papaccio, G., Tirino, V., 2015. Surface biocompatibility of differently textured titanium implants with mesenchymal stem cells. *Dent. Mater.* 31, 235–243. <https://doi.org/10.1016/j.dental.2014.12.015>
- Nel, A., Xia, T., Mädler, L., Li, N., 2006. Toxic Potential of Materials at the Nanolevel. *Science* 311, 622–627. <https://doi.org/10.1126/science.1114397>
- Nichols, S.P., Koh, A., Storm, W.L., Shin, J.H., Schoenfisch, M.H., 2013. Biocompatible Materials for Continuous Glucose Monitoring Devices. *Chem. Rev.* 113, 2528–2549. <https://doi.org/10.1021/cr300387j>
- Ohta, S., Inasawa, S., Yamaguchi, Y., 2012. Real time observation and kinetic modeling of the cellular uptake and removal of silicon quantum dots. *Biomaterials* 33, 4639–4645. <https://doi.org/10.1016/j.biomaterials.2012.03.029>
- Ong, K.J., MacCormack, T.J., Clark, R.J., Ede, J.D., Ortega, V.A., Felix, L.C., Dang, M.K.M., Ma, G., Fenniri, H., Veinot, J.G.C., Goss, G.G., 2014. Widespread Nanoparticle-Assay Interference: Implications for Nanotoxicity Testing. *PLOS ONE* 9, e90650. <https://doi.org/10.1371/journal.pone.0090650>



- Osaka, T., Nakanishi, T., Shanmugam, S., Takahama, S., Zhang, H., 2009. Effect of surface charge of magnetite nanoparticles on their internalization into breast cancer and umbilical vein endothelial cells. *Colloids Surf. B Biointerfaces* 71, 325–330. <https://doi.org/10.1016/j.colsurfb.2009.03.004>
- Östberg, A.-K., Dahlgren, U., Sul, Y.-T., Johansson, C.B., 2015. Inflammatory cytokine release is affected by surface morphology and chemistry of titanium implants. *J. Mater. Sci. Mater. Med.* 26, 155. <https://doi.org/10.1007/s10856-015-5486-3>
- Ostrovská, L., Broz, A., Fuciková, A., Belinová, T., Sugimoto, H., Kanno, T., Fujii, M., Valenta, J., Kalbacová, M.H., 2016. The impact of doped silicon quantum dots on human osteoblasts. *RSC Adv.* 6, 63403–63413. <https://doi.org/10.1039/C6RA14430F>
- Ostrovská, L., Vistejnová, L., Dzukan, J., Slama, P., Kubina, T., Ukraintsev, E., Kubies, D., Kralicková, M., Kalbacová, M.H., 2015. Biological evaluation of ultra-fine titanium with improved mechanical strength for dental implant engineering. *J. Mater. Sci.* 51, 3097–3110. <https://doi.org/10.1007/s10853-015-9619-3>
- Pal, D., Sahu, C.K., Haldar, A., 2014. Bhasma : The ancient Indian nanomedicine. *J. Adv. Pharm. Technol. Res.* 5, 4–12. <https://doi.org/10.4103/2231-4040.126980>
- Pang, J., Su, Y., Zhong, Y., Peng, F., Song, B., He, Y., 2016. Fluorescent silicon nanoparticle-based gene carriers featuring strong photostability and feeble cytotoxicity. *Nano Res.* 9, 3027–3037. <https://doi.org/10.1007/s12274-016-1185-8>
- Pankhurst, Q.A., Thanh, N.T.K., Jones, S.K., Dobson, J., 2009. Progress in applications of magnetic nanoparticles in biomedicine. *J. Phys. Appl. Phys.* 42, 224001. <https://doi.org/10.1088/0022-3727/42/22/224001>
- Papasani, M.R., Wang, G., Hill, R.A., 2012. Gold nanoparticles: the importance of physiological principles to devise strategies for targeted drug delivery. *Nanomedicine Nanotechnol. Biol. Med.* 8, 804–814. <https://doi.org/10.1016/j.nano.2012.01.008>
- Parak, W.J., Gerion, D., Pellegrino, T., Zanchet, D., Micheel, C., Williams, S.C., Boudreau, R., Gros, M.A.L., Larabell, C.A., Alivisatos, A.P., 2003. Biological applications of colloidal nanocrystals. *Nanotechnology* 14, R15. <https://doi.org/10.1088/0957-4484/14/7/201>
- Parida, P., Behera, A., Mishra, S.C., 2012. Classification of Biomaterials used in Medicine. *Int. J. Adv. Appl. Sci.* 1, 125–129.
- Parveen, S., Misra, R., Sahoo, S.K., 2012. Nanoparticles: a boon to drug delivery, therapeutics, diagnostics and imaging. *Nanomedicine Nanotechnol. Biol. Med.* 8, 147–166. <https://doi.org/10.1016/j.nano.2011.05.016>
- Pedone, D., Moglianetti, M., Luca, E.D., Bardi, G., Pompa, P.P., 2017. Platinum nanoparticles in nanobiomedicine. *Chem. Soc. Rev.* 46, 4951–4975. <https://doi.org/10.1039/C7CS00152E>
- Pendegrass, C.J., Gordon, D., Middleton, C.A., Sun, S.Ng.M., Blunn, G.W., 2008. Sealing the skin barrier around transcutaneous implants. *J. Bone Joint Surg. Br.* 90-B, 114–121. <https://doi.org/10.1302/0301-620X.90B1.19580>
- Perevedentseva, E., Hong, S.-F., Huang, K.-J., Chiang, I.-T., Lee, C.-Y., Tseng, Y.-T., Cheng, C.-L., 2013. Nanodiamond internalization in cells and the cell

- uptake mechanism. *J. Nanoparticle Res.* 15, 1–12. <https://doi.org/10.1007/s11051-013-1834-8>
- Pizzoferrato, A., Ciapetti, G., Stea, S., Cenni, E., Arciola, C.R., Granchi, D., Lucia, 1994. Cell culture methods for testing Biocompatibility. *Clin. Mater.* 15, 173–190. [https://doi.org/10.1016/0267-6605\(94\)90081-7](https://doi.org/10.1016/0267-6605(94)90081-7)
- Polikov, V.S., Tresco, P.A., Reichert, W.M., 2005. Response of brain tissue to chronically implanted neural electrodes. *J. Neurosci. Methods* 148, 1–18. <https://doi.org/10.1016/j.jneumeth.2005.08.015>
- Polo, E., Collado, M., Pelaz, B., del Pino, P., 2017. Advances toward More Efficient Targeted Delivery of Nanoparticles in Vivo: Understanding Interactions between Nanoparticles and Cells. *ACS Nano* 11, 2397–2402. <https://doi.org/10.1021/acsnano.7b01197>
- Polyakov, A.V., Semenova, I.P., Valiev, R.Z., 2014. High fatigue strength and enhanced biocompatibility of UFG CP Ti for medical innovative applications. *IOP Conf. Ser. Mater. Sci. Eng.* 63, 012113. <https://doi.org/10.1088/1757-899X/63/1/012113>
- Prapainop, K., Witter, D.P., Wentworth, P., 2012. A Chemical Approach for Cell-Specific Targeting of Nanomaterials: Small-Molecule-Initiated Misfolding of Nanoparticle Corona Proteins. *J. Am. Chem. Soc.* 134, 4100–4103. <https://doi.org/10.1021/ja300537u>
- Qi, C., Yan, X., Huang, C., Melerzanov, A., Du, Y., 2015. Biomaterials as carrier, barrier and reactor for cell-based regenerative medicine. *Protein Cell* 6, 638–653. <https://doi.org/10.1007/s13238-015-0179-8>
- Rabe, M., Verdes, D., Seeger, S., 2011. Understanding protein adsorption phenomena at solid surfaces. *Adv. Colloid Interface Sci.* 162, 87–106. <https://doi.org/10.1016/j.cis.2010.12.007>
- Rai, M., Ingle, A.P., Birla, S., Yadav, A., Santos, C.A.D., 2016. Strategic role of selected noble metal nanoparticles in medicine. *Crit. Rev. Microbiol.* 42, 696–719. <https://doi.org/10.3109/1040841X.2015.1018131>
- Rehfeldt, F., Engler, A.J., Eckhardt, A., Ahmed, F., Discher, D.E., 2007. Cell responses to the mechanochemical microenvironment—Implications for regenerative medicine and drug delivery. *Adv. Drug Deliv. Rev., Natural and Artificial Cellular Microenvironments for Soft Tissue Repair* 59, 1329–1339. <https://doi.org/10.1016/j.addr.2007.08.007>
- Rejman, J., Oberle, V., Zuhorn, I.S., Hoekstra, D., 2004. Size-dependent internalization of particles via the pathways of clathrin- and caveolae-mediated endocytosis. *Biochem. J.* 377, 159–169. <https://doi.org/10.1042/BJ20031253>
- Ren, B., Wan, Y., Wang, G., Liu, Z., Huang, Y., Wang, H., 2018. Morphologically modified surface with hierarchical micro-/nano-structures for enhanced bioactivity of titanium implants. *J. Mater. Sci.* 53, 12679–12691. <https://doi.org/10.1007/s10853-018-2554-3>
- Reznickova, A., Slavikova, N., Kolska, Z., Kolarova, K., Belinova, T., Hubalek Kalbacova, M., Cieslar, M., Svorcik, V., 2019. PEGylated gold nanoparticles: Stability, cytotoxicity and antibacterial activity. *Colloids Surf. Physicochem. Eng. Asp.* 560, 26–34. <https://doi.org/10.1016/j.colsurfa.2018.09.083>
- Reznikov, N., Shahar, R., Weiner, S., 2014. Bone hierarchical structure in three dimensions. *Acta Biomater., Biomineralization* 10, 3815–3826. <https://doi.org/10.1016/j.actbio.2014.05.024>

- Rho, J.-Y., Kuhn-Spearing, L., Zioupos, P., 1998. Mechanical properties and the hierarchical structure of bone. *Med. Eng. Phys.* 20, 92–102. [https://doi.org/10.1016/S1350-4533\(98\)00007-1](https://doi.org/10.1016/S1350-4533(98)00007-1)
- Richert, L., Vetrone, F., Yi, J.-H., Zalzal, S.F., Wuest, J.D., Rosei, F., Nanci, A., 2008. Surface Nanopatterning to Control Cell Growth. *Adv. Mater.* 20, 1488–1492. <https://doi.org/10.1002/adma.200701428>
- Rivera-Gil, P., Jimenez De Aberasturi, D., Wulf, V., Pelaz, B., Del Pino, P., Zhao, Y., De La Fuente, J.M., Ruiz De Larramendi, I., Rojo, T., Liang, X.-J., Parak, W.J., 2013. The Challenge To Relate the Physicochemical Properties of Colloidal Nanoparticles to Their Cytotoxicity. *Acc. Chem. Res.* 46, 743–749. <https://doi.org/10.1021/ar300039j>
- Roduner, E., 2006. Size matters: why nanomaterials are different. *Chem. Soc. Rev.* 35, 583–592. <https://doi.org/10.1039/B502142C>
- Rong, G., Corrie, S.R., Clark, H.A., 2017. In Vivo Biosensing: Progress and Perspectives. *ACS Sens.* 2, 327–338. <https://doi.org/10.1021/acssensors.6b00834>
- Rothen-Rutishauser, B.M., Schürch, S., Haenni, B., Kapp, N., Gehr, P., 2006. Interaction of Fine Particles and Nanoparticles with Red Blood Cells Visualized with Advanced Microscopic Techniques. *Environ. Sci. Technol.* 40, 4353–4359. <https://doi.org/10.1021/es0522635>
- Rupp, F., Scheideler, L., Olshanska, N., de Wild, M., Wieland, M., Geis-Gerstorfer, J., 2006. Enhancing surface free energy and hydrophilicity through chemical modification of microstructured titanium implant surfaces. *J. Biomed. Mater. Res. A* 76A, 323–334. <https://doi.org/10.1002/jbm.a.30518>
- Ryu, J.H., Lee, S., Son, S., Kim, S.H., Leary, J.F., Choi, K., Kwon, I.C., 2014. Theranostic nanoparticles for future personalized medicine. *J. Controlled Release, 30th Anniversary Special Issue* 190, 477–484. <https://doi.org/10.1016/j.jconrel.2014.04.027>
- Saito, T., Hayashi, H., Kameyama, T., Hishida, M., Nagai, K., Teraoka, K., Kato, K., 2010. Suppressed proliferation of mouse osteoblast-like cells by a rough-surfaced substrate leads to low differentiation and mineralization. *Mater. Sci. Eng. C* 30, 1–7. <https://doi.org/10.1016/j.msec.2009.06.010>
- Salvati, A., Pitek, A.S., Monopoli, M.P., Prapainop, K., Bombelli, F.B., Hristov, D.R., Kelly, P.M., Åberg, C., Mahon, E., Dawson, K.A., 2013. Transferrin-functionalized nanoparticles lose their targeting capabilities when a biomolecule corona adsorbs on the surface. *Nat. Nanotechnol.* 8, 137–143. <https://doi.org/10.1038/nnano.2012.237>
- Schindelin, J., Arganda-Carreras, I., Frise, E., Kaynig, V., Longair, M., Pietzsch, T., Preibisch, S., Rueden, C., Saalfeld, S., Schmid, B., Tinevez, J.-Y., White, D.J., Hartenstein, V., Eliceiri, K., Tomancak, P., Cardona, A., 2012. Fiji: an open-source platform for biological-image analysis. *Nat. Methods* 9, 676–682. <https://doi.org/10.1038/nmeth.2019>
- Schwartz, Z., Olivares-Navarrete, R., Wieland, M., Cochran, D.L., Boyan, B.D., 2009. Mechanisms Regulating Increased Production of Osteoprotegerin by Osteoblasts Cultured on Microstructured Titanium Surfaces. *Biomaterials* 30, 3390–3396. <https://doi.org/10.1016/j.biomaterials.2009.03.047>
- Schwerdtle, T., Ebert, F., Thuy, C., Richter, C., Mullenders, L.H.F., Hartwig, A., 2010. Genotoxicity of Soluble and Particulate Cadmium Compounds: Impact

- on Oxidative DNA Damage and Nucleotide Excision Repair. *Chem. Res. Toxicol.* 23, 432–442. <https://doi.org/10.1021/tx900444w>
- Shen, P., Ohta, S., Inasawa, S., Yamaguchi, Y., 2011. Selective labeling of the endoplasmic reticulum in live cells with silicon quantum dots. *Chem. Commun.* 47, 8409–8411. <https://doi.org/10.1039/C1CC12713F>
- Shi, J., Sun, X., Zheng, S., Li, J., Fu, X., Zhang, H., 2018. A new near-infrared persistent luminescence nanoparticle as a multifunctional nanoplatform for multimodal imaging and cancer therapy. *Biomaterials* 152, 15–23. <https://doi.org/10.1016/j.biomaterials.2017.10.032>
- Shin, M.H., Hong, W., Sa, Y., Chen, L., Jung, Y.-J., Wang, X., Zhao, B., Jung, Y.M., 2014. Multiple detection of proteins by SERS-based immunoassay with core shell magnetic gold nanoparticles. *Vib. Spectrosc.* 72, 44–49. <https://doi.org/10.1016/j.vibspec.2014.02.007>
- Siegel, J., Kolářová, K., Vosmanská, V., Rimpelová, S., Leitner, J., Švorčík, V., 2013. Antibacterial properties of green-synthesized noble metal nanoparticles. *Mater. Lett.* 113, 59–62. <https://doi.org/10.1016/j.matlet.2013.09.047>
- Slepička, P., Michaljaničová, I., Slepičková Kasálková, N., Kolská, Z., Rimpelová, S., Ruml, T., Švorčík, V., 2013. Poly-l-lactic acid modified by etching and grafting with gold nanoparticles. *J. Mater. Sci.* 48, 5871–5879. <https://doi.org/10.1007/s10853-013-7383-9>
- Soenen, S.J., Parak, W.J., Rejman, J., Manshian, B., 2015. (Intra)Cellular Stability of Inorganic Nanoparticles: Effects on Cytotoxicity, Particle Functionality, and Biomedical Applications. *Chem. Rev.* 115, 2109–2135. <https://doi.org/10.1021/cr400714j>
- Svedman, C., Dunér, K., Kehler, M., Möller, H., Gruvberger, B., Bruze, M., 2006. Lichenoid reactions to gold from dental restorations and exposure to gold through intracoronary implant of a gold-plated stent. *Clin. Res. Cardiol.* 95, 689–691. <https://doi.org/10.1007/s00392-006-0448-x>
- Tan, J., Zhao, C., Zhou, J., Duan, K., Wang, J., Lu, X., Weng, J., Feng, B., 2017. Co-culturing epidermal keratinocytes and dermal fibroblasts on nano-structured titanium surfaces. *Mater. Sci. Eng. C* 78, 288–295. <https://doi.org/10.1016/j.msec.2017.04.036>
- Tang, J., Huang, N., Zhang, X., Zhou, T., Tan, Y., Pi, J., Pi, L., Cheng, S., Zheng, H., Cheng, Y., 2017. Aptamer-conjugated PEGylated quantum dots targeting epidermal growth factor receptor variant III for fluorescence imaging of glioma [WWW Document]. *Int. J. Nanomedicine.* <https://doi.org/10.2147/IJN.S133166>
- Teng, F.-Y., Ko, C.-L., Kuo, H.-N., Hu, J.-J., Lin, J.-H., Lou, C.-W., Hung, C.-C., Wang, Y.-L., Cheng, C.-Y., Chen, W.-C., 2012. A Comparison of Epithelial Cells, Fibroblasts, and Osteoblasts in Dental Implant Titanium Topographies. *Bioinorg. Chem. Appl.* 2012, e687291. <https://doi.org/10.1155/2012/687291>
- Tlotleng, N., Vetten, M.A., Keter, F.K., Skepu, A., Tshikhudo, R., Gulumian, M., 2016. Cytotoxicity, intracellular localization and exocytosis of citrate capped and PEG functionalized gold nanoparticles in human hepatocyte and kidney cells. *Cell Biol. Toxicol.* 32, 305–321. <https://doi.org/10.1007/s10565-016-9336-y>

- Toy, R., Peiris, P.M., Ghaghada, K.B., Karathanasis, E., 2014. Shaping cancer nanomedicine: the effect of particle shape on the in vivo journey of nanoparticles. *Nanomed.* 9, 121–34. <http://dx.doi.org/10.2217/nnm.13.191>
- Treuel, L., Jiang, X., Nienhaus, G.U., 2013. New views on cellular uptake and trafficking of manufactured nanoparticles. *J. R. Soc. Interface* 10. <https://doi.org/10.1098/rsif.2012.0939>
- Valentin, J.E., Turner, N.J., Gilbert, T.W., Badylak, S.F., 2010. Functional skeletal muscle formation with a biologic scaffold. *Biomaterials* 31, 7475–7484. <https://doi.org/10.1016/j.biomaterials.2010.06.039>
- Valiev, R.Z., Estrin, Y., Horita, Z., Langdon, T.G., al, et, 2006. Producing Bulk Ultrafine-Grained Materials by Severe Plastic Deformation. *JOM* 58, 33–39.
- Verdanova, M., Broz, A., Kalbac, M., Kalbacova, M., 2012. Influence of oxygen and hydrogen treated graphene on cell adhesion in the presence or absence of fetal bovine serum. *Phys. Status Solidi B* 249, 2503–2506. <https://doi.org/10.1002/pssb.201200099>
- Verma, S., Domb, A.J., Kumar, N., 2011. Nanomaterials for regenerative medicine. *Nanomed.* 6, 157–81. <http://dx.doi.org.ezproxy.is.cuni.cz/10.2217/nnm.10.146>
- Verrier, S., Pallu, S., Bareille, R., Jonczyk, A., Meyer, J., Dard, M., Amédée, J., 2002. Function of linear and cyclic RGD-containing peptides in osteoprogenitor cells adhesion process. *Biomaterials* 23, 585–596. [https://doi.org/10.1016/S0142-9612\(01\)00145-4](https://doi.org/10.1016/S0142-9612(01)00145-4)
- Vert, M., Doi, Y., Hellwich, K.-H., Hess, M., Hodge, P., Kubisa, P., Rinaudo, M., Schué, F., 2012. Terminology for biorelated polymers and applications (IUPAC Recommendations 2012). *Pure Appl. Chem.* 84, 377–410. <https://doi.org/10.1351/PAC-REC-10-12-04>
- Wang, Q., Ding, X., Wang, Y., Du, Q., Xu, T., Du, B., Yao, H., 2018. The ratiometric fluorescence nanoparticle based on SiRB for pH detection of tumor. *Eur. J. Pharm. Sci.* 118, 32–39. <https://doi.org/10.1016/j.ejps.2018.03.015>
- Wang, T., Bai, J., Jiang, X., Nienhaus, G.U., 2012. Cellular Uptake of Nanoparticles by Membrane Penetration: A Study Combining Confocal Microscopy with FTIR Spectroelectrochemistry. *ACS Nano* 6, 1251–1259. <https://doi.org/10.1021/nn203892h>
- Wang, T., Jiang, H., Wan, L., Zhao, Q., Jiang, T., Wang, B., Wang, S., 2015. Potential application of functional porous TiO<sub>2</sub> nanoparticles in light-controlled drug release and targeted drug delivery. *Acta Biomater.* 13, 354–363. <https://doi.org/10.1016/j.actbio.2014.11.010>
- Wang, X., Sun, X., Lao, J., He, H., Cheng, T., Wang, M., Wang, S., Huang, F., 2014. Multifunctional graphene quantum dots for simultaneous targeted cellular imaging and drug delivery. *Colloids Surf. B Biointerfaces* 122, 638–644. <https://doi.org/10.1016/j.colsurfb.2014.07.043>
- Williams, D.F., 2009. On the nature of biomaterials. *Biomaterials* 30, 5897–5909. <https://doi.org/10.1016/j.biomaterials.2009.07.027>
- Williams, D.F., 2008. On the mechanisms of biocompatibility. *Biomaterials* 29, 2941–2953. <https://doi.org/10.1016/j.biomaterials.2008.04.023>
- Williams, D.F., 1999. *The Williams Dictionary of Biomaterials*. Liverpool University Press, Liverpool.

- Williams, D.F., 1987. Definitions in Biomaterials: Proceedings of a Consensus Conference of the European Society for Biomaterials, Chester, England, March 3-5, 1986. Elsevier.
- Wittmaack, K., 2011a. Excessive Delivery of Nanostructured Matter to Submersed Cells Caused by Rapid Gravitational Settling. *ACS Nano* 5, 3766–3778. <https://doi.org/10.1021/nn200112u>
- Wittmaack, K., 2011b. Novel Dose Metric for Apparent Cytotoxicity Effects Generated by in Vitro Cell Exposure to Silica Nanoparticles. *Chem. Res. Toxicol.* 24, 150–158. <https://doi.org/10.1021/tx100331w>
- Wolfram, J., Yang, Y., Shen, J., Moten, A., Chen, C., Shen, H., Ferrari, M., Zhao, Y., 2014. The nano-plasma interface: Implications of the protein corona. *Colloids Surf. B Biointerfaces, Biointerfaces: Global Perspectives* 124, 17–24. <https://doi.org/10.1016/j.colsurfb.2014.02.035>
- Yakimova, R., Petoral, R.M., Yazdi, G.R., Vahlberg, C., Spetz, A.L., Uvdal, K., 2007. Surface functionalization and biomedical applications based on SiC. *J. Phys. Appl. Phys.* 40, 6435–6442. <https://doi.org/10.1088/0022-3727/40/20/S20>
- Yan, Y., Such, G.K., Johnston, A.P.R., Best, J.P., Caruso, F., 2012. Engineering Particles for Therapeutic Delivery: Prospects and Challenges. *ACS Nano* 6, 3663–3669. <https://doi.org/10.1021/nn3016162>
- Yu, S.S., Lau, C.M., Thomas, S.N., Jerome, W.G., Maron, D.J., Dickerson, J.H., Hubbell, J.A., Giorgio, T.D., 2012. Size- and charge-dependent non-specific uptake of PEGylated nanoparticles by macrophages. *Int. J. Nanomedicine* 7, 799–813. <https://doi.org/10.2147/IJN.S28531>
- Zarschler, K., Rocks, L., Licciardello, N., Boselli, L., Polo, E., Garcia, K.P., De Cola, L., Stephan, H., Dawson, K.A., 2016. Ultrasmall inorganic nanoparticles: State-of-the-art and perspectives for biomedical applications. *Nanomedicine Nanotechnol. Biol. Med.* 12, 1663–1701. <https://doi.org/10.1016/j.nano.2016.02.019>
- Zhang, L., Webster, T.J., 2009. Nanotechnology and nanomaterials: Promises for improved tissue regeneration. *Nano Today* 4, 66–80. <https://doi.org/10.1016/j.nantod.2008.10.014>
- Zhang, L.-N., Deng, H.-H., Lin, F.-L., Xu, X.-W., Weng, S.-H., Liu, A.-L., Lin, X.-H., Xia, X.-H., Chen, W., 2014. In Situ Growth of Porous Platinum Nanoparticles on Graphene Oxide for Colorimetric Detection of Cancer Cells. *Anal. Chem.* 86, 2711–2718. <https://doi.org/10.1021/ac404104j>
- Zhang, L.W., Monteiro-Riviere, N.A., 2009. Mechanisms of Quantum Dot Nanoparticle Cellular Uptake. *Toxicol. Sci.* 110, 138–155. <https://doi.org/10.1093/toxsci/kfp087>
- Zhang, Y., Mi, L., Wang, P.-N., Lu, S.-J., Chen, J.-Y., Guo, J., Yang, W.-L., Wang, C.-C., 2008. Photoluminescence Decay Dynamics of Thiol-Capped CdTe Quantum Dots in Living Cells under Microexcitation. *Small* 4, 777–780. <https://doi.org/10.1002/smll.200701034>
- Zhao, L., Mei, S., Chu, P.K., Zhang, Y., Wu, Z., 2010. The influence of hierarchical hybrid micro/nano-textured titanium surface with titania nanotubes on osteoblast functions. *Biomaterials* 31, 5072–5082. <https://doi.org/10.1016/j.biomaterials.2010.03.014>
- Zhong, Y., Sun, X., Wang, S., Peng, F., Bao, F., Su, Y., Li, Y., Lee, S.-T., He, Y., 2015. Facile, Large-Quantity Synthesis of Stable, Tunable-Color Silicon

- Nanoparticles and Their Application for Long-Term Cellular Imaging. *ACS Nano* 9, 5958–5967. <https://doi.org/10.1021/acsnano.5b00683>
- Zhu, J., Tang, C., Kottke-Marchant, K., Marchant, R.E., 2009. Design and Synthesis of Biomimetic Hydrogel Scaffolds with Controlled Organization of Cyclic RGD Peptides. *Bioconjug. Chem.* 20, 333–339. <https://doi.org/10.1021/bc800441v>
- Zhu, X., Peng, Y., Qiu, L., 2017. Amino-functionalized nano-vesicles for enhanced anticancer efficacy and reduced myelotoxicity of carboplatin. *Colloids Surf. B Biointerfaces* 157, 56–64. <https://doi.org/10.1016/j.colsurfb.2017.05.041>
- Zinger, O., Anselme, K., Denzer, A., Habersetzer, P., Wieland, M., Jeanfils, J., Hardouin, P., Landolt, D., 2004. Time-dependent morphology and adhesion of osteoblastic cells on titanium model surfaces featuring scale-resolved topography. *Biomaterials* 25, 2695–2711. <https://doi.org/10.1016/j.biomaterials.2003.09.111>

## 12 Original Publications Used for Ph.D. Thesis in Full

A. Lucie Ostrovská, Lucie Vištejnová, Jan Džugan, Peter Sláma, Tomáš Kubina, Egor Ukraintsev, Dana Kubies, Milena Králíčková, Marie Hubálek Kalbáčová (2016): **Biological evaluation of ultra-fine titanium with improved mechanical strength for dental implant engineering.** Journal of Materials Science 51, 3097-3110. IF = 2.993



## Biological evaluation of ultra-fine titanium with improved mechanical strength for dental implant engineering

Lucie Ostrovska<sup>1</sup> · Lucie Vistejnova<sup>1</sup> · Jan Dzugan<sup>2</sup> · Peter Slama<sup>2</sup> · Tomas Kubina<sup>2</sup> · Egor Ukraintsev<sup>3</sup> · Dana Kubies<sup>4</sup> · Milena Kralickova<sup>1</sup> · Marie Hubalek Kalbacova<sup>1,5</sup>

Received: 12 October 2015 / Accepted: 23 November 2015 / Published online: 7 December 2015  
© Springer Science+Business Media New York 2015

**Abstract** Titanium, the gold standard for dental implant materials, is distinguished by its exceptional biocompatibility; however, from a long-term perspective, titanium still lacks sufficient loading strength. Commercially pure titanium with grain size 30  $\mu\text{m}$  was processed by equal channel angular pressing, and two novel mechanically improved types of titanium material with grain size 4.6 and  $\leq 1 \mu\text{m}$  were obtained. The surfaces of these ultra-fine grained titanium samples were further mechanically treated by grinding and polishing, and their surfaces were characterized by atomic force microscopy and contact angle measurement. Osteoblast-like cells and human mesenchymal stem cells were used to evaluate the cytocompatibility of these titanium samples. The cell metabolic activity, cell number, cell area, morphology, and cell adhesion quality during the early stage (2 h) and prolonged cultivation (48 h) were determined. Both cell types displayed increased initial attachment to all tested titanium materials

in comparison to reference tissue culture plastic. Importantly, results revealed that the novel titanium materials with improved strength were equivalent to the original commercially pure titanium, thus confirming their suitability for osteoblast and mesenchymal stem cell growth and proliferation. The present study proved the cytocompatibility of the novel forms of titanium with superior mechanical properties and revealed their potential for manufacturing of long-term dental implants.

### Introduction

Modern dentistry represents well-established field of medicine dealing with the increasing patient demands on implant function, permanence, and esthetics. Due to technological and medical progress, biocompatible materials with excellent mechanical properties have been

✉ Marie Hubalek Kalbacova  
marie.kalbacova@lf1.cuni.cz

Lucie Ostrovska  
Lucie.Ostrovska@lfp.cuni.cz

Lucie Vistejnova  
Lucie.Vistejnova@lfp.cuni.cz

Jan Dzugan  
jan.dzugan@comtesfht.cz

Peter Slama  
peter.slama@comtesfht.cz

Tomas Kubina  
tomas.kubina@comtesfht.cz

Egor Ukraintsev  
ukraints@fzu.cz

Dana Kubies  
kubies@imc.cas.cz

Milena Kralickova  
Milena.Kralickova@lfp.cuni.cz

<sup>1</sup> Biomedical Center, Faculty of Medicine in Pilsen, Charles University in Prague, Alej Svobody 76, 323 00 Pilsen, Czech Republic

<sup>2</sup> COMTES FHT a.s., Prumyslova 995, 334 41 Dobruška, Czech Republic

<sup>3</sup> Institute of Physics, Academy of Sciences of the Czech Republic, Na Slovance 1999/2, 182 21 Prague, Czech Republic

<sup>4</sup> Institute of Macromolecular Chemistry, Academy of Sciences of the Czech Republic, Heyrovského náměstí 2, 162 06 Prague, Czech Republic

<sup>5</sup> Institute of Inherited Metabolic Disorders, 1st Faculty of Medicine, Charles University in Prague, Ke Karlovu 2, 128 08 Prague, Czech Republic

successfully designed; however, ensuring their longevity, particularly under load-bearing conditions, remains difficult [1–3].

Titanium (Ti) is one of the best materials for the production of dental and orthopedic implants. Many metallic materials are not suitable for applications in living organisms due to their high reactivity and inflammatory process activation; therefore, currently, only suitable metallic alloys are being used [4, 5]. Ti is distinguished by its biocompatibility, low reactivity in tissue, and corrosion resistance, which is provided by a passive layer of TiO<sub>2</sub> that forms spontaneously on the surface. This layer represents an inert barrier between the material and the biological environment, which in clinical practice means that the implant is prevented from releasing ions into the organism [6]. Moreover, Ti is characterized by its light weight and high formability, which enables the easy fabrication of different low-weight medical devices [7]. The low elastic modulus of Ti is advantageous over other metals because it decreases the shield stress of the implant, which is particularly important in bone tissue. Nevertheless, the primary issue of the insufficient loading strength of Ti remains [8]. A significant improvement of this characteristic was achieved by fabricating a duplex alloy with aluminum and vanadium, which resulted in the formation of the most successful and widely used Ti alloy, Ti-6Al-4 V. Originally, this alloy was designed for utilization in aerospace engineering, and its suitable properties for use in biomedicine were discovered as an afterthought [9]. Unfortunately, from a long-term perspective, the utilization of Ti-6Al-4V increases the risk of the passive dissolution of metal ions into the surrounding tissue because the layer of TiO<sub>2</sub> loses its barrier function in alloys after recurrent wear and fretting. Slow and gradual ion release is dangerous because this process can lead to the accumulation of toxic amounts of aluminum and vanadium in an organism, thus posing a risk of severe systemic tissue damage. Therefore, Ti-alloys with toxic elements are not used for the replacement of movable joints where sliding contact occurs [6, 10].

Currently, new approaches to improve the mechanical characteristics of Ti include the following: (a) replacing the potentially toxic elements in the alloys with non-toxic elements, and (b) grain refinement [11]. New alloys composed of tantalum (Ta), nickel (Ni), zirconium (Zr), molybdenum (Mo), or niobium (Nb) have been already generally in use [12], although their manufacturing sometimes requires high costs (Mo, Ta). However, the sensitivity of the population to previously non-toxic elements increases (for example, Ni) when these alloys are used [13]. In contrast, strengthening commercially pure Ti (cp Ti) by refining the grain size to the nanoscale can extend its long-term performance and improve the mechanical

strength of an implant, while preserving its exceptional biocompatibility due to eliminated release of toxic ions. Specific criteria must be met when developing methods for nanostructuring Ti for further biomedical utilization. Selected production techniques must guarantee the manufacture of uniformly defined microstructures within the bulk material that are stable after further processing. A widely used technology for metal nanostructuring is severe plastic deformation (SPD), which forms ultra-fine grain (UFG) materials from a bulk coarse-grained material using extremely high strain [14]. One of the most developed techniques of SPD is equal channel angular pressing (ECAP), which works on the principle of a simple shear force applied on a rod-shaped billet [15]. Thermal stability of Ti-Alloys processed by SPD techniques, such as ECAP, is up to 450 °C as referred in [16, 17]. Additionally, surface of the materials should mimic the three-dimensional extracellular environment of bone tissue and thus stimulate cell attachment and proliferation. Specific surfaces of bio-implants with micro/nano-topographies can greatly enhance the adhesion of cells, particularly in mesenchymal stem cells and osteoblasts [18–20]. Such treatment can be performed by many techniques, including acid etching, plasma blasting, sand/grit blasting or mechanical polishing and grinding [21]. Enhanced cell adhesion to the surface is crucial for better acceptance of the implant by an organism, and proper long-term cell contact with the material can avoid the creation of deep pockets on the interface, which can lead to bacterial infection [22].

The aim of our study was to evaluate the cytocompatibility of cp Ti Grade 2 processed by ECAP-Conform using the human osteoblast-like cell line SAOS-2 and human mesenchymal stem cells (hMSCs). Six types of Ti with different grain sizes and different mechanical surface treatments were tested. The interactions and viability of the cells with the materials were investigated during the early stages of attachment after short (2 h) and long (48 h) periods.

## Materials and methods

### Sample fabrication and mechanical characterization

Ti samples were supplied by COMTES FHT a.s. (Dobruška, Czech Republic) in the form of discs with diameters of 8 mm (~0.5 cm<sup>2</sup>). The Grade 2 cp Ti (S) was used as a substrate for subsequent processing by ECAP-Conform [15]. The chemical purity and composition of the bulk Ti material were measured using a Q4 Tasman optical emission spectrometer (Bruker, USA) and a G8 Galileo gas analyzer (Bruker, USA). The original material (S) was passed once (M) or three times (Z) through ECAP-



Conform, and three different Ti samples with the following grain sizes were obtained: *Z* ( $\leq 1 \mu\text{m}$ ), *M* ( $4.6 \mu\text{m}$ ), and *S* ( $30 \mu\text{m}$ ). The microstructure of *Z* and *M* materials was confirmed by electron backscatter diffraction (EBSD) maps acquired in SEM JEOL 7400F (JEOL Ltd., Japan) by EBSD camera Oxford Nordlys (Oxford Instruments, United Kingdom). Very fine grains of the material *Z* were investigated by TEM JEOL 200CX (JEOL Ltd., Japan). Quasi-static tensile tests were performed according to ISO 6892-1 on triplicates of the investigated Ti samples at room temperature. Round tensile specimens with threaded shoulders of diameter 4 mm and with gauge lengths of 20 mm were tested. Tests were performed using a Zwick Z 250 electro-mechanical testing system (Zwick Roell, Germany) fitted with hydraulic grips. The strain on the sample was measured directly using a Messphysik laser speckle extensometer (Messphysik materials testing, Austria), which allows for biaxial strain measurement until the specimen fractures. The specimens' dimensions were measured using a micrometer before testing, and their gauge lengths were marked for elongation evaluation. The appropriate dimensions were measured after the tests to evaluate elongation and cross-section reduction. The elongation shown in Fig. 1 is evaluated from marks on the specimen. The surface of each Ti sample was treated by polishing with diamond paste and colloidal silica (p) or by grinding with abrasive grinding paper (1200) (g). Thus, six types of Ti samples were evaluated, i.e., Zp, Zg, Mp, and Mg, representing the new titanium materials with improved mechanical properties, and Sp and Sg, representing the original Ti material. All Ti samples were compared with common polystyrene material for cell cultivation (PS control).

### Surface topography characterization

Qualitative and quantitative analyses of the surface morphology of the Ti samples and PS control were performed using atomic force microscopy (AFM). A Ti sample area of  $50 \times 50 \mu\text{m}$  was studied in air using a Peakforce AFM system (ICON, Bruker, USA) in quantitative nanomechanical mapping mode with a Multi75Al cantilever (BudgetSensors, Innovative Solutions Bulgaria Ltd, Bulgaria). In this mode, the interaction between the tip and the sample is controlled and measured at each point. The cantilever was treated using  $\text{CF}_4$  plasma to reduce the contamination and interaction with the surfaces of the Ti samples. The primary advantage of this mode is its ability to measure using small forces; moreover, measuring the elastic modulus of the material and the adhesion between the AFM tip and the sample is possible using this mode [23]. Two samples of each type of surface were scanned, their topographic features were examined, and the root

mean square roughness ( $R_{\text{RMS}}$ ) of each Ti sample was quantitatively estimated.

### Wettability measurement

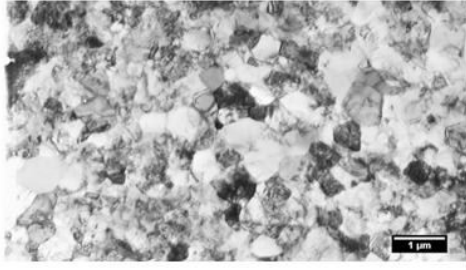
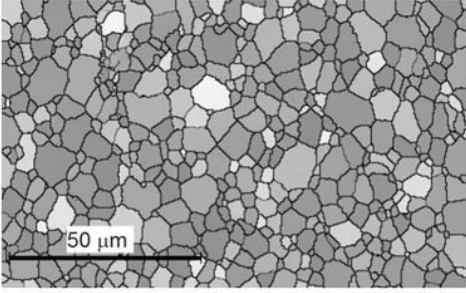
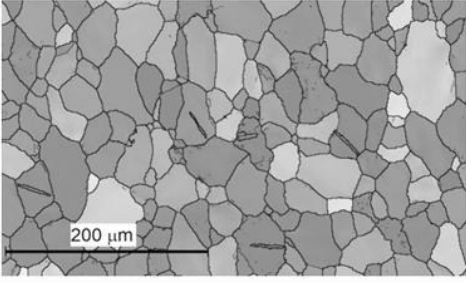
The surface wettability of the Ti samples and of the PS control was examined with a static and dynamic sessile water drop method using an OCA 20 contact angle apparatus (DataPhysics, Germany). Before the analysis, the Ti samples were cleaned by gentle rinsing in petroleum ether, methanol, and then water to remove impurities due to sample processing [24]. Then, the samples were sterilized in 70 % ethanol for 10 min and rinsed two times with deionized water to simulate the conditions of in vitro experiments. Finally, the Ti samples were dried under a stream of nitrogen in a flow box and subjected to analysis. For the static method analysis, each sample was characterized using two drops with volumes of  $2 \mu\text{l}$ . The data were evaluated using the Young–Laplace method. For the dynamic method analysis, a  $3 \mu\text{l}$  drop was placed on the surface, and advancing and receding contact angles were determined, while the volume of the drop was increased to  $8 \mu\text{l}$  and decreased at a flow rate of  $0.2 \mu\text{l/s}$ . The data were evaluated using the tangent leaning method. Three Ti samples of each surface type were measured twice by the static method and once by the dynamic method.

### Cell culture

The SAOS-2 cells (DSMZ, Germany) were cultured in McCoy's 5A medium without phenol red (HyClone, USA) supplemented with heat-inactivated 15 % fetal bovine serum (GE Healthcare, UK), 10,000 U/ml penicillin (Sigma-Aldrich, USA), and  $10 \mu\text{g/ml}$  streptomycin (Sigma-Aldrich, USA). The cells were seeded at a density of  $15,000 \text{ cells/cm}^2$ .

The hMSCs (General University Hospital, Prague and University Hospital, Pilsen) were obtained from four patients undergoing diagnostic trephine biopsies for suspected hematological disease without tumor-affected bone marrow and from volunteers after giving written consent. This research conforms to general ethical principles and standards—all the procedures involving living human participants were approved by the Ethical Committee of General University Hospital in Prague and by University Hospital and Medical Faculty in Pilsen, Charles University in Prague. The isolated cells were cultured in alpha minimum essential medium ( $\alpha$ -MEM; Gibco, USA) supplemented with heat-inactivated 10 % fetal bovine serum (GE Healthcare, UK), 10,000 U/ml penicillin (Sigma-Aldrich, USA), and  $10 \mu\text{g/ml}$  streptomycin (Sigma-Aldrich, USA). The hMSCs were seeded at a density of  $10,000 \text{ cells/cm}^2$  and cultured up to the 5th passage.

**Fig. 1** Summary of strength and plastic characteristics of Ti samples including representative microstructural images of Ti samples showing grain size of materials. **a** Transmission electron microscope (TEM) image; **b** and **c** electron backscatter diffraction (EBSD) maps

<b>(a)</b>	<b>Grain size (<math>\mu\text{m}</math>)</b>	$\leq 1.0$		<b>Z</b>
	<b>Yield stress (MPa)</b>	$575.8 \pm 8.8$		
	<b>Tensile strength (MPa)</b>	$656.8 \pm 6.3$		
	<b>Elongation (%)</b>	$22.4 \pm 5.1$		
	<b>Cross section reduction (%)</b>	$60.4 \pm 0.7$		
<b>(b)</b>	<b>Grain size (<math>\mu\text{m}</math>)</b>	4.6		<b>M</b>
	<b>Yield stress (MPa)</b>	$409.9 \pm 7.7$		
	<b>Tensile strength (MPa)</b>	$516.2 \pm 1.8$		
	<b>Elongation (%)</b>	$30.9 \pm 1.7$		
	<b>Cross section reduction (%)</b>	$59.6 \pm 1.5$		
<b>(c)</b>	<b>Grain size (<math>\mu\text{m}</math>)</b>	30.0		<b>S</b>
	<b>Yield stress (MPa)</b>	$332.6 \pm 1.8$		
	<b>Tensile strength (MPa)</b>	$468.2 \pm 1.9$		
	<b>Elongation (%)</b>	$31.4 \pm 1.4$		
	<b>Cross section reduction (%)</b>	$62.9 \pm 0.5$		

Ti samples were placed on the bottom of 24-well plates (Techno Plastic Products, Switzerland) in doublets. The sterilization process was performed before cultivation. The samples were rinsed with 70 % ethanol for 10 min and then washed twice with deionized water.

Each cell type was plated onto the Ti samples at the density listed above using the droplet technique. Briefly, 100  $\mu\text{l}$  of cell suspension was dropped onto Ti samples, and 380  $\mu\text{l}$  of the cell suspension was dropped onto PS control wells to obtain identical cell densities on the surface. The cells were cultured for 2 or 48 h in a humidified 5 %  $\text{CO}_2$  atmosphere at 37 °C. To prevent droplet evaporation, the Ti samples and PS control were covered with additional complete culture media to a volume of 1000  $\mu\text{l}$  at 1 h after initial attachment, and the cells were further cultured until the desired time points.

### Metabolic activity

The metabolic activity of the cells at 48 h after plating was assessed by MTS assay (Cell Titer96<sup>®</sup> AqueousOne,

Promega, USA). The principle of this colorimetric assay is the reduction of the MTS ((3-(4,5-dimethylthiazol-2-yl)-5-(3-carboxymethoxyphenyl)-2-(4-sulfophenyl)-2H-tetrazolium)) compound into a soluble colored formazan product by mitochondrial dehydrogenases. The assay was performed according to the manufacturer's protocol. After the cells were incubated for 2 h with MTS reagent, the optical density was measured using a microplate reader (Infinite<sup>®</sup> 200 PRO, Tecan Group Ltd., Switzerland) at 490 nm, subtracting the background at 655 nm. The obtained results were compared to the results of the cells on the PS control. These results are expressed as percentages.

### Fluorescence microscopy

After 2 and 48 h, the cells were fixed in 4 % paraformaldehyde. Then, the nuclei were stained with DAPI (1:1000, Sigma-Aldrich, USA), actin filaments were stained with Phalloidin-Alexa Fluor 488 (1:1000, Invitrogen, USA), and the vinculin protein in cell focal adhesions was visualized by antibodies (mouse monoclonal anti-



vinculin antibody, 1:500, Sigma-Aldrich, USA and Alexa Fluor 568-conjugated goat anti-mouse antibody, 1:500, Invitrogen, USA). An Eclipse Ti-S or Eclipse Ti-U epifluorescence microscope (Nikon, Japan) and a DS-Qi1Mc digital camera (Nikon, Japan) were used to acquire fluorescence images of the stained cells.

### Cell number and cell area

For cell number determination, ten random fluorescence images of DAPI-stained nuclei from every Ti sample and PS control were acquired using a fluorescence microscope at 10× magnification. For cell area determination, ten random fluorescence images of DAPI-stained nuclei and phalloidin-Alexa488-stained actin filaments were acquired for every Ti sample and PS control using a fluorescence microscope at 20 × magnification. The cell nuclei were automatically counted, and the single cell area was estimated using ImageJ [25] and Cell Profiler [26]. The cell number is expressed as the number of cells per cm<sup>2</sup>. The cell area is expressed as the mean area of the cell in μm<sup>2</sup> for every substrate. The results obtained from both analyses were compared to the results of cells on the PS control. These results are expressed as percentages.

### Statistical analysis

All presented data were derived from at least two independent experiments performed in duplicate. The results are presented as the mean values with error bars indicating standard deviations. Data distribution was evaluated using the Shapiro–Wilk test. The non-parametric Wilcoxon matched-pairs test was used to determine significant differences between the datasets from the Ti samples and the PS control. An ANOVA was used to compare Ti samples to each other. *P* values of less than 0.05 were considered statistically significant. Statistical analysis was performed using the software STATISTICA (StatSoft, Inc., USA).

## Results

### Chemical and mechanical characterization of Ti samples

The chemical purity and composition of the original Ti material (S) were examined before undergoing the ECAP-Conform process. The listed weight percentages of the elements (Table 1) show that the bulk material was composed of 99.80 % Ti. The mechanical characterization of each of the three Ti samples without surface treatment involved determining their strength characteristics (yield stress and tensile strength) and plastic characteristics

(elongation and cross-section reduction). The measured values and representative microstructure images are summarized in Fig. 1, and the resultant stress–strain curves for each Ti sample are shown in Fig. 2. The original *S* samples exhibited the lowest strength parameters and had the grains with the largest area. The *M* samples exhibited slight increases in their mechanical properties of approximately 15 %, while maintaining almost the same deformation behavior as the *S* samples. The highest stress–strain curves were obtained in the case of the *Z* samples, as they exceeded the *S* samples by more than 30 % while maintaining sufficient ductility for potential further product formation. The *Z* samples exhibited superior properties to the other investigated samples.

### Surface topography of Ti samples

Characterization of the surface topography of all Ti samples and the PS control was performed by AFM. The surface profiles are presented in diagrams in Fig. 3. Quantitative measurements of the  $R_{RMS}$  were also conducted for each material (Table 2). The obtained AFM data show that the polished samples have a fine topography and lack distinctive surface roughness and tall peaks. The *Zp* samples revealed many small 10 nm deep holes and occasional large-scale roughness (~5 μm in *X–Y* directions). On the *Mp* samples, many 10–20 nm tall Ti particles above a flat layer were detectable. *Sp* samples were of a similar topography as *Mp* samples, with fewer tall particles, which was most likely caused by the larger grain size of the *S* samples.

In contrast, all ground samples had an RMS roughness of approximately 270 nm, irrespective of the grain size. The width of the 500–1000 nm tall peaks was  $10 \pm 3$  μm for all Ti samples. Even on a smaller scale (10 μm), the morphologies of *Zg*, *Mg*, and *Sg* samples were similar (data not shown). Furthermore, AFM data showed that tall objects, holes, and flat regions of all Ti samples had similar elastic moduli (data not shown), confirming that the tall objects on the surface are of Ti origin.

### Surface wettability of Ti samples

The wettability of Ti samples and the PS control was determined by water contact angle ( $\theta$ ) measurements using static and dynamic (advanced and receding  $\theta$ ) sessile drop methods. The results are presented in Table 2. The tested

**Table 1** Chemical composition of Ti bulk material (wt%)

Fe	O	C	H	N	Ti
0.0460	0.1200	0.0230	0.0026	0.0074	99.8010

**Fig. 2** Mechanical characteristics of Ti samples. Stress–strain curves of Ti samples (triplets)

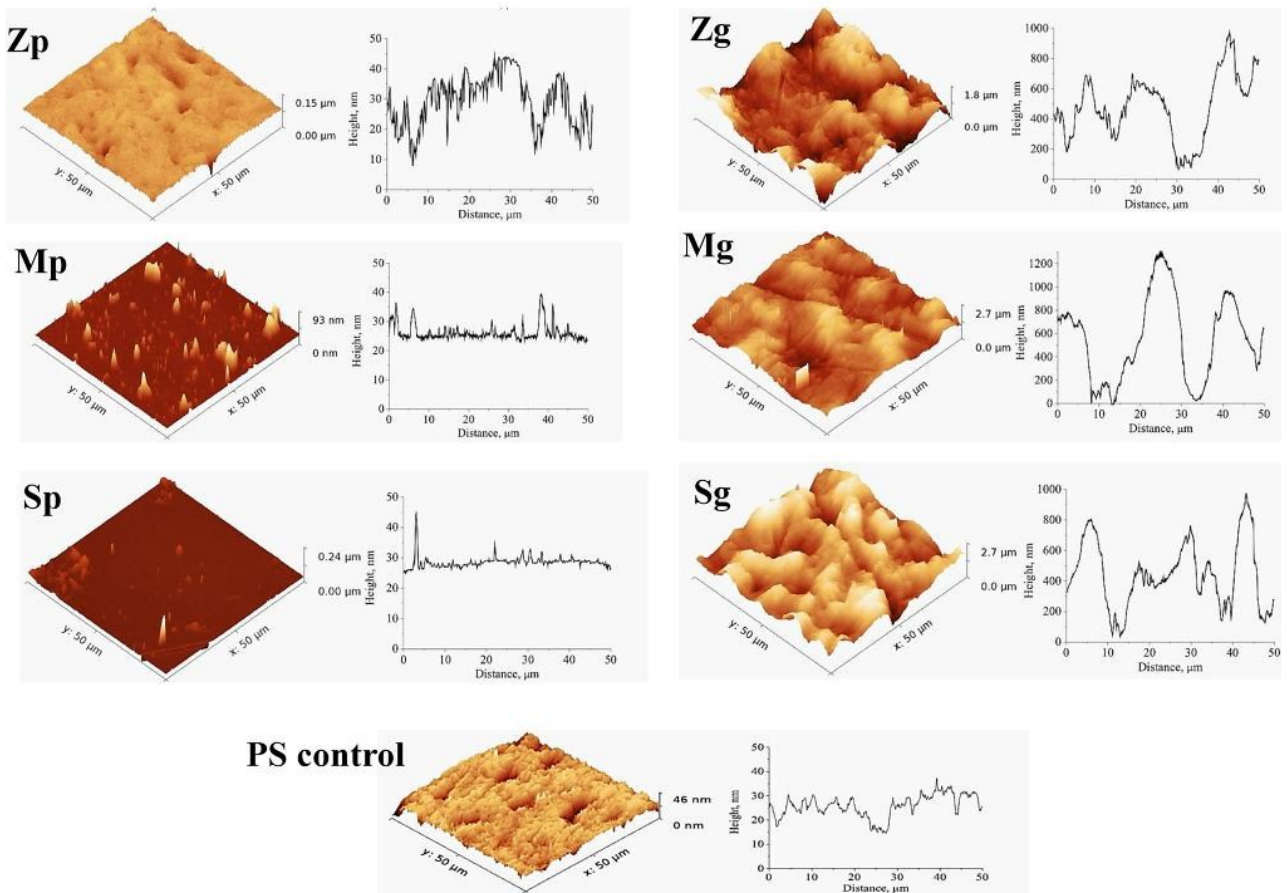
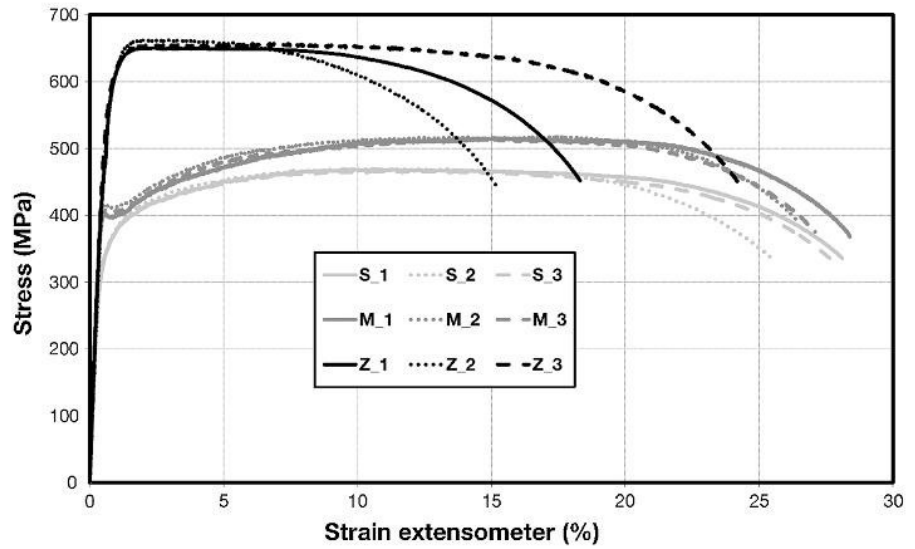


**Fig. 3** AFM images of Ti samples and polystyrene (PS) control with corresponding 2D diagrams of height profiles

Ti samples represented hydrophilic surfaces with a static  $\theta$  between  $30^\circ$  and  $45^\circ$  based on the surface treatment.  $\theta$  values obtained by the static measurement method were generally  $5^\circ$  lower than the values of the advanced  $\theta$  ( $\theta_A$ )

obtained by the dynamic method. However, the trend between Ti samples remained similar. Importantly, the receding  $\theta$  ( $\theta_R$ ) was not determined by the dynamic method in the case of all Ti samples, indicating profound water



**Table 2** Quantitative characterization of the surface of Ti samples and polystyrene (PS) control

Surface	Grain size ( $\mu\text{m}$ )	Surface treatment	$R_{\text{RMS}}$ (nm)	Static contact angle $\theta$ ( $^\circ$ )	Dynamic contact angle	
					$\theta_{\text{A}}$ ( $^\circ$ )	$\theta_{\text{R}}$ ( $^\circ$ )
PS control	–	–	4.7	$69.0 \pm 1.4$	$71.0 \pm 1.1$	$22.7 \pm 0.5$
Zp	$\leq 1.0$	Polished	2.0–5.0	$44.0 \pm 1.3$	$49.0 \pm 0.5$	N/A
Mp	4.6	Polished	2.0–5.0	$43.0 \pm 1.3$	$47.0 \pm 1.8$	N/A
Sp	30.0	Polished	5.0–12.0	$41.0 \pm 0.8$	$46.0 \pm 0.1$	N/A
Zg	$\leq 1.0$	Ground	$\sim 270.0$	$34.0 \pm 0.5$	$37.0 \pm 0.6$	N/A
Mg	4.6	Ground	$\sim 270.0$	$30.0 \pm 1.0$	$35.0 \pm 0.0$	N/A
Sg	30.0	Ground	$\sim 270.0$	$34.0 \pm 0.3$	$41.0 \pm 0.9$	N/A

$R_{\text{RMS}}$  root mean squared roughness,  $\theta_{\text{A}}$  advancing contact angle,  $\theta_{\text{R}}$  receding contact angle

interactions with Ti samples that could not be evaluated using only the static  $\theta$  analysis. Water was adsorbed and retained on all Ti samples more strongly than on the PS control, with  $\theta_{\text{R}}$  of  $22^\circ$ .

The surfaces of the polished samples (Zp, Mp, Sp) showed dynamic  $\theta_{\text{A}}$  values between  $46^\circ$  and  $49^\circ$ . A slight tendency of  $\theta_{\text{A}}$  to decrease with increasing grain size was also observed. The  $\theta_{\text{A}}$  values obtained for the ground samples (Zg, Mg, Sg) were approximately  $10^\circ$  lower than the values of the polished samples. Here, the grain sizes of the material did not affect the surface wettability. Thus, treatment by grinding resulted in more hydrophilic surfaces.

### Cell metabolic activity on Ti samples

The metabolic activity of the cells on the Ti samples was assessed after 48 h of incubation. For SAOS-2 cells, no significant difference was observed between the Ti samples and the PS control (Fig. 4a). Moreover, no obvious difference was observed even among the different Ti samples. The slightly decreased metabolic activity of the cells plated on both *M* samples compared to the cells plated on PS control was not statistically significant. In the case of hMSCs (Fig. 4b), the metabolic activity did not differ significantly between the cells cultivated on Ti samples and on the PS control, except for ground *M* and *S* samples, where the slight decrease was statistically significant.

### Cell number

The number of cells on the Ti samples was measured after 2 and 48 h of cultivation to assess the extent of the initial attachment of the cells to the material and to define their growth during cultivation (Fig. 5).

The number of adherent SAOS-2 cells on Ti samples during the first 2 h was substantially higher than the number of these cells on the PS control (Fig. 5a). This considerable increase in the number of adherent SAOS-2 cells at this

initial phase was comparable among all Ti samples. The difference between the Ti samples and the PS control remained significant even after 48 h of incubation. However, the increase in the cell numbers on the Ti samples in comparison to the PS control was more pronounced after 2 h (3-fold) than after 48 h (2-fold) of incubation (Fig. 5c), suggesting a slower growth of SAOS-2 cells on Ti samples.

hMSCs also showed higher numbers of adherent cells on the Ti samples compared to the PS control after a 2-h incubation (Fig. 5b); however, the increases were not significant in all cases. In contrast, after 48 h, the cell number on the PS control was higher compared to all Ti samples. Similar to SAOS-2, the increase in the cell number on the Ti samples was slower than on the PS control. However, in the case of hMSCs, the difference was even more pronounced (Fig. 5d), which led to the lowered cell number on the Ti samples after 48 h in comparison to the PS control.

### Cell area

The areas of single cells were determined after 2 and 48 h of cultivation. The determination of both cell type areas indicated very similar features for both time points of the assessment (Fig. 6). The real cell area on the PS samples is presented in Fig. 6a. From the beginning, both cell types plated on the Ti samples were smaller than those plated on the PS control. After 2 h of incubation, the area of SAOS-2 cells cultivated on the Ti samples was only fractionally smaller than that on the PS control (Fig. 6b), with significant differences found only for Zp, Mp, and Sg. In contrast, hMSCs were significantly smaller on most of the Ti samples compared to those cultivated on the PS control (approximately, a 20 % size reduction) (Fig. 6c).

The area differences were more pronounced after 48 h of cultivation. The areas of SAOS-2 cells were reduced by approximately 20 %; however, the areas of hMSCs on all Ti samples were reduced even more (by approximately 50 % in comparison to the PS control).

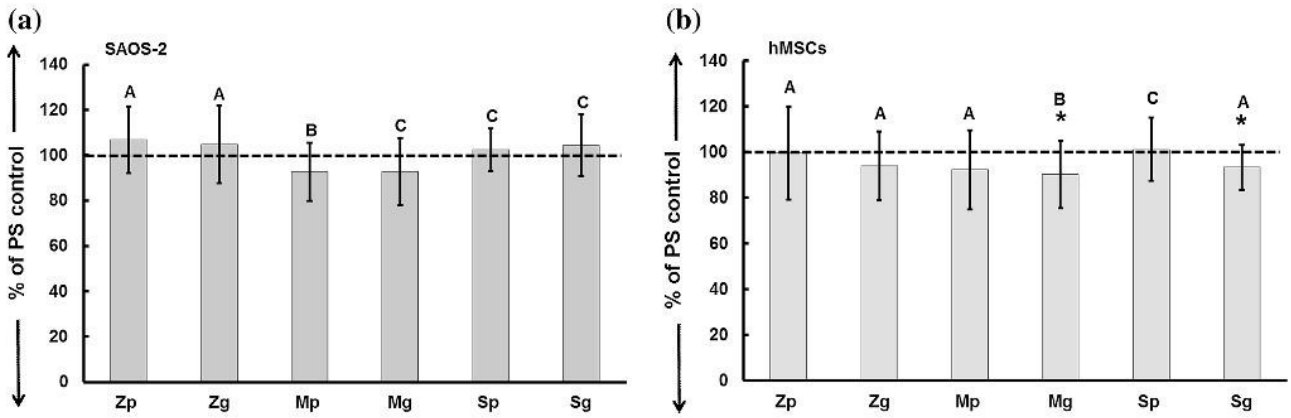


**Fig. 4** Metabolic activity after 48 h of cultivation on Ti samples. **a** Osteoblasts (SAOS-2), **b** human mesenchymal stem cells (hMSC). Relative values are expressed as a percentage of PS control (dashed line). Asterisk (\*) means a significant difference from PS control

(Wilcoxon matched-pairs test,  $p < 0.05$ ). Groups marked with different letters express significant inter-group difference within samples (ANOVA, LSD post hoc test,  $p < 0.05$ )

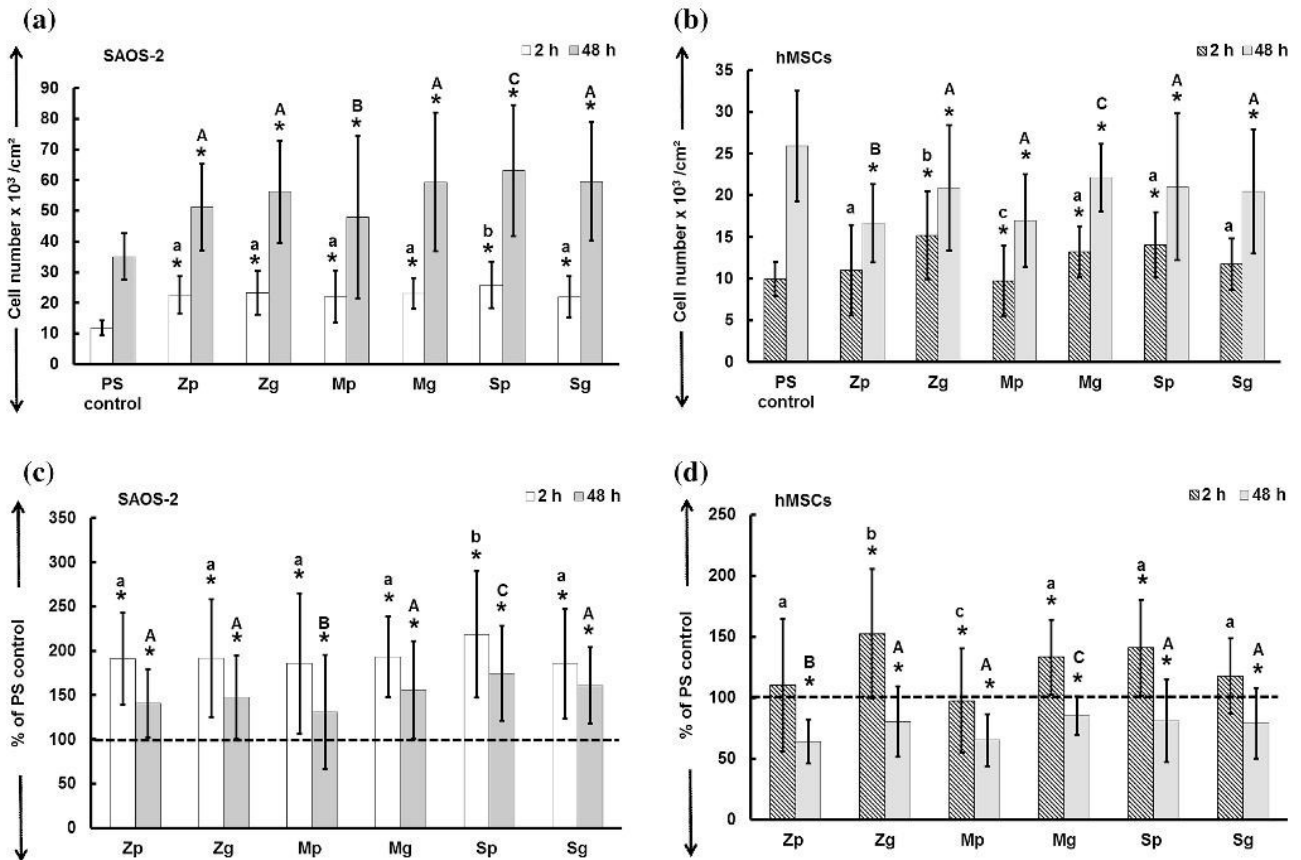


**Fig. 5** Cell number after 2 and 48 h of cultivation on Ti samples. **a** Osteoblasts (SAOS-2)—values of cell number/cm<sup>2</sup>, **b** human mesenchymal stem cells (hMSCs)—values of cell number/cm<sup>2</sup>, **c** osteoblasts (SAOS-2)—relative values expressed as a percentage of PS control (dashed line), **d** human mesenchymal stem cells (hMSCs)—relative values expressed as a percentage of PS control

(dashed line). Asterisk (\*) means a significant difference from PS control (Wilcoxon matched-pairs test,  $p < 0.05$ ). Groups marked with different lower-case letters (2 h) or with different upper-case letters (48 h) express significant inter-group difference within samples (ANOVA, LSD post hoc test,  $p < 0.05$ )



**Cell morphology and adhesion**

The cell morphology on different Ti samples was analyzed by the double fluorescence staining of actin filaments and nuclei after 48 h (Fig. 7). Moreover, vinculin, as an intracellular protein participating in the formation of focal adhesions, was also visualized by immunofluorescence staining to investigate the quality of focal adhesion plaques of SAOS-2 cells on different Ti samples (Fig. 8). Representative images of cells cultivated on the different substrates are shown in Fig. 7. A common cuboidal-like morphology was displayed by SAOS-2 cells on all Ti samples (Fig. 7b, c) as well as on the PS control (Fig. 7a). Thus, in spite of the observed smaller sizes of these cells on Ti samples, their morphology and cytoskeleton quality were comparable to those cultivated on the PS control and were not altered. The morphology of hMSCs grown on Ti samples (Fig. 7e, f) and on the PS control (Fig. 7d) differed. hMSCs cultured on ground samples displayed noticeable elongation and filopodia extensions, and their spreading to the orientation of valley-like structures was

more intense. Polished samples enabled the growth and spreading of hMSCs in all directions; thus, their morphology varied, and they often grew in vertical layers.

The most pronounced focal adhesions were observed in SAOS-2 cells, as shown in Fig. 8. In particular, the cells cultured on ground samples displayed noticeable focal adhesion plaques (Fig. 8e–g), where the most of the vinculin signal was localized in the form of circular structures on the edges and extensions of the cells. By contrast, SAOS-2 cells grown on polished samples exhibited elongated focal adhesions localized on the entire basal pole of the cells and displayed strong similarity with the cells cultured on the PS control (Fig. 8b–d).

**Discussion**

The biocompatibility of the material is not the only parameter that defines the lifespan of an implant. Long-term stress conditions demand a material that represents an excellent combination of strength and plastic properties.

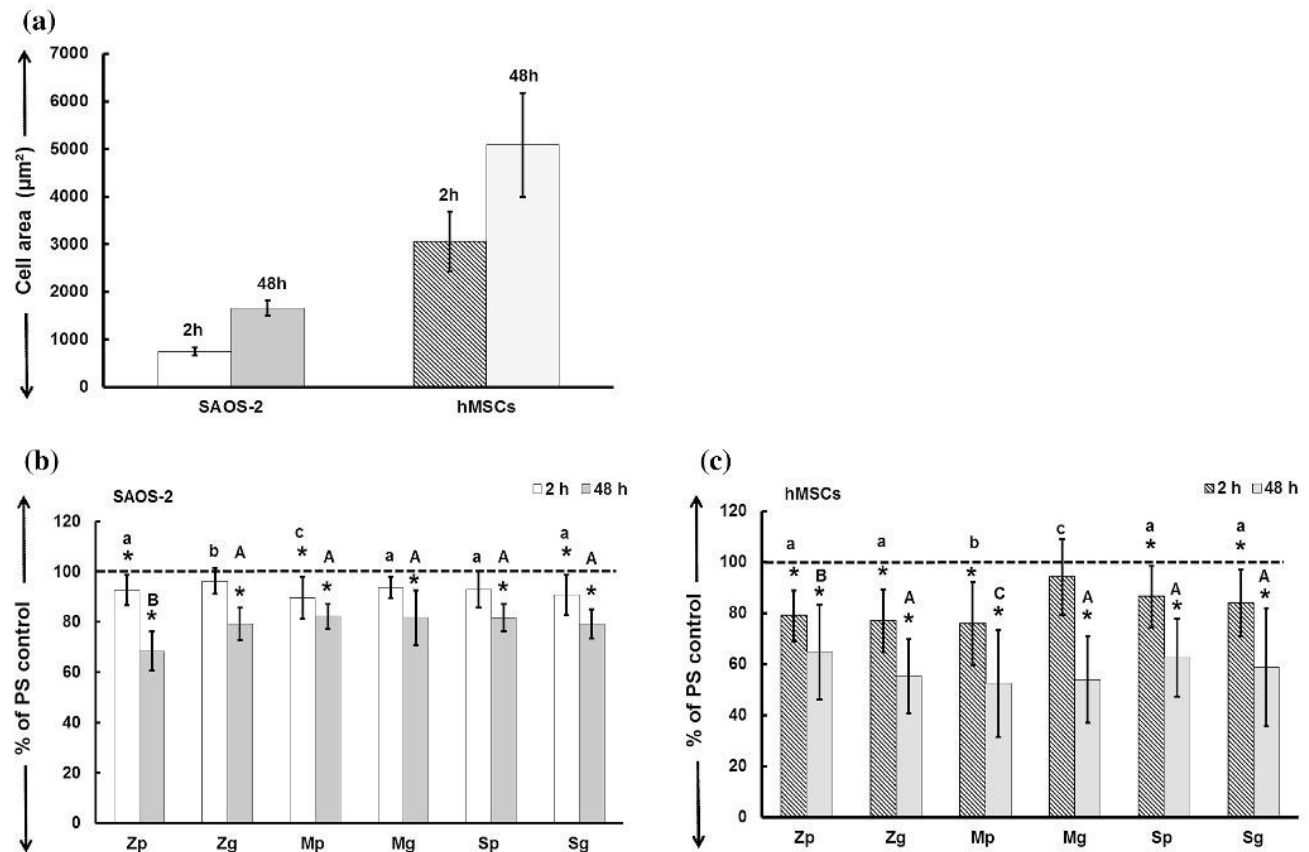


**Fig. 6** Cell area after 2 and 48 h of cultivation on Ti samples. **a** Values of cell area on PS control in μm<sup>2</sup>, **b** osteoblasts (SAOS-2)—relative values expressed as a percentage of PS control (dashed line), **c** human mesenchymal stem cells (hMSCs)—relative values expressed as a percentage of PS control (dashed line). Asterisk

means a significant difference from PS control (Wilcoxon matched-pairs test,  $p < 0.05$ ). Groups marked with different lower-case letters (2 h) or with different upper-case letters (48 h) express significant inter-group difference within samples (ANOVA, LSD post hoc test,  $p < 0.05$ )



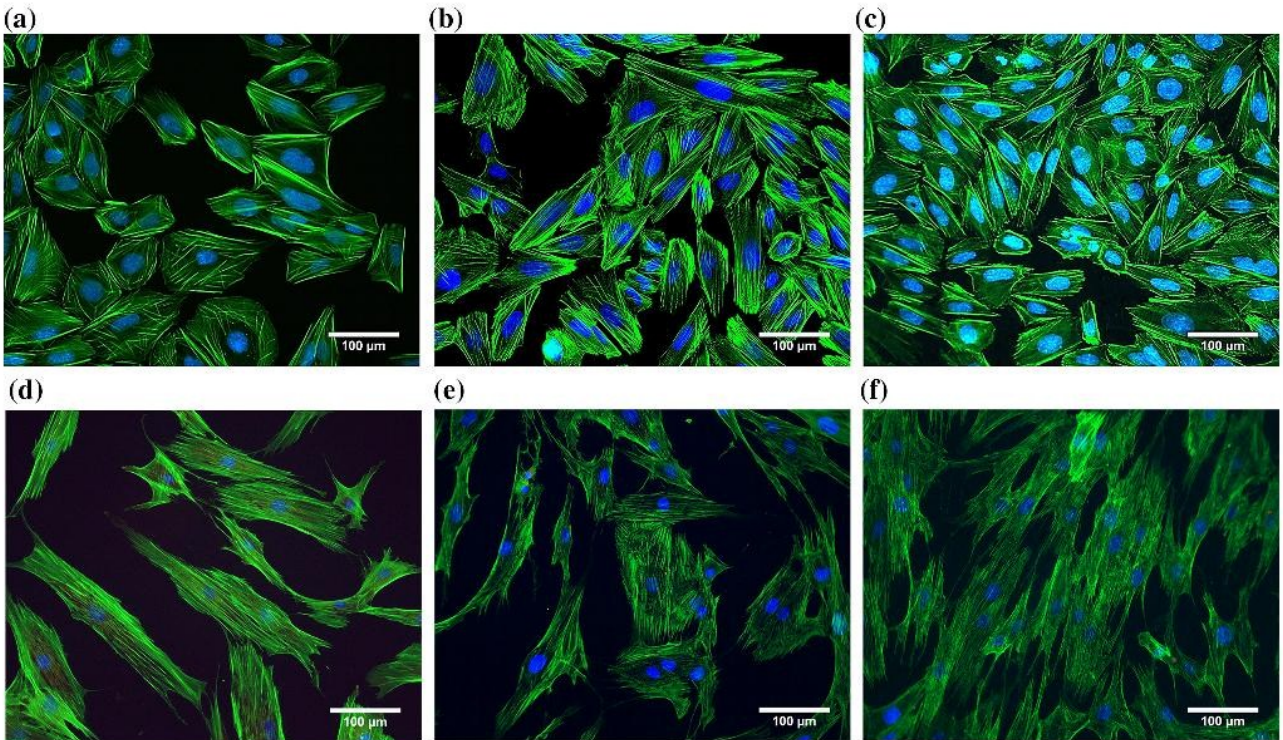


**Fig. 7** Representative images of cells on different substrates after 48 h of cultivation. Osteoblasts (SAOS-2) (a–c) and human mesenchymal stem cells (hMSCs) (d–f) on PS control (a, d), polished

sample (b, e), ground sample (c, f). Actin cytoskeleton stained by phalloidin-AF488 (green), nucleus stained by DAPI (blue)

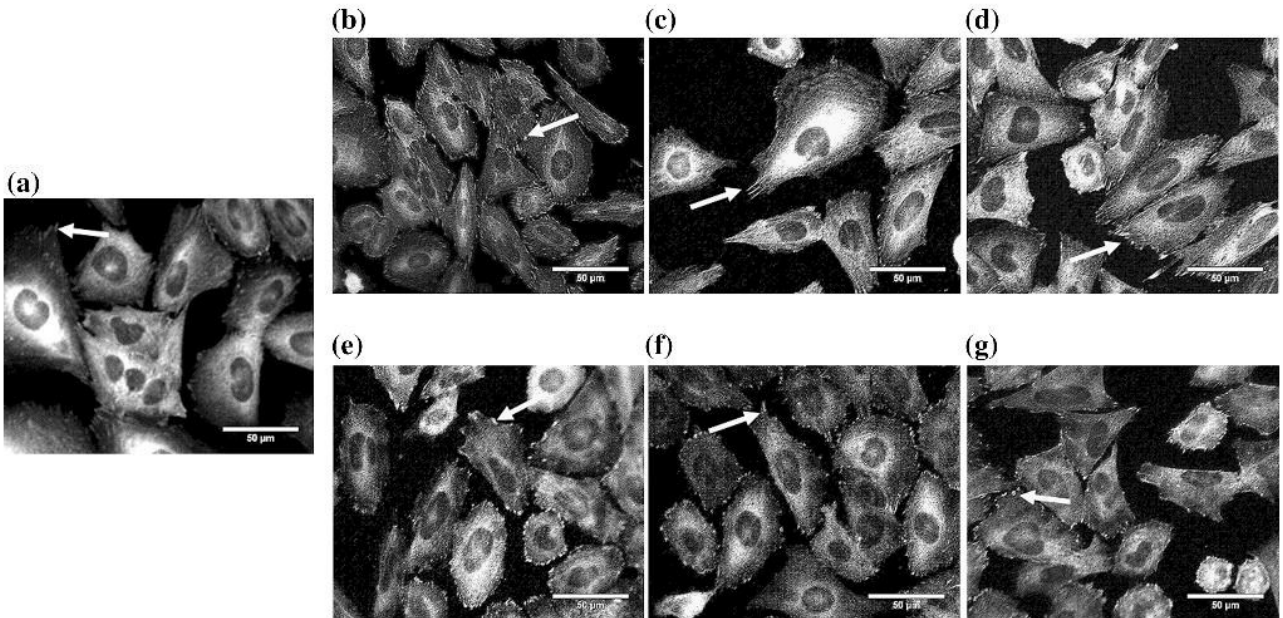


**Fig. 8** Vinculin staining of osteoblasts (SAOS-2) on different substrates after 48 h of cultivation. a PS control, b Z polished sample, c M polished sample, d S polished sample, e Z ground sample, f M ground sample, g S ground sample. Vinculin as a protein of focal

adhesion is stained by indirect immunofluorescent staining (secondary antibody conjugated with AF568). Arrows in the images point to the focal adhesion plaques



This study describes two novel UFG Ti materials with improved mechanical properties and different grain sizes produced by ECAP-Conform. This technique represents a repetitive modification of the standard ECAP, which can significantly reduce the costs of the previously expensive grain-refinement techniques and therefore enables a higher availability of UFG materials for biomedicine [27, 28]. The negligible number of impurities in our employed bulk cpTi Grade 2 (Table 1) is an important input parameter that is often difficult to achieve [29]. Recently, there have been a number of studies of materials that are distinguished for their immense mechanical strength during excessive stress [30, 31]. This report, however, focuses on the fact that implant materials must not only meet the criteria of sufficient tensile strength to fulfill their main purpose in tissue replacement, but they also must have an appropriate level of ductility. A balanced combination of these parameters was achieved in our tested UFG Ti (Fig. 1).

The influence of polishing and grinding on the surface topography of Ti samples characterized by AFM showed that polished samples differed despite the fact that the identical polishing method was used; therefore, grain size influenced the final surface topography after the samples were polished. For examples, AFM image of the sample Mp (Fig. 3) shows many spikes. The size of those spikes corresponds well to the size of Ti grains (4.6  $\mu\text{m}$ ) used for Mp sample preparation. Thus, those spikes can be the top parts of Ti grains drawn into Ti sample, which were not removed during polishing. On the other hand, the surfaces of ground samples were most likely defined by the morphology of the abrasive paper and not by the grain size. The number of different topographical features (pits, peaks, tall objects) could have a strong influence on the adhesion, growth, and morphology of cultivated cells. High amounts of nano-scaled peaks are not recognized by the cells as a rough surface; thus, the cells tend to behave as if they are seeded on a completely flat surface. Moreover, these nano-sized objects appear to have no strong influence on cell behavior [32]. In contrast, many tall micro-scaled objects are considered unsuitable for cell growth because of a lack of places for proper cell attachment [32]. Generally, the combination of nano- and micro-scaled structures is currently considered the most suitable surface topography for supporting cell adhesion and growth [19, 33]. This statement was also approved for in vitro [34] and in vivo dental applications [35]. According to the literature, Ti samples represent usually the surfaces with contact angles around 70°–80° [18, 19, 33]. Significantly lower  $\theta_A$  values (46°–49°) observed for the polished Ti samples in our study resulted from a proper removal of the oily impurities from the machine fabrication. The grinding process provided surfaces with the roughness  $R_{\text{RMS}}$  of two orders higher than that of the polished surfaces. The increasing surface

roughness imprinted on further decrease in  $\theta_A$ . This observation correlates with the literature where wettability increased with increasing roughness of hydrophilic surfaces [36]. This effect is explained by spreading the water drop through the rough features, thus decreasing the values of  $\theta$  [37]. Additionally, Webb et al. [38] confirmed that the hydrophilic character of the materials increases the initial cell attachment and spreading compared to more hydrophobic materials. Although the polished samples were stated to be more hydrophobic compared with the ground samples, both samples had hydrophilic character, with  $\theta$  values of approximately 40°, and should both be favorable for cell attachment.

Based on the cell metabolic activity results, a key observation is that none of the tested Ti samples had a significant negative effect on the metabolic activity of SAOS-2 cells and hMSCs after 48 h of cultivation. All the measured values of metabolic activity were higher than 75 % of the control, which is the value that determines cytotoxicity [39]. We determined that all manufactured types of Ti samples are non-cytotoxic and do not extensively harm the cells. Other authors have shown that more pronounced differences in osteoblast metabolic activity are noticeable after longer incubation times up to 7 days, when the hampered cell–cell communication on the rough surface may depress cell functions and the differences between cells cultivated on different materials may be more evident [40]. Comparing the results of cell number and metabolic activity, despite the high level of initial SAOS-2 cell attachment to the Ti samples, the further growth of cells was slowed. This statement is consistent with the findings of Kubo et al. [41], who found that the number of osteoblasts was dramatically higher on a rugged surface during the first hours of attachment, but that the proliferation rate on the rugged surfaces was lower compared to that on smooth surfaces after 24 h of incubation. Surprisingly, after 48 h of cultivation, the cell number of SAOS-2 on the Ti samples was higher than that on the PS control, but the metabolic activity remained similar on all the tested surfaces (Fig. 4a). This controversy could be explained by the adaptation of the cells to the surface of the Ti samples, accompanied by a slight reduction in metabolic activity during the 48 h of cultivation compared to the PS control, possibly indicating the initiation of the differentiation process, which appears earlier on osteoinductive materials such as Ti than on materials prepared only for optimal cell adhesion and growth [42]. Additionally, an MTS assay is often used as a tool for the assessment of the number of cells [40, 43]; however, we suggest that this assay is not suitable for the present study. To prevent the over- or underestimation of cell growth [44], the MTS assay should be accompanied by a method based on different principles (cell count, protein, or DNA quantification).



The decreased proliferation found in osteoblasts was found also in hMSCs. The decrease in hMSC proliferation could also be the consequence of their adaptation to the ultra-fine topography of the Ti sample surfaces within 48 h or of earlier initiation of differentiation induced by the material.

Although the results showed that the cells on the Ti samples were significantly smaller than those on the PS control, a visual inspection (Fig. 7) demonstrated that they spread on all tested surfaces, evenly forming high-density clusters. However, notably, the hMSCs were isolated from different donors; thus, the results of each measurement were highly dependent on the state of the donor at the time of the biopsy. The possible influence of the material on the size of the cells was also observed by Zinger et al. [45], who found a correlation between rough surface topography and decreased cell area. These authors hypothesized that the rougher the surface, the thicker the cells are as they spread more into the structures and minimally into the horizontal line.

The influence of the material surface topography on the cell morphology and spreading was previously described and confirmed [20, 32, 33]. In our study, we observed that the polished surfaces with nano-topography approaching a flat surface did not force the cells to spread and elongate to find better places to fit. In contrast, the cells cultivated on the rough ground surfaces with a combination of nano- and microstructures were usually elongated or had a greater number of variable shapes as they attempted to cope with the rugged substrate (Fig. 8e–g). The findings of focal adhesions suggest that SAOS-2 cells cultured on the rough surface of the ground samples tend to form focal adhesions on their extensions while they grow and mimic the surface. Smooth topography does not force the cells to exhibit large focal adhesions, and SAOS-2 cells are anchored around their bottom poles (Fig. 8b–d). The same statement was also confirmed for hMSCs. However, their vinculin signal was hardly detectable; thus, the data are not shown.

Taken together, our study highlighted the possibility of a cost-saving fabrication of the mechanically advanced Ti material (Z sample), while maintaining the excellent biological properties of the original Ti (S sample), and the usage of this material in dental implant applications.

## Conclusion

The aim of this work was to evaluate the short-time biological responses of human osteoblasts and mesenchymal stem cells to the newly developed ultra-fine grain Ti materials with enhanced mechanical resistance and long-term performance. Two novel types of the original Ti were produced, and the surfaces of all tested Ti samples were

subsequently treated by polishing or grinding. The samples differed in grain size, final surface topography, and wettability, where the rough ground samples showed increased hydrophilicity compared to the polished samples, irrespective of the grain size. Both cell types attached onto all Ti samples in a significantly higher amount than onto the PS control. Additionally, the cytocompatibility of the Ti samples was evaluated by metabolic activity, and the favorable spreading of osteoblasts confirmed that all the Ti samples had exceptional properties suitable for osteoblast growth and future bone implant development. Although the hMSCs displayed lower cell numbers and metabolic activity compared to osteoblasts, the Ti samples were shown to be suitable surfaces for their growth and possible osteoblast-like differentiation.

The increased strength and longevity of commercially pure Grade 2 Ti are highly demanded dental implant material properties, and the construction of reliable implants remains a topic of discussion. This new ultra-fine grain Ti can successfully compete with the present materials utilized in dentistry due to its balanced mechanical properties which provide high toughness in the stress conditions in the oral cavity while keeping its formability for further processing of various implants. Moreover, its considerably lower production costs and excellent biocompatibility make this Ti an affordable material for subsequent utilization in the development of dental implants.

**Acknowledgements** This work was supported by the projects CZ.1.05/2.1.00/03.0076, CZ.1.05/2.1.00/03, and CZ.1.05/1.1.00/02.0109 of the European Regional Development Fund, National Sustainability Program I (NPU I) Nr. LO1503 provided by the Ministry of Education Youth and Sports of the Czech Republic, project NT/13297-4 provided by Grant Agency of the Ministry of Health of the Czech Republic, project PRVOUK-P24/LF1/3 of First Faculty of Medicine and project PRVOUK P36 of Faculty of Medicine in Pilsen, and the program of support and co-operation of companies and universities in the Pilsen region called “Innovation Vouchers.”

## References

1. Cordova LA, Stresing V, Gobin B, Rosset P, Passuti N, Gouin F et al (2014) Orthopaedic implant failure: aseptic implant loosening—the contribution and future challenges of mouse models in translational research. *Clin Sci (Lond)* 127:277–293
2. Chrcanovic BR, Albrektsson T, Wennerberg A (2014) Immediate nonfunctional versus immediate functional loading and dental implant failure rates: a systematic review and meta-analysis. *J Dent* 42:1052–1059
3. Ren K, Dusad A, Zhang Y, Purdue PE, Fehring EV, Garvin KL et al (2014) Early diagnosis of orthopedic implant failure using macromolecular imaging agents. *Pharm Res* 31:2086–2094
4. Gawkrödger DJ (2003) Metal sensitivities and orthopaedic implants revisited: the potential for metal allergy with the new metal-on-metal joint prostheses. *Br J Dermatol* 148:1089–1093
5. Plecko M, Sievert C, Andermatt D, Frigg R, Kronen P, Klein K et al (2012) Osseointegration and biocompatibility of different

- metal implants—a comparative experimental investigation in sheep. *BMC Musculoskelet Disord* 13:32
6. Browne M, Gregson PJ (2000) Effect of mechanical surface pretreatment on metal ion release. *Biomaterials* 21:385–392
  7. Mishnaevsky L, Levashov E, Valiev RZ, Segurado J, Sabirov I, Enikeev N et al (2014) Nanostructured titanium-based materials for medical implants: modeling and development. *Mater Sci Eng R* 81:1–19
  8. Greger M, Cerny M, Kander L, Kliber J (2009) Structure and properties of titanium for dental implants. *Metallurgija* 48:249–252
  9. Niinomi M (2002) Recent metallic materials for biomedical applications. *Metall Mater Trans A* 33:477–486
  10. Hallab NJ, Anderson S, Caicedo M, Brasher A, Mikecz K, Jacobs JJ (2005) Effects of soluble metals on human peri-implant cells. *J Biomed Mater Res Part A* 74:124–140
  11. Greger M, Kander L, Masek V, Vlcek M (2010) Ultra fine grain titanium using for medical applications—structure and properties. In: *Nanocon 2010, 2nd international conference*, pp 502–507
  12. Yu ZT, Zhang MH, Tian YX, Cheng J, Ma XQ, Liu HY et al (2014) Designation and development of biomedical Ti alloys with finer biomechanical compatibility in long-term surgical implants. *Front Mater Sci* 8:219–229
  13. Schram SE, Warshaw EM, Laumann A (2010) Nickel hypersensitivity: a clinical review and call to action. *Int J Dermatol* 49:115–125
  14. Valiev RZ, Estrin Y, Horita Z, Langdon TG, Zehetbauer MJ, Zhu YT (2006) Producing bulk ultrafine-grained materials by severe plastic deformation. *JOM* 58:33–39
  15. Valiev RZ, Langdon TG (2006) Principles of equal-channel angular pressing as a processing tool for grain refinement. *Prog Mater Sci* 51:881–981
  16. Kubina T, Dlouhy J, Kover M, Domankova M, Hodek J (2015) Preparation and thermal stability of ultra-fine and nano-grained commercially pure titanium wires using conform equipment. *Mater Tehnol* 49:213–217
  17. Kubina T, Dlouhy J, Kover M, Hodek J (2014) Study of thermal stability of ultra fine-grained commercially pure titanium wire prepared in conform equipment. *Metallography Xv* 782:415–420
  18. Estrin Y, Ivanova EP, Michalska A, Truong VK, Lapovok R, Boyd R (2011) Accelerated stem cell attachment to ultrafine grained titanium. *Acta Biomater* 7:900–906
  19. Gittens RA, McLachlan T, Olivares-Navarrete R, Cai Y, Berner S, Tannenbaum R et al (2011) The effects of combined micron-/submicron-scale surface roughness and nanoscale features on cell proliferation and differentiation. *Biomaterials* 32:3395–3403
  20. Teng FY, Ko CL, Kuo HN, Hu JJ, Lin JH, Lou CW et al (2012) A comparison of epithelial cells, fibroblasts, and osteoblasts in dental implant titanium topographies. *Bioinorg Chem Appl* 2012:687–792
  21. Le Guehennec L, Soueidan A, Layrolle P, Amouriq Y (2007) Surface treatments of titanium dental implants for rapid osseointegration. *Dent Mater* 23:844–854
  22. Weber HP, Cochran DL (1998) The soft tissue response to osseointegrated dental implants. *J Prosthet Dent* 79:79–89
  23. Rezek B, Ukraintsev E, Kratka M, Taylor A, Fendrych F, Mandys V (2014) Epithelial cell morphology and adhesion on diamond films deposited and chemically modified by plasma processes. *Biointerphases* 9:031012
  24. Pop-Georgievski O, Kubies D, Zemek J, Neykova N, Demianchuk R, Mazl Chanova E et al (2015) Self-assembled anchor layers/polysaccharide coatings on titanium surfaces: a study of functionalization and stability. *Beilstein J Nanotechnol* 6:617–631
  25. Schneider CA, Rasband WS, Eliceiri KW (2012) NIH Image to ImageJ: 25 years of image analysis. *Nat Methods* 9:671–675
  26. Carpenter AE, Jones TR, Lamprecht MR, Clarke C, Kang IH, Friman O et al (2006) Cell Profiler: image analysis software for identifying and quantifying cell phenotypes. *Genome Biol* 7:R100
  27. Dyakonov GS, Gu CF, Toth LS, Valiev RZ, Semenova IP (2014) Microstructure and mechanical properties of continuous equal channel angular pressed titanium. In: 6th international conference on nanomaterials by severe plastic deformation (Nanospd6), vol. 63
  28. Polyakov AV, Semenova IP, Valiev RZ (2014) High fatigue strength and enhanced biocompatibility of UFG CP Ti for medical innovative applications. In: 6th international conference on nanomaterials by severe plastic deformation (Nanospd6), vol. 63
  29. Li HL, Oppenheimer SM, Stupp SI, Dunand DC, Brinson LC (2004) Effects of pore morphology and bone ingrowth on mechanical properties of microporous titanium as an orthopaedic implant material. *Mater Trans* 45:1124–1131
  30. Mall S, Cunningham SR (2007) Fatigue behavior of integrally fabricated joints between titanium matrix composite and titanium alloy. *Compos Struct* 80:65–72
  31. Zhao XC, Fu WJ, Yang XR, Langdon TG (2008) Microstructure and properties of pure titanium processed by equal-channel angular pressing at room temperature. *Scr Mater* 59:542–545
  32. Broz A, Baresova V, Kromka A, Rezek B, Kalbacova M (2009) Strong influence of hierarchically structured diamond nanotopography on adhesion of human osteoblasts and mesenchymal cells. *Phys Status Solidi A* 206:2038–2041
  33. Chen XY, Cai KY, Lai M, Zhao L, Tang LL (2012) Mesenchymal stem cells differentiation on hierarchically micro/nano-structured titanium substrates. *Adv Eng Mater* 14:B216–B223
  34. Naddeo P, Laino L, La Noce M, Piattelli A, De Rosa A, Iezzi G et al (2015) Surface biocompatibility of differently textured titanium implants with mesenchymal stem cells. *Dent Mater* 31:235–243
  35. Elias CN, Fernandes DJ, Resende CRS, Roestel J (2015) Mechanical properties, surface morphology and stability of a modified commercially pure high strength titanium alloy for dental implants. *Dent Mater* 31:E1–E13
  36. Garbassi F, Mora M, Ochiello E (1994) *Polymer surfaces: from physics to technology*, 1st edn. Wiley, New York
  37. Pisonnet L, Reybier K, Jaffrezic N, Comte V, Lagneau C, Lissac M et al (2003) Relationship between surface properties (roughness, wettability) of titanium and titanium alloys and cell behaviour. *Mater Sci Eng C* 23:551–560
  38. Webb K, Hlady V, Tresco PA (1998) Relative importance of surface wettability and charged functional groups on NIH 3T3 fibroblast attachment, spreading, and cytoskeletal organization. *J Biomed Mater Res* 41:422–430
  39. Flahaut E, Durrieu MC, Remy-Zolghadri M, Bareille R, Baquay C (2006) Investigation of the cytotoxicity of CCVD carbon nanotubes towards human umbilical vein endothelial cells. *Carbon* 44:1093–1099
  40. Zhao LZ, Mei SL, Chu PK, Zhang YM, Wu ZF (2010) The influence of hierarchical hybrid micro/nano-textured titanium surface with titania nanotubes on osteoblast functions. *Biomaterials* 31:5072–5082
  41. Kubo K, Tsukimura N, Iwasa F, Ueno T, Saruwatari L, Aita H et al (2009) Cellular behavior on TiO<sub>2</sub> nanonodular structures in a micro-to-nanoscale hierarchy model. *Biomaterials* 30:5319–5329
  42. Klein MO, Bijelic A, Toyoshima T, Gotz H, von Koppenfels RL, Al-Nawas B et al (2010) Long-term response of osteogenic cells on micron and submicron-scale-structured hydrophilic titanium surfaces: sequence of cell proliferation and cell differentiation. *Clin Oral Implant Res* 21:642–649
  43. Guida L, Oliva A, Basile MA, Giordano M, Nastri L, Annunziata M (2013) Human gingival fibroblast functions are stimulated by oxidized nano-structured titanium surfaces. *J Dent* 41:900–907

44. Maghni K, Nicolescu OM, Martin JG (1999) Suitability of cell metabolic colorimetric assays for assessment of CD4+ T cell proliferation: comparison to 5-bromo-2-deoxyuridine (BrdU) ELISA. *J Immunol Methods* 223:185–194
45. Zinger O, Anselme K, Denzer A, Habersetzer P, Wieland M, Jeanfils J et al (2004) Time-dependent morphology and adhesion of osteoblastic cells on titanium model surfaces featuring scale-resolved topography. *Biomaterials* 25:2695–2711

C. **Lucie Ostrovská**, Antonín Brož, Anna Fučíková, Tereza Bělinová, Hiroshi Sugimoto, Takashi Kanno, Minoru Fujii, Jan Valenta, Marie Hubálek Kalbáčová (2016): **The impact of doped silicon quantum dots on human osteoblasts**. RSC ADVANCES 6, 63403-63413. IF = 2.936





Cite this: *RSC Adv.*, 2016, 6, 63403

## The impact of doped silicon quantum dots on human osteoblasts

Lucie Ostrovska,<sup>ab</sup> Antonin Broz,<sup>bc</sup> Anna Fucikova,<sup>d</sup> Tereza Belinova,<sup>e</sup> Hiroshi Sugimoto,<sup>f</sup> Takashi Kanno,<sup>f</sup> Minoru Fujii,<sup>f</sup> Jan Valenta<sup>d</sup> and Marie Hubalek Kalbacova<sup>\*ab</sup>

Silicon (Si) nanostructures allow for the expansion of the application spectrum of this important semiconductor material with respect to the fields of optoelectronics and photonics. At the same time, the significant potential of Si quantum dots (SiQDs) has been revealed in terms of their potential application in the areas of biology and medicine due to their biocompatibility, low toxicity and natural biodegradability, unlike currently used semiconductor quantum dots. As far as this study is concerned, SiQDs co-doped with boron and phosphorus were used for the *in vitro* evaluation of their cytotoxicity in human osteoblasts. Two chemically identical types of SiQD differing in terms of their size and photoluminescence (PL) were studied. They both display long-lasting dispersion in methanol and even in aqueous media as well as PL which is not sensitive either to changes in the environment or surface modifications. Our experiments revealed significant differences between the two types of SiQD tested in regard to their behavior in a cell culture environment depending on increasing concentration (25–125  $\mu\text{g ml}^{-1}$ ) and cultivation conditions (the presence or absence of proteins from the fetal bovine serum – a component of the cultivation medium). A detailed description of their optical parameters and the evaluation of zeta potential enhance the understanding of the complexities of the *in vitro* results obtained.

Received 3rd June 2016  
Accepted 26th June 2016

DOI: 10.1039/c6ra14430f

[www.rsc.org/advances](http://www.rsc.org/advances)

### 1 Introduction

Various types of nanoparticles have been studied and used in different fields of science including their application in the field of bio-medicine. In general, nanoparticles (so-called quantum dots – QD) based on a variety of materials provide a promising tool with regard to potential as drug and gene carriers and as imaging and diagnostic platforms.

Silicon-based nanoparticles make up one of the most promising platforms yet determined for medicinal application due to their high level of biocompatibility and biodegradability which arise from the fact that silicon (Si) is an essential trace element in the human body. Currently, the development of various types of Si-based nanoparticles is focused principally on silica (SiO<sub>2</sub>) and pure silicon materials which are biodegradable

due to the nature of their Si–Si and Si–O bonds.<sup>1,2</sup> In addition, it is essential to note that most Si-based nanoparticles possess the quality of fluorescence (photoluminescence) and therefore facilitate their own imaging without any additional intervention into their structure being required.<sup>3,4</sup> Moreover, their dispersibility in aqueous solutions is also crucial for bio-application.<sup>5</sup> Such properties are similar to the afore-mentioned QDs, thus the term silicon quantum dots (SiQD) is particularly appropriate.

This study is concerned particularly with the assessment of cytotoxicity since this makes up the most important initial step preceding the actual application of any of the materials studied in terms of human medicine. Previous studies have shown that the cytotoxicity of Si-based nanoparticles is influenced by a range of properties such as particle shape, size, zeta potential, dose and chemical composition<sup>6–12</sup> and some of these properties may play a role in the formation of so-called biomolecular coronas. This term describes a layer of biomolecules, mainly proteins (protein corona), originating from the biological environment surrounding nanoparticles which accord them a new identity which differs from that of bare nanoparticle in terms of a number of characteristics especially their reaction with organisms.<sup>13,14</sup> Generally, the concept of the protein corona is given as a biological identity *via* which nanoparticles are presented to cells. It has been suggested that the presence, and possibly the composition, of the protein corona provides the key

<sup>a</sup>Biomedical Center, Faculty of Medicine in Pilsen, Charles University in Prague, Pilsen, Czech Republic. E-mail: [marie.kalbacova@lf1.cuni.cz](mailto:marie.kalbacova@lf1.cuni.cz)

<sup>b</sup>Institute of Inherited Metabolic Disorders, 1st Faculty of Medicine, Charles University in Prague, Prague, Czech Republic

<sup>c</sup>Institute of Physiology, Academy of Sciences of the Czech Republic, Prague-Krč, Czech Republic

<sup>d</sup>Faculty of Mathematics and Physics, Prague, Czech Republic

<sup>e</sup>Department of the Cell Biology, Faculty of Science, Charles University in Prague, Prague, Czech Republic

<sup>f</sup>Department of Electrical and Electronic Engineering, Graduate School of Engineering, Kobe, Japan



to the determination of the cytotoxicity of nanoparticles.<sup>15,16</sup> *In vivo*, the composition of the attached proteins is spatial (lung fluids, bloodstream) and time dependent and, moreover, the condition of the living organism should be considered.<sup>16</sup> On the other hand, *in vitro* conditions are limited by the presence of certain types of proteins contained within the selected supplemented serum; thus, it appears that the protein corona is not subject to the same degree of significant dynamic change in composition as it is *in vivo*.<sup>17</sup>

Previous studies that have focused on the impact of silica nanoparticles (SiO<sub>2</sub> NPs) on keratinocytes revealed that the viability of cells is both dose- and size-dependent and, in addition, that this particular type of particle causes damage to the cellular membrane which may be of either chemical or mechanical stress origin.<sup>7,8</sup> It has been proposed that cytotoxicity caused by SiO<sub>2</sub> NPs may be the result of oxidative stress induced by the production of intracellular reactive oxygen species.<sup>11,18</sup> However, when compared to other types of nanoparticles, e.g. ZnO particles, SiO<sub>2</sub> NPs reveal lower cytotoxicity levels dependent on the cell type.<sup>7,9,19</sup> Moreover, a number of papers has reported a significant correlation between cytotoxicity and the dose of Si-based nanoparticles (irrespective of the actual concentration range used for a particular cellular type). Generally, the higher the nanoparticle dose applied to the cells, the higher is the cytotoxicity observed following a certain period of time, an example of which is provided by studies by Bhattacharjee *et al.* wherein increasing concentrations from 0.1 ng ml<sup>-1</sup> to 100 µg ml<sup>-1</sup> of nanoparticles were added to a cell culture of NR8383 macrophages. The same cytotoxicity trend was also evident with respect to keratinocytes, although the concentrations applied were significantly higher (25–500 µg ml<sup>-1</sup>).<sup>8,10,11</sup> It is possible to obtain a better understanding of the causes of the cytotoxicity of particular nanoparticles by means of a description of specific cell-nanoparticle interactions.

It is widely accepted that nanoparticles of different types enter cells by means of endocytosis, *i.e.* a form of active transport; however, the specific ways in which individual particles enter certain cell types remain to be discovered. Considerable interest has been devoted to the discovery of principal nanoparticle uptake pathways and most of the experiments conducted in this respect were performed *via* the selective gradual blocking of different pathways and the subsequent determination of which was most frequently used. Clathrin- and caveolin-dependent endocytotic pathways have been suggested as the main routes used by silicon-based particles; however, a number of studies also suggest the use of the flotillin-dependent pathway.<sup>12,20</sup> It has been implied that the principal pathway is determined not only by particle size and shape but also by cellular type. It is important to gain an understanding of all the interactions which take place between cells and nanoparticles so as to avoid any harmful effects in terms of potential use in human medicine.

This study employed two types of SiQD of different characteristics (SiQD 1050 – 3 nm size, 750 nm peak emission and SiQD 1100 – 4 nm size, 850 nm peak emission) and their influence on a biological system represented by a human osteoblast-like cell line (SAOS-2) was compared. The main focus

of the study was (i) to determine the appropriate concentration of both types of SiQD based on the induced cytotoxicity and (ii) to evaluate the cellular uptake of both SiQDs at 2, 6 and 24 hours by means of fluorescence wide-field and confocal microscopy. The influence of the presence of fetal bovine serum (FBS) in the cultivation media made up an important variable parameter in terms of understanding the impact of the protein corona on SiQD behavior *in vitro*.

## 2 Experimental

### 2.1 The fabrication of co-doped SiQDs

P and B co-doped colloidal Si QDs were synthesized by means of a previously reported procedure.<sup>21,22</sup> Si-rich borophosphosilicate (BPSG) films were deposited on thin stainless steel plates *via* the co-sputtering of Si, SiO<sub>2</sub>, B<sub>2</sub>O<sub>3</sub>, and P<sub>2</sub>O<sub>5</sub> using the rf-sputtering apparatus. The films were then peeled from the plates and crushed to powder form in a mortar. The powder was then annealed at different temperatures (1050 °C and 1100 °C thus obtaining SiQD 1050 and SiQD 1100 respectively) in an N<sub>2</sub> gas atmosphere for 30 minutes so as to cultivate SiQDs of differing size in BPSG matrices. During the growth of the SiQDs, P and B atoms were incorporated into Si-NCs from the BPSG matrices.

### 2.2 The detailed optical characterization of co-doped Si-QD

Transmission electron microscopy images were obtained using JEOL JEM-200CX, and the IR absorbance of the suspensions measured by means of drop-casting on a gold covered silicon substrate in an FT-IR spectrometer (Perkin Elmer, Spectrum GX). UV-VIS spectra were measured by UV-3101PC (Shimadzu). The PL spectra (Fig. 1d) were obtained using a spectrofluorometer (Fluorolog-3, Horiba Jobin-Yvon).

The photoluminescence external quantum yield (EQY) of the SiQD suspensions was measured in specially-designed equipment based on an integrating sphere.<sup>23</sup> Excitation wavelengths were tuned over a broad spectral range from UV to yellow using either a set of light-emitting diodes or a white-light emitting laser-driven light source (LDLS, Energetiq) coupled to a 15 cm monochromator. The absorption cross-section  $\sigma$  was obtained by means of the intensity-dependent PL-modulation technique applied to a thin liquid layer of SiQD in methanol.<sup>24</sup> Under 405 nm excitation and an emission between 700 and 900 nm,  $\sigma$  was determined at around  $3 \times 10^{-16}$  cm<sup>2</sup> for both of the samples studied.

The PL kinetics of SiQDs under high-repetition short pulses (simulating the conditions of a confocal microscope with a “white” fiber laser) were tested for SiQD 1050 in a cuvette excited *via* a pulsed diode laser at 408 nm (pulse duration below 0.1 ns, 20 MHz repetition rate and 840 W cm<sup>-2</sup> power density) (Fig. 3b).

### 2.3 Zeta-potential assessment

$\zeta$  was measured using a Malvern Zetasizer Nano ZS equipped with MPT-2 titration unit where 0.25 M NaOH, 0.2 M HCl and 0.02 M HCl were used as titration agents. The SiQD suspensions were titrated in the acid to base and base to acid direction.



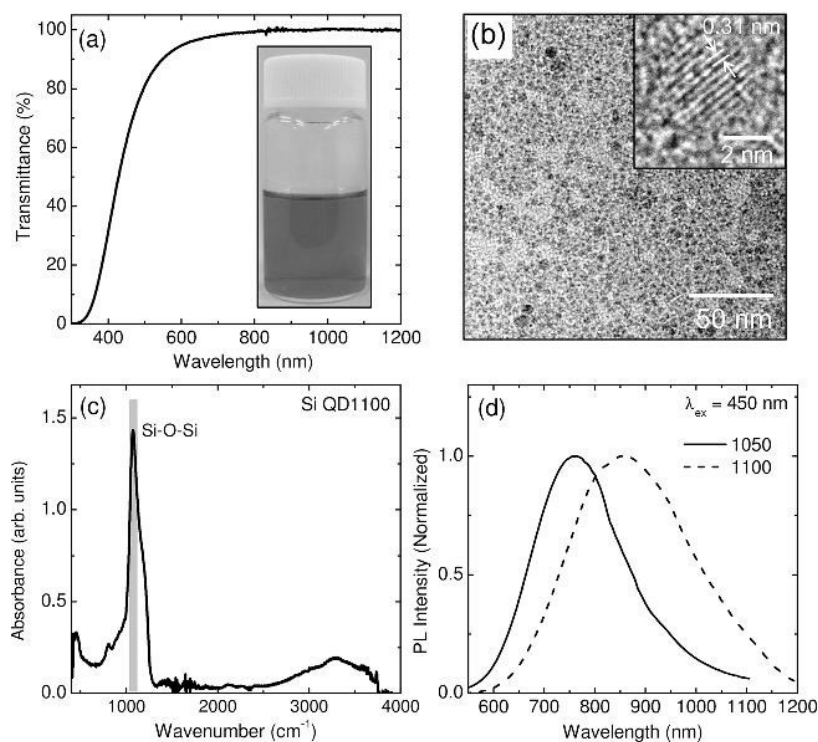


Fig. 1 (a) Optical transmittance spectrum and photograph of colloidal dispersion (methanol) of SiQD 1100; (b) TEM image of SiQD 1100, inset: high-resolution TEM image of a QD with lattice fringes corresponding to {111} plane of Si crystals; (c) IR absorption spectrum of SiQD 1100; (d) PL spectra of SiQD 1050 and 1100 (d).

## 2.4 Cell cultivation with SiQDs

SAOS-2 cells (DSMZ, Germany) were cultured in McCoy's 5A medium without phenol red (HyClone) and supplemented with 10 000 U ml<sup>-1</sup> penicillin (Sigma-Aldrich) and 10 µg ml<sup>-1</sup> streptomycin (Sigma-Aldrich) and, in some of the experiments, with 15% fetal bovine serum (Biosera). The cells were seeded at a density of 10 000 cells per cm<sup>2</sup> onto a 96-well plate (Techno Plastic Products) in triplets for the measurement of cytotoxicity (100 µl) or onto cell imaging dishes with a 145 µm glass bottom in singlets (Eppendorf) for microscopy purposes (500 µl). The cells were cultured for 24 hours in a humidified 5% CO<sub>2</sub> atmosphere at 37 °C.

The required amount of SiQD colloid in pure methanol was added to an equal amount of distilled water and the resulting mixture was subsequently incubated in a dry bath incubator (Major Science) set to 70 °C until half of the liquid had evaporated. The final SiQD colloid was ready for immediate dilution into the appropriate cultivation media. Two types of cultivation media were used in the experiments – McCoy's 5A medium without phenol red (HyClone) with 10 000 U ml<sup>-1</sup> penicillin (Sigma-Aldrich) and 10 µg ml<sup>-1</sup> streptomycin (Sigma-Aldrich) with no serum proteins (serum-free) or supplemented with 5% fetal bovine serum (Biosera) (serum-supplemented). The final concentrations of SiQD in the media used for cell treatment consisted of 125 µg ml<sup>-1</sup>, 50 µg ml<sup>-1</sup> and 25 µg ml<sup>-1</sup>.

The cells were gently rinsed with phosphate buffer saline (PBS) prior to the addition of the cultivation media containing SiQDs. Subsequently, the cells were cultivated to different time

points depending on the type of assessment. In the case of the serum-free media, an additional volume of 50 µl (96-well plate) or 250 µl (cell imaging dish) of the medium with 5% FBS was added after 6 hours of cultivation and cultivated for an additional 18 hours or 42 hours (in the case of 24 hours or 48 hours of cultivation time respectively).

## 2.5 Cytotoxicity assessment

The cytotoxicity of various concentrations of SiQDs in different media was assessed by means of the measurement of the metabolic activity of the cells at 6, 24 and 48 hours following the addition of SiQDs to the cells. Assessment was performed by means of MTS assay (Cell Titer96® AqueousOne, Promega). The principle of this colorimetric assay consists of the reduction of an MTS ((3-(4,5-dimethylthiazol-2-yl)-5-(3-carboxymethoxyphenyl)-2-(4-sulfophenyl)-2H-tetrazolium)) compound into a soluble colored formazan product *via* mitochondrial dehydrogenases. The assay was performed according to the manufacturer's instructions. The cells were rinsed three times with PBS and then incubated for 2 hours with an MTS reagent diluted in the appropriate media. Optical density was measured using a microplate reader (Synergy H1, BioTek) at 490 nm subtracting the background at 655 nm. The subtraction of blank values was conducted for each type of medium separately. All the results obtained were compared to the results of the control cells cultivated in a medium supplemented with 5% FBS; the results were expressed as percentages.



## 2.6 Fluorescence wide-field and confocal microscopy

After 2, 6 and 24 hours the cells were rinsed three times with PBS so as to remove any un-internalized SiQDs and then fixed in 4% paraformaldehyde. An Eclipse Ti-S epi-fluorescence microscope (Nikon) with Mercury Arc Lamp Intensilight HGF1 and equipped with DS-Qi1Mc digital camera (Nikon) was used in order to acquire 2D fluorescence images of SiQDs at an excitation wavelength of 330–380 nm and emission wavelength of 510–590 nm. The extent of the penetration of SiQDs in the z-axis of the cells was analyzed with respect solely to the 24 hour samples by means of a Leica TCS SP8X confocal laser scanning microscope (Leica Microsystems). The SiQDs were excited using a pulse continuum white light laser (475–499 nm, 80 MHz) and emissions were collected *via* a hybrid detector at 700–795 nm. The elimination of cell autofluorescence from SiQD signals was achieved by the gating of signal detection with a 5 ns delay from the excitation pulse while maintaining a detection width of 7 ns. Multiple line accumulation scanning and prolonged pixel dwell were set so as to allow for the more intense and precise imaging of the SiQDs. All the confocal 3D images were acquired by means of a Leica DFC365 FX monochrome digital CCD camera and further analyzed using LAS X core software (Leica Microsystems). The confocal images were processed using Hyugens software for deconvolution and maximum intensity projection. ImageJ software was subsequently used for contrast and smoothness correction purposes.

## 2.7 Statistical analysis

All the data presented was derived from three independent experiments performed in triplicate. The results are presented in the form of mean values with error bars indicating standard deviations. Data distribution was evaluated using the Shapiro–Wilk test. The nonparametric Wilcoxon matched pairs test was used in order to determine significant differences between the datasets and the control with 5% FBS and the rest of the variables. An ANOVA was used to compare differing SiQD concentrations at certain time points with each other. *p* values of less than 0.05 were considered statistically significant. Extreme values were excluded from the analysis. Statistical analysis was performed using STATISTICA (StatSoft, Inc.) software.

# 3 Results and discussion

## 3.1 The optical characterization of co-doped SiQD

Phosphorus (P) and boron (B) co-doped colloidal SiQDs were synthesized by means of a previously reported procedure.<sup>21,22</sup> The transmittance spectrum and an image of the colloid are shown in Fig. 1a. Transmittance around the band gap of bulk Si crystal ( $\sim 1100$  nm) is almost 100%, which indicates the absence of significant light scattering by QD agglomerates. Fig. 1b shows a transmission electron microscope (TEM) image demonstrating a QD monolayer without the formation of three-dimensional agglomerates. Fig. 1c shows an infrared (IR) absorption spectrum of SiQD 1100 stored in methanol for 60 days. An absorption peak at  $\sim 1080$   $\text{cm}^{-1}$  assigned to Si–O–Si stretching vibrations can be clearly observed while no

absorption peak is evident from C–H<sub>x</sub> ( $\sim 2900$   $\text{cm}^{-1}$ ). This suggests that following long-term storage in methanol, the surface of SiQDs is terminated principally by oxygen. After around one month's storage in methanol, the photoluminescence (PL) spectra of SiQD 1050 and 1100 under excitation at 450 nm exhibit PL peaks of around 750 and 850 nm respectively (Fig. 1d). The size-dependence of the PL peak wavelength of B and P co-doped Si QDs has already been studied in detail.<sup>25</sup>

With respect to the imaging of SiQD in cell cultures by means of fluorescence microscopy (wide-field or confocal), the presence of so-called autofluorescence (AF) – *i.e.* the natural fluorescence of cell proteins and other molecules without artificial staining must be considered. AF usually peaks in green but extends far into the red spectral region in which it overlaps with the PL of the tested SiQDs. This is illustrated in Fig. 2 which shows the local PL spectra of the AF and PL of SiQD 1100 under excitation by means of a laser at 405 nm. In general, three measures can be applied so as to improve the ratio of SiQD PL *versus* AF:

(i) The shifting of the excitation wavelength into the green region (*e.g.* the Ar-ion laser line at 488 nm) since AF decreases faster with red-shift excitation than does SiQD PL.

(ii) The selection of SiQDs with an emission peaking at long wavelengths where AF disappears but where microscope detectors remain efficient; this usually means between 700 and 800 nm.

(iii) The use of different PL decay kinetics under pulsed excitation. While AF decays within a few nanoseconds, SiQDs have a lifetime in the order of tens of microseconds. Therefore, gated detection can be applied which is delayed following pulsed excitation by around 5 ns. Fig. 3a shows the slow rate of PL decay for both the SiQD samples and Fig. 3b illustrates that PL decay under excitation by sub-ns pulse with high repetition rate (20 MHz – such a degree of excitation is deliverable by a large number of currently available confocal microscopes) was unable to follow the pulse sequence and thus quasi-constant PL was detected – the yellow rectangle indicates the temporal position of the detection gate (delay 5–12 ns) as used later in this paper (such excitation and detection options are available in a large number of the current models of confocal microscopes).

Finally, we draw attention to the aging of the luminescence properties of SiQDs. During long-term storage (around 1 year) a slow change in the PL peak position and the external quantum yield (EQY) can be observed in methanol suspensions of SiQDs, which is further accelerated in water-based suspensions used in bio-studies. Both types of SiQD exhibit a blue-shift and the EQY changes as illustrated in Fig. 2c roughly following a curve which has a maximum EQY of 12% for a peak at 750 nm (similar optimal conditions were reported by Liu *et al.*).<sup>26</sup> Such optimum conditions for fluorescence imaging are characteristic of fresh SiQD 1050 samples; however, upon aging such samples degrade in terms of EQY while SiQD 1100 shifts to the optimum position (a shift from 850 nm to 750 nm). In brief, it is essential that aging properties are characterized in order to be able to anticipate PL evolution and select the ideal sample.



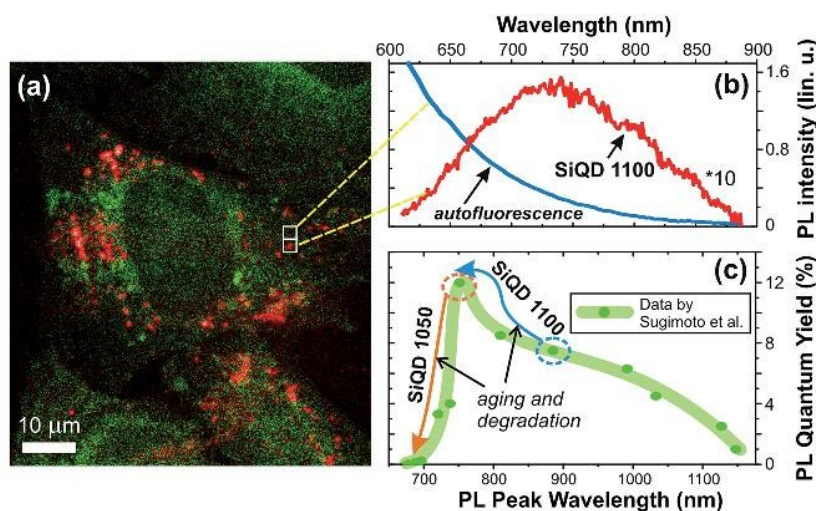


Fig. 2 Wide-field fluorescence microscopy and spectroscopy under cw excitation at 405 nm: (a) combined fluorescence image with the green layer showing the full signal (dominated by cell autofluorescence) and the orange layer showing signal above 785 nm (dominated by SiQD luminescence). The vertical stripe shows area of the spectrometer slit introduced for spectral measurements. (b) Luminescence spectrum of cell autofluorescence (blue) and emission of SiQD cluster (red line) from area indicated by a rectangle in the panel (a). The autofluorescence signal estimated from area around the SiQD cluster was subtracted and spectral shape corrected to the sensitivity of the experimental apparatus. The peak is around 730 nm. (c) Observed shift of PL peak and quantum yield of SiQDs with time is plotted together with data from the paper by Sugimoto *et al.*<sup>20</sup> The slow changes due to aging of SiQD suspensions in methanol are accelerated in water based media during bio-studies. The data (green line and points) on PL QY dependence on PL peak position (size of QDs) explains well why SiQD 1100 sample is well observed in cell cultures while luminescence of SiQD 1050 vanishes.

### 3.2 Zeta potential assessment

The zeta potential ( $\zeta$ ) of water suspensions of SiQD 1050 and 1100 as a function of pH was determined using 0.25 M NaOH, 0.2 M HCl and 0.02 M HCl titration agents. The SiQDs had been titrated in the acid  $\rightarrow$  base and base  $\rightarrow$  acid direction (Fig. 4). The iso-electric point of both samples was determined at around pH 2. While SiQD 1100 reacted relatively smoothly to changes in pH, the SiQD 1050 reaction to the addition of acid/base was slow and followed by sudden jumps in  $\zeta$ . Moreover, a two-peak distribution of  $\zeta$  was observed for SiQD 1050 at each pH point (Fig. 4d) indicating the presence of distinct SiQD fractions. For a pH of 7.5 (the value relevant to biological experiments) the mean value of  $\zeta$  was around  $-64$  mV ( $-16$  mV for the smaller peak) for SiQD 1050 and  $-57$  mV for SiQD 1100 (with an uncertainty of around 8 mV).

### 3.3 The effect of different SiQD concentrations on cell metabolic activity in serum-supplemented and serum-free media

Osteoblastic cells were cultivated in a medium supplemented with 5% fetal bovine serum (5% FBS-medium) with gradually increasing concentrations (25, 50 and 125  $\mu\text{g ml}^{-1}$ ) of two types of SiQD which was followed by the determination of their metabolic activity after 6, 24 and 48 hours (Fig. 5a and b). It is apparent that SiQD 1100 in a fully-supplemented medium had no impact on cell metabolic activity irrespective of concentration at the 6 hour time point; however, after 24 hours the highest concentration of SiQD 1100 decreased cell activity significantly and, after 48 hours, the medium concentration was seen to have a similar effect.

On the other hand, SiQD 1050 (lowest and medium concentrations) surprisingly increased cell metabolic activity after 6 hours and, after 24 hours of incubation, the metabolic activity of SiQD 1050-treated cells was comparable to that of controls with no treatment. Only after 48 hours did the highest concentration of SiQD 1050 significantly decrease cell metabolic activity.

In order to distinguish between the effect of SiQDs and the role of the protein corona (originating from serum proteins), osteoblastic cells were cultivated in a medium containing no supplements (serum free – 0% FBS-medium). The same concentrations of SiQDs were then added and the same tests performed as described above (under standard conditions). It is apparent (Fig. 5c and d) that the serum-free medium only (with no SiQDs) had a negative effect on cell metabolic activity at the 6 hour time point; however, the decrease was not so strong as to be considered cytotoxic.<sup>27</sup>

Those cells treated in the serum-free medium with the lowest and medium concentrations of SiQD 1100 exhibited a metabolic activity level similar to the control sample (cells cultivated in a 5% FBS-medium) and only in the highest SiQD concentration did cell activity decrease significantly to the cytotoxic level after 6 hours (in contrast to standard conditions). Subsequently, after 24 hours, both the medium and the highest concentrations of SiQD 1100 were found to strongly affect cell activity and, finally (after 48 hours) all the tested concentrations of SiQD 1100 in the serum-free medium were determined as being cytotoxic.

On the other hand, SiQD 1050 did not affect cell behavior at any concentration after 6 hours; however, after 24 hours of incubation, all the tested concentrations were found to be



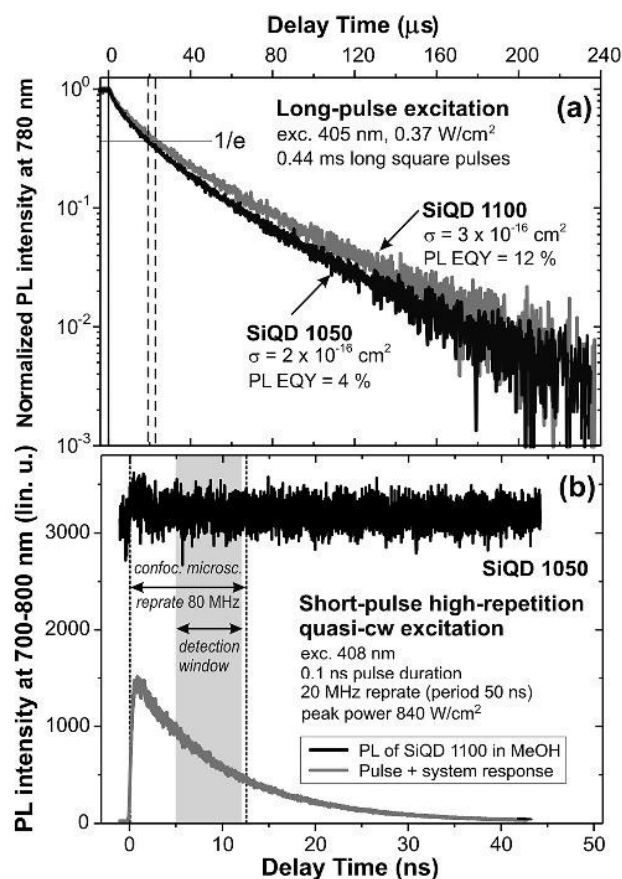


Fig. 3 (a) Kinetics of PL decay under long square pulses and (b) short high-repetition rate (quasi-cw) excitation. The conditions applied in the confocal imaging (80 MHz repetition rate, detection window of 7 ns delayed by 5 ns) is indicated by the yellow rectangle.

cytotoxic, the level of which was further enhanced following 48 hours of incubation.

### 3.4 The microscopy assessment of SiQD effects on cell morphology and metabolic activity in serum-supplemented and serum-free media

Osteoblasts were treated with  $50 \mu\text{g ml}^{-1}$  of SiQD 1050 and SiQD 1100 (medium concentration) in a 5% FBS-medium for 2, 6 and 24 hours and then visualized by means of wide-field fluorescence microscopy accompanied by a phase contrast for the more precise localization of the SiQD fluorescence signal within the cells (Fig. 6a and b). Confocal microscopy images of cells treated with the same SiQD concentrations were acquired at the 24 hour time point only (Fig. 6c and d).

Fig. 6a shows that a very bright fluorescence signal is visible in those cells treated with SiQD 1100 as soon as after 2 hours and that it is even stronger at the 6 hour time point. However, it is apparent from the phase contrast image that the signal originates from a culture medium in which aggregates of SiQD with proteins originating within the FBS had formed and not from the cells themselves. After 24 hours, the fluorescence signal of SiQD 1100 is apparent from inside the cells as well as

from the culture medium itself. The confocal image (Fig. 6c) taken at the same time confirms the localization of these SiQDs inside cells in a vesicular form with no apparent changes in cell morphology. In addition, cell metabolic activity tests (Fig. 8a) indicated that these SiQDs had no negative impact on the cells at the same time point; only after 48 hours of incubation did the SiQD 1100 cause a significant decrease in cell metabolic activity but not to such an extent as to include cytotoxic effects.<sup>27</sup>

In the case of SiQD 1050 an even stronger fluorescence signal of SiQD and proteins in the cultivation medium was detected after 6 hours but only a very weak signal could be detected in the cells after 24 hours (Fig. 6b). The image of cells treated with SiQD 1050 for 24 hours presented was intentionally selected so as to show the cells in the region not totally covered with SiQD-protein aggregates; notwithstanding, most of the sample area was found to be covered with these foggy aggregates. This observation was confirmed by means of confocal imaging (Fig. 6d) which revealed a weak fluorescence signal distributed diffusely within the cells (autofluorescence) and a concentrated signal issuing from the culture medium in which SiQD 1050 aggregates and FBS proteins were formed. Indeed, this corresponds well with the data presented in Fig. 8b according to which no reduction in metabolic activity (compared to the untreated control in the 5% FBS-medium) was detected in either evaluation using the same concentration of SiQD 1050.

Subsequently, the same experiments were performed with using the serum-free medium (0% FBS-medium). Fig. 7a shows that a fluorescence signal is visible in those cells treated with SiQD 1100 as soon as after 2 hours of incubation and it is even stronger at the 6 hour point at which all the cells exhibit a fluorescence signal. After 24 hours, SiQD and protein aggregates were visible in the medium. The proteins originated from the FBS added to the culture medium after 6 hours due to the cells being unable to survive (*i.e.* to avoid significant behavioral changes) any longer without the addition of FBS. It was expected that all the SiQDs would already have entered the cells by this time point and that they would no longer be present in the medium. However, microscope images demonstrate that after 6 hours a certain amount of SiQD 1100 was still present in the medium available to react with the FBS proteins. Nevertheless, SiQD 1100 were present on a massive scale inside the cells at 24 hours (Fig. 7a) and had a negative impact on cell morphology; moreover, this led to a significant decrease in cell metabolic activity (Fig. 8a). The confocal image (Fig. 7c) confirms the presence of high quantities of SiQD 1100 inside the cells in the diffused form which is in contrast to the localization of SiQD 1100 in those cells cultivated in the 5% FBS-medium (Fig. 6c). Results concerning metabolic activity indicate that the cells were dying at a rapid rate at the 24 hour point and had died at the 48 hour time point.

Conversely, SiQD 1050 were practically invisible at all time points in those cells cultivated in the serum-free medium; a very faint signal was detectable at the 2 hour time point which disappeared over time (Fig. 7b). The wide-field microscopy data was confirmed by the confocal images in which the fluorescence signal was very faint and originated from cell autofluorescence. However, the results presented in Fig. 8b suggest that

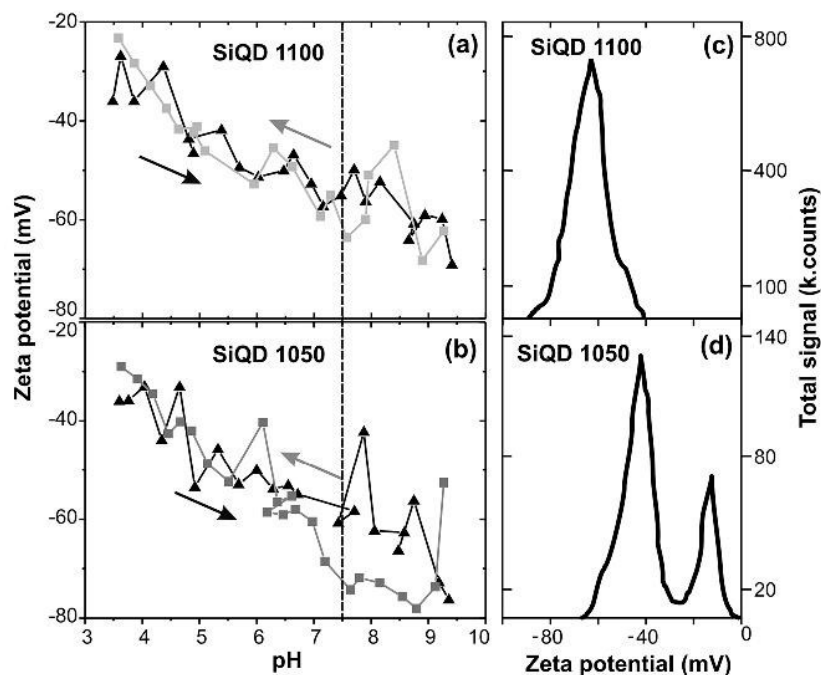


Fig. 4 Zeta-potential evaluation: (a) titration curves of SiQD 1100 and (b) SiQD 1050 (each point is average of three measurements). Small graphs show an example of single measurement of zeta potential at pH 7.5 in (c) SiQD 1100 and (d) SiQD 1050.

a reduction in metabolic activity occurred after 24 hours of incubation (also apparent in the form of changed cell morphology in Fig. 7b) and that at the 48 hour point the cells had already died.

This report presents the first study performed on the impact of novel Si-based nanoparticles on a biological environment consisting of a human osteoblast cell culture. The most unique property of the B and P co-doped SiQDs used consists of their

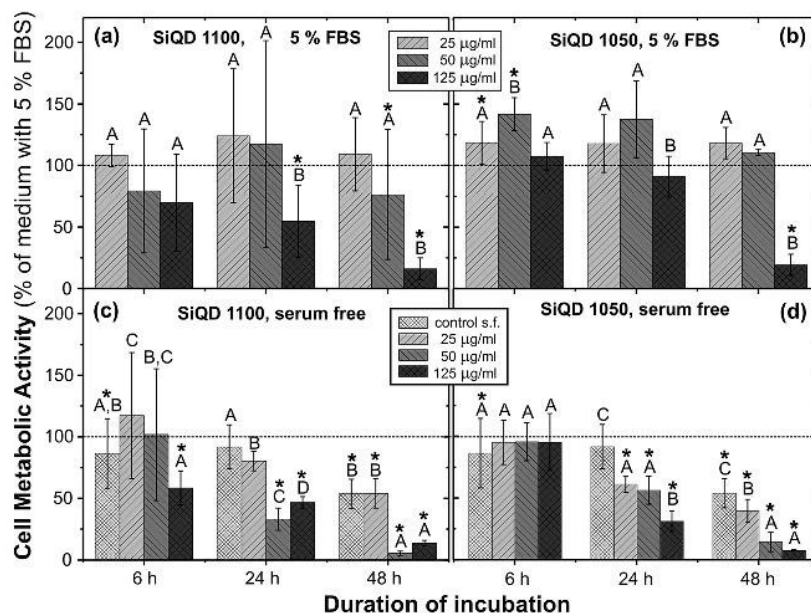


Fig. 5 Metabolic activity of osteoblasts cultivated in a cultivation medium supplemented with 5% FBS (a, b) and in serum free medium (c, d) for increasing concentration of SiQD 1100 (a, c) and SiQD 1050 (b, d). Relative values are expressed as a percentage of control sample in the cultivation medium with 5% FBS (dashed line). The star symbol (\*) highlights a significant difference from the control in cultivation medium with 5% FBS (Wilcoxon matched-pairs test,  $p < 0.05$ ). Groups marked with different letters express significant inter-group differences within time points (ANOVA, LSD *post hoc* test,  $p < 0.05$ ).



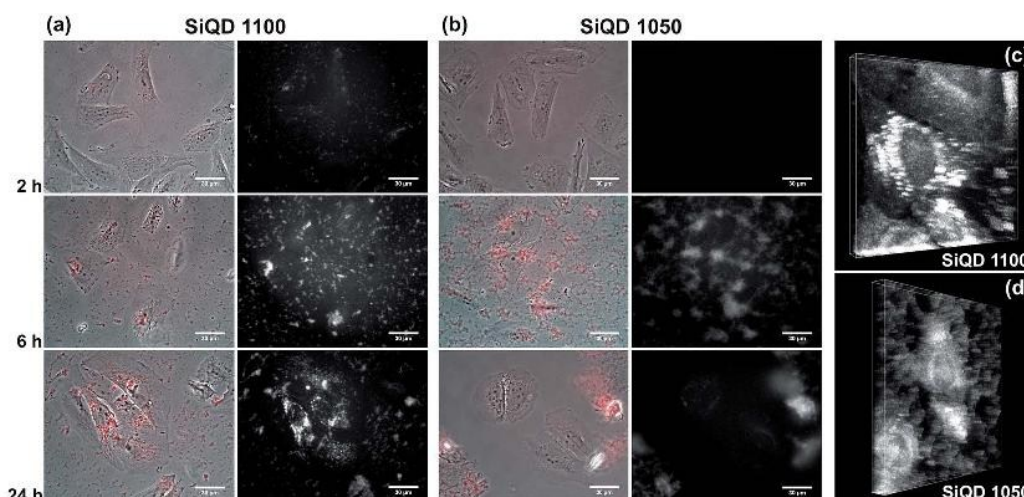


Fig. 6 Wide-field fluorescence and phase contrast microscope images of osteoblasts treated with (a) SiQD 1100 and (b) SiQD 1050 in 5% FBS-supplemented medium in different time points (the scale bar is 30  $\mu\text{m}$ ) and confocal images after 24 h of incubation with (c) SiQD 1100 (imaged volume 75.0  $\times$  75.0  $\times$  7.6  $\mu\text{m}$ ) and (d) SiQD 1050 (imaged volume 112.6  $\times$  112.6  $\times$  9.5  $\mu\text{m}$ ).

ability to form stable colloidal suspensions in the absence of surfactants and organic passivation. Moreover, these SiQDs required no protective shell layer and were of a very small size (3–4 nm in diameter) in contrast with other semiconductor quantum dots with a core-shell structure and which are substantially larger than 10 nm (not taking into account possible surface passivation) in order that they exhibit a stable emission in a similar spectral region on the border of red and infrared (700–850 nm).<sup>28</sup> We selected two types of SiQDs with sizes of 3 and 4 nm (SiQD 1050 and 1100 respectively) the PL emission peaks of which are situated in the afore-mentioned spectral range which is optimal in terms of fluorescence microscopy. Somewhat surprisingly, our experiments revealed significant differences with respect to the interaction of the two types of SiQD with cell cultures which could not be ascribed simply to the 1 nm size difference – at the cellular level such a small difference does not influence particle cytotoxicity and only a slight change in cellular uptake is able to occur.<sup>29–31</sup>

Zeta-potential ( $\zeta$ ) is related to colloidal suspension stability. The critical value of  $\zeta$  below which a suspension is unstable (and at which agglomeration can take place) is around  $\pm 30$  mV.<sup>32</sup> Generally,  $\zeta$  is result of the net electrical charge contained within the region bounded by the slipping plane. This charge is strongly dependent on ions present in the solution and therefore changes with pH value. The pH value, for which the net electrical charge is null, is called isoelectric point. Around this point the nanoparticles aggregate rapidly. With concern to biology, the surface potential of a particle is important in terms of the formation of protein corona – nanoparticles with different potentials will bind to different proteins or to different active sites on individual proteins which, in turn, may significantly influence the overall toxicity of nanomaterials. An example of the varying degree of toxicity of Si nanoparticles depending on the value of  $\zeta$  and the particle covering is reported in;<sup>10,11</sup> however, this effect has also been observed with respect

to other types of nanoparticles.<sup>33,34</sup> Our experiments resulted in different values of  $\zeta$  for Si QD 1050 and 1100; therefore we suspect the formation of a differing protein corona under the same biological conditions.

Both of the tested SiQDs caused harm to the cells in a different manner – SiQD 1100 exhibited a measurable harmful effect at the highest applied concentration level (125  $\mu\text{g ml}^{-1}$ ) as soon as after 24 hours of incubation in the fully-supplemented medium, while the negative effect of SiQD 1050 was not apparent until after 48 hours of incubation (Fig. 5). It is conjectured that this difference may be linked to the observed formation of dense clusters of SiQD 1050 with serum proteins (see the fluorescence images in Fig. 6). These clusters act as reaction centers and continue to grow thus forming huge aggregates which cover the outside membranes of the cells and prevent SiQD 1050 from entering the cells. When subjected to fluorescence microscopy, protein/SiQD 1050 aggregates are visible as fog-like structures which grow over time (Fig. 6b and d). Despite this effect, however, a number of uncovered locations were detected after 48 hours thus providing coarse information on the incorporation of SiQD 1050 into the cells (Fig. 6b). This phenomenon was also witnessed with respect to SiQD 1100 but to a significantly lesser extent which, nevertheless, still allowed for the visualization of the cells and their incorporation of SiQD 1100. Notably, literature describes this aggregation effect with respect to other types of nanoparticles.<sup>35,36</sup> Therefore, it is safe to conclude that the presence of FBS proteins in the cultivation medium strongly influence specific SiQD behavior and thus their availability and absorption by cells. It may be speculated from the fluorescence images (Fig. 6c) that the SiQD 1100 visible in cell cytoplasm are localized in vesicles and thus potentially enter cells by means of endocytosis as has been previously described.<sup>37–40</sup>

When SiQDs were incubated with cells in the serum-free medium, SiQD 1100 exhibited a cytotoxic effect at the highest



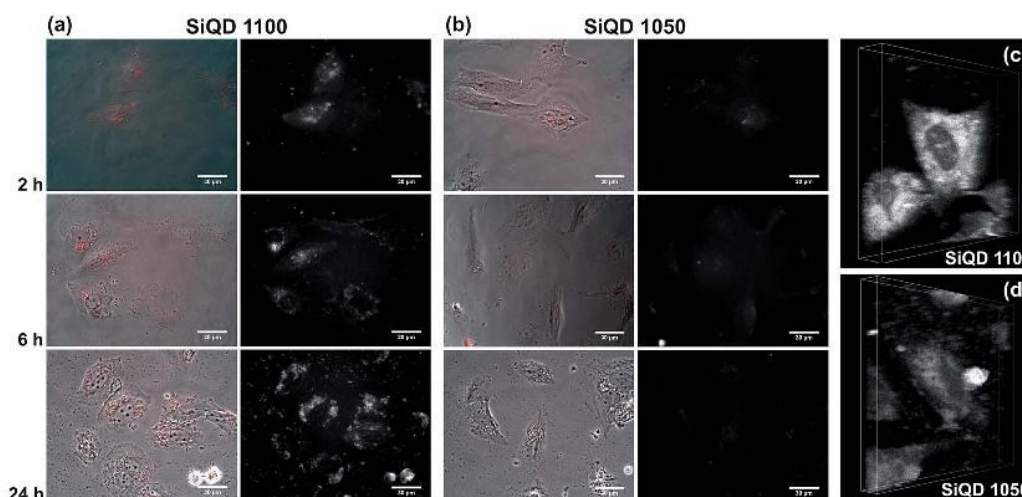


Fig. 7 Wide-field fluorescence and phase contrast microscope images of osteoblasts treated with (a) SiQD 1100 and (b) SiQD 1050 in the serum-free medium in different time points (the scale bar is 30  $\mu\text{m}$ ) and confocal images after 24 h of incubation with (c) SiQD 1100 (imaged volume 85.0  $\times$  85.0  $\times$  11.6  $\mu\text{m}$ ) and (d) SiQD 1050 (imaged volume 102.0  $\times$  102.0  $\times$  9.6  $\mu\text{m}$ ). Note – after 6 h of cell incubation in serum-free medium, FBS was added due to the cell survival purposes.

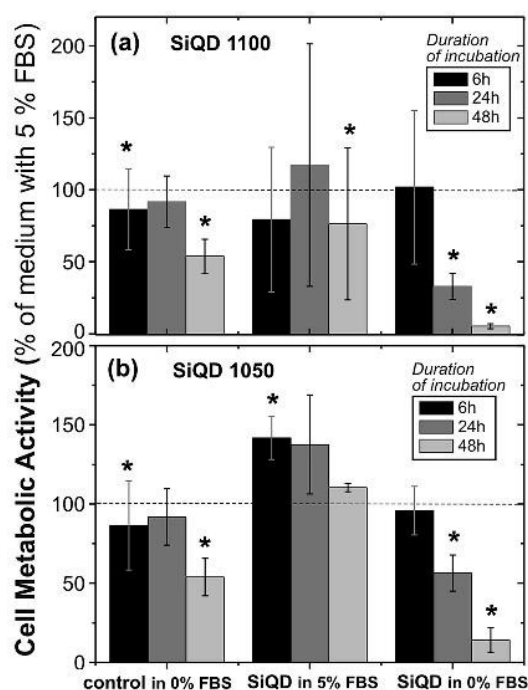


Fig. 8 Metabolic activity of osteoblasts treated with 50  $\mu\text{g ml}^{-1}$  of (a) SiQD 1100 and (b) SiQD 1050 for different time points.

applied concentration level (125  $\mu\text{g ml}^{-1}$ ) as soon as after 6 hours of incubation (Fig. 5c). Therefore, it was concluded that bare SiQDs (without a protein corona) are able to cross cell membranes more easily and efficiently than treated SiQDs. This statement was subsequently proven by means of fluorescence imaging (Fig. 7a) which revealed the presence of SiQD 1100 in the cell cytoplasm but, surprisingly, that it was localized diffusely rather than in the form of whole spots as in the case of

standard cultivation conditions with the presence of FBS. It would appear that the way in which SiQD 1100 enter cells varies under different conditions (with or without a protein corona), a fact that might be studied in greater detail in the future. SiQD 1050 required a longer incubation time (24 hours) before they entered the cells under serum-free conditions; importantly, however, the effect was significantly stronger – all the concentrations of SiQD 1050 tested were found to be cytotoxic after 24 hours (Fig. 5d). Both SiQDs in the serum-free medium were seen to harm the cells earlier and at a lower concentration than under fully-supplemented medium conditions. It has already been mentioned that nanoparticles lower their surface free energy *via* strong non-specific interaction with cell membranes. However, the amount of free energy is lowered by the presence of a protein corona and both the degree of adhesion to the membrane and cell uptake are reduced.<sup>41,42</sup> Thus the observed effect of proteins bound to SiQDs inducing a delay in the onset of cytotoxic effects is not surprising and is in agreement with previous observations.<sup>43,44</sup>

SiQD 1100 were detected within the cells under both test conditions – both with and without proteins originating from FBS; however, it was found that without proteins they enter the cells more rapidly, are distributed diffusely and have a stronger negative effect on metabolic activity. On the other hand, SiQD 1050 were not detected in the cells by means of fluorescence microscopy under either of the test conditions; however, the cytotoxic effect thereof was determined (Fig. 8b) which may indicate their entry into the cells. Moreover, the cytotoxic effect was found to be stronger under non-FBS protein presence conditions. This may imply the easier cell entry of SiQD 1050 without a protein corona. However, they were not observable *via* fluorescence microscopy images. We suspect, as PL aging studies suggest (Fig. 2c), that the PL of these SiQDs degrades to a significant extent in aqueous media (*i.e.* in the natural biological experiment environment). Moreover, it should be noted



that SiQD 1050 exhibit three times lower PL EQY and a slightly lower absorption cross-section, which renders them more difficult to observe by means of fluorescence microscopy (Fig. 6b and d).

The formation and structure of the protein corona is crucial in terms of the fate of all nanoparticles located in living organisms as has been demonstrated by a large number of previous studies.<sup>13,35,36,45</sup> Bare nanoparticles are unable to survive within a biological system since they are immediately covered by a layer of proteins from the fluid which forms the hard protein corona and which continues to grow until they attain a stable state, which is often a long-term process as observed in the case of SiQD 1050. Experiments conducted prior to *in vivo* application should always mimic the environment of the organism as precisely as possible. *In vitro* dose-dependent tests of nanoparticles should be performed using biological fluids only before forming conclusions on the cytotoxicity of the material. As was apparent especially in the case of SiQD 1050, the presence of bare SiQDs or protein-coated SiQDs in the cell culture makes a huge difference in terms of cytotoxicity and the immense aggregation of SiQD 1050 with proteins leads to fatal consequences for organisms.

## 4 Conclusion

We attempted to demonstrate to what extent novel co-doped SiQDs react upon being introduced into a natural biological environment consisting of human osteoblasts and a cell culture medium with or without the addition of fetal bovine serum. A series of experiments was conducted at various concentration levels of two types of SiQD (1100 and 1050), an evaluation was made of their cytotoxicity and their localization within the cell culture was assessed by means of fluorescence wide-field and confocal microscopy.

The detailed luminescence characterization of the SiQDs in colloidal suspensions at different times following fabrication as well as of the SiQDs inside cell cultures and water-based media enabled the research team to uncover the continuous changes which took place due to the aging of the SiQDs (a shift in the PL peak to shorter wavelengths and related EQY changes, Fig. 2). A detailed knowledge of PL aging allowed us to select the optimum type of SiQD (*i.e.* SiQD 1100) for fluorescence imaging purposes in cells with an optimal PL peak of around 750 nm and an ensemble EQY of 12%.

Zeta potential measurement indicated that the tested SiQDs differ from each other not only in terms of their size and PL properties but also with respect to zeta potential values. Consequently, the formation of a protein corona differs on the surface of SiQDs, which affects the reaction with the biological components of the cell culture medium and overall cytotoxicity. SiQD 1050 in particular were almost completely entrapped within growing aggregates of proteins which hindered their access into the cells which, in turn, led to the cytotoxicity of SiQD 1050 appearing to be relatively low. However, the real extent of cytotoxicity was revealed under serum-free conditions indicating that a high amount of SiQD 1050 enter cells despite the fact that they become undetectable by fluorescence

microscopes (due to a PL shift to shorter wavelengths with strong cell autofluorescence and the degradation of PL yield). On the other hand, SiQD 1100 exhibited a low level of interaction with proteins which enabled cell incorporation even in the serum-supplemented medium. Thus, these particles are able to enter cells in the bare state as well as with the addition of a protein corona although in each case the pathways most probably differ.

The results provide important findings concerning the *in vitro* toxicity of novel co-doped SiQDs and enhance our understanding of the complexity of processes acting between SiQDs and biological environments.

## Acknowledgements

This study was supported by the project LH14246 Kontakt II of Ministry of Education, Youth and Sports of the Czech Republic and by the Visegrad Group (V4)-Japan Joint Research Program on Advanced Materials (project NaMSeN) and by the project of National Sustainability Program I No. LO1503. This study was also supported by Charles University in Prague, First Faculty of Medicine (project PRVOUKP24/LF1/3) and Faculty of Medicine in Pilsen (SVV 260 279/2016).

## References

- 1 K. K. Qian and H. R. Bogner, *J. Pharm. Sci.*, 2012, **101**, 444–463.
- 2 E. J. Anglin, M. P. Schwartz, V. P. Ng, L. A. Perelman and M. J. Sailor, *Langmuir*, 2004, **20**, 11264–11269.
- 3 F. Erogbogbo, K.-T. Yong, I. Roy, G. Xu, P. N. Prasad and M. T. Swihart, *ACS Nano*, 2008, **2**, 873–878.
- 4 Y. Zhong, X. Sun, S. Wang, F. Peng, F. Bao, Y. Su, Y. Li, S.-T. Lee and Y. He, *ACS Nano*, 2015, **9**, 5958–5967.
- 5 X. Pi, T. Yu and D. Yang, *Part. Part. Syst. Charact.*, 2014, **31**, 751–756.
- 6 S. E. A. Gratton, P. A. Ropp, P. D. Pohlhaus, J. C. Luft, V. J. Madden, M. E. Napier and J. M. DeSimone, *Proc. Natl. Acad. Sci. U. S. A.*, 2008, **105**, 11613–11618.
- 7 X. Yang, J. Liu, H. He, L. Zhou, C. Gong, X. Wang, L. Yang, J. Yuan, H. Huang and L. He, *Part. Fibre Toxicol.*, 2010, **7**, 1–12.
- 8 H. Liang, C. Jin, Y. Tang, F. Wang, C. Ma and Y. Yang, *J. Appl. Toxicol.*, 2014, **34**, 367–372.
- 9 J. Kim, H. Kim and M. Kim, *Int. J. Nanomed.*, 2014, **9**, 235–241.
- 10 S. Bhattacharjee, L. H. J. de Haan, N. M. Evers, X. Jiang, A. T. M. Marcelis, H. Zuilhof, I. M. C. M. Rietjens and G. M. Alink, *Part. Fibre Toxicol.*, 2010, **7**, 25.
- 11 S. Bhattacharjee, I. M. C. M. Rietjens, M. P. Singh, T. M. Atkins, T. K. Purkait, Z. Xu, S. Regli, A. Shukaliak, R. J. Clark, B. S. Mitchell, G. M. Alink, A. T. M. Marcelis, M. J. Fink, J. G. C. Veinot, S. M. Kauzlarich and H. Zuilhof, *Nanoscale*, 2013, **5**, 4870–4883.
- 12 H. Herd, N. Daum, A. T. Jones, H. Huwer, H. Ghandehari and C.-M. Lehr, *ACS Nano*, 2013, **7**, 1961–1973.

- 13 M. Cui, R. Liu, Z. Deng, G. Ge, Y. Liu and L. Xie, *Nano Res.*, 2014, **7**, 345–352.
- 14 E. Roduner, *Chem. Soc. Rev.*, 2006, **35**, 583–592.
- 15 A. Lesniak, F. Fenaroli, M. P. Monopoli, C. Åberg, K. A. Dawson and A. Salvati, *ACS Nano*, 2012, **6**, 5845–5857.
- 16 M. P. Monopoli, C. Åberg, A. Salvati and K. A. Dawson, *Nat. Nanotechnol.*, 2012, **7**, 779–786.
- 17 M. Hadjidemetriou, Z. Al-Ahmady, M. Mazza, R. F. Collins, K. Dawson and K. Kostarelos, *ACS Nano*, 2015, **9**, 8142–8156.
- 18 H.-J. Eom and J. Choi, *Environ. Health Toxicol.*, 2011, **26**, e2011013.
- 19 S. W. Ha, J. A. Sikorski, M. N. Weitzmann and G. R. Beck, *Toxicol. In Vitro*, 2014, **28**, 354–364.
- 20 J. Kasper, M. I. Hermanns, C. Bantz, S. Utech, O. Koshkina, M. Maskos, C. Brochhausen, C. Pohl, S. Fuchs, R. E. Unger and C. James Kirkpatrick, *Eur. J. Pharm. Biopharm.*, 2013, **84**, 275–287.
- 21 M. Fukuda, M. Fujii, H. Sugimoto, K. Imakita and S. Hayashi, *Opt. Lett.*, 2011, **36**, 4026–4028.
- 22 H. Sugimoto, M. Fujii, K. Imakita, S. Hayashi and K. Akamatsu, *J. Phys. Chem. C*, 2012, **116**, 17969–17974.
- 23 J. Valenta, *Nanosci. Methods*, 2014, **3**, 11–27.
- 24 J. Valenta, M. Greben, Z. Remeš, S. Gutsch, D. Hiller and M. Zacharias, *Appl. Phys. Lett.*, 2016, **108**, 023102.
- 25 H. Sugimoto, M. Fujii, K. Imakita, S. Hayashi and K. Akamatsu, *J. Phys. Chem. C*, 2013, **117**, 11850–11857.
- 26 X. Liu, Y. Zhang, T. Yu, X. Qiao, R. Gresback, X. Pi and D. Yang, *Part. Part. Syst. Charact.*, 2016, **33**, 44–52.
- 27 E. Flahaut, M. C. Durrieu, M. Remy-Zolghadri, R. Bareille and C. Baquey, *Carbon*, 2006, **44**, 1093–1099.
- 28 E. Petryayeva, W. R. Algar and I. L. Medintz, *Appl. Spectrosc.*, 2013, **67**, 215–252.
- 29 R. G. Mendes, B. Koch, A. Bachmatiuk, A. A. El-Gendy, Y. Krupskaya, A. Springer, R. Klingeler, O. Schmidt, B. Büchner, S. Sanchez and M. H. Rummeli, *Biochim. Biophys. Acta*, 2014, **1840**, 160–169.
- 30 S. Chen, C. Zhang, G. Jia, J. Duan, S. Wang and J. Zhang, *Mater. Sci. Eng., C*, 2014, **43**, 330–342.
- 31 W. Zhang, M. Kalive, D. G. Capco and Y. Chen, *Nanotechnology*, 2010, **21**, 355103.
- 32 D. Fennell Evans and H. Wennerström, *The Colloidal Domain: Where Physics, Chemistry, Biology, and Technology Meet*, Wiley, New York, 2nd edn, 1999.
- 33 A. Asati, S. Santra, C. Kaittanis and J. M. Perez, *ACS Nano*, 2010, **4**, 5321–5331.
- 34 A. M. El Badawy, R. G. Silva, B. Morris, K. G. Scheckel, M. T. Suidan and T. M. Tolaymat, *Environ. Sci. Technol.*, 2011, **45**, 283–287.
- 35 M. P. Calatayud, B. Sanz, V. Raffa, C. Riggio, M. R. Ibarra and G. F. Goya, *Biomaterials*, 2014, **35**, 6389–6399.
- 36 W. Jiang, K. Lai, Y. Wu and Z. Gu, *Arch. Pharmacol. Res.*, 2013, **37**, 129–141.
- 37 L. W. Zhang and N. A. Monteiro-Riviere, *Toxicol. Sci.*, 2009, **110**, 138–155.
- 38 S. Ohta, S. Inasawa and Y. Yamaguchi, *Biomaterials*, 2012, **33**, 4639–4645.
- 39 A. Anas, T. Okuda, N. Kawashima, K. Nakayama, T. Itoh, M. Ishikawa and V. Biju, *ACS Nano*, 2009, **3**, 2419–2429.
- 40 P. Shen, S. Ohta, S. Inasawa and Y. Yamaguchi, *Chem. Commun.*, 2011, **47**, 8409–8411.
- 41 A. Lesniak, A. Salvati, M. J. Santos-Martinez, M. W. Radomski, K. A. Dawson and C. Åberg, *J. Am. Chem. Soc.*, 2013, **135**, 1438–1444.
- 42 P. Foroozandeh and A. A. Aziz, *Nanoscale Res. Lett.*, 2015, **10**, 221.
- 43 X. Jiang, S. Weise, M. Hafner, C. Röcker, F. Zhang, W. J. Parak and G. U. Nienhaus, *J. R. Soc., Interface*, 2010, **7**(1), S5–S13.
- 44 F. Catalano, L. Accomasso, G. Alberto, C. Gallina, S. Raimondo, S. Geuna, C. Giachino and G. Martra, *Small*, 2015, **11**, 2919–2928.
- 45 N. A. Monteiro-Riviere, M. E. Samberg, S. J. Oldenburg and J. E. Riviere, *Toxicol. Lett.*, 2013, **220**, 286–293.

D. Tereza Bělinová, **Lucie Vrabcová**, Iva Machová, Anna Fučíková, Jan Valenta, Hiroshi Sugimoto, Minoru Fujii, Marie Hubálek Kalbáčová (2018): **Silicon Quantum Dots and Their Impact on Different Human Cells**. Phys. Status Solidi B, 255, 1700597. IF = 1.729



# Silicon Quantum Dots and Their Impact on Different Human Cells

Tereza Belinova, Lucie Vrabcová, Iva Machová, Anna Fuciková, Jan Valenta, Hiroshi Sugimoto, Minoru Fujii, and Marie Hubalek Kalbacová\*

Silicon quantum dots (SiQDs) are interesting low-dimensional nanostructures whose unique optical and electronic properties can be exploited for imaging, biosensing, or drug delivery. SiQDs with a diameter of around 4 nm co-doped with boron and phosphorus and evincing fluorescence and dispersibility in aqueous solutions were studied with respect to their impact on different human cells. The level of SiQD cytotoxicity in different types of human cells – osteoblasts, monocytes, macrophages, and mesenchymal stromal cells – was determined. Exposing the cells to increasing concentrations of quantum dots under different conditions and the subsequent evaluation of their cytotoxicity provided an overview of cell-specific reactions to identical doses. The results revealed the importance of cultivation conditions (e.g., the formation of a protein corona on nanoparticles originating from the media supplement) as well as the significant impact of cell type (the increased sensitivity of monocytes to quantum dots in comparison to other cell types).

particularly suitable for use in single molecule tracking experiments in live cells. However, QDs are mostly made up of heavy metals which can be highly toxic with respect to the biological environment; moreover, this toxicity may influence the results (e.g., the triggering of different reactions such as cell stress resulting in apoptosis (programmed, physiological cell death) or necrosis (accidental, non-physiological cell death)). Silicon provides a promising material with respect to QDs due to its high degree of biocompatibility, biodegradability and chemical resistance to pH and temperature changes.<sup>[3,4]</sup>

Several methods are employed for the introduction of QDs into cells, commonly used is direct addition of QDs to cultivation media *in vitro* or intravenous injection *in vivo*. Particles thus administered firstly interact with the biological environment:

## 1. Introduction

Quantum dots (QDs) are used in the field of biology as an alternative to traditional organic dyes due to their high luminescence quantum yields and low photobleaching coefficients.<sup>[1,2]</sup> Thanks to their optical properties, QDs are

*in vitro* – interaction with the various components of the cultivation medium (fetal bovine serum (FBS) as a supplement and a source of proteins, aminoacids, etc.); *in vivo* – interaction with body fluids (plasma as an important component) – prior to coming into contact with the cells. Interaction with the various components of the biological environment allows the particles to acquire a so-called biomolecular corona, that is a layer of molecules (e.g., proteins, lipids, etc.) extracted from the environment that bind to the particles in dependence on their physico-chemical properties (zeta potential, surface termination, shape etc.).<sup>[5,6]</sup> This layer then provides the “new surface” of particles with an identity which is responsible for cell interaction. By altering the conditions under which QDs are introduced to the cells, it is possible to alter the way in which cells interact with the QDs and so modulate the results.<sup>[7]</sup> Moreover, biomolecular corona may not only modify the way of cell-nanoparticle interaction but also can cause quenching or enhancing of QDs fluorescence.<sup>[8,9]</sup>


The cells used in this study consisted primarily of stable cell lines (SAOS-2 human osteoblast cell line and THP-1 human monocytic cell line) and primary cells (hMSCs – human mesenchymal stem cells). SAOS-2 cells were used due to their well-described properties and behavior. The monocytic cell line was employed since, if one considers real application in the field of human medicine, immune cells will be the first cells to interact with the particles. Moreover, this cell line can be used in two stages – suspension monocytes and adherent macrophages.

T. Belinova, L. Vrabcová, Dr. I. Machová, Prof. M. Hubalek Kalbacová  
Faculty of Medicine in Pilsen  
Biomedical Center  
Charles University  
Pilsen, Czech Republic  
E-mail: marie.kalbacova@lf1.cuni.cz

Dr. A. Fuciková, Prof. J. Valenta  
Faculty of Mathematics and Physics  
Department of Chemical Physics and Optics  
Prague, Czech Republic

Dr. H. Sugimoto, Prof. M. Fujii  
Department of Electrical and Electronic Engineering  
Graduate School of Engineering  
Kobe, Japan

Prof. M. Hubalek Kalbacová  
1st Faculty of Medicine  
Institute of Pathological Physiology  
Charles University  
Pilsen, Czech Republic

 The ORCID identification number(s) for the author(s) of this article can be found under <https://doi.org/10.1002/pssb.201700597>.

DOI: 10.1002/pssb.201700597



Healthy mesenchymal stem cells were then used to test the reaction of primary cells, as opposed to stable lines that are derived from cancerous cells.

This study involved the testing of silicon-based quantum dots co-doped with phosphorus and boron on several types of human cells (monocytes, macrophages, osteoblasts and mesenchymal stem cells) in order to determine their influence on cellular viability (metabolic activity and necrosis detection) and, possibly, the mechanism behind this influence. In addition, the biomolecular corona variable was studied and its importance subsequently proved.

## 2. Results and Discussion

### 2.1. SiQDs

Figure 1a depicts a transmission electron microscope (TEM) image of SiQDs placed on a carbon-coated TEM mesh. The QDs were perfectly dispersed throughout the methanol and, thus, no agglomerates are evident in the TEM image. The average diameter of the QDs is 3.9 nm. The lattice fringe visible in the high-resolution TEM image in the inset corresponds to {111} plan of Si crystal. Figure 1b shows the PL spectrum of a methanol solution of SiQDs excited at 405 nm; broad luminescence is observed around 740 nm. This wavelength lies within the near-infrared window in biological tissue and is suitable for bio-imaging. The luminescence peak wavelength is slightly longer than that commonly reported for undoped SiQDs with comparable sizes.<sup>[7,10,11]</sup>

### 2.2. Cytotoxicity Experiments

#### 2.2.1. Determination of Metabolic Activity

Metabolic activity reflects the activity of mitochondria, which in other words, reflects cell viability. Different types of cells (osteoblasts, monocytes, macrophages, and human mesenchymal stem cells) were incubated with SiQDs over differing time intervals (6, 24 and 48 h) following which their metabolic activity

was measured. The used SiQD concentrations were selected on the basis of our previous study with similar SiQDs.<sup>[7]</sup> Incubation was performed under standard cultivation conditions (the medium plus 5% FBS) and non-standard conditions (no FBS presence in the first 6 h of incubation) aimed at preventing the formation of biomolecular coronas on the SiQDs – the interaction of the cells with “naked” nanoparticles.

The metabolic activity of osteoblasts (SAOS-2) decreased over time with respect only to the highest concentration of SiQD applied ( $100 \mu\text{g ml}^{-1}$ ) under standard conditions (Figure 2a), and the cytotoxic level (75% of control) was attained as early as following 6 h of incubation.<sup>[12]</sup> Under non-standard conditions, a decrease in cell metabolic activity was also evident with concern to those cells incubated with  $50 \mu\text{g ml}^{-1}$  SiQD for 48 h (Figure 2b). The difference between the cell reactions to SiQD under differing conditions might be explained by the presence of biomolecular corona on those SiQD cultivated under standard conditions altering, and possibly preventing, the entering of the particles into the cells and the consequent disruption of cell processes or organelles.<sup>[13]</sup>

On the other hand, the metabolic activity of hMSCs was comparable to or slightly less than that of the control cells; however, in neither case did they reach cytotoxic levels (Figure 2c,d). Thus, no effects stemming from the formation of biomolecular corona were apparent with respect to these primary cells following 24 h of incubation.

An evaluation of the effect of SiQDs with the immune cell line (THP-1) was conducted employing the two forms thereof, that is a suspension of monocytes (cells freely circulating in blood) and adherent macrophages (cells activated by for example pathogens).

The SiQDs had no impact on monocyte metabolic activity under standard cultivation conditions (Figure 2e); indeed, they even appeared to stimulate the cells within the first 6 h of cultivation. After 24 h under non-standard conditions, however, the cellular metabolic activity decreased to below a cytotoxic level of 75% with concern to both the 50 and  $100 \mu\text{g ml}^{-1}$  concentrations (Figure 2f) which shows that the presence of corona-forming molecules within the first few hours of incubation is crucial in terms of the fate of such cells. It is apparent that “naked” SiQDs damage monocytes in a concentration-dependent manner. Surprisingly, the significant activation of monocytes’ metabolic activity was observed after 6 h, especially under standard cultivation conditions, which may be connected with the commencement of an inflammatory response; however, this supposition must be subjected to further testing.

The adherent-type immune cells – macrophages – exhibited very similar results to those of the suspension monocytes. No reaction to SiQD presence was observed under standard cultivation conditions; however, a decrease was evident in metabolic activity after 24 h under non-standard conditions (Figure 2g,h). The reaction under non-standard conditions was more drastic than in the case of the monocytes, that is even the lowest concentration of SiQDs decreased metabolic activity to below the cytotoxic level. Interestingly, the decrease was not concentration-dependent.

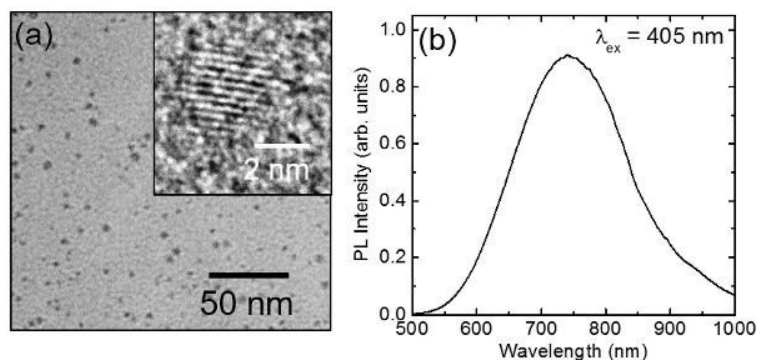
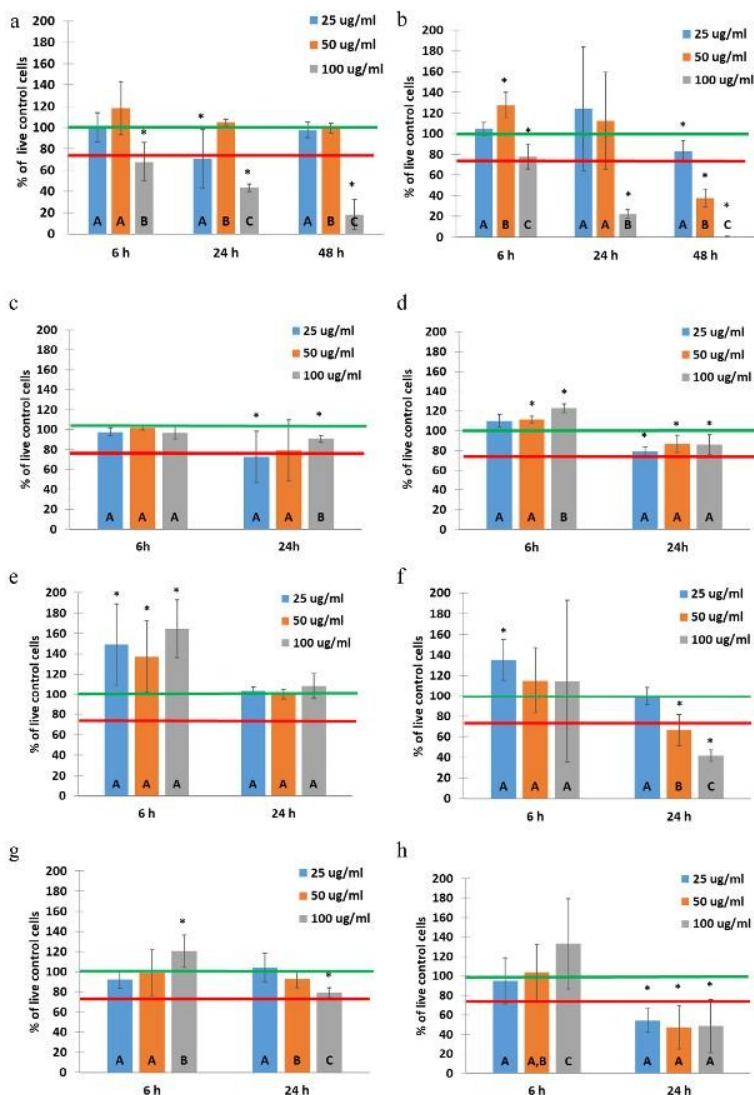


Figure 1. a) Transmission electron microscope (TEM) image of SiQDs. Inset: High resolution TEM image of a Si QD. b) Photoluminescence spectrum of Si QDs excited at 405 nm.





**Figure 2.** Metabolic activity of different cells (a,b) SAOS-2, (c,d) hMSC, (e,f) monocytes THP-1 and (g,h) macrophages THP-1, incubated with SiQD under standard (with FBS – a, c, e, g) and non-standard conditions (without FBS – b, d, f, h). Relative values are expressed as a percentage of control sample (untreated cells in adequate cultivation medium). The star symbol (\*) highlights a significant difference from the control in cultivation medium with 5% FBS (Wilcoxon matched-pairs test,  $p < 0.05$ ). Letters (A, B, C) represent grouping according to statistical similarity of the values within one time point (ANNOVA, Fischer LSD test). Green line shows 100% of control (live cells). Red line shows 75% of control (cytotoxicity level).

The presence or absence of FBS in the cultivation medium proved to be a key factor in terms of influencing SiQD-induced metabolic activity. As can be seen in Figure 2, practically no reaction can be observed with concern to most of the tested cell types under standard cultivation conditions in cases where a biomolecular corona is present. Under non-standard conditions, the situation changed, that is the reaction of the cells was very much dependent on cell type. The primary hMSCs evinced no significant reaction to these SiQDs; however, the stable cell lines (THP-1 and SAOS-2) responded to the presence of SiQDs after

24 h with a decrease in metabolic activity. This discrepancy may be due to the fact that immortalized cell lines are of cancerous origin and thus have different properties to primary mesenchymal stem cells extracted from healthy donors. Our results confirm that the biomolecular corona exerts a significant impact on the cytotoxicity of nanoparticles.<sup>[7,14]</sup>

### 2.2.2. Determination of Cell Death (Necrosis)

In order to determine the mechanism of the reduction effect of SiQDs on metabolic activity, the presence of lactate dehydrogenase (LDH) in the supernatants of osteoblasts and hMSCs was examined (Figure 3). LDH is an enzyme present inside all living cells and is detectable in the culture media only when cellular membrane is disrupted, which is typical hallmark of necrosis (accidental cell death). For positive control, the cells were killed using 10% Triton X and the level of detected LDH was set at 100% (black column). Untreated cells were used for the negative control (green column). With concern to the SAOS-2 cells, a certain level of LDH was detectable in all the samples; while a significant increase was detected in comparison to the negative control regarding only the highest concentration ( $100 \mu\text{g ml}^{-1}$ ) after 48 h under standard conditions and at the same concentration, it occurred significantly earlier (24 h) under non-standard conditions. A comparison of the results from metabolic activity of these cells (Figure 2a,b) with those of LDH led to an interesting discovery. Even though metabolic activity decreased significantly with the highest SiQD concentration after 24 h under both conditions, the level of detected LDH proved that no necrosis occurred. The results obtained under non-standard conditions after 48 h subsequently showed a decrease in metabolic activity as well as high levels of LDH in the cell supernatant. Therefore, it might be concluded that the cells were significantly stressed and underwent apoptosis after 24 h of incubation, but that after 48 h, necrosis provided the metabolic activity decrease mechanism.

Napierska et al. stated that small nanoparticles (under 15 nm in diameter) rapidly affect cellular viability.<sup>[15]</sup> In our case, however, it seems that the cells initially attempt to “deal with” the particles, but that after longer periods, their toxic impact under non-standard conditions leads to sudden necrotic death.

Only a very low level of LDH comparable with that of the healthy non-treated control was detected in hMSCs (Figure 3c,d). The slight decrease in the metabolic activity of hMSCs and the lack of an increase in the LDH level above the negative control implies that the mechanism of the SiQD effect most probably consists of apoptosis rather than necrosis. Apoptosis induced by silicon-based nanoparticles has been reported previously; thus, this mechanism should be subjected to further study.<sup>[16,17]</sup>



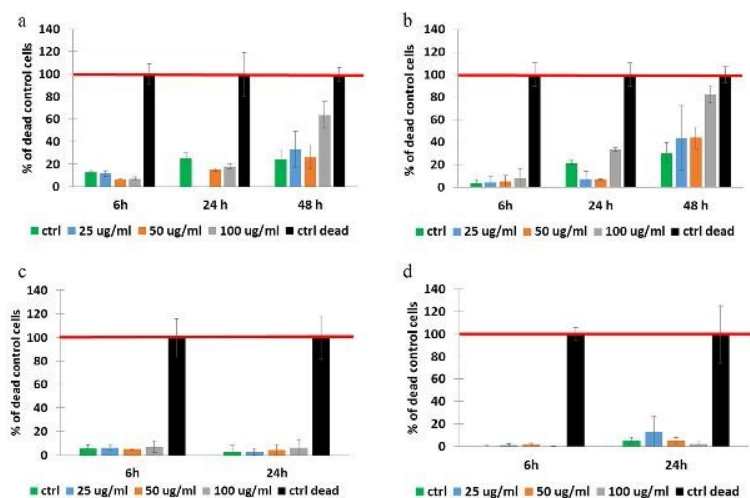


**Figure 3.** Determination of lactate dehydrogenase activity in cell supernatants indicating necrosis. SAOS-2 (a) and hMSC (c) cells with SiQD under standard conditions, SAOS-2 (b) and hMSC (d) under non-standard conditions. Relative values are expressed as a percentage of positive control sample (CTRL dead – cells killed within Triton X). Red line shows 100 % necrosis.

The possible apoptotic cell death caused by the cultivation of cells with SiQDs is supported by the microscopic observation of hMSCs cultivated under non-standard conditions (Figure 4). Their morphology apparently changed in relation to increasing concentrations of SiQDs. With respect to the highest SiQD concentration, the cells were present in comparable amounts to the control cells but were shrunken. The observed morphology is commonly known to be related to cellular stress, which, however,

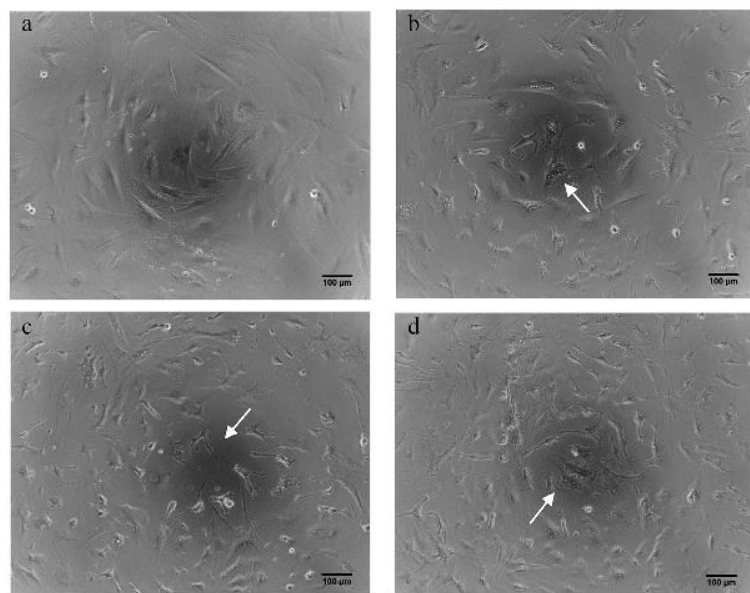


**Figure 4.** Bright field phase-contrast images of hMSC cells after 24 h in non-standard conditions (without FBS). a) Control cells without SiQDs, b)  $25 \mu\text{g ml}^{-1}$  SiQDs, c)  $50 \mu\text{g ml}^{-1}$  SiQDs, d)  $100 \mu\text{g ml}^{-1}$  SiQDs. Arrows mark distinctive changes in cellular morphology.

was not reflected in terms of metabolic activity. Thus, it might be speculated that the morphology changes may represent the display of the early stage of apoptosis, which is not detectable via methods employed to date. Further experiments are currently underway aimed at proving this supposition.

### 3. Conclusion

The results presented herein provide an interesting overview of the impact of P and B co-doped SiQD on different types of human cells. The importance of the biomolecular corona was demonstrated for all the cell types employed except for hMSCs. The absence of a biomolecular corona led to a significant decrease in cellular metabolic activity. The mechanism of this influence is not yet clear; however, the results obtained imply that cells may undergo apoptosis. Further research will focus on both the specific mechanisms involved in apoptosis induction and on inflammatory response activation of immune cells. The results provide a general insight into the potential biomedical application of these quantum dots.

### 4. Experimental Section

**SiQDs Preparation and Characterization:** The SiQDs co-doped with phosphorus and boron were prepared by means of previously reported technique.<sup>[10,18,19]</sup> Co-doped SiQDs can be dispersed in polar solvents (water, alcohol) due to the negative surface potential (zeta potential:  $-50 \text{ mV}$ ) induced in the highly phosphorus and boron co-doped surface, and they exhibit bright size-controllable luminescence in water over a wide pH range. The surface of co-doped SiQDs immediately following preparation is hydrogen-terminated and slowly oxidizes during storage in the solution, thus the SiQDs were stored in methanol for more than 30 days prior to use to replace completely of surface hydrogen atoms with oxygen atoms and rendered the surface inactive. This replacement was previously confirmed by FT-IR data that showed almost complete absence of hydrogen atoms on the surface.<sup>[20]</sup>

The TEM observation of SiQDs was performed using JEM-2100F electron microscope (JEOL Ltd.) operated at 200 kV. The SiQD solution was drop-casted on a carbon coated TEM mesh in order to obtain viewable sample. The PL spectra were excited by monochromatized Xenon lamp at 405 nm. Detection was performed by photomultiplier at 500–850 nm and an InGaAs photodiode at 800–1400 nm using spectrophotometer (Fluorolog-3, HORIBA Jobin Yvon).

**Cultivation Conditions:** SAOS-2 osteoblastic cell line (DSMZ, Germany) was seeded at a concentration of  $10\,000 \text{ cells cm}^{-2}$  in McCoy's 5A medium (GE Healthcare – HyClone) supplemented with 15% FBS (Biosera), L-glutamine (Life technologies),  $10\,000 \text{ U ml}^{-1}$  penicillin and  $10 \mu\text{g ml}^{-1}$  streptomycin (both Sigma-Aldrich).

Human MSC obtained from bone marrow blood aspirated from the posterior iliac crest from healthy donors after they had provided informed, written consent, were seeded at the same concentration in alpha-MEM with phenol red (Thermo Fischer Scientific), L-glutamine (Life



Technologies) and 10 000 U ml<sup>-1</sup> penicillin and 10 µg ml<sup>-1</sup> streptomycin (both Sigma-Aldrich) and supplemented with 10% FBS (Biosera).

A human monocytic cell line THP-1 (suspension monocytes) was seeded at a concentration of 25 000 cells cm<sup>-2</sup> in RPMI 1640 medium (Biowest) supplemented with 10% FBS (Biosera), L-glutamine (Life Technologies), 10 000 U ml<sup>-1</sup> penicillin and 10 µg ml<sup>-1</sup> streptomycin (both Sigma-Aldrich). In order to obtain adherent macrophages, 160 000 cells cm<sup>-2</sup> of monocytic THP-1 was seeded on 6-well plate (Techno Plastic Products) and cultivated for 72 h in a standard cultivation medium additionally supplemented with 100 nM phorbol 12-myristate 13-acetate (PMA, Sigma-Aldrich). Following the subsequent stimulation, the macrophages were seeded at a concentration of 25 000 cells cm<sup>-2</sup>.

The cells were pre-cultivated on 96-well plates in a CO<sub>2</sub> incubator at 37 °C for 24 h, then they were washed with pre-warmed phosphate buffer saline (PBS, Thermo Fisher Scientific – Gibco) and the SiQDs were added.

Particles provided in methanol were mixed with deionized water and placed in a dry bath at 70 °C to allow for the evaporation of the methanol and thus form an aqueous stock for immediate usage. The stock particles were diluted in the appropriate cultivation medium (DMEM for SAOS-2 cells, alpha-MEM for hMSCs and RPMI for THP-1 cells) supplemented with 5% FBS (or not supplemented) and added to the cells for 6, 24 and 48 h. After 6 h, FBS was added to the non-supplemented wells so as to attain a final concentration of 5% FBS aimed at avoiding cell inhibition and damage due to a lack of nutrients.

**Metabolic Activity Measurements:** Colorimetric assay (MTS, Cell Titer96<sup>®</sup> AqueousOne, Promega) based on the reduction of tetrazolium in metabolically active cells to formazan was used to establish metabolic activity. After 6, 24 and 48 h, the supernatant was stored at -20 °C for the subsequent determination of LDH. The cells were washed with PBS followed by the addition of 10% MTS solution in the corresponding media. In the case of the THP-1 cell suspension, the MTS was added directly to the samples to form a 10% solution inside the plate. Optical density was measured by means of a microplate reader (Synergy 2, BioTek Instruments, Inc.) at 490 nm, subtracting the background at 655 nm. The values obtained were related to the corresponding controls (non-treated cells) in terms of percentage.

**Microscopy Observations:** Bright field phase-contrast images for the visual evaluation of cellular conditions were acquired using a Nikon Eclipse Ti-S with a Nikon DS-Qi1Mc camera and a Nikon Plan Fluor 10x Ph1 DL objective.

**Detection of Necrosis:** A Cytotoxicity Detection Kit (LDH, Roche applied sciences) was used for the determination of the lactate dehydrogenase activity of the cell supernatants (markers of disrupted cell membranes and cell death) according to the manufacturer's instructions. Optical density was measured using a microplate reader (Synergy 2, BioTek Instruments, Inc.) at 490 nm, subtracting the background at 600 nm. The values obtained were related to the corresponding controls (the positive control was acquired via treatment with 10% Triton X (Sigma Aldrich) – dead cells).

**Statistical Analysis:** The data presents the means of all the experiments with error bars representing standard deviations. The non-parametric Wilcoxon matched pairs test and ANOVA (Fischer LSD test) were used for significance determination (P value of 0.05 and less) and grouping respectively. The statistical analysis was performed using STATISTICA software (StatSoft, Inc.).

## Acknowledgements

This study was supported by the V4 Joint Research Program Nr. 8F15001, by the project of National Sustainability Program I No. LO1503, both provided by Ministry of Education, Youth and Sports of the Czech

Republic and by PROGRES Q26 and SVV 260390 provided by Charles University. This study is also partly supported by JSPS KAKENHI Grant Number 16H03828.

## Conflict of Interest

The authors declare no conflict of interest.

## Keywords

cytotoxicity, necrosis, quantum dots, silicon

Received: October 27, 2017

Revised: March 9, 2018

Published online: April 3, 2018

- [1] J. Li, J.-J. Zhu, *Analyst* **2013**, *138*, 2506.
- [2] A. Valizadeh, H. Mikaeili, M. Samiei, S. M. Farkhani, N. Zarghami, *Nanoscale Res. Lett.* **2012**, *7*, 1.
- [3] E. J. Anglin, M. P. Schwartz, V. P. Ng, L. a. Perelman, M. J. Sailor, *Langmuir* **2004**, *20*, 11264.
- [4] I. I. Slowing, J. L. Vivero-Escoto, C.-W. Wu, V. S.-Y. Lin, *Adv. Drug Deliv. Rev.* **2008**, *60*, 1278.
- [5] M. P. Monopoli, C. Aberg, A. Salvati, K. A. Dawson, *Nat. Nanotechnol.* **2012**, *7*, 779.
- [6] E. Casals, V. F. Puentes, *Nanomedicine (Lond.)* **2012**, *7*, 1917.
- [7] L. Ostrovska, A. Broz, A. Fucikova, T. Belinova, H. Sugimoto, T. Kanno, M. Fujii, J. Valenta, M. H. Kalbacova, *RSC Adv.* **2016**, *6*, 63403.
- [8] L. Shang, G. U. Nienhaus, *Mater. Today* **2013**, *16*, 58.
- [9] M. M. Yallapu, N. Chauhan, S. F. Othman, V. Khalilzad-sharghi, C. Ebeling, S. Khan, M. Jaggi, S. C. Chauhan, *Biomaterials* **2015**, *46*, 1.
- [10] H. Sugimoto, M. Fujii, K. Imakita, S. Hayashi, K. Akamatsu, *J. Phys. Chem. C* **2013**, *117*, 11850.
- [11] M. Fujii, H. Sugimoto, K. Imakita, *Nanotechnology* **2016**, *27*, 262001.
- [12] E. Flahaut, M. C. Durrieu, M. Remy-Zolghadri, R. Bareille, C. Baquey, *Carbon (N.Y.)* **2006**, *44*, 1093.
- [13] G. Caracciolo, S. Palchetti, V. Colapicchioni, L. Digiacomio, D. Pozzi, A. L. Capriotti, G. La Barbera, A. Lagan, *Langmuir* **2015**, *31*, 10764.
- [14] A. Lesniak, F. Fenaroli, M. P. Monopoli, C. Aberg, K. A. Dawson, A. Salvati, *ACS Nano* **2012**, *6*, 5845.
- [15] D. Napierska, L. C. J. Thomassen, V. Rabolli, D. Lison, L. Gonzalez, M. Kirsch-volders, J. A. Martens, P. H. Hoet, *Small* **2009**, *5*, 846.
- [16] J. S. Nowak, D. Mehn, P. Nativo, C. P. Garcia, S. Gioria, I. Ojea-jimenez, D. Gilliland, *Toxicol. Lett.* **2014**, *224*, 84.
- [17] Y. Wu, W. Tang, P. Wang, C. Liu, Y. Yuan, J. Qian, *Part. Part. Syst. Charact.* **2015**, *32*, 779.
- [18] M. Fujii, H. Sugimoto, K. Imakita, *Nanotechnology* **2016**, *27*, 262001.
- [19] H. Sugimoto, M. Fujii, K. Imakita, S. Hayashi, K. Akamatsu, *J. Phys. Chem. C* **2013**, *117*, 6807.
- [20] T. Kojima, H. Sugimoto, M. Fujii, *J. Phys. Chem. C* **2018**, *122*, 1874.



G. Markéta Pišlová, Marie Hubálek Kalbáčová, Lucie Vrabcová, P. Slepíčka, Zdeňka Kolská, V. Švorčík (2018): **Preparation of Noble Nanoparticles by Sputtering – Their Characterization**. Digest Journal of Nanomaterials And Biostructures 13, 1035-1044. IF = 0.673

## PREPARATION OF NOBLE NANOPARTICLES BY SPUTTERING – THEIR CHARACTERIZATION

M. PIŠLOVÁ<sup>a,\*</sup>, M. H. KALBÁČOVÁ<sup>b,c</sup>, L. VRABCOVÁ<sup>b,c</sup>, P. SLEPIČKA<sup>a</sup>,  
Z. KOLSKÁ<sup>d</sup>, V. ŠVORČÍK<sup>a</sup>

<sup>a</sup>*Department of Solid State Engineering, University of Chemistry and Technology, Technická 5, 166 28 Prague, Czech Republic*

<sup>b</sup>*Biomedical Center, Faculty of Medicine in Pilsen, Charles University in Prague, alej Svobody 1655, 323 00 Pilsen, Czech Republic*

<sup>c</sup>*Institute of Pathological Physiology, 1<sup>st</sup> Faculty of Medicine, Charles University in Prague, U nemocnice 5, 128 53, Prague, Czech Republic*

<sup>d</sup>*Faculty of Science, J. E. Purkyně University in Ústí nad Labem, České Mládeže 8, 400 96*

In this work we present gold (AuNPs) and platinum (PtNPs) nanoparticles prepared by direct sputtering into liquid medium polyethylene glycol (PEG) with molecular weight of 600 g Mol<sup>-1</sup>. PEG was chosen for its properties and ability to stabilize NPs. The metal/PEG dispersions were mixed with water for their stabilization. This approach for nanoparticles preparation can be realized without harmful reducing agents or additional stabilizers and resulted in preparation of spherical AuNPs and rod PtNPs of the size below 10 nm. The D<sub>0,9</sub> diameter of AuNPs was 6.3 nm. On contrary, the D<sub>0,9</sub> diameter of PtNPs was 3.9 nm. The nanoparticles were characterized by transmission electron microscopy, atomic absorption spectroscopy, ultraviolet-visible spectroscopy and by dynamic light scattering. *In vitro* tests of cytotoxicity were carried out with prepared AuNPs and PtNPs and human osteoblastic cells and more cytotoxic effect was observed for AuNPs in comparison with PtNPs of similar concentrations.

(Received August 6, 2018; Accepted October 29, 2018)

*Keywords:* Au and Pt nanoparticles, Sputtering, Cytotoxicity, Characterization

### 1. Introduction

Nowadays nanoparticles represent one of the most studied topic. They have an important role in many areas such as catalytic reactions [1], medicine [2-4], food industry [5], etc. So this research topic is studied by scientists from different fields of science e.g. physicists, scientists, architects and researcher [6]. In recent years metal nanoparticles were used from industry to fine medical or biochemical utilization [7]. In medicine, metal nanoparticles were used as drug delivery systems, e.g. functionalized AuNPs or contrast agents. For example, magnetic resonance imaging (MRI) supported with Pt or PdNPs on Al<sub>2</sub>O<sub>3</sub> can provide high sensitivity during magnetic resonance imaging. Other well-known metal nanoparticles used in medicine are AgNPs. They are used as antimicrobial wound dressings [8]. The development in the field of nanotechnology focused on nanoparticle preparation is influenced by several requirements including disease diagnosis and therapy, energy and environmental protection. There are several approaches for gold nanoparticle preparation. The solutions based on polyethylenglycol, glycerol and several other liquids were proposed as liquid media for gold nanoparticle preparation and consequent testing as potentially suitable for antibacterial applications [9-11] or in tissue engineering for analysis of cell adhesion [12-14].

Many of chemical and physical methods have been used to prepare nanoparticles. Chemical approaches are based on reduction of metal compound to form colloidal solutions. These

---

\*Corresponding author: marketa.pislova@vscht.cz

solutions contain stabilizers to prevent aggregation of nanoparticles. There is problem with by-product and it is necessary to perform purifying steps after synthesis. Also almost all of these methods require the stabilizers, that means other chemical substances. Physical methods of preparation nanoparticles include sputtering, evaporation, laser ablation, ion ejection and electron-beam lithography. The sputtering is one of the cheapest physical methods how to prepare pure materials and nanomaterials. Nanoparticles prepared by the direct sputtering into liquid medium usually contains fewer impurities than those which were prepared by chemical synthesis. And these nanoparticles are often also very stable for a long time [15].

Nowadays there is also an effort to prepare nanoparticles without any harmful reducing agents, chemical stabilizers and to reduce generated waste, which can be achieved by direct sputtering of metals into liquid medium e.g polyethylene glycol (PEG) or glycerol. Sputtering is a well-established method, which is environmentally friendly [16, 17]. In all applications of nanotechnology, the size and shape of the nanoparticles play one of the most important role [13]. Nanoparticles are studied because they have unique physical and chemical properties that are different from "bulk" materials [7]. Concentration and particle size of nanoparticles can be regulated (influenced) by the target-substrate distance, the chamber pressure, the substrate temperature and the sputtering time [15]. Hatakeyama et al. [18] prepared solution of AuNPs in pure polyethylene glycol with particle size less than 50 nm. On the other hand Siegel et al. [10] prepared solutions of AgNPs and AuNPs by sputtering into glycerol/water mixture with particle size of  $3.5 \pm 1.4$  and  $3.5 \pm 2.4$  nm, respectively. Sputtering allows preparation of the spherical nanoparticles. Cha et al. [19] used liquid substrate which contains carbon and polyethylene glycol for sputtering of PtNPs. The particle size of these NPs was about 2 nm.

The application of nanomaterials has gained an increasing attention in medicine. Several kinds of metal-based NPs were established for biomedical application, such as gold (AuNPs), silver (AgNPs) and other metal nanoparticles [20, 21]. One of the most important applications of metal nanoparticles (NPs) are in drug delivery systems and in disease diagnosis and treatment of human beings as imaging probes. AuNPs have been tested as targeted delivery agents because of their high chemical stability and surface plasmon properties [22].

It was demonstrated that sole modulation of the surface area would make it possible to use AuNPs for therapeutic purposes [22]. Interactions between nanoparticles (NPs) and biomembranes depend on the physicochemical properties of the NPs, such as size, shape and surface charge. For example hydrophobic gold core can embed into the hydrophobic membrane interior and thus influence the cytotoxicity of NPs [21]. The influence of the cultivation medium was also studied with the aim to estimate nanotoxicity. It was observed that AuNPs can undergo an oxidation process in the supernatants and only a small amount of AuNPs and dissolved  $\text{Au}^{3+}$  was associated with cells. It was showed that 10 nm AuNPs exhibit a slight toxic effect [23]. The internalization of nanoparticles by cells (and more broadly the nanoparticle/cell interaction) is a crucial issue both for biomedical applications (for the design of nanocarriers with enhanced cellular uptake to reach their intracellular therapeutic targets, while many parameters can influence the nanoparticle/cell interaction, among them, the nanoparticle physico-chemical features) [24]. AuNPs showed interesting properties compared with natural materials and traditional polymer based materials with wide potential of antitumor activity [25] or as a carrier for in vivo gene activation in tissue regeneration [26], suggesting its potential as a multifunctional system with both gene delivery and antibacterial abilities in clinic [27]. Different sizes of PtNPs were employed for photothermal treatment of Neuro 2A cell lines [28].

We would like follow the published study which was focused on stabilization of gold and silver nanoparticle in PEG/water colloid solutions [9]. In this work we present a simple, reproducible and environmentally friendly approach of Au and PtNPs preparation by direct sputtering of Au or Pt into liquid polyethylene glycol (PEG). We studied properties of prepared inert Au and PtNPs dispersions. We characterized concentration, particle size and shape of Au and PtNPs (with AAS, TEM, DLS). We studied also their cytotoxicity at different concentrations with potential application as anti-bacterial agents [29, 30] or cell markers [31]. We chose these metal NPs because their cytotoxicity is relatively poorly studied.

## 2. Experimental

### 2.1 Materials, apparatus and procedures

Au and Pt targets (Safina s.r.o., purity of 99.9999%) were carried out at room temperature in a sputter coater device SCD 050 (Baltec, argon pressure 8 Pa), with the current of 30 mA and the distance of electrode about 50 mm. Polyethylene glycol with molecular weight 600 g Mol<sup>-1</sup> (PEG, Sigma Aldrich) was used as a medium for nanoparticles sputtering. The PEG volume for the Au or Pt deposition was 2 mL. The mixtures were diluted in distilled water at ratio 1:9 (PEG/water) [9, 32]. The schema of NPs preparation by direct sputtering of Au into pure PEG is presented in Fig. 1.

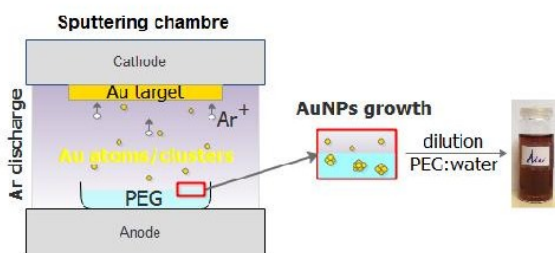


Fig. 1. Principle of AuNPs solution preparation by direct sputtering into liquid (PEG). The description corresponds to AuNPs.

### 2.2 Analytical methods

#### 2.2.1 Atomic absorption spectrometry (AAS)

Au and Pt concentrations were determined by AAS (AAS spectrometer Varian AA 880 with flame automatization to determine the total amount of elements, experimental error  $\pm 5\%$ ).

#### 2.2.2 Transmission electron microscopy (TEM)

Size and shape of AuNPs and PtNPs were examined by TEM (JEOL JEM-1010 (Japan), their images were taken by Megaview III digital camera (Soft Imaging Systems-Olympus, acceleration voltage of 80 kV) and analyzed by AnalySIS 2.0 software. Au and PtNPs in dispersions were analyzed also by HRTEM. HRTEM characterization was carried out on JEOL JEM-2200FS (JEOL Ltd., Japan) operand at 220 kV. Samples for transmission electron microscopy (TEM, HRTEM) were prepared by putting a drop of the colloidal solution on a copper grid coated with a thin amorphous carbon film placed on filter paper. Excess of solvent was removed. Samples were dried and kept under vacuum in a desiccator before putting them in a specimen holder [26]. Particle size was measured from the TEM micrographs and calculated by taking into account at least 400 particles.

#### 2.2.3 Dynamic light scattering (DLS)

Electrokinetic analyses (zeta potential determination) and size and distribution determination of the samples were performed with a Zetasizer Ver. 6.32 device, and Malvern software was used for data evaluation. As a light source, a laser with 366 nm wavelength was used. All samples were analyzed in 24 h from the preparation, at constant pH and room temperature [9, 33].

#### 2.2.4 Ultraviolet-visible spectroscopy (UV-Vis)

UV-Vis spectroscopy was used to characterize optical properties of Au and PtNPs in dispersions. Absorbance was measured in a 10-mm cell (Hellma Analytics cell, Quartz SUPRASIL, Type No. 100-QS) using a Perkin-Elmer Lambda 25 spectrophotometer (USA). Spectra were acquired in the range of 300-800 nm for AuNPs and for PtNPs in the range of 200-800 nm.



### **2.2.5 Cells and culture conditions**

The human osteoblast-like cell line SAOS-2 was obtained from DSMZ, Germany. SAOS-2 cells were cultivated in McCoy's 5A medium without phenol red (PromoCell, Germany) and supplemented with 15% heat-inactivated FBS (PAA, Austria), penicillin ( $20 \text{ U mL}^{-1}$ , Sigma-Aldrich, USA) and streptomycin ( $20 \mu\text{g mL}^{-1}$ , Sigma-Aldrich, USA) at  $37 \text{ }^\circ\text{C}$  and in a 5%  $\text{CO}_2$  atmosphere. Cells were collected at 60 – 90% confluence using trypsin and seeded onto 96-well plate (TPP, Switzerland) at a density of  $1 \times 10^4 \text{ cells cm}^{-2}$  and cultivated in this medium for 24 h. Then different concentration of AuNPs and PtNPs were added and cells were incubated for 24 h when the images were taken and metabolic activity was determined (see later).

### **2.2.6 Cell imaging**

Phase contrast images of the cells were acquired using an Eclipse Ti-S microscope (Nikon, Japan) with a Plan Fluor 10x (N.A. 0.30) objective and DS-U2 digital camera (Nikon, Japan).

### **2.2.7 Determination of Cell Metabolic Activity**

The cell metabolic activity test (Cell Titer 96 AQueous One Solution Cell Proliferation Assay, MTS, Promega, USA) was performed according to the standard protocol. Absorbance was determined using a multi-detection micro-plate reader (Synergy™ 2, BioTek, USA). The results were normalized (in percentage) with respect to the control cells with no NPs added.

All the data presented was derived from three independent experiments performed in triplicate. The results are presented in the form of mean values with error bars indicating standard deviations. The nonparametric Wilcoxon matched pairs test was used in order to determine significant differences between the datasets of the untreated control and the rest of the variables. An ANOVA was used to compare differing concentrations of Au or Pt with each other. P values of less than 0.05 were considered statistically significant. Extreme values were excluded from the analysis. Statistical analysis was performed using STATISTICA (StatSoft, Inc.) software.

## **3. Results and Discussion**

### **3.1 Concentration and morphology of NPs**

The concentration of AuNPs and PtNPs was determined by atomic absorption spectroscopy (AAS). Au/PEG solution contained  $56 \text{ mg L}^{-1}$  of Au and the Pt/PEG solution contained  $60 \text{ mg L}^{-1}$  of Pt. Particle size and shape of prepared NPs were studied with TEM (see Fig. 2) and HRTEM (see Fig. 3). From Fig. 2 it is apparent that AuNPs are smaller than 10 nm and they had spherical shape. Particle size distribution of AuNPs is presented in histogram ( $D_{0.9} = 6.3 \text{ nm}$ ). On contrary, PtNPs are even smaller and they embodied the rod shape of two different sizes. Particle size distribution of PtNPs is presented in histogram ( $D_{0.9} = 3.9 \text{ nm}$ ). It is known that gold (Au) and platinum (Pt) grows in a square fcc crystal structure. Fig. 3 shows prepared NPs studied with HRTEM.

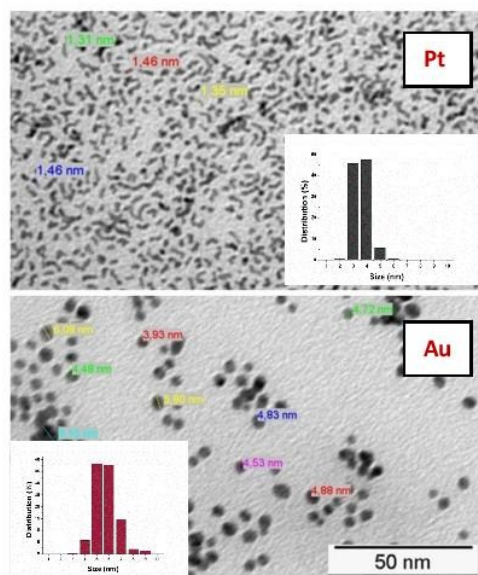


Fig. 2. TEM images of AuNPs and PtNPs sputtered into PEG after deposition diluted with water in ratio 1:9 with inset figure of size distribution histograms.

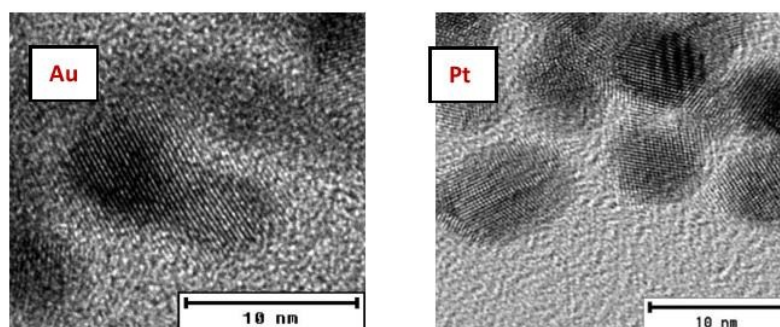


Fig. 3. HRTEM images of AuNPs and PtNPs sputtered into PEG after deposition diluted with water in ratio 1:9.

### 3.2 Zeta potential and NPs size

Dynamic light scattering (DLS) served for (i) zeta potential determination and for (ii) NPs size and distribution determination. Results are presented in Fig. 4 for freshly prepared NPs (fresh) and NPs diluted in cell cultivation medium (diluted). Zeta potential values of prepared NPs ( $-66.5 \pm 0.9$  mV for AuNPs and  $-64.2 \pm 8.7$  mV) indicate very good stability of nanoparticles colloids. In a literature the zeta potential about  $\pm 30$  mV indicate stable colloidal samples, zeta potential about  $\pm 50$  mV even the good stability [33, 34]. It is evident the zeta potential both of NPs samples dramatically have changed after dilution in cell cultivation medium (to the values of  $-7.3 \pm 0.8$  mV for AuNPs and  $-4.8 \pm 0.3$  mV) which indicated a poor stability. It can be explained by the fact the cultivation medium changed dramatically concentration of liquid medium surrounding NPs due the presence of salts of quiet high concentration. This higher concentration of medium resulted in press of electrical double layer on the nanoparticle surface and due to this to the dramatic changes of surface charge. Surface charge plays the important role on nanoparticle size. For zeta potential below 30 mV the stability of nanoparticles decreases and particles agregates. This is visible in Fig. 4 (right) where sizes of nanoparticles are presented. While size for Au NPs (fresh) was determined by DLS as  $15.8 \pm 0.9$  nm, which indicate spherical particles of uni-



dispersed size of very small distribution, size of AuNP diluted in cell cultivation medium was determined as  $33.7 \pm 17.7$  nm which indicates bigger particles of quite wide distribution. DLS study of size of PtNPs resulted in three dimensions for fresh PtNPs ( $1.5 \pm 0.5$  nm,  $4.2 \pm 0.4$  nm and  $7.9 \pm 0.9$  nm) which indicated particles of rod shape which had the uniform wide of  $1.5 \pm 0.5$  nm and two different lengths  $4.2 \pm 0.4$  nm or  $7.9 \pm 0.9$  nm, which is visible in Figure 4 right in details. Also after dilution in cell cultivation medium the PtNPs sizes increase to the  $8.0 \pm 1.5$  nm and  $37.9 \pm 7.6$  nm which indicate the rod shape have stayed for PtNPs but their size is bigger and distribution is wider.

Estimated sizes and shapes of NPs correspond well with that obtained by TEM analyses.

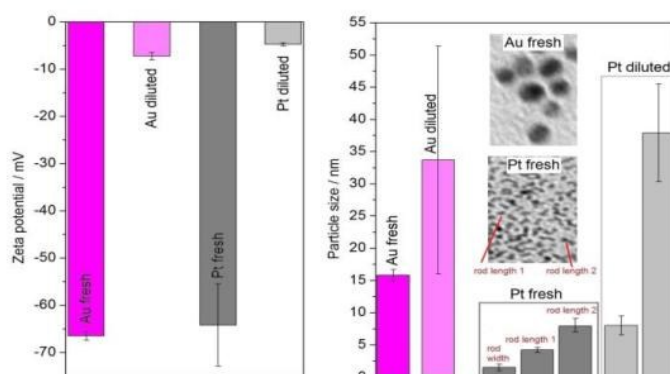


Fig. 4. Zeta potential (left) and nanoparticle size (right) of AuNPs and PtNPs after deposition diluted with water in ratio 1:9 (fresh) and subsequently diluted in cell cultivation medium (diluted).

### 3.3 Optical properties

Optical properties of Au and PtNPs in dispersions were measured by UV-Vis spectroscopy. Fig. 5 shows UV-Vis spectra of Au and PtNPs. The colloidal dispersion of AuNPs have a significant absorption peak maxima. Prepared AuNPs solution has absorption peak maxima at 515 nm and it is in accordance with [9], where the peak maximum of prepared AuNPs was determined at 517 nm. The position of peak maxima depends on particles size, shape and concentration of NPs in solutions [9]. UV-Vis spectrum of PtNPs exhibits an increasing absorption at a part of ultraviolet wavelength. It is in accordance with measurements of pure PtNPs in [35, 36]. At detail of PtNPs spectrum in Fig. 5, there are two small peaks. First peak has absorption maximum at 202 nm and second at 206 nm. These two small peaks can indicate two dimension of PtNPs rods. There is no literature which could be used for comparison of this results and presumption. But, in our cases, we can confirm our observation due to the size and shape of PtNPs were confirmed by transmission electron microscopy (TEM) and dynamic light scattering (DLS) with the similar results. Similar case was published about gold nanorods. Because of different plasmon oscillations, one of peaks corresponding to the transverse and second to the longitudinal plasmon oscillation [37, 38].

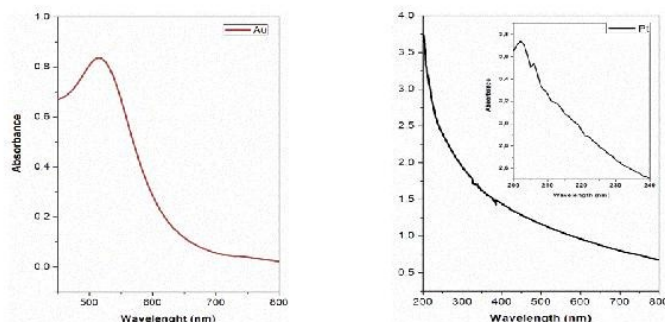


Fig. 5. UV-Vis spectra of AuNPs (left) and PtNPs (right) with inset images of prepared NPs solutions.

### 3.4 Cytotoxicity

To find out the effect of AuNPs and PtNPs on cells (osteoblasts) were cultivated in a medium supplemented with 15 % FBS with gradually increasing concentrations of AuNPs and PtNPs (0.56, 2.8, 5.6, 8.4, 11.2 and 14.0 mg L<sup>-1</sup> of AuNPs and 0.6, 3.0, 6.0, 9.0, 12.0 and 15.0 mg L<sup>-1</sup> of PtNPs, respectively) which was followed by the determination of their metabolic activity after 24 hours (Fig. 6). It is apparent that both particles in dependence on their concentration had cytotoxic effect on these cells. Despite similar concentrations of AuNPs and PtNPs used in the experiment more cytotoxic effect was observed in case of cells treated with AuNPs. Significant reduction of cell metabolic activity with cytotoxic effect (25 % of reduction) [39] was observed in cells treated with AuNPs of 11.2 mg L<sup>-1</sup>, whereas the same was observed with PtNPs only after using 15.0 mg L<sup>-1</sup>). The dying cells treated with the highest concentration of AuNPs (14.0 mg L<sup>-1</sup>) are presented in Fig. 7, where also unaffected cells treated with lower concentrations of AuNPs and low and high concentration of PtNPs are presented. According to results presented in Fig. 4, despite the fact that freshly prepared AuNPs and PtNPs differ in size, shape and zeta potential, after their addition to the cell cultivation medium they equalize in these parameters. Thus their different cytotoxic effect is most probably caused by other properties, which can be different surface chemistry, reactivity or catalytic properties. To conclude, both prepared AuNPs and PtNPs can be applied as delivery vehicles to cells, however, their concentration used should be well controlled.

On the basis of the results of this work and published results [40, 41], it can be assumed that the NPs thus prepared could find the application in tissue engineering and in medicine such as biosensors [42], drug carriers [19], or for example contrast agents for imaging (e.g. MRI) [8]. It is very important to know the particles' cytocompatibility for all these applications.

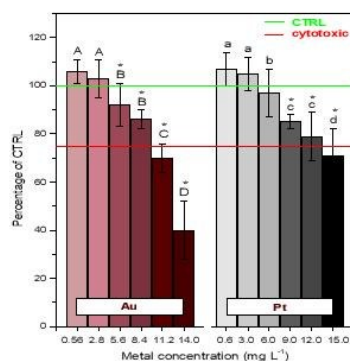


Fig. 6. Metabolic activity of osteoblasts incubated with different concentrations of Au and PtNPs for 24 h. Relative values are expressed as a percentage of untreated cells (CTRL). (Wilcoxon matched-pairs test,  $p < 0.05$ ). Different upper case letters express significant inter-group differences for the group of Au concentrations and lower case letters for the group of Pt concentrations (ANOVA, LSD post hoc test,  $p < 0.05$ ).

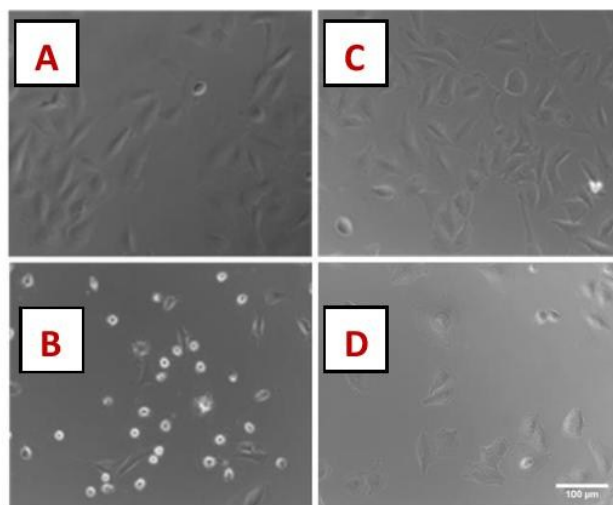


Fig. 7. Microscopic images of osteoblasts incubated with different concentrations of Au (A,B) and PtNPs (C,D) for 24 h: A–osteoblasts incubated with  $0.56 \text{ mg L}^{-1}$  AuNPs, B–osteoblasts incubated with  $14.0 \text{ mg L}^{-1}$  AuNPs, C–osteoblasts incubated with  $0.6 \text{ mg L}^{-1}$  PtNPs, D–osteoblasts incubated with  $15.0 \text{ mg L}^{-1}$  PtNPs.

#### 4. Conclusions

We prepared Au and PtNPs by direct sputtering into liquid polyethylene glycol with molecular weight of  $600 \text{ g Mol}^{-1}$ . The metal/PEG solutions were mixed with water. It is a simple and environmentally friendly method for preparing metal nanoparticles without any harmful reducing agents and chemical stabilizers. Sputtering is other way how to prepare nanoparticles by the so called green chemistry. The particle size of AuNPs and PtNPs were smaller than 10 nm. AuNPs had spherical shape of unique size.

The  $D_{0.9}$  diameter of AuNPs was 6.3 nm. PtNPs had rod shape of two lengths and the  $D_{0.9}$  diameter of PtNPs was 3.9 nm. UV-Vis spectra both of NPs colloidal samples were measured. AuNPs has significant absorption peak maxima at 515 nm. On the other hand colloid of PtNPs has two small peaks in wavelength about 200 nm. These two small peaks can indicate two dimensions of PtNPs rods. Their cytotoxicity was tested and despite the comparable properties of AuNPs and PtNPs in cultivation medium, AuNPs were significantly more toxic.

#### Acknowledgements

Financial support of this work from the Grant Agency of Czech Republic project no. 17-00885S and National Sustainability Program I no. LO1503 is gratefully acknowledged. Special thanks for technical support to Blanka Bilkova.

#### References

- [1] A. Corma, H. Garcia, *Chemical Society Reviews* **37**(9), 2096 (2008).
- [2] D. A. Giljohann, D. S. Seferos, W. L. Daniel, M. D. Massich, P. C. Patel, C. A. Mirkin, *Angewandte Chemie, International Edition in English* **49**(19), 3280 (2010).
- [3] O. V. Salata, *Journal Nanobiotechnology* **2**(1), 3 (2004).
- [4] L. Zhang, F. Gu, J. Chan, A. Wang, R. Langer, O. Farokhzad, *Clinical Pharmacology and*



- Therapeutics **83**(5), 761 (2008).
- [5] P. Sanguansri, M. A. Augustin, Trends in Food Science & Technology **17**(10), 547 (2006).
- [6] V. Saklani, J. V. Suman, K. Jain, Journal of Biotechnology Biomaterial (2012).
- [7] J. Siegel, A. Řezníčková, P. Slepíčka, V. Švorčík, Nanoparticles Technology, InTech, 2015.
- [8] R. J. White, R. Luque, V. L. Budarin, J. H. Clark, D. J. Macquarrie, Chemical Society Reviews **38**(2), 481(2009).
- [9] P. Slepíčka, R. Elashnikov, P. Ulbrich, M. Staszek, Z. Kolská, V. Švorčík, Journal of Nanoparticle Research **17**(1), 11 (2015).
- [10] J. Siegel, O. Kvítek, P. Ulbrich, Z. Kolská, P. Slepíčka, V. Švorčík, Materials Letters **89**, 47 (2012).
- [11] D.-Y. Kim, M. Kim, S. Shinde, J.-S. Sung, G. Ghodake, Colloids and Surfaces B **149**, 162 (2017).
- [12] M. Coluccio, S. De Vitis, G. Strumbo, P. Candeloro, G. Perozziello, E. Di Fabrizio, F. Gentile, Microelectronic Engineering **158**, 102 (2016).
- [13] V. Švorčík, T. Hubáček, P. Slepíčka, J. Siegel, Z. Kolská, O. Bláhová, A. Macková, V. Hnatowicz, Carbon **47**(7), 1770 (2009).
- [14] P. Slepíčka, I. Michaljaničová, N.S. Kasálková, Z. Kolská, S. Rimpelová, T. Ruml, V. Švorčík, Journal of Materials Science **48**(17), 5871 (2013).
- [15] M. Nie, K. Sun, D. D. Meng, Journal of Applied Physics, **106**(5), 054314 (2009).
- [16] V. K. Sharma, R. A. Yngard, Y. Lin, Advances in Colloid and Interface Science **145**(1-2), 83 (2009).
- [17] M. Staszek, J. Siegel, M. Polívková, V. Švorčík, Materials Letters **186**, 341 (2017).
- [18] Y. Hatakeyama, T. Morita, S. Takahashi, K. Onishi, K. Nishikawa, The Journal of Physical Chemistry C **115**(8), 3279 (2011).
- [19] I. Y. Cha, M. Ahn, S. J. Yoo, Y. E. Sung, RSC Advances **4**(73), 38575 (2014).
- [20] J. Broda, J. Setzler, A. Leifert, J. Steitz, R. Benz, U. Simon, W. Wenzel, Nanomedicine: Nanotechnology, Biology and Medicine **12**(5), 1409 (2016).
- [21] P. Slepicka, N.S. Kasalkova, J. Siegel, Z. Kolska, L. Bacakova, V. Svorcik, Biotechnology Advances **33**(6), 1120 (2015).
- [22] B. B. Karakoçak, R. Raliya, J. T. Davis, S. Chavalmane, W.-N. Wang, N. Ravi, P. Biswas, Toxicology in Vitro **37**, 61 (2016).
- [23] S. López-Sanz, N. R. Fariñas, R. S. Vargas, R. D. C. R. Martín-Doimeadios, Á. Ríos, Talanta **164**, 451 (2017).
- [24] V. Forest, J. Pourchez, Materials Science and Engineering: C **70**(Pt 1), 889 (2017).
- [25] T. Muthukumar, B. Sambandam, A. Aravinthan, T. P. Sastry, J.-H. Kim, Process Biochemistry **51**(3), 384 (2016).
- [26] L.-H. Peng, Y.-F. Huang, C.-Z. Zhang, J. Niu, Y. Chen, Y. Chu, Z.-H. Jiang, J.-Q. Gao, Z.-W. Mao, Biomaterials **103**, 137 (2016).
- [27] Z. Liu, Y. Jiao, Y. Wang, C. Zhou, Z. Zhang, Advanced Drug Delivery Reviews **60**(15), 1650 (2008).
- [28] M. Manikandan, N. Hasan, H.-F. Wu, Biomaterials **34**(23), 5833 (2013).
- [29] J. Siegel, K. Kolářová, V. Vosmanská, S. Rimpelová, J. Leitner, V. Švorčík, Materials Letters **113**, 59 (2013).
- [30] V. Vosmanská, K. Kolářová, S. Rimpelová, Z. Kolská, V. Švorčík, RSC Advances. **5**(23), 17690 (2015).
- [31] N. Tlotleng, M. A. Vetten, F. K. Keter, A. Skepu, R. Tshikhudo, M. Gulumian, Cell Biology and Toxicology **32**(4), 305 (2016).
- [32] A. Reznickova, P. Slepicka, N. Slavikova, M. Staszek, V. Svorcik, Colloids Surfaces A: Physicochemical and Engineering Aspects **523**, 91 (2017).
- [33] Z. Kolská, M. Čemoušek, M. Staszek, J. Leitner, V. Švorčík, Journal of Molecular Liquids **218**, 363 (2016).
- [34] P. C. Hiemenz, R. Rajagopalan, Principles of colloid and surface chemistry, CRC press, 1997.
- [35] L. Chen, W. Zhao, Y. Jiao, X. He, J. Wang, Y. Zhang, Spectrochimica Acta Part A: Molecular and Biomolecular Spectroscopy **68**(3), 484 (2007).
- [36] H. Hei, H. He, R. Wang, X. Liu, G. Zhang, Soft Nanoscience Letters **2**(03), 34 (2012).

- [37] P. K. Jain, S. Eustis, M. A. El-Sayed, *The Journal of Physical Chemistry B* **110**(37), 18243 (2006).
- [38] A. Řezníčková, Z. Kolská, P. Sajdl, V. Švorčík, *Materials Letters* **91**, 341 (2013).
- [39] E. Flahaut, M.-C. Durrieu, M. Remy-Zolghadri, R. Bareille, C. Baquey, *Carbon* **44**(6), 1093 (2006).
- [40] P. Slepíčka, J. Siegel, O. Lyutakov, N. Slepíčková Kasálková, Z. Kolská, L. Bačáková, V. Švorčík, *Biotechnology Advances* **36**(3), 839 (2018).
- [41] Y. Kalachyova, A. Oshtrem, O. A. Guselnikova, P. S. Postnikov, R. Elashnikov, P. Ulbrich, S. Rimpelova, V. Svorcik, O. Lyutakov, *ChemistryOpen* **6**(2), 254 (2017).
- [42] P. D. Howes, R. Chandrawati, M. M. Stevens, *Science* **346**(6205), 1247390 (2014).